ProQuest Number: 10700874

ProQuest 10700874

Published by ProQuest LLC (2017). Copyright of the Dissertation is held by the Author.

ProQuest LLC.
789 East Eisenhower Parkway
P.O. Box 1346
Ann Arbor, MI 48106 – 1346

EFFECTS OF ULTRASONIC IMPACT TREATMENT ON FATIGUE LIFE OF PRE-EXFOLIATED AA-2024-T351

Srinivas Pilli

A thesis submitted in partial fulfilment of the requirements of

Sheffield Hallam University

for the degree of Doctor of Philosophy

October 2008

Collaborating Organisation: Applied Ultrasonic's, Europe

I

Acknowledgements

Abstract

In this study investigations were made into the effects of Ultrasonic Impact Treatment (UIT) on pre-exfoliated AA 2024 T351. Electrochemical tests were conducted to determine any changes in electrochemical behaviour of the alloys due to UIT condition. Uniaxial monotonic, cyclic and fatigue crack propagation (FCG) tests were conducted on material in As-Received (AR) condition and UIT condition in air and in a corrosive environment by pre-exfoliating the test specimens at pre-defined set of time periods and temperature range (20 ^{0}C). It was clear that the fatigue performance was severely reduced by the introduction of the corrosion environment for AR specimens. SEM analysis suggests that UIT conditioned AA 2024-T351 exhibits resistance to exfoliation corrosion at ambient and temperatures ranging between 20°C to 40°C when compared to AR specimens. However, these results are not supported by potentiodynamic polarisation curves which show a decrease in corrosion resistance of UIT specimens. Also it is understood that there is a considerable amount of Cu refinement and enrichment near the surface when the AA 2024-T351 is subjected to exfoliation corrosion tests. Whilst hydrogen is in an atomic state, it can be adsorbed onto the metal surface and consequently diffuses into the matrix and can have serious detrimental effects. A reference line for minimal pre-existing hydrogen in the alloy is identified and the magnitude of hydrogen is found to be 180 Arbitrary Hydrogen Units (AHU). It is also found that in corrosion environment, the hydrogen ingress and further charging is prominent at ambient temperatures for AR samples, and showed damage over the full width of cross-section.

The following conclusions were drawn:

1.   UIT surface treatments, followed by exfoliation corrosion have shown increased resistance to a reduction in mechanical properties, notably tensile and yield strength. Fractographic analysis further supported this finding by showing smaller average brittle failure depths for UIT specimens when compared to AR specimens. SEM analysis of AR samples (without exfoliation) showed a crystallographic contribution to the mode of failure where high density slip bands are formed and the initial failure exhibits a step format.

2.   It is observed that during exfoliation, hydrogen ingress and adsorption is more prominent at ambient temperatures for AR samples.

3.   A slight improvement In Low Cycle Fatigue (LCF) life is observed for pre-exfoliated and UIT conditioned sample but not for UIT conditioned samples only. Little effect is observed for either treatment in the High Cycle Fatigue (HCF) region.

4.   Fatigue crack initiation occurred from the edges for all samples.

5.   Fatigue crack propagation of exfoliated specimens exhibited faster crack propagation than As-Received specimens. UIT caused retardation in crack propagation rate in AR samples but not in corroded samples. Failure of pre-exfoliated, UIT treated samples failed within the treated strip. It is also noted that crack deviation can occur when the crack tip reaches a secondary phase particle.

6.   Nanocrystallisation generates uniformity of the surface which refines the secondary phase particles and helps mitigate crack initiation sites.

Presentations

Presentations:

1. Oral Presentation at IOP held at University of Southampton, 2007

Topic – "Effects of Ultrasonic Impact Treatment as an effective Surface Engineering Treatment to Improve Corrosion Fatigue Properties of Pre-Exfoliated Al 2024 T351."

2. Oral Presentation at Corrosion Science Symposium, Sheffield Hallam University 2007

Topic – "Effects of Ultrasonic Impact Treatment and their corrosion fatigue properties of Pre-Exfoliated Al 2024 T351."

3. Oral Presentation at MERI Research Day 2005

Topic – "Use of Ultrasonic Impact Treatment to Improve Corrosion Fatigue Properties of Pre-exfoliated Al 2024 T351."

Poster Presentations

Poster Presentation at ICAM-IMURS, Bangalore, India 2007

Poster Presentation at EUROMAT, Nuremburg, Germany 2007

Contents

List of Figures

XIII

XIV

XVI

Nomenclature

a, a_0, a_f	crack length, initial crack length, final crack length	[m]
AR	As-Received AA 2024-T351	
AHU	Arbitrary Hydrogen Units	
C, m	empirical factors in Paris type relation	
d	depth of compressive stress region, grain size	[m]
D	grain size	[m]
E	Young's Modulus of Elasticity	[GPa]
E_{pit}	pitting potential	[V]
f	mathematical function	
i	half grain number (i = 1, 3, 5, …)	
K_c	material fracture toughness	[MPa√m]
K_{CL}	closure stress intensity factor	[MPa√m]
K_{eff}	effective stress intensity factor	[MPa√m]
K_I	mode I stress intensity factor	[MPa√m]
K_{max}	maximum stress intensity factor	[MPa√m]
K_{op}	opening stress intensity factor	[MPa√m]
k_y	locking parameter in Petch-Hall equation	
m_1, m_i	orientation factor of the first grain, of the ith grain	
N, N_f	life of component, cycles to failure	[cycles]
P	load	[m]
R	stress ratio	
UIT	Ultrasonic Impact Treatment	
UIT-C	Ultrasonic Impact Treated - Corroded	
Y	geometry factor	

ΔK	stress intensity factor range	[MPa$\sqrt{m}$]
%wt	Percentage weight	
δ, δ_t	displacement, crack tip opening displacement, CTOD	[m]
$\Delta\delta_t$	cyclic crack tip opening displacement	[m]
ΔK_{th}	threshold stress intensity range	[MPa$\sqrt{m}$]
K_{IC}	local stress intensity	[MPa$\sqrt{m}$]
ΔP	change in load, load range	[N]
$\Delta\sigma_{eff}$	effective stress range	[MPa]
$\Delta\sigma$	nominal stress range	[MPa]
σ	applied stress	[MPa]
σ_{max}	maximum stress	[MPa]
σ_{op}	opening stress	[MPa]
σ_y	yield strength of a polycrystalline material	[MPa]

CHAPTER   1

Introduction

1.1 Ageing Aircraft

Ageing of an aircraft is a process of systematic structural degradation of components as a result of various detrimental processes occurring during the life cycle of an aircraft. Potentially all aircraft are subjected to the issues of ageing. These aircraft have been and continue to be a safety concern internationally with a high public profile. Aircraft panels initially designed to meet fail safe design requirements can be significantly affected by the number of years and numbers of flying hours in service. Today, there is a growing number of aircraft which fall under the general title "ageing aircraft". Problems associated with structural failure were brought to world's attention with the 1988 Aloha Airlines 737 accident [1, 2] as shown in **Figure 1**. This accident raised concerns that structures could lose their inherent fail-safe condition as a result of fatigue damage and/or extensive corrosion.

Figure 1: A nineteen-year-old Boeing 737 aircraft lost a major portion of the upper fuselage near the front of the plane, in full flight at 24,000 feet.

1

Many civil transport aircraft were originally believed to be able to meet continuing structural airworthiness requirements for an indefinite period – in practice this has not always proved to be the case. The requirements for aircraft utilization have been steadily increasing in recent years. Current schedules and route structures are such that aircraft could see as many as 16 hours per day of service. High utilization could approach 6000 hours in a year, a number that has been steadily increasing over the past 10–15 years, resulting in fewer opportunities to allow an aircraft in for maintenance [3].

The structural integrity of aircrafts is of concern since factors such as fatigue cracking and corrosion are flight cycle and time dependent. Intensive investigations carried out over the last couple of decades have shown that the occurrence of corrosion appreciably reduces the mechanical performance of aluminium alloys, facilitates the onset of fatigue cracks and reduces appreciably the fatigue life and the fatigue crack growth resistance [4].

1.1.1 Lap joints and Corrosion Detection Problems

A particular corrosion inspection problem is the detection of hidden corrosion in lap joint structures. A lap joint is formed by at least two metallic skins joined together by fasteners. The presence of corrosion between the two skins will lead to thinning of the metal skin as well as pillowing (bulging) of the surface of the lap joint (caused by the presence of corrosion by-products). *When the thinning of the metal skin reaches a specified level, normally 10% of the nominal skin thickness, the section of the lap joint must be replaced.* Presently, this type of corrosion is detected mainly by visual inspection, e.g., by observing the pillowing of the surface when a beam of light (flash lamp) is directed onto the lap joint at a grazing angle. This method of detection is tedious, time consuming, very dependent on the operator as well as being qualitative in nature. Quantitative methods such as ultrasonic inspection are needed if the aerospace industry wishes to shift from a reactive mode toward corrosion (i.e. "find and fix") to a managed proactive approach (i.e. "predict and plan").

1.2 Aims & Objectives

The work presented in this PhD thesis addresses the structural degradation and crack growth characteristics of Al 2024-T351 and improvement of alloy performance using Ultrasonic Impact Treatment (UIT).

The aims of this study were initially defined as follows:

- To understand the effects of nanocrystallisation and compressive residual stresses on behaviour of untreated, corroded and UIT specimens.
- To correlate the UIT conditions with fatigue performance of corroded samples.
- To understand the effect of hydrogen induced embrittlement on untreated samples and corroded samples.
- To understand the structural degradation of Al 2024-T351 alloy subjected to exfoliation corrosion.
- To characterise the corrosion resistance of as-received and UIT conditioned samples.

1.3 Outline of this Thesis

Apart from this introduction, this thesis is organised as follows:-

In chapter 2, a comprehensive literature review focuses attention on scientific concepts, mechanisms pertaining to corrosion, corrosion fatigue and fracture mechanics of metallic materials. Fatigue mechanism both in air fatigue and corrosion fatigue are given. Additionally, the basics of hydrogen embrittlement are summarised and various existing models both in air and corrosive environments are analysed.

Chapter 3 considers the various existing surface engineering treatments and a brief description of these are illustrated.

Chapter 4 considers the experimental equipment used during this PhD project. It also provides the measurement and analysis methods used to obtain and interpret information.

The Chapter 5 to 10 comprises the knowledge obtained during this study.

Chapter 5 and chapter 6 provide results on corrosion and hydrogen embrittlement effects on untreated Al 2024-T351. A subsequent corrosion investigation was provided on UIT Al 2024-T351 and their results are compared.

Chapter 7 presents the influence of UIT on mechanical properties of Al 2024-T351 by comparing UIT specimens and As-Received (AR) specimens.

Chapter 8 presents the fatigue life and crack propagation results comparing untreated and UIT specimens.

Finally, chapter 9 brings together the main results and discussion of this thesis.

Chapter 10 & Chapter 11 provide conclusions of this thesis along with suggestions for future areas of work respectively.

CHAPTER 2

Literature Survey

2.1 Corrosion

2.1.1 Economic Impact and Effects

Corrosion is a natural process. A given corrosion problem usually concerns a specific environment. Just like water flows to the lowest level, all natural processes tend toward the lowest possible energy states. In other words, *Corrosion* is electrochemical reaction between a material and its environment that produces a deterioration of the material and its properties. According to a report presented to the Institute of Materials, Minerals and Mining (IoM3) corrosion damage is estimated to be between *2-3%* of GNP per year for the UK economy or on a more personal note that corrosion costs around £600 per capita per year; that's equivalent to around 1-2p/£ for each tax-payer [5].

2.1.2 Corrosion Classification

Aqueous corrosion can be classified in many ways. An important way of classification relevant to research would be according to the visual observation or use of magnification as shown in **Figure 2**. The mode of corrosion attack would be the basis of the classification.
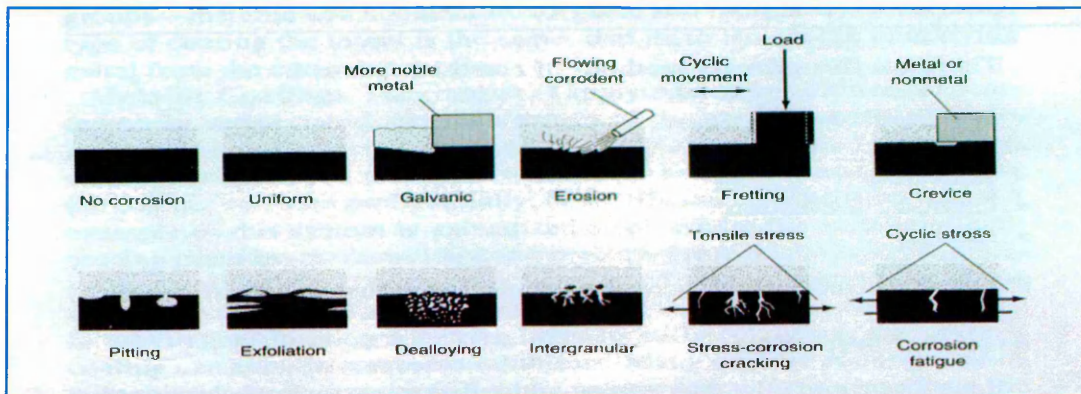
Figure 2: Schematics of common forms of corrosion [6].

5

However, not all corrosion cases would fit in more than one category. Nevertheless, corrosion classification system is quite useful to study its problems. **Figure 3** is a schematic chart which will categorise most of the corrosion cases.


```
                        ┌──────────────────┐
                        │    Corrosion     │
                        └──────────────────┘
              ┌──────────────────┐  ┌──────────────────┐
              │     Uniform      │  │    Localized     │
              └──────────────────┘  └──────────────────┘
```

Macroscopic	Microscopic
1. Pitting	1. Intergranular
2. Crevice	2. Stress Corrosion Cracking
3. Galvanic	3. Hydrogen Damage
4. Erosion-Corrosion	4. Corrosion Fatigue
5. Exfoliation	5. Fretting Corrosion
6. Selective Leaching	6. Cavitations
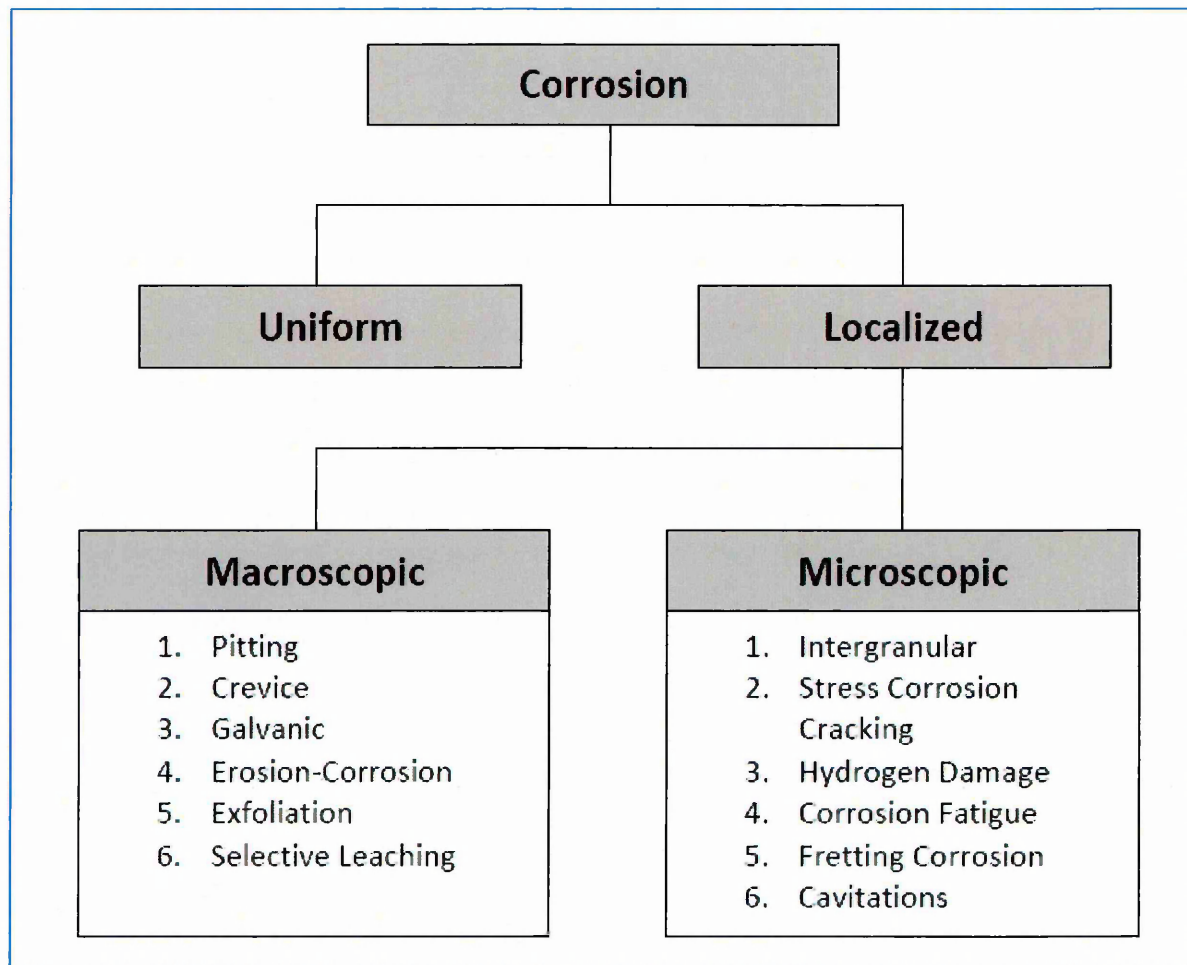
Figure 3: A chart categorising the various corrosion types.

2.1.3 Corrosion Processes

Most metals, especially important engineering ones such as iron and aluminium, are required to be extracted from their ores before they are of practical use. In the form of an ore the metal is in a low energy state. To remove the metal from its ore requires an input of energy, some of which is retained by the metal. The metal will readily give up this energy to revert to its original condition which it is able to do through corrosion processes.

An electrochemical process takes place during the corrosion of a metal or alloy in an electrolyte. This involves the transfer of electric charge and some metallic mass loss, which take place by means of two reactions. One reaction is known as oxidation (anodic reaction), whereby the metal gives up electrons and dissolution of the metal occurs. The other is known as reduction (cathodic reaction), where the newly flowing electrons are consumed. Examples of the reactions are given below.

Oxidation (anodic reaction):

$$Al \rightarrow Al^{3+} + 3e^-$$ (Aluminium oxidation) **Equation 1**

Reduction (cathodic reaction):

$$2H^+ + 2e^- \rightarrow H_2$$ (Hydrogen evolution/reduction) **Equation 2**

$$O_2 + 2H_2O + 4e^- \rightarrow 4OH^-$$ (Oxygen reduction) **Equation 3**
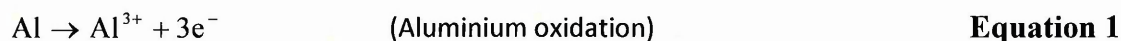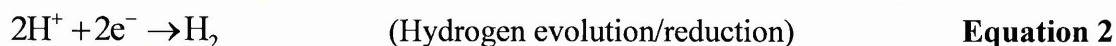
Other reactions may also occur between the ions within the electrolyte solution such as:

$$Al^{3+} + 3OH^- \rightarrow Al(OH)_3$$ (Formation of aluminium hydroxide) **Equation 4**
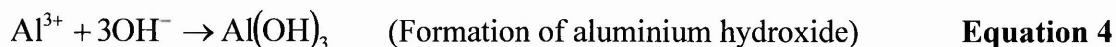
If the surface of a metal, which is in contact with an electrolyte, contains many active anodic and cathodic sites, then general corrosion of the metal will occur. However, if the surface has a good protective layer, such as aluminium oxide on aluminium, then, in general, these sites will not be able to react and the metal is passive. If, for some reason, a breach in the protective layer, or passive film, exists then corrosion can occur on a localised scale, however passivation may occur depending upon solution conditions.

2.1.4 Polarisation

In general terms, the deviation from equilibrium potential is called polarisation. Polarisation can also be defined as the displacement of electrode potential resulting from a net current. The driving force for the corrosion reaction is the potential difference between the anode and the cathode in the corrosion cell, and the reaction rate is equal to the current that flows through the cell. The total resistance throughout the corrosion cell is the total of the resistance associated with the anode plus the resistance of the ionic path plus the resistance associated with the cathode plus the resistance of the electronic path. As with the Ohm's law, i.e. $V = IR$ for the simple electrical circuit, the potential, current, and resistance in a corrosion cell are related. For a given potential difference between the anode and the cathode, the current or corrosion rate will increase as the resistance throughout the cell decreases and vice versa.

2.1.5 Passivity

Passivity is the characteristic of a metal exhibited when that metal does not become active in the corrosion reaction. Passivity is caused by the build up of a stable, tenacious layer of metal oxide on the surface of the metal. This oxide layer is formed by corrosion on a clean metal surface, where the corrosion products are insoluble in the particular environment to which the metal is exposed. Once the layer, or film, is formed, it acts as a barrier separating the metal surface from the environment. For further corrosion to occur, the reactants must diffuse through the oxide film. Such diffusion is very slow or non-existent, thus corrosion either decreases markedly or stops.

2.2 Modes of Corrosion in Al 2024-T351

2.2.1 Pitting

Pitting can be broadly classified as a form of localised corrosion of a metal surface, confined to a point or small area, which takes the form of cavities called pits as shown in **Figure 4**. Pitting is one of the most insidious forms of corrosion [6]. It causes equipment to fail because of through-wall perforation in pipes can occur which represents only a small percentage weight loss of the entire structure. Pitting can also accelerate the fatigue processes by generating preferential sites which act as stress concentration features where cracks can initiate and grow [7,8]. Furthermore it is often difficult to detect pits because the pits are often covered with corrosion products.

Micrograph 1
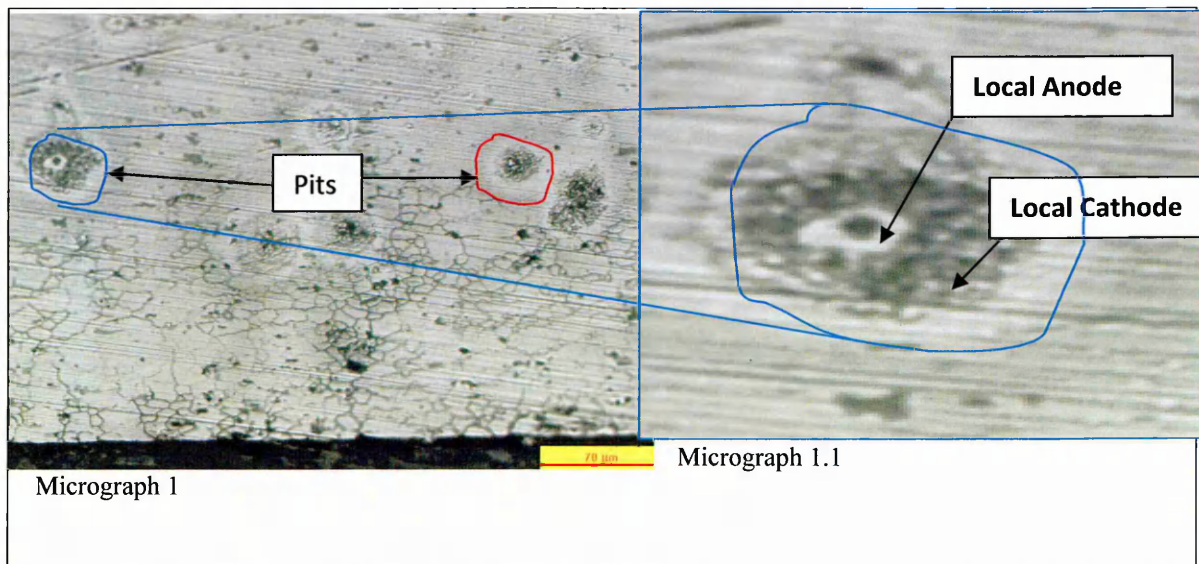
Micrograph 1.1

Figure 4: A cross-sectional SEM image for 24 hours exfoliation showing pit formation. Micrograph 1.1 shows an exploded view of a pit with a surrounding local cathodic region.

Pit growth is not always continuous, sometimes a pit may initiate but growth will cease if the conditions required for growth are no longer present, for example, if the potential difference between the anode and cathode is reduced as shown in **Figure 5**. Two important potentials exist for pit growth behaviour [9,10]. The first is the pitting potential, a potential above which pits nucleate and develops. The second is the re-passivation potential, below which pitting will cease and it is possible that the passive film may reform. At potentials between these two, pits already nucleated may continue to grow, although no new pits will nucleate. However, in some circumstances, pit growth will continue through a self perpetuating mechanism [2, 7]. When metal ions are produced within the pit, anions in the solution, such as chloride ions in aqueous solutions, are attracted towards the pitting area. Due to a hydrolysis process, the metal chloride will become a metal hydroxide and the chlorine will combine with the hydrogen ions to produce an acid, thus producing increased acidity within the pit. In the presence of hydrogen and chloride ions, dissolution of most metals will readily occur.

Aluminium depends on a protective film for corrosion resistance; it is susceptible to localized forms of corrosion due to the following reasons;

1. Chemical (acidity, low O_2 concentrations, Cl_2 concentrations/alkaline environments) or mechanical damage (scratches) to the protective oxide film [11].
2. Presence of secondary phase particles (Cu, Mg) or non-metallic inclusions.

Pitting occurs at local sites of passive film breakdown. Thus, corrosion resistance of aluminium alloys particularly 2xxx series depends on the extent of ability of the surface to form a passive oxide film.
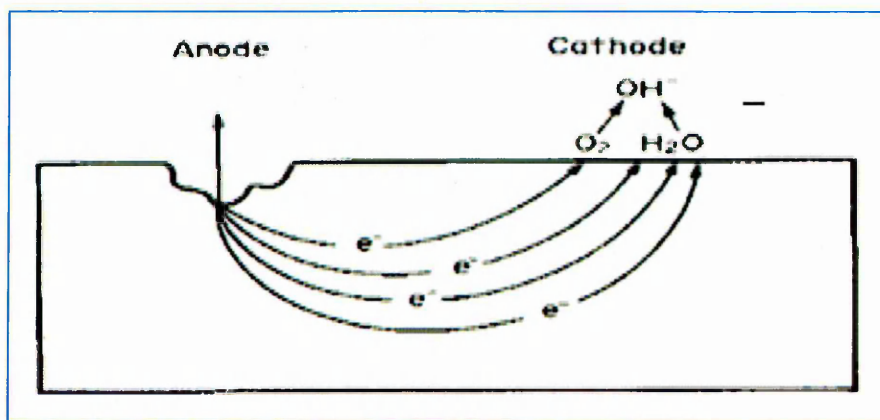
Figure 5: A schematic of anodic and cathodic sites in a corrosion cell.

Another driving power for pitting corrosion is the lack of oxygen around a small area. This area becomes anodic while the area with excess of oxygen becomes cathodic.

2.2.2 Intergranular Corrosion

Intergranular corrosion is localised attack along the grain boundaries, or immediately adjacent to grain boundaries, while the bulk of the grains remain largely unaffected. This form of corrosion is usually associated with chemical segregation effects (impurities have a tendency to be enriched at grain boundaries) or specific phases precipitated on the grain boundaries. Such precipitation can produce zones of reduced corrosion resistance in the immediate vicinity.

Aluminium is susceptible to intergranular corrosion due to the following reasons;

Preferential attack on the grain-boundary phase: The attack is usually related to the segregation of specific elements such as copper in 2xxx series of aluminium alloys or the formation of a compound in the boundary. Corrosion then occurs by *preferential attack on the grain-boundary phase*, thus making the grain boundary anodic relative to the remainder of the surface. The attack usually progresses along a narrow path along the grain boundary and, in a severe case of grain-boundary corrosion; entire grains may be dislodged due to complete deterioration of their boundaries. **Figure 6** shows a typical intergranular attack on Al 2024-T351 subjected to ASTM G110 [12] standards at ambient conditions for 48 hours.
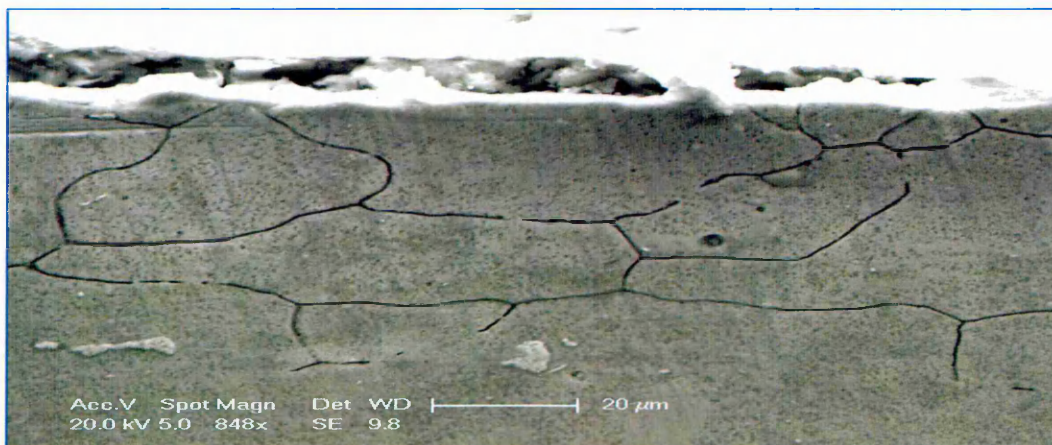
Figure 6: 48 hours of intergranular corrosion in ambient conditions according to ASTM G110 showing preferential path of intergranular attack along grain boundary

Voluminous effects: The corrosion products and the second phase particles form oxides and higher corrosion products which tend to create a typical tensile pressure in the affected

10

zones and this voluminous expansion mainly leads to loss of cross sectional area by removing material from surface along the rolling direction.

In **Figure 7,** the surrounded white region represents corrosion products formed due to exfoliation corrosion and as a results of these corrosion products, separation occurs along the rolling direction.
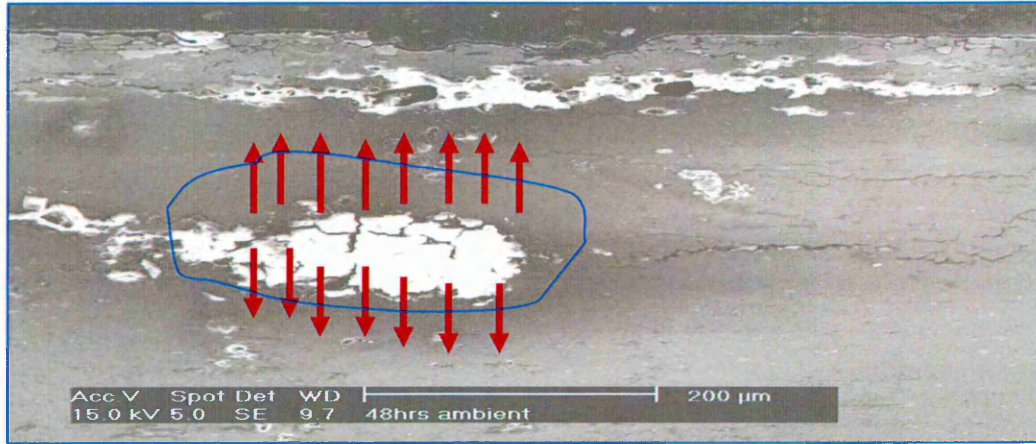
Figure 7: 48 hours of exfoliation corrosion according to ASTM G34 depicts intergranular corrosion due to voluminous effects of the corrosion products.

2.2.3 Stress Corrosion Cracking

Stress corrosion, or stress corrosion cracking (SCC), is caused by the combination of an applied or residual tensile stress and a corrosive environment. When SCC occurs there is usually no or little appreciable other corrosion damage. SCC can occur in mildly corrosive environments such as 3.5% NaCl solution and under stresses which would otherwise cause no damage to the metal. If either one of the two components required is removed, then the remaining component may have limited damaging effects on its own.

Mechanisms for SCC include: the breakdown of the protective oxide film and subsequent inter-granular or trans-granular cracking, accelerated by the applied stress; and a dissolution mechanism, whereby the anodic dissolution of the metal is accelerated by the applied stress because it increases the thermodynamic energy of the atomic bonds within the crystal lattice.

A large number of experimental results indicate that a major effect of hydrogen in solid solution on the plastic behaviour of Face Centred Cubic (F.C.C) crystals is to promote plastic strain localisation [13]. Hydrogen induced plasticity is increasingly invoked in many SCC cases. Delafosse [14] conducted experiments where a potential change from E_o to E_c after a 0.8% plastic strain is produced a macroscopic reduction of the elongation to failure, showing that hydrogen effects cannot be excluded.

The obvious assumption of hydrogen decreasing the local stress intensity (K_{IC}) via a decrease of surface energy due to absorbed hydrogen is the most straightforward mechanism one can propose to account for the embrittlement of metals subjected to hydrogen ingress. In F.C.C metals, dislocation sources are expected to be numerous in the vicinity of any SCC crack tip, and can easily be activated at any stress level and temperature.

2.3 Fatigue of Metallic Materials

2.3.1 Introduction
This chapter presents an overview of progress made in understanding the behaviour of corrosion fatigue and the importance of the current research. The classification of the literature review is as follows:

1. **Plain Fatigue**
2. **Corrosion Fatigue**

2.3.2 Plain fatigue

2.3.2.1 Introduction
The phenomenon of fatigue first became a topic of scientific investigation in the early 19th century. In fact, in 1838 Albert [15] first introduced the term "*fatigue*" while investigating the cyclic proof strength of cast iron mine hoist chains. However, detailed studies of the phenomenon were not conducted until later in 1843, when as a result of a number of tragic railway accidents attributed to fatigue, W. J. M Rankine was funded to investigate the fatigue of railway materials. In his work Rankine did numerous cyclic bending tests and noticed the general characteristics of metal fatigue. Components of machines, vehicles and structures are frequently subjected to repeated loads, also called cyclic loads, and the resulting cyclic stresses can lead to microscopic physical damage to the materials involved. Even at stresses well below the materials ultimate strength, this microscopic damage

accumulates with continued cycling until it develops into a crack or other macroscopic damage that leads to failure of the component. This process of damage and failure due to cyclic loading is called "fatigue". The understanding of mechanical failures from fatigue has been the subject of engineering efforts for more than 150 years. Albert was considered as the first person to explore the damage mechanism which occurs due to fatigue; he also tested mine hoist chains, made of iron, under cyclic loading, in Germany around 1828. The term "fatigue" was introduced by Poncelet [15] in his book on mechanics. The railway accident near Versailles in France, which resulted in the loss of many human lives, resulted in greater efforts by scientists to investigate the fatigue mechanism.

A British railway engineer, Rankine recognised some of the distinctive characteristics of fatigue fractures and noted the dangers of stress inducing concentration features in mechanical components. In the mid-1800s many researchers exerted significant efforts to study and understand the fatigue behaviour of mechanical components. Hodgkinson [15] is also one of the many investigators who studied the fatigue of wrought and cast iron used in railway bridges; this was done with the assistance of the British government. In 1860, Wohler [15] conducted systematic investigations of fatigue failures in railroad axles for the German railway industry. In addition to this Wohler was the first to characterise fatigue behaviour in terms of stress amplitude-life (S-N) curves and to introduce the concept of a fatigue endurance limit.

Significant progress has been achieved in the development and understanding of fatigue life approaches in last few decades. Before turning to a detailed review of the fatigue assessment of aluminium alloys, some books are mentioned which give an introduction to the subject and summarize the fundamentals as well as recent developments. Among others, Suresh [15] gives a comprehensive description of the mechanics and micro-mechanics of fatigue in metals. The topic of the textbook by Dowling [16] is the mechanical behaviour of materials in general, but emphasis is placed on practical methods of predicting the fatigue life of mechanical parts and structural members. He also emphasised the fatigue mechanism in materials (**See Section 2.3.2.2 Fatigue failure mechanism**) and how the mechanism can be affected by a wide variety of practical conditions.

Theories used for fatigue analysis, based on local surface strains, have been developed from the 1950's. A major feature of local strain fatigue is that fatigue lives to crack

initiation can be calculated. This is of increasing importance as more emphasis is being placed on product safety and product liability legislation, and as a result the traditional approach to 'total life' based on stress-life curves alone is becoming much less relevant. Simple cyclic plasticity models were developed to estimate elastic-plastic stresses from the measured strains, so that the effects of mean stress could be included.

2.3.2.2 Fatigue failure mechanism

The Institution of Mechanical Engineers, in Britain, explored the so called crystallisation theory of fatigue during 1840s. The pioneering work of Ewing and Humphrey [17] on interpretation of fatigue mechanisms based on the old re-crystallisation theory became the basis for the work of further research.

The mathematical framework for the quantitative modelling of fatigue failures was pioneered by the study of Irwin [18], with the help of the stress analyses concept developed by Inglis [19] in 1913, and the energy concept developed by Griffith in 1921. Griffith showed that the amplitude of stress singularity ahead of a crack could be expressed in terms of the scalar quantity known as stress intensity factor. Paris et al [20] were the first to suggest that the increment of fatigue crack advance per stress cycle, da/dN could be related to the stress intensity factor range, ΔK during constant amplitude cyclic loading.

Fatigue crack initiation can be a contentious subject. Often, fatigue life is considered to comprise three regimes: initiation; propagation; and failure. However, the initiation period is subject to the scale of observation [21]. Some assume initiation to be the cyclic period required for a crack to reach a detectable size, whereas others may regard initiation to be the onset of changes, at the microstructural level, in the material under scrutiny. As can be seen from the ensuing paragraphs, the fatigue phenomenon can be expected to start from the very first loading cycle.

As has been mentioned previously, fatigue failures can occur at stresses below the ultimate tensile stress or the yield stress of a material. However, for permanent changes to occur, i.e. the formation and propagation of a fatigue crack, localised plasticity must be present; therefore the yield stress must be achieved. Although the applied stress may be below the yield stress, local stresses at certain points within the stressed body may exceed the yield stress due to stress raisers. Some early observations of stress concentrations were made on a macroscopic level by Wohler [22] when he noted that on shafts with a sharply stepped

14

change in diameter, failure would occur at the sharp corner, and he suggested that this was due to irregularities in the stress distribution. Neuber [23] and Peterson [24] have published much information on stress concentrations found in engineering components due to notches, keyways etc. Using such works as design guides, the stresses produced by such features can be limited.

However, even when the stress due to a macroscopic *stress concentration* is kept below the yield stress, fatigue cracks can still occur. This is due to microscopic stress concentrations such as surface roughness (micro-notches), second phase particles, inclusions or corrosion pits, or from microstructural features such as twin or grain boundaries [25,26,15].

Another important feature of the fatigue process is the *formation of persistent slip bands (PSBs)*. Slip bands that form within crystals can be seen on the surface by a characteristic peak and valley (intrusions and extrusions) formation during cyclic loading [17]. PSBs are so called as it was found that the intrusions and extrusions re-emerged after their removal by electro-polishing, once cyclic loading was recommenced [26]. PSBs are formed when a crystal undergoes cyclic plastic straining, during which dislocation movement results in dislocation structures being formed, such as the ladder or labyrinth structure [15]. It has been suggested that cracks form from PSBs, either by micro-crack formation from an intrusion [27], or from the PSB – matrix interface, where a sharp drop in the dislocation density from the PSB to the matrix gives rise to a weakening of the interface [15]. The latter is said to be strongly influenced by the roughening of the surface caused during the PSB formation [28].

2.3.2.3 Fatigue life approaches

Nowadays engineers are very conscious of fatigue problems and the approaches to predict the possible total-life of mechanical components have an enormous significance. There are three different concepts of design [15];

Safe-life concept: The components are analysed or tested in the laboratory under load conditions which are typical of service spectra and a useful fatigue life is estimated for the component. The safe-life approach depends on achieving a specified life without the development of a fatigue crack so that the emphasis is on the prevention of crack initiation.

Fail-safe concept: This concept, by contrast, is based on the argument that, even when an individual member of a large structure failed, there should be sufficient structural integrity in the remaining parts to enable the structure to operate safely.

Damage-tolerant concept: The basic idea here is that all the engineering components are inherently flawed. The useful fatigue life is then defined as the number of fatigue cycles or time to propagate the dominant crack from this initial size to some critical dimension. The prediction of crack propagation life using the defect-tolerant approach involves empirical crack growth laws based on fracture mechanics.

2.3.2.4 Factors affecting fatigue damage

2.3.2.4.1 Mean Stress Effect

Methods for characterising the fatigue life in terms of nominal stress amplitude, using experimental data obtained from uniaxial tests on smooth specimens, was introduced by Wohler in 1860 [15]. The S-N approach is a simple method of representing the uniaxial fatigue data in a single graph, with the stress amplitude plotted on a linear scale against the number of cycles to failure plotted typically on a logarithmic scale. In 1910, Basquin [15] observed a linear relationship between the stress amplitude and the number of cycles to failure when he plotted these two components on a log-log scale. Later the Basquin equation became popular and was widely used in assessing the fatigue life of many engineering component, based on a stress life approach. The Basquin equation is: -

$$\frac{\Delta\sigma}{2} = \sigma_a = \sigma'_f \left(2N_f\right)^b \qquad\qquad \textbf{Equation 5}$$

where σ'_f is the fatigue strength coefficient, which is approximately equal to the true fracture strength obtained from monotonic tension test, b is known as the fatigue strength exponent or Basquin exponent, σ_a is the stress amplitude and N_f is the number of cycles to

failure.

Basquin's empirical relationship applies to fully reversed fatigue loads with zero mean stress. However, fully reversed stress cycles with zero mean stress are not always representative of practical applications. A method used to calculate the different levels of cyclic stress effect, on fatigue life calculations, was explained by Gerber in 1874 [29]. Some years later, in 1899, Goodman [30] also proposed an approach to account for the mean stress effects in fatigue damage calculations. The concept that the elastic limit of metals in fully reversed loading can be different from that observed in monotonic deformation was popularised by Bauschinger in 1886 [31]. Concepts of cyclic softening and hardening were investigated and presented by Bairstow in 1910 [15]. The constant life plots represented in **Figure 8** are described by the following expressions:

Modified Goodman relation [30] $$\frac{\sigma_a}{\sigma_{ar}} + \frac{\sigma_m}{\sigma_u} = 1$$ **Equation 6**

Soderberg relation [32] $$\frac{\sigma_a}{\sigma_{ar}} + \frac{\sigma_m}{\sigma_y} = 1$$ **Equation 7**

Gerber relation [33] $$\frac{\sigma_a}{\sigma_{ar}} + \left(\frac{\sigma_m}{\sigma_u}\right)^2 = 1$$ **Equation 8**
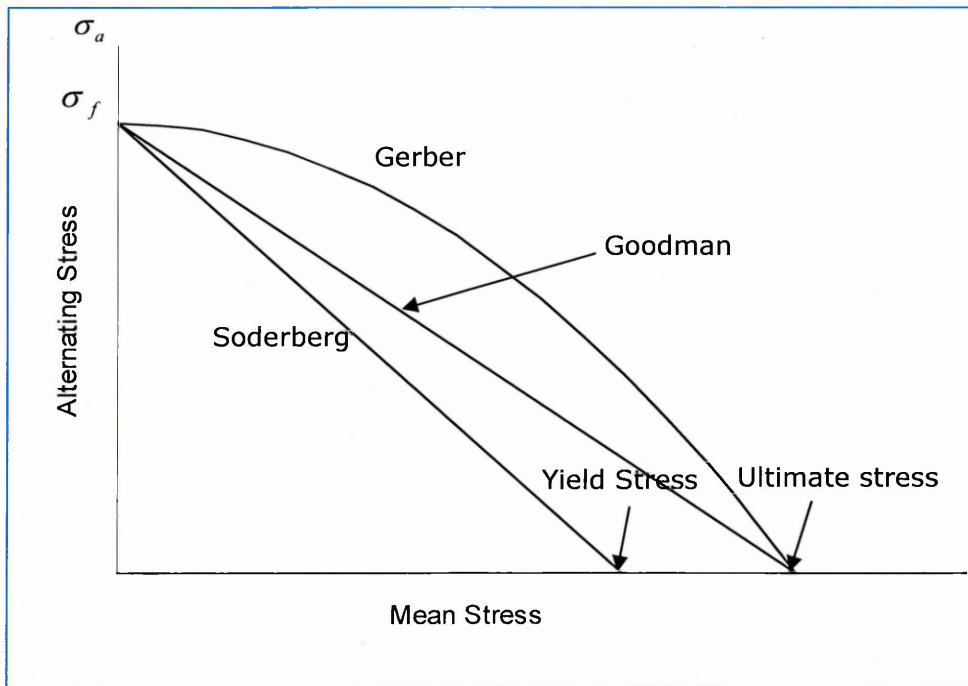
Figure 8: Constant life curves for fatigue loading with non-zero mean stress
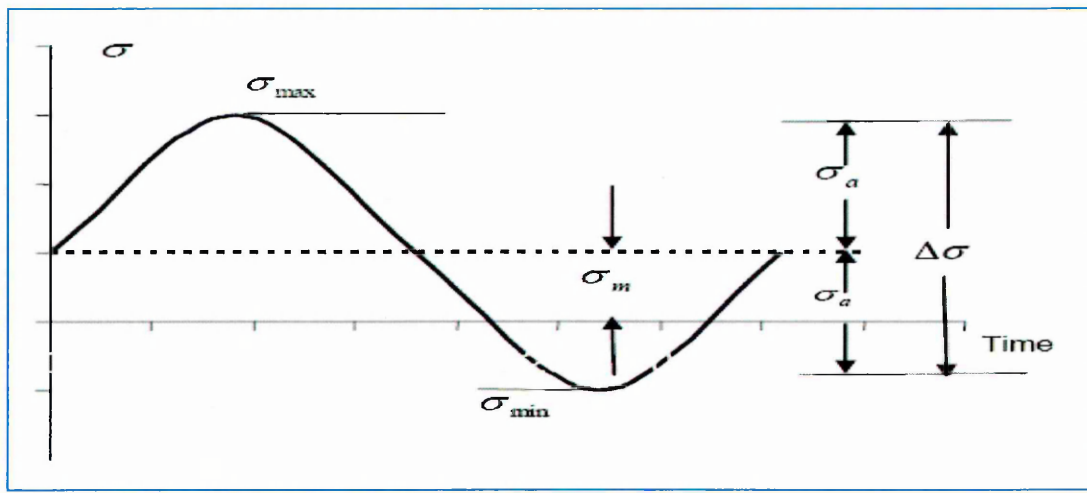
Figure 9: Nomenclature for stress parameters which affect fatigue life, the variation of stress with time

Figure 8 shows that significant differences in the predictions of fatigue behaviour will result from these equations. Therefore, in order to be confident about which of these is the most appropriate for a particular application, it would be necessary to a complete series of experimental tests, with different stress ratios (R) where R is the ratio of minimum to maximum stress values.

2.3.2.4.2 Grain Size

In general, grain size has a marked effect on the phenomena associated with the yield point. The Hall-Petch relationship [34] has been found to apply to the dependence of the lower yield stress on grain size. It is assumed that grain boundaries are good obstacles to the propagation of the fatigue crack as they are for the propagation of a brittle crack [35]. However, as the flow stress attains a certain degree of saturation due to high cyclic strains, the crack propagation in a Face Centred Cubic (F.C.C) structure becomes independent of grain size as they are now more susceptible to dislocation cells [36]. Thus, as the flow stress is larger than yield stress, there is little effect of grain size as the second term in Hall-Petch equation becomes of negligible.

2.3.2.4.3 Role of Surface on crack initiation

A given surface finish may influence the fatigue properties in many ways. The jargon of words in relation to the surface finish and crack initiation will all relate back to smoothness and metallurgical structure. Protrusions and intrusions on the surface generate slip bands at the surface [17]. These protrusions and intrusions along with stress concentrations at the root of the intrusions promote crack initiations sites.

18

A good surface finishing technique like bead peening, burnishing and other similar operations can induce compressive residual stresses at the sub-surface which can be beneficial to mitigate the crack propagation rates.

2.3.2.5 Fatigue Mechanism – Crack Propagation

Fatigue cracks generally propagate through three regimes of crack growth. Known as stages I, II and III, the extent to which the crack propagates during each is governed by the size of the crack tip plasticity [37].
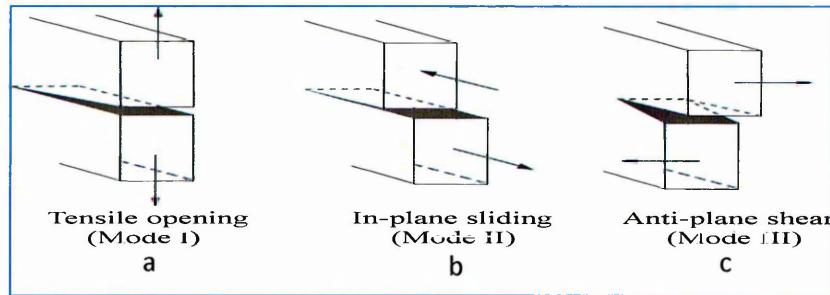
Figure 10: The three basic opening modes.

The applied stress, the crack length, the microstructure, the environment and the loading conditions are amongst the main parameters that control the crack tip plasticity. The three modes are shown schematically in **Figure 10**.

2.3.2.5.1 Stage I Crack Growth

Stage I crack growth occurs along slip planes that are orientated at approximately 45° to the applied stress. This is due to the crack growing under a single shear mechanism. This shear propagation mechanism is known as mode II (in-plane sliding mode) as defined in **Figure 10b**. As can be determined using the Schmidt law [15], the resolved shear stress is found to be a maximum on planes that lie 45° to the applied stress. This is done by considering a stress, σ as a force, F acting on an area, A so that the resolved shear stress τ is calculated by:

$$\tau = \sigma \cos\lambda \cos\theta \hspace{4cm} \textbf{Equation 9}$$

19

where 'λ' is the angle between the shear force and the applied force 'F', and 'θ' is the angle between the plane that the force 'F' acts on and the plane that the shear forces are acting on. Thus, 'τ' can be found to be maximum when both angles are 45°. In a polycrystalline material, it can be expected that many grains will have slip planes at 45° to the applied stress and therefore cracks will be expected to initiate in these favourably orientated grains. As the crack grows, its path across successive grains will continue to follow the most favourable slip system within each grain. This can lead to a zigzag crack path, as described by Forsyth [38], and the resulting fracture surface can be described as having a faceted profile. This growth process will continue whilst the plastic zone ahead of the crack tip is of dimensions comparable to the microstructure, i.e. up to a few grain diameters in size.

During stage I crack growth; the microstructure has a large influence on the propagation. The rate of crack advance is hindered by microstructural barriers such as grain or phase boundaries, and the crack growth rate per cycle fluctuates [39].

2.3.2.5.2 Stage II Crack Growth

As the crack grows, the crack tip stress intensity increases, and correspondingly, the plastic zone size will expand. It is now possible for the stress field at the crack tip to initiate slip along two planes, one plane inclined at a positive angle to the perpendicular of the applied stress and the other at a negative angle. The resulting crack path is then along the perpendicular direction to the applied stress. This growth mode is known as stage II crack growth [38]. Due to the double slip mechanism, the fracture surface has a rippled texture, known as fatigue striations as shown in **Figure 11**, which were first observed by Zappfe and Worden [40].
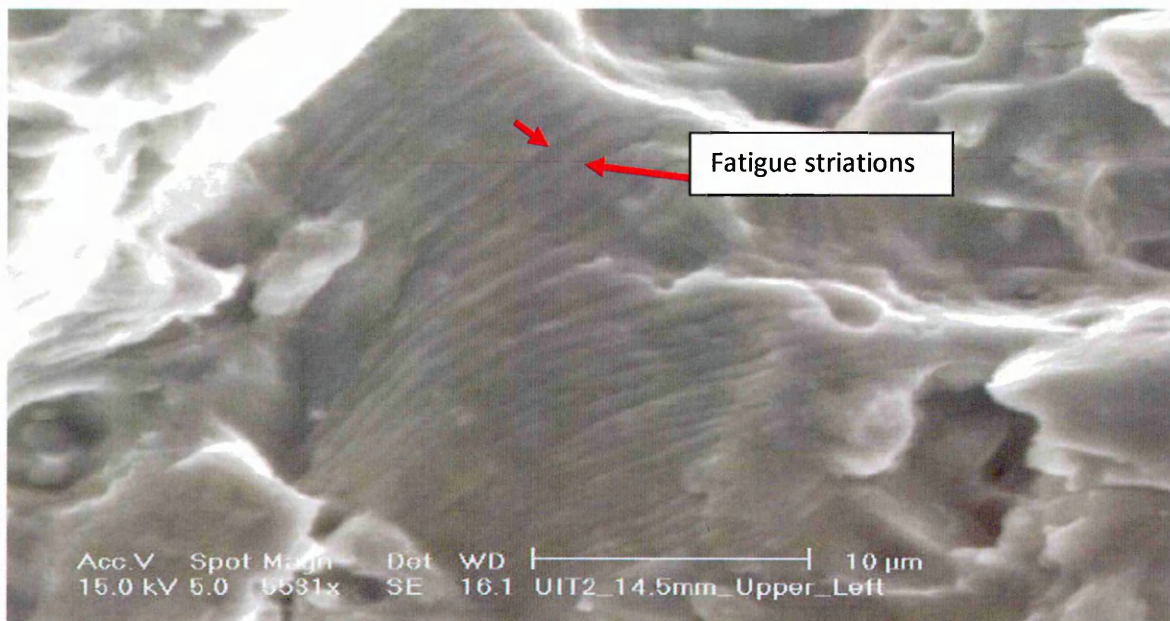
Figure 11: An SEM image of fatigue Striations on Ultrasonic Impact Treated (UIT) Al 2024 T351 at 14.5mm from the surface of the specimen subjected to cyclic loading at 25Hz [41].

These striations, most evident in pure metals and ductile alloys, have been shown to be spaced at distances correlating to the crack advance per cyclic loading [41]. It should be noted that observations of fatigue striations depend on ΔK levels, material and environment [15].

This second stage of crack growth is also known as the *Paris regime*. The microstructure now has little influence on the crack propagation, and the propagation rate increases in proportion to crack length. Fracture now occurs by means of a tensile opening mode, mode I, as shown in **Figure 10a**.

2.3.2.5.3 Stage III Crack Growth

The crack enters the third stage of propagation when the growth rate becomes much higher than that experienced during the *Paris regime*. This is said to be unstable crack propagation. An almost negligible portion of life is spent in stage III and, consequently, not much research has been performed in this area. The stress intensity approaches the material fracture toughness, K_c, and static fracture modes can be observed [42], such as void coalescence, cleavage and ductile tearing. Due to the static fracture modes, the microstructure, once again, can have a significant bearing on the propagation rate.

2.3.2.6 Describing cracking propagation

The fatigue crack growth regimes that are of primary concern are stage I and stage II (**see Figure 12**), also known as short and long crack growth stages respectively.
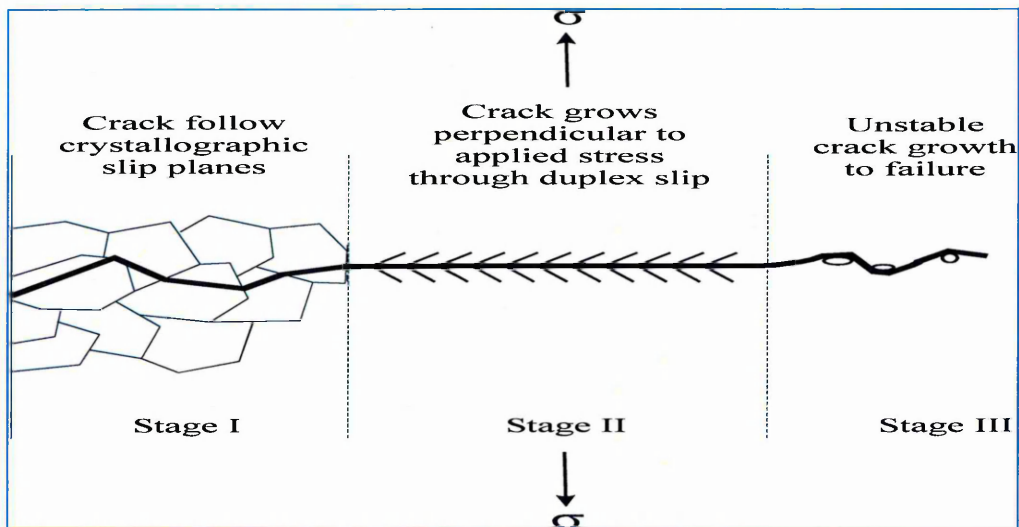
Figure 12: Three stages of fatigue crack propagation

Due to the recent changes in design methodologies towards a damage tolerance approach, much effort has been directed towards predicting long crack growth behaviour and the so called anomalous short crack growth behaviour.

The ability to describe conditions at the crack tip brought about the inception of Linear Elastic Fracture Mechanics (LEFM) [43]. However, for LEFM to be applicable, certain conditions concerning the crack tip plasticity must be observed these are discussed in **Section 2.3.2.6.1**. When these conditions are breached, it is possible to use Elastic Plastic Fracture Mechanics (EPFM) which is discussed in **Section 2.3.2.6.2**. For the case of a short fatigue crack, LEFM is no longer applicable, and if the crack is small enough for the microstructure to influence the growth, then EPFM is also unable to describe the short crack growth phenomenon which is discussed in **Section 2.3.2.6.4** [44]. Thus, in Microstructural Fracture Mechanics (MFM), much attention is paid to the factors that affect the growth of the crack, such as the microstructural features, in order to describe crack growth.

2.3.2.6.1 Linear Elastic Fracture Mechanics

LEFM is based on the concept of the stress intensity factor (SIF, ΔK). This factor, denoted K, was introduced by Irwin [43] to describe the stress conditions around the vicinity of a crack tip. Irwin showed that the near tip stress field, σ_{ij}, can be described through K, thus:

$$\sigma_{ij} = \frac{K}{\sqrt{2\pi r}} f_{ij}(\theta) + \text{higher order terms of r} \qquad \textbf{Equation 10}$$

where 'r' and 'θ' define the location from the crack tip in polar coordinates and 'f_{ij}' is a dimensionless function of θ at different modes of fracture. K_I, K_{II} & K_{III} are defined for each fracture mode (**Figure 10**). For the majority of cases of cracked components, the far field applied stress imposes a mode I type fracture mechanism [45]. It can be seen that K characterises the stress conditions at the crack tip. It is a factor of the applied stress, the crack length and the crack geometry, given by:

$$K = \sigma \sqrt{\pi a} \, Y \qquad \textbf{Equation 11}$$

where 'σ' is the applied stress, 'a' is the crack length and 'Y' is a dimensionless geometrical factor which describes how the crack shape affects the severity of the crack tip stresses. The real significance of K is its ability to describe crack propagation. Paris et al [20] proposed the following relationship, commonly referred to as the Paris law, linking the crack propagation rate to the stress intensity factor range:

$$\frac{da}{dN} = C(\Delta K)^m \qquad \textbf{Equation 12}$$

where $\dfrac{da}{dN}$ is the incremental crack extension per loading cycle, 'C' and 'm' are experimentally determined material constants and 'ΔK' = (K_{max} - K_{min}) is the stress intensity factor range, related to the applied cyclic stress range, $\Delta\sigma$ (σ_{max} - σ_{min}), through **Equation 11**. This is evidenced when plotting the propagation rate against ΔK on a log-log

plot as seen in **Figure 13**, where the linear relationship produced by this power law is demonstrated.

Figure 13 also introduces the two terms ΔK_{th} and K_{IC}. ΔK_{th} is the threshold stress intensity factor range, below which long cracks do not propagate. This is usually determined by reducing the ΔK level, affected by reducing the applied $\Delta \sigma$ level, of an observed stage II crack until the propagation rate is less than some predetermined value, often in the region of 10^{-10} m/cycle [46]. ΔK_{th} value only applies when LEFM conditions are met, for example, whilst a long crack would be expected to arrest, or to propagate at very low rates (10^{-10} m/cycle), around or below ΔK_{th}, short cracks may still propagate and at rates much higher
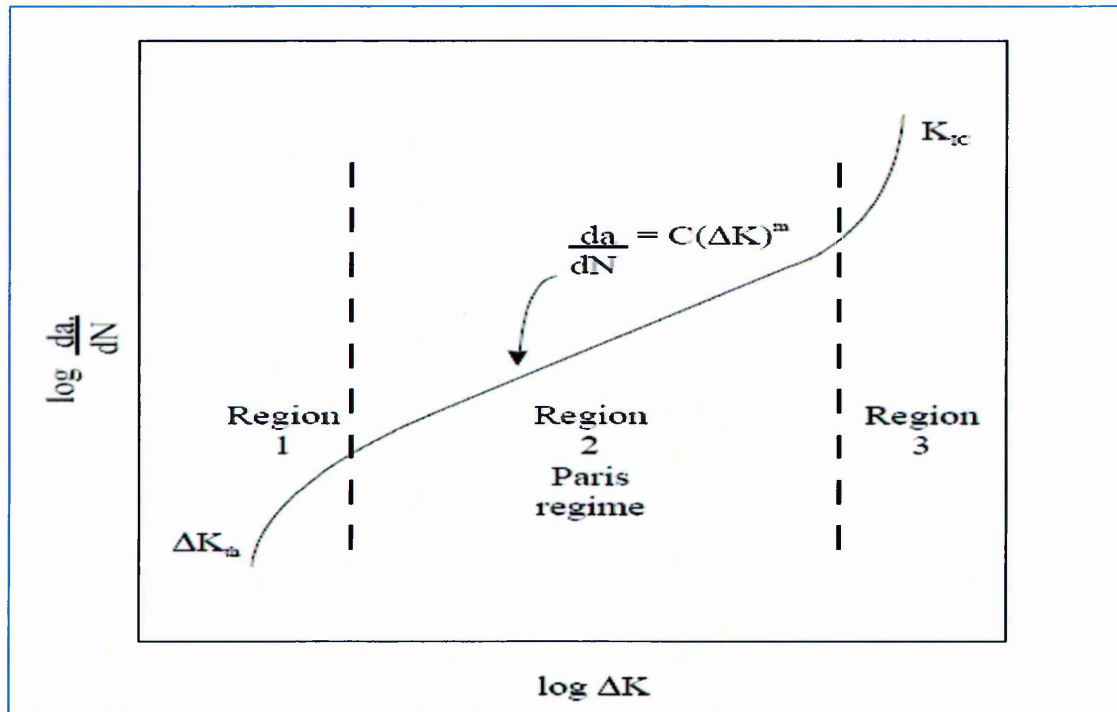
Figure 13: Typical log-log plot of crack propagation rate vs. stress intensity range

than this [47]. The term K_{IC} refers to the mode I fracture toughness. As K_{max} approaches K_{IC}, unstable stage III crack propagation occurs, and when K_{max} attains the critical K_{IC} value, the result will be a brittle fracture failure. K_{IC} can be determined by methods such as fracture toughness test, employing plane strain conditions to provide conservative fracture toughness values. As well as the parameters C and m in *Paris equation* being dependent upon material microstructure, temperature, environment and stress ratio, R ($\sigma_{min}/\sigma_{max}$), the fracture toughness, K_{IC}, is also sensitive to material and testing conditions such as microstructure, temperature and loading rate [16].

24

LEFM analysis assumes that the bulk of the material is behaving in an elastic manner. As a plastic zone will always exist ahead of a fatigue crack, in practice, for small scale yielding conditions to be met, the plastic zone size should be no greater than one twentieth of the crack length [48]. This is also known as *K-dominance*, whereby the area under consideration ahead of the crack tip must be reasonably larger than the plastic zone size, in order that any redistribution the of stresses, due to the plasticity, does not affect the validity of the solutions of K, yet this area must be small enough so that approximate solutions derived from Irwin's analysis do not deviate significantly from the exact solutions.

2.3.2.6.2 Elastic Plastic Fracture Mechanics

When substantial amounts of plasticity are developed, and the use of LEFM is no longer valid, a line integral method developed by Rice [49], known as the *J integral*, can be used to define the conditions for fracture. The line integral is taken along any path, Γ encircling the crack tip from one crack flank to the other. In his work, Rice showed that the integral was independent of the path and could be given by:

$$J = \int_\Gamma \left(w\,dy - T\frac{\partial u}{\partial x}\,ds \right) \qquad \textbf{Equation 13}$$

where T are tractions, stress vectors, acting on the path, x and y are rectangular coordinates from the crack tip, s is the distance travelled along the path, u are displacement vectors and w is the material's strain energy density.

Hutchinson [50] and Rice and Rosengren [51] showed that the stress field in a nonlinear elastic solid could be described through the J integral parameter along the same lines as K does for LEFM, thus:

$$\sigma_{ij} = \sigma_y \left(\frac{J}{\alpha\sigma_y\varepsilon_y I_n r} \right)^{\frac{1}{n+1}} \tilde{\sigma}_{ij}(\theta,n) \qquad \textbf{Equation 14}$$

where n is the reciprocal of the strain hardening exponent, I_n is a factor relating to the strain hardening exponent, $r^{-1/(n+1)}$ is the stress field singularity, $\varepsilon/\varepsilon_y = \alpha(\sigma/\sigma_y)^n$ where ε_y and σ_y are yield strain and stress respectively and are related through $\varepsilon_y = \sigma_y/E$, where E = Young's modulus and α is the constant from Ramberg-Osgood relationship [52], $\alpha = K(\sigma_0/E)^{n-1}$, where K and n are constants that depend on the material being considered [15].

Finally, $\tilde{\sigma}_{ij}$ (θ, n) varies with the strain hardening exponent and the polar angle θ, and also depends on stress state, either plane stress or plane strain.

A drawback of the J integral approach arises because of the assumption that the material is behaving in a nonlinear elastic way, so that the stress–strain curve is nonlinear and reversible. This then implies that this approach is only valid as long as no unloading occurs. Therefore, it is not fully substantiated for use when describing cyclic loading, but it does enable the prediction of the onset of crack extension. However, these limitations have been shown not to be as severe as is suggested. Hutchinson and Paris [53] have shown a possible use for stable crack propagation, and Dowling and Begley [54] have correlated propagation rates from cyclic loading to the change in J.

An important aspect of the J integral approach is the ability to determine fracture toughness values using specimens of a smaller size than those that would be necessary when employing formulae derived from LEFM analyses. Estimations of K_{IC} can be achieved using:

$$J_{IC} = \frac{K_{IC}^2}{E'}\left(1 - \upsilon^2\right)$$

Equation 15

where υ is Poisson's ratio and $E\square$ is young's modulus of the material.

Another method to describe fracture when the level of plasticity exceeds LEFM restrictions is through the crack tip opening displacement (CTOD). This approach was first developed by Wells [55]. From the K and J analysis it is seen that fracture occurs at critical values of stress
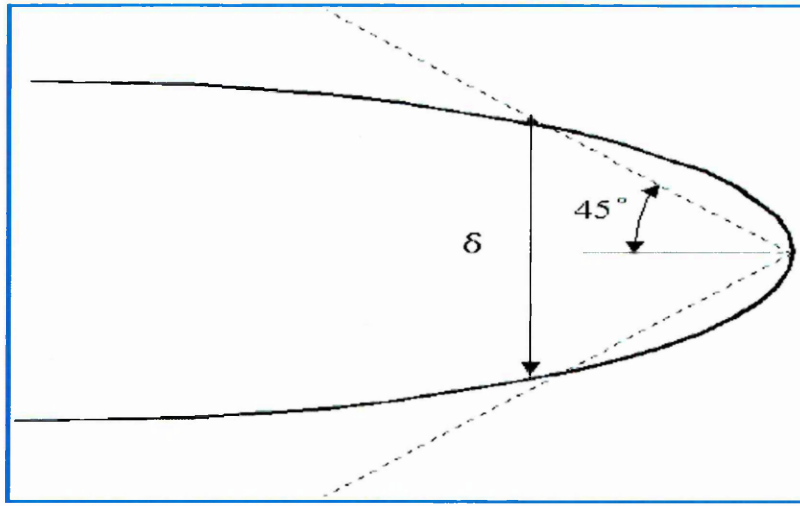
Figure 14: Definition of crack tip opening displacement, δ_t

or plastic strain. Methods employing CTOD, denoted δ_t, assume fracture to occur when a critical displacement is achieved between two points on opposite crack flanks. Burdekin and Stone [56] utilised the Dugdale strip yield model to define the CTOD, δ_t, as:

$$\delta_t = \frac{8\sigma_y a}{\pi E} \ln \sec\left(\frac{\pi\sigma}{2\sigma_y}\right) \qquad \textbf{Equation 16}$$

where E is young's modulus of elasticity, σ_y is yield stress, a is crack length and σ is far field stress. K and J can be estimated through the CTOD by the following approximations:

$$\delta_t = \frac{K^2}{E\sigma_y} \text{ (for LEFM)}$$

$$\delta_t = \frac{J}{\sigma_y} \text{ (for EPFM)}$$

27

2.3.2.6.3 Crack Closure

The possibility that a fatigue crack can close even at a far-field tensile load was first rationalised by Elber[57] has increasingly concerned researchers of fatigue crack growth behaviour, particularly in the near-threshold stress intensity levels of long cracks. This is because the fractured surfaces in the wake of an advancing crack tip close when the far-field load is still tensile before the attainment of the minimum load. Premature contact of the fracture flanks occurs and as a result, the crack tip does not experience the full range of ΔK, i.e., the real driving force or effective stress intensity range, ΔK_{eff} ($\Delta K_{eff} = K_{max} - K_{op}$) is lower than the nominal ΔK and therefore a lower $\dfrac{da}{dN}$ is expected. Here, K_{op} is the stress intensity when the crack is fully opened ($\geq K_{min}$).

Elber suggested that a mechanism for such an effect is that of the constraint effect on the residual plastically stretched material which is left on the wake of the crack front by the elastic material which surrounds it, when the crack tip continues advancing through the plastic zone. However, several other mechanisms are envisaged as possible, e.g., due to the presence of corrosion debris within the crack (oxide induced closure), due to the contact between rough fracture surfaces (roughness induced closure), due to viscous fluid, obstacles and crack bridging by fibres [15].

2.3.2.6.4 Short Fatigue Cracks

It is well documented that short cracks (SCs) behave markedly different to long cracks [58]. Microstructural crack growth occupies a significant portion of the total fatigue life of several structures. The SC problem was originally proposed by Pearson [59] with his experimental work performed on aluminium alloys. It was realised that cracks of the order of the grain size tend to propagate at rates far higher than LEFM predictions suggest and thus is no longer appropriate.

2.3.2.6.4.1 Introduction

Acceleration, deceleration and crack arrest is commonly correlated to microstructure as long as the crack doesn't cross the microstructural barrier (**See Figure 16**). Lankford [60] suggested that such behaviour is caused by the difficulty of cracks to nucleate microplasticity in certain crystallographic orientations and/or smaller grains.

A comprehensive review on short fatigue crack behaviour has been published by Miller [61,62]. Other researchers indicated that SCs may be divided into two primary zones of interest [63]:

➢ The microstructurally short crack zone/regime (MSC) in which the crack is small in relation to the surrounding microstructural features (e.g. cracks which are comparable to the grain size). Crack growth is strongly influenced by microstructure. The micromechanical description of its propagation is expressed by means of the MFM. **(See Figure 15a)**.

➢ Physically small cracks (PSC), which are significantly larger than the microstructural dimension and the scale of local plasticity, but are physically small with length typically smaller than a millimetre or two. Here, the microstructure is not the main parameters affecting their propagation but rather, PSC are strongly dependent on the stress level.

A) MICROSTRUCTURALLY SHORT CRACK	B) PHYSICALLY SMALL CRACK	C) LONG CRACK
a= 2 μm	a=0.1 mm	a= 10 mm
a< 1 grain	a<10 grains	a>100 grains
FEATURES HIGH STRESS MFM-MODE II AND III STAGE I (SHEAR) CRACK a/rp <1	**FEATURES** HIGH STRESS EPFM-MODES I, II AND III STAGE II CRACK a/rp intermediate values	**FEATURES** LOW STRESS LEFM-MODE I(STAGE II) TENSILE CRACK a/rp >>1
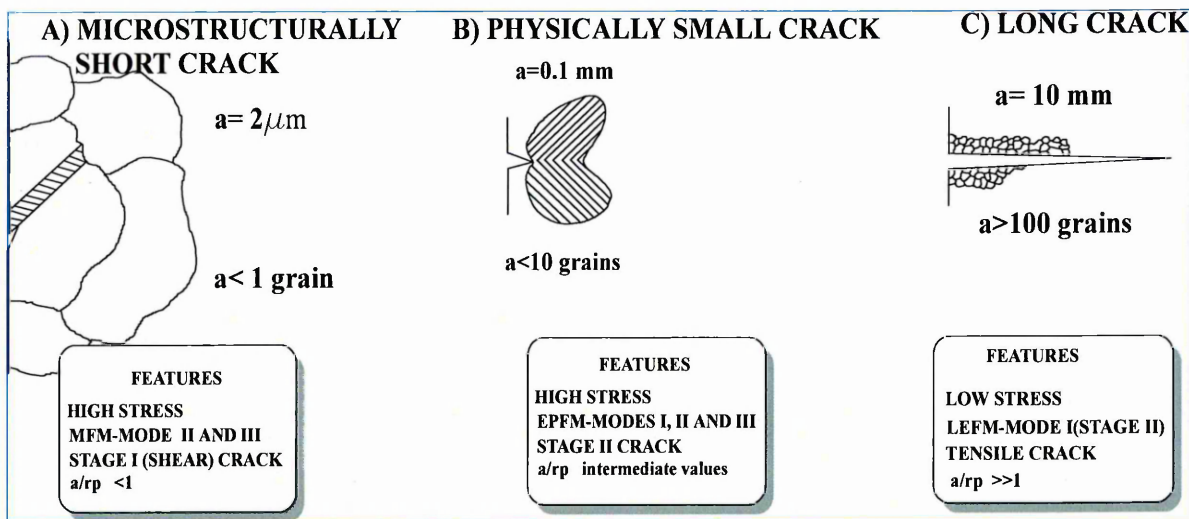
Figure 15: Classification of SCs

On similar grounds Suresh & Ritchie [15] later suggested a various scale sizes below which the growth rates of a fatigue crack may be found to exhibit crack size dependence:-

➔ Microstructurally small flaws

➔ Mechanically small flaws

➔ Physically small cracks

➔ Chemically small cracks

2.3.2.6.4.2 Brown-Hobson Model (air)

Brown-Hobson Model considered the conditions required for both stage I shear crack growth and the transition to stage II tensile fatigue crack growth. In their model the cyclic crack growth rate is given by

$$\frac{da}{dN} = A\Delta\varepsilon^{\alpha}(d-a)$$ **Equation 17 (For Stage I)**

$$\frac{da}{dN} = B\Delta\varepsilon^{\beta}(a-D)$$ **Equation 18 (For Stage II)**
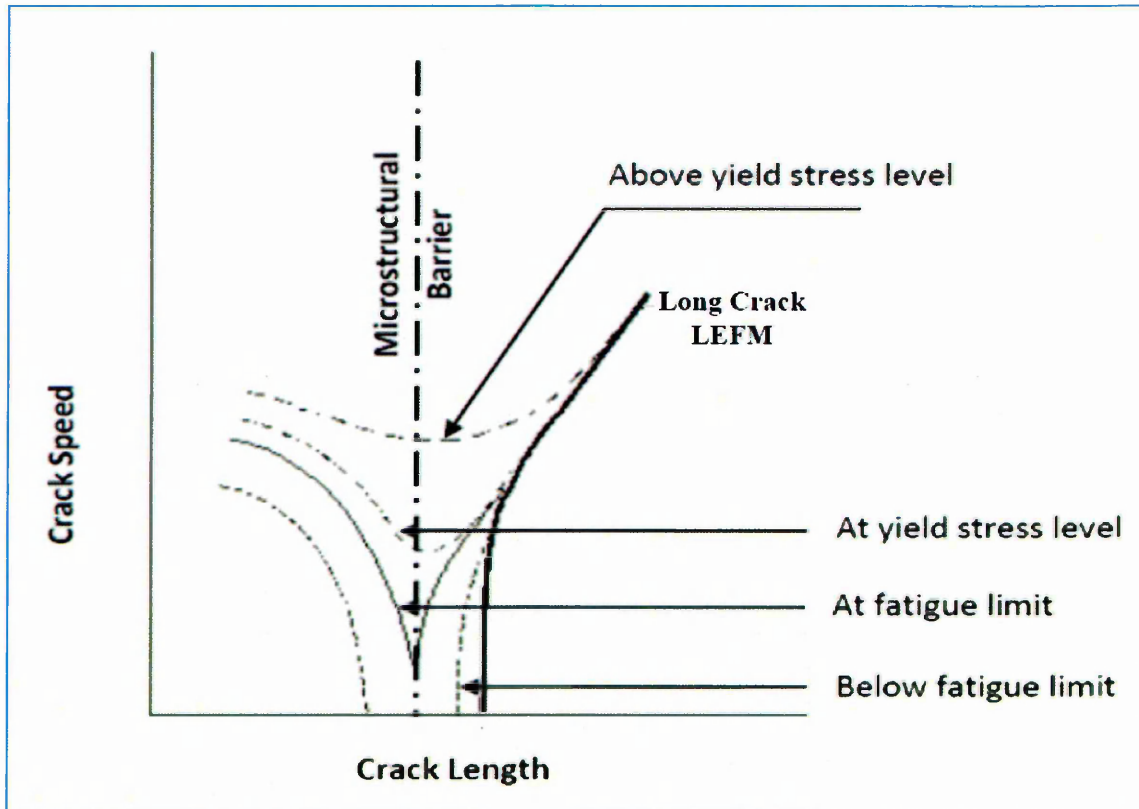
Figure 16: Brown-Hobson's graph of the short crack behaviour at different stress levels.

where A, B, α and β are material constants, Δε is the applied cyclic axial strain range, 'a' is the crack length, 'd' is the microstructural barrier distance and 'D' is a threshold condition dependent on the level of the applied stress-strain state. **Figure 16** illustrates the **Equation**

17 and **Equation 18** and show how a microstructural crack will behave at various stress levels.

A significant contribution towards the understanding of SCs was put forward by Kitagawa and Takahashi [64] who developed the Kitagawa-Takahashi diagram (K-T). They showed

that $\Delta\sigma_{th,}$ the threshold stress range for crack propagation, produced a straight line when

plotted against crack length on log-log scales showing a relationship pertaining to **Equation 7**, giving a constant ΔK_{th}. However, of significance to short cracks, they demonstrated that as the crack length reduced, this line tapered away so as to asymptotically approach the fatigue limit. Thus, they had produced a map indicating the border between regions of propagating and non-propagating cracks.

Using various relationships and conventions, Brown [65] expanded the K-T diagrams to include all areas of crack propagation, with the exception to chemically short and notch affected cracks as shown in Figure 17.
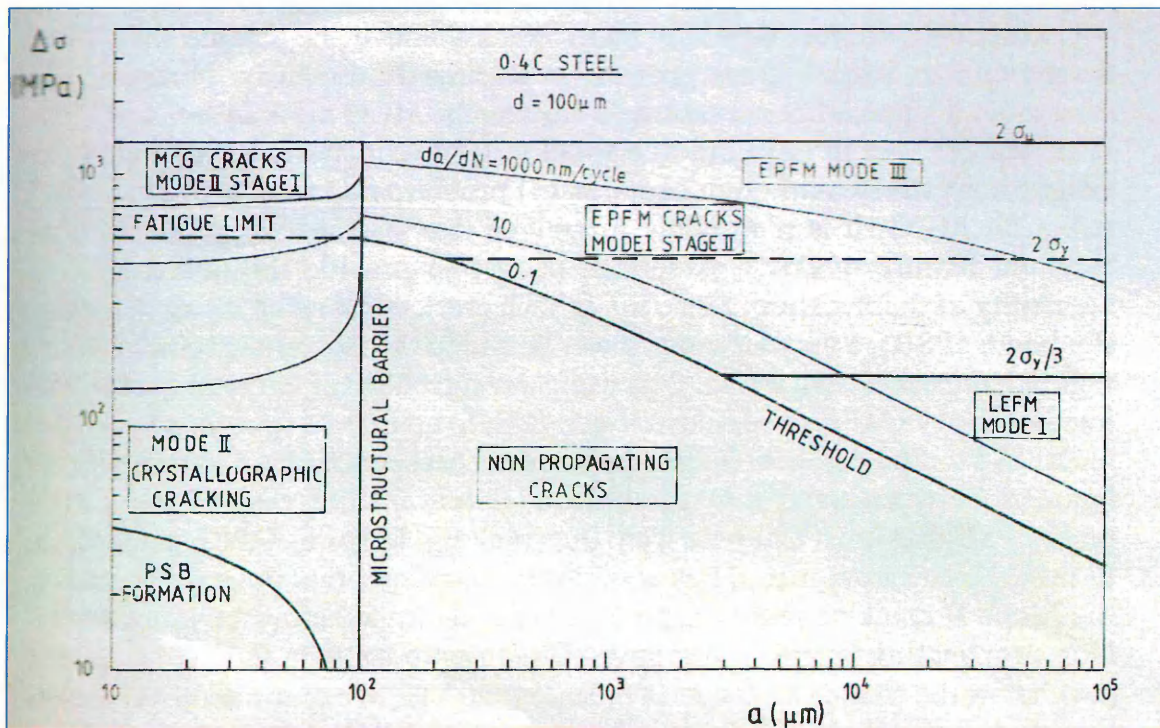
Figure 17: Brown map showing various fatigue crack regimes.

2.3.2.6.4.3 Navarro de los Rios Model (NR Model) (air)

The NR model is based on the continuous distribution of dislocations. The fatigue damage (crack and plastic zone) of any sized crack can be represented by three zones as shown in **Figure 18**. The first zone represents the crack, the second the crack tip plasticity and the third a microstructural barrier (grain boundary). In terms of the material resistance to crack propagation, the crack is considered as stress free unless some closure stress, σ_1, is acting on the crack flanks: the stress at the plastic zone is equal to the resistance of the material to plastic deformation (cyclic yield stress), σ_y^c; and at the grain boundary, of width r_0 the stress developed due to the constraint exerted on the plastic zone is σ_2. This stress represents a measure of the reaction stress developed on the barrier due to the blocking of the Persistent Slip Bands.
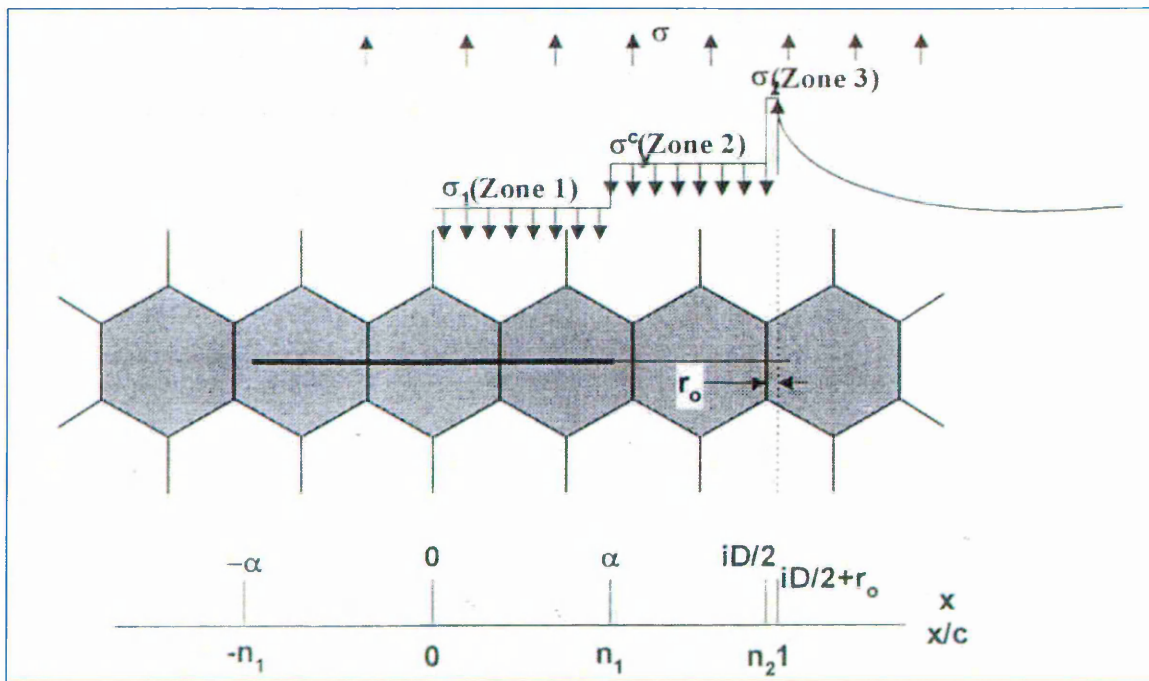
Figure 18: Three zones that constitute fatigue damage. The parameter $i=2\alpha/D$ represents the normalised crack length in half grain intervals (i=1, 3, 5,). The parameter $iD/2$ represents the extent of the fatigue damage and D is the grain size.

Based on the equilibrium of dislocations along the three zones, the constraint stress ahead of the slip band for an opening mode loading, σ, is given by,

$$\sigma_2 = (\frac{1}{\cos^{-1} n_2})[(\sigma_y^c - \sigma_1)\sin^{-1} n_1 - \sigma_2 \sin^{-1} n_2 + \frac{1}{2}\sigma\pi] \qquad \textbf{Equation 19}$$

$$n_1 = \frac{\alpha}{iD/2 + r_o}, \qquad \textbf{Equation 20}$$

$$n_2 = \frac{iD/2}{iD/2 + r_o} \qquad \textbf{Equation 21}$$

where the parameters n_1 and n_2 represent in a dimensionless form the crack length and the fatigue damage size, respectively. The parameter σ_y^c represents the cyclic yield stress of the material.

As the crack propagates σ_2 increases in value and will reach a level equal to the strength of the boundary when the crack reaches a critical length denoted by $n_1 = n_c$. The grain boundary will be overcome and crack tip plasticity is able to extend to the next grain boundary where it is again blocked. However, if σ_2 does not attain the level of the grain boundary strength before the crack tip reaches the barrier, the crack arrests. The steps according to the NR model are shown in **Figure 19**.
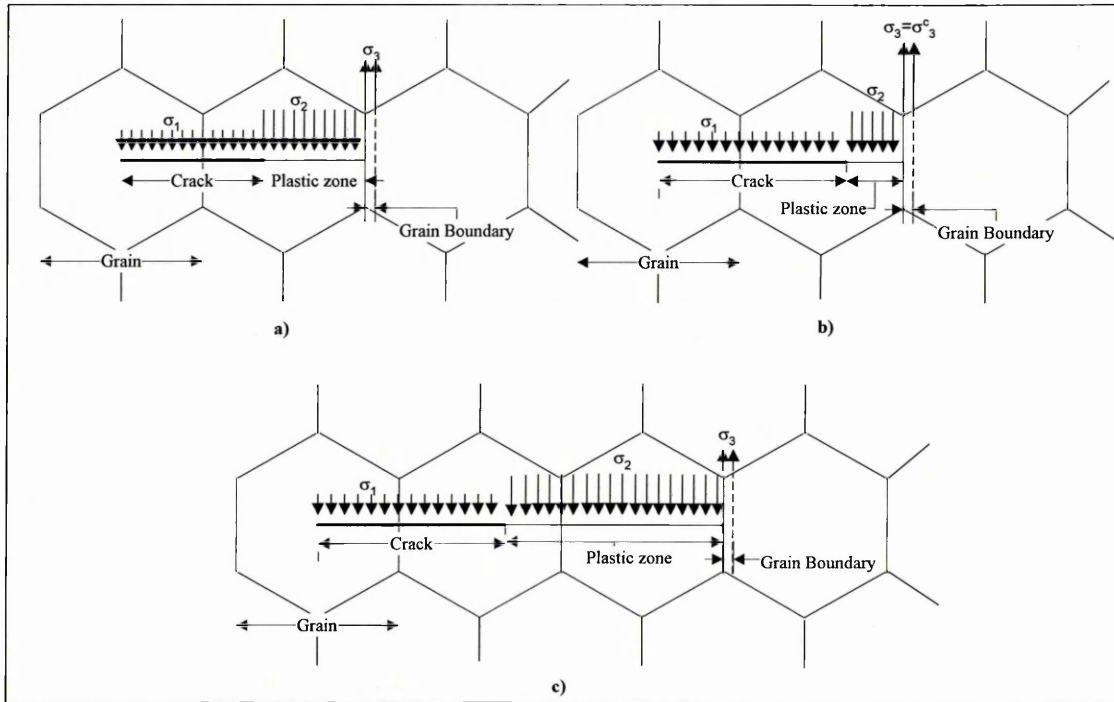
Figure 19: The effect of slip-band locked by the grain boundary on stress concentration in three stages: a) blockage of the plastic zone by the grain boundary increases σ_3; b) further crack propagation until $\sigma_3=$

σ_3^c results in new slip-band development and c) relaxation of σ_3 and yielding on a new grain. The parameters σ_1 and σ_2 represent crack closure stress and cyclic yield stress respectively.

Thus, the magnitude of stress for crack arrest is:

$$\frac{2}{\pi}\sigma_2 \cos^{-1} n_2 + \sigma_1 = \sigma_{arrest} \qquad \textbf{Equation 22}$$

It has been shown that crack arrest is achieved when:

$$\frac{m_i}{m_1}\frac{\sigma_{FL} - \sigma_1}{\sqrt{i}} + \sigma_1 = \sigma_{arrest} \qquad \textbf{Equation 23}$$

where $i = \dfrac{2a}{D}$, σ_1 is the crack closure stress which is set to $\sigma_1 = 0$ for stress free cracks, a is the crack length, D is the grain diameter and σ_{FL} is the fatigue limit. The term $\dfrac{m_i}{m_1}$ is the effect of grain orientation, which was evaluated and incorporated by de los Rios and Navarro on SC propagation using the following empirical relationship:

$$\frac{m_i}{m_1} = 1 + 0.5\,\ln(i) \qquad \textbf{Equation 24}$$
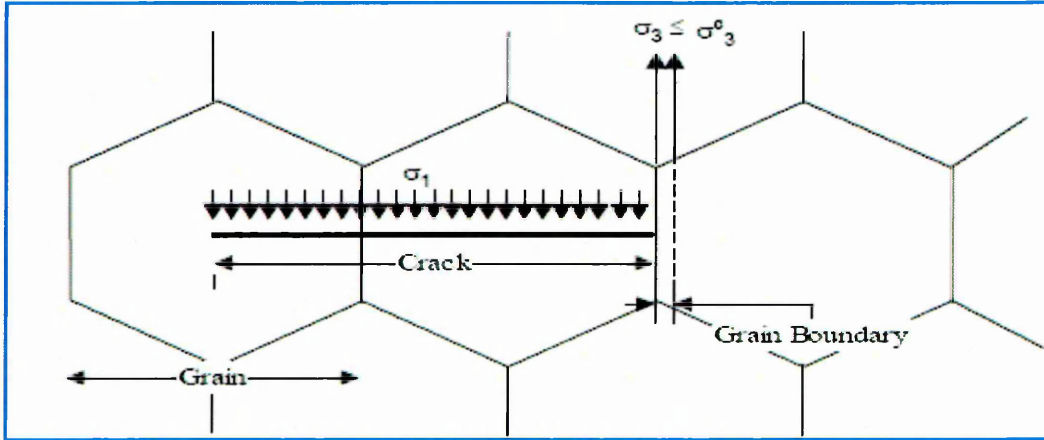
Figure 20: Schematic representation of crack arrest.

34

2.4 Corrosion Fatigue

2.4.1 Introduction

ASTM F1801-97 [66] defines corrosion fatigue as: the process by which fatigue failure occurs prematurely under conditions of simultaneous corrosion and cyclic loading at lower stress levels or fewer cycles than would be required in the absence of the corrosive environment. However, although this definition clearly demonstrates the importance of cyclic loading in an aggressive environment, the occurrence of prior corrosion can still have detrimental effects on the fatigue properties of materials, although this is not always strictly considered to be a corrosion fatigue process.

It can be seen from prior discussion that the nature of both fatigue and corrosion is complex and therefore the subject of corrosion fatigue will be equally complex. In fact, due to the two processes acting simultaneously, the resulting corrosion fatigue process can be even more complex, with more parameters needing to be considered. This is demonstrated when considering that the synergistic effects of corrosion and fatigue together are more damaging than the sum of the constituent parts. Some of the additionally required parameters that affect corrosion fatigue will now be considered.

2.4.2 Influencing Parameters

The factors that influence the corrosion fatigue performance can be split up into areas such as: the waveform characteristics, frequency etc; the environment, temperature etc; and mechanical parameters, stress ratio etc. These are summarised in which follows the discussion on their influences.
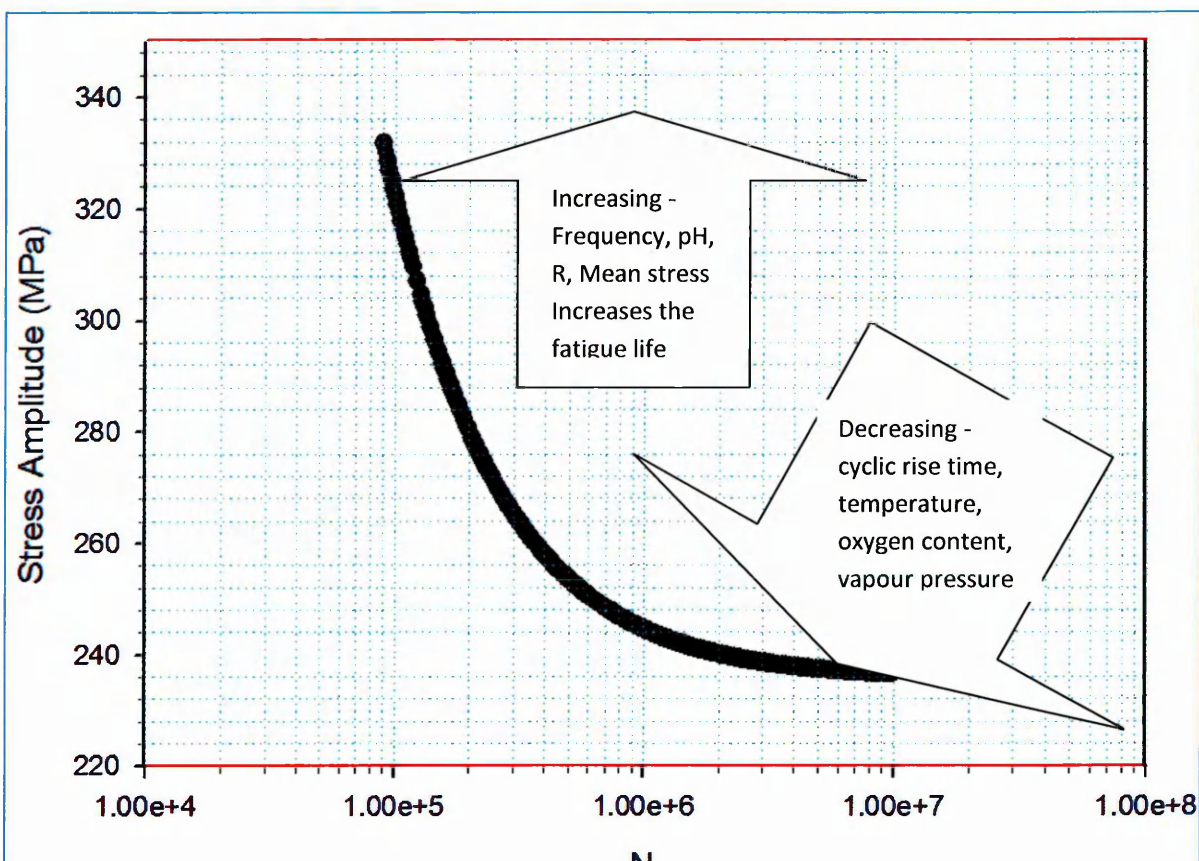
Figure 21: Summary of general influence of parameters on corrosion fatigue.

2.4.2.1 Frequency Effects

When performing fatigue tests in laboratory air, the frequency is not often considered with regard to the fatigue performance. It is usually only considered so that the testing time is relatively short to save on time required to gain results and also to make financial savings [67]. However, in a corrosive environment, frequency can play a role in the fatigue performance of a material. Vogelesang [68] showed that, for a high strength 7000 series aluminium alloy in artificial sea water, reducing the frequency from 20 Hz to 0.5 Hz resulted in an increased crack growth rate for equivalent ΔKs. Blinn et al [69] conducted tests on a 2000 series aluminium alloy in a 10% relative humidity environment and also in an artificial sea water solution. Their results showed an increase in crack growth rate with a decrease in frequency, from 10 Hz to 0.1 Hz, for the 10% relative humidity tests, but were inconclusive for the artificial sea water. An increase in growth rate with decreasing frequency has also been demonstrated in a variety of steels [70]. Bowles [71] conducted tests whereby he varied the frequency from a segment of low frequency cycles to a segment of high frequency cycles. On inspection of the fracture surfaces, he concluded that an environmental effect was noticeable during the low frequency cycles, but not during the high frequency cycles. The evidence for this conclusion was that the low frequency cycles produced fatigue striations, whereas the high frequency did not, as was consistent with tests performed in vacuum. Bowles made an interesting observation that, the striations produced at the low frequencies persisted for a small number of cycles during the high frequency regime. He suggested that this was because sufficient additional water, from the environment, or hydrogen remained during the step up in frequency to produce a transient period.

Corrosion is a time dependent process, therefore, if the environment is only in contact with the crack surfaces whilst the crack is open, then it can be envisaged that lower frequencies

will induce higher corrosion processes. In another study by Bowles [72], he performed tests introducing holding periods at either the maximum or minimum stress level. His results showed that a greater effect of the environment was produced when the stress was held at the maximum level. With reference to frequency effects, Schutz [73] concluded that the effect is small when the complete life to failure consists of long initiation phase and a short propagation phase. Therefore, frequency has a greater effect on propagation than it does on the early stages of fatigue life for long cracks.

2.4.2.2 Cyclic Waveform

Many corrosion fatigue tests are conducted under constant amplitude, sinusoidal waveforms. Tests performed using different wave shapes and variable amplitude stress cycles have shown that both these factors can influence the corrosion fatigue performance. Barsom [74] performed tests using positive and negative saw tooth waveforms in air and in corrosive environment. His results indicated that neither shape waveform had an effect in air, compared with a sinusoidal wave. However, in a corrosive environment, the negative waveform gave similar results to air, but the positive waveform yielded a pronounced reduction in fatigue performance. A reason proposed for this effect is that new crack surfaces are produced during the opening portion of the stress cycle and therefore a positive saw tooth waveform generates more time for corrosion processes to take place during the crack extension period [75].

From tests performed for the Fatigue in Aircraft Corrosion Testing (FACT 1989) programme [76], using variable amplitudes, results showed that, for an aluminium alloy, no significant effect of the corrosive environment occurred. In the same programme, under constant amplitude loading, a large effect was detected. Similar results were obtained by Schutz [77] when performing tests on steels.

2.4.2.3 Environmental Aspects

The environment is an obvious factor in corrosion fatigue. Different metal-environment combinations will produce different corrosion reactions, or rates of reaction. However, when considering individual metal-environment combinations, several aspects of the environment can cause variations in the corrosion fatigue performance. Some of these contributory factors include: temperature; pH; oxygen content; and pressure.

A basic principle of chemistry indicates that, generally, an increase in temperature produces an increase in chemical reaction. This is also true of corrosion reactions. An investigation by Nakai et al [78] was performed to ascertain the effects of frequency and temperature on the corrosion fatigue properties of steel. Their results showed that increasing the temperature brought increases in crack growth rates. From their tests, a plateau was achieved, whereby, further reduction in frequency showed negligible increases in crack growth rates. At these low frequencies the effect of temperature was also negligible. At higher frequencies, where the crack growth rates were below the plateau, a significant effect of temperature was observed. These results allude to the aforementioned increase in chemical reaction time with increasing temperature. Other investigations have shown similar results [79].

The oxygen content of a solution can have a significant effect on corrosion fatigue results. Testing a low carbon steel in salt solution and changing the solution conditions from aerated to deaerated, Duquette and Uhlig [80] found that the higher oxygen content reduced the fatigue lives of the tested specimen. In fact, the outcome for the deaerated solution was similar to air. Wan et al [81] made similar observations for an aluminium alloy, but noted that the crack length and ΔK levels had an influence on the effects of oxygen concentration.

The pressure of the environment is usually concerned with tests conducted in corrosive vapour environments and not fully immersed tests. Bradshaw and Wheeler [82] conducted experiments on aluminium alloys in water vapour environments. They saw that upper and lower saturation levels were achieved in the crack growth rate when alternating the water vapour pressure. With increasing water vapour pressure, a maximum growth rate was eventually reached, and vice versa. When changing the frequency of the tests, the same saturation levels existed. However, for the low frequency tests, the points at which the growth rate left the lower saturation level and reached the upper saturation level, occurred at lower water vapour pressures in comparison with the high frequency tests.

2.4.2.4 Mechanical Aspects

The mean stress, or stress ratio, are known to have an influence on fatigue. For purely mechanical fatigue, i.e. no environmental contribution, the fatigue strength is seen to

38

increase as the stress ratio is reduced. It is, therefore, a valid assumption that the same effect will be seen during corrosion fatigue. However, during corrosion fatigue, the degree of environmental effect will depend on the accessibility of the environment to the crack tip, see frequency effects. Some analyses of stress ratio effects on corrosion fatigue have been made, such as that of Chu and Macco [83]. These investigators showed that reductions in stress ratio yield reductions in fatigue strength. More importantly, however, they showed corrosion fatigue in seawater to be more sensitive to stress ratio than air fatigue. The reduction in fatigue performance as compared to air fatigue due to the environment was more pronounced at higher stress ratios. Such findings were also described by Corsetti and Duquette [84]. Therefore, it can be seen that whilst increasing the stress ratio increases the corrosion fatigue life, this also has the effect of creating a larger difference between air and environmental fatigue lives. This can be reasoned by considering that the crack will be open, or open wider, for a longer portion of the stress cycle. Hence, the crack tip area is more accessible to the environment.

2.4.3 Mechanisms for Life Reduction

Discussed so far have been the factors that can influence corrosion fatigue, and the commonly experienced effects of each parameter. In some cases, a brief insight into why the environment diminishes fatigue life is given, or can be implied. During the next three sections, a more precise account will be given into why certain environments seriously reduce fatigue life.

2.4.3.1 Pitting

The contribution of corrosion pits to the reduction in fatigue performance is generally attributed to the generation of favourable crack initiation sites. This is evidenced through the finding of pits at the initiation point of corrosion fatigue cracks [85,86]. We know from previous discussions that cracks will often initiate where a stress raiser exists, and in the immediate vicinity of a pit, it can be expected that the stresses will increase.

Pitting is a time dependent process, i.e. some time is often required for a pit to form, and the size of the pit will then increase with time. The dependency of the size of the pit on time is said to fit a power law function [87,88], such as:

Where d is a chosen pit dimension, t is time and A and B and empirically determined constants. The parameters A and B, are corrosion rate dependent and therefore require will identification for each metal-environment combination, and, in addition to this, they have also been identified as having a dependency on stress and frequency [87].

During corrosion fatigue, the corrosion process will affect crack propagation as well as promoting premature crack development. Therefore, investigations have been conducted to see the effects of the pit alone. Lindley et al [85] carried out such experiments by pre-pitting test specimens and subsequently performing fatigue tests on them in air. Their results showed that the greater the pit depth, the greater the reduction in fatigue life. It was seen that a pit depth of 250μm could produce a reduction as large as 70% of the air fatigue life.

Characterisation of the pit with regard to modelling the point, at which transformation from pit growth to crack growth occurs, is generally viewed in two ways. The pit can be viewed as acting like a notch, and the stresses developed by that notch are then addressed [89,90,91,92]. These investigations applied theoretical approaches to determine the stress intensification of the pit. Another approach has been to assume the pit to be an equivalent surface crack [85, 86, 87, 88]. In two of these cases [87,88], the equivalent crack dimension is determined using an approach by Murakami and Endo [93,94]. The other two cases simply use the pit dimensions directly. In all the cases mentioned, where the pit is considered to be a crack like defect, the crack, or equivalent crack, is considered to grow when a critical value of ΔK is reached. This implies that the crack is growing under LEFM conditions, or more precisely, no short crack growth region is considered. However, Akid [95] has shown that short crack growth can be observed during corrosion fatigue and that the environment can have significant effects on the short crack region, i.e. the barriers to short crack growth are weakened and the transition from short to long crack growth occurs at a shorter crack length. Observations of corrosion affected short crack growth have also been observed by Rios et al [96].

2.4.3.2 Crack Tip Dissolution

The role of anodic dissolution of a metal has already been shown to be a key factor in corrosion fatigue, as, on a localised scale, it results in pits. The detrimental effects of dissolution are, however, believed to continue beyond pit development, and cause enhancement of the crack propagation rates. This is due to dissolution of freshly created bare metal at the crack tip. The rate, at which dissolution, or crack advancement through dissolution, occurs, will depend upon, amongst other things, the rate of newly created metal surfaces and the rate at which these surfaces may oxidise, and therefore protect from further dissolution [97]. Methods proposed to accommodate crack tip dissolution into corrosion fatigue crack growth rates have applied a simple summation of the dissolution rate plus the air fatigue crack growth rate [98]. Congleton et al [99] suggested that the anodic currents measured in their experiments are sufficient to account for crack growth by anodic dissolution.

However, it is argued that simple summation of the two rates would suggest that barriers to corrosion fatigue crack growth would retain the same strength as for air fatigue. The strength of these barriers is known to reduce, and therefore a simple summation may not be totally correct. Such conclusions have been drawn by Wang et al [100], where they showed that superposition of the two rates did not account for the corrosion fatigue crack growth rate that they measured. Although crack tip dissolution would not appear to account for all the detrimental effects the environment has on corrosion fatigue crack growth rates, it will bear some influence, the extent of which will, again, be dependent upon mechanical and environmental factors, i.e. frequency, load ratio and temperature [101].

2.4.3.3 Hydrogen Embrittlement

As stated in the Section 2.4.3.3, anodic dissolution, or the electrochemical removal of material from the crack tip, during corrosion fatigue, cannot fully account for the increases observed in crack propagation rates when comparing corrosion fatigue with air fatigue. Generally, hydrogen is believed to be a major contributory factor to the enhanced corrosion fatigue crack growth rates [102].

An important aspect of the presence of hydrogen within a metal matrix is the effect it can have on the mechanical properties of the metal. One such aspect is known as hydrogen embrittlement. The embrittlement of the metal is manifest in the reduction in ductility (elongation to failure) of a metal and the lowering of the fracture toughness values [103,104,105,106]. Various reasons have been suggested for apparent embrittlement. Some of the suggested mechanisms are: the production of molecular hydrogen within voids creating large internal pressures [107]; atomic bond de-cohesion [108,109]; surface adsorbed hydrogen reducing the surface energy [110]; and brittle hydride formation in metals that are susceptible to producing hydrides, such as titanium.

A second damaging characteristic of hydrogen within a metal is the effect it can have on the yield strength. It has been shown that the yield strength can be reduced by prolonged exposure to corrosive environments. On a macroscopic scale, the effect of hydrogen is not as damaging to the yield properties as it was to the ductility [111]. However, with respect to fatigue, the reduction in flow resistance was said to play an important role in the shortening of the fatigue life in the presence of a corrosive environment. It was also suggested that the effectiveness of the grain boundaries to hinder short crack propagation was lessened.

With the application of an adequate heat treatment, the effects of hydrogen have been shown to be reversible to a great extent.

In the absence of an applied stress, the hydrogen will diffuse deeper into the material by a process of natural lattice diffusion [112]. Therefore, to affect the bulk material properties, long periods of time may be required for diffusion of the hydrogen. However, in the case of a growing crack with an applied stress, hydrogen transportation is more rapid, facilitated by trapping of the hydrogen atoms at dislocations and subsequent dislocation motion. One investigation found that two hydrogen concentration peaks exist ahead of a crack tip, one due to the dislocation build up ahead of the crack, and the second caused by the hydrostatic stress [112]. Therefore, whilst hydrogen effects due to corrosion may take time when no stresses are present, under the combined condition of corrosion and stresses, not only is the hydrogen migration process increased, but the nature of the transportation of the hydrogen atoms leads them to critical locations within the metal matrix, i.e. ahead of a crack tip. Also, atomic sizes of hydrogen gain the benefit of being small in comparison to other atoms in metal matrix and thus, easily penetrate into the substrate.

In the present context, hydrogen is assumed to be introduced to a metal by the presence of an aqueous media. This assumption applies for the vast majority of corrosion fatigue studies. However, there are instances where hydrogen alone may be present in the environment and may directly contaminate metals, without corrosion processes taking place. Hydrogen gas cooled turbine generators, or hydrogen fuelled rocket engines are such instances. Therefore, fatigue studies on the effects of hydrogen are necessary, and not only for determination of the hydrogen contribution to fatigue in aqueous environments. Investigations have been conducted by either pre-charging specimens with hydrogen by conducting the EXCO tests [113].

Glow Discharge Optical Emission Spectroscopy (GDOES) and their subsequent tensile testing of the samples in same conditions have shown the surfaces created during EXCO tests in a hydrogen environment to be of a brittle nature.

Some results of hydrogen pre-charged specimens have also indicated increased crack growth rates. Mittal [114] showed, for three positive stress ratios, that pre-charging with hydrogen induced crack growth rates of an order 2 – 15 times that of air fatigue. Rios et al [115] also showed that pre-charging generated higher crack growth rates, but here they demonstrated the effect was also evident during short fatigue crack growth. After performing monotonic tests, they concluded that the short crack region was affected by: reduced frictional stresses on the Persistent Slip Bands (PSB) are, therefore generating larger crack tip plastic displacements; and reductions in the grain boundary strength. Both of these investigations suggested that, for the stage II crack growth, hydrogen transportation to favourable sites could be the cause for embrittlement ahead of the crack tip. Such ideas were proposed by Troiano [116], where hydrogen, transported by dislocations to positions of high triaxial stresses, generates de-cohesive zones. Studies have been conducted, which showed that areas of high hydrogen concentration exist ahead of a crack tip [117].

Other investigations have indicated that hydrogen can aid dislocation generation as well as increase the dislocation velocities [118,119]. In any case, it is obvious that hydrogen can play an important role in the enhancement of crack propagation rates during corrosion fatigue.

2.4.4 Corrosion Fatigue Models

Many models have been proposed to describe corrosion fatigue of various materials in various environments. The majority include two portions of life, one for pit growth and a second for corrosion fatigue crack growth from that pit. More often than not, this method involves a critical pit depth to produce stress concentration factor, K_t, whereby a crack will propagate from the pit. However, other methods have been employed, based on corrosion rates, stress corrosion cracking rates and environmental influences on mechanical parameters, to name but a few.

Wei et al [120] has produced corrosion fatigue models, with subsequent developments. One of the earliest was the superposition model he produced with Landes [120]. This model suggests that corrosion fatigue propagation rates consist of a simple summation of the *air fatigue increment* and a *stress corrosion cracking increment*, thus:

$$\frac{da}{dN_{cf}} = \frac{da}{dN_{af}} + \frac{da}{dN_{scc}}$$

Equation 26

where $\dfrac{da}{dN_{cf}}$ is the total crack growth rate and the growth rates $\dfrac{da}{dN_{af}}$ and $\dfrac{da}{dN_{scc}}$ represent air fatigue and stress corrosion cracking respectively. However, this method implies no synergistic effects of the environment and the fatigue crack growth, and it does not account for corrosion fatigue in the event that the metal-environment combination does not induce stress corrosion cracking. In other words, when $\dfrac{da}{dN_{scc}} = 0$, the corrosion fatigue and air fatigue behaviour will be identical.

However, this model was later modified [121,122,123] to recognise that mechanical fatigue and cycle dependent corrosion fatigue proceed by different micro-mechanisms and can occur concurrently. The chemical modelling effort considered the processes that can be involved, in part or in total, in the enhancement of fatigue crack growth. These processes include: transport of the deleterious environment to the crack tip; reactions of the environment with the newly produced crack surfaces to evolve hydrogen or to effect localised dissolution; hydrogen entry; diffusion of hydrogen to the fracture (or embrittlement) site; partitioning of hydrogen among the various micro-structural sites; and hydrogen metal interactions leading to embrittlement. These processes are considered to operate consecutively. For a dissolution mechanism only, then only the first two steps need be considered, where the anodic dissolution reactions of the second step are directly responsible for crack growth enhancement. However, if hydrogen embrittlement is the responsible mechanism then the reaction step serves only to produce hydrogen, then all the remaining steps must be considered.

Wei also produced probability based models with Harlow [124,125]. These models used probability density functions (pdfs) to describe factors involved in corrosion fatigue, assuming them to be random processes. This approach was developed to account for realistic conditions, to extend life predictions beyond laboratory experiments.

Another model, which, like Wei's original model, includes a stress corrosion cracking component, is the **Process Competition Model** [126]. This was developed on the premise that, rather than *stress corrosion cracking* and *corrosion fatigue* being additive methods for *crack advance*, the *two processes were mutually competitive*. On this basis, the crack advances by whichever process is the faster. Methods to model corrosion fatigue, that include stress corrosion cracking parameters, have still been attracting attention in recent years.

Of the numerous corrosion fatigue models based upon critical pit sizes, two will be considered here as being representative examples. Hoeppner [127] proposed a model which is constructed by determining experimentally, characteristics of the corrosion fatigue process. Pit growth rate calculations are made so that a critical pit depth can be described by the number of cycles required for it to develop. The pit dimensions are described in terms of a flaw so that K can be determined through **Equation 7**. The threshold stress intensity, ΔK_{th}, is then found by extrapolating a growth rate versus ΔK curve, for a Mode I crack. The number of cycles for the Mode I crack to grow from the pit/flaw size to failure is obtained using fatigue crack growth prediction methodology, such as LEFM. A simple summation of the two calculated cycles, pit growth and crack growth, is then left to give total life.

Kondo [128] proposed a model along similar lines to Hoeppner's. Again, an expression for pit growth was determined in terms of cycles. However, once this was achieved, he substituted into the pit growth rate equation a term to describe ΔK. From here two curves were plotted on the same axes of growth rate versus ΔK. One curve showing the decreasing growth rate behaviour of the pit, and the second describing the accelerating growth rate behaviour of the crack. The point of intersection was described as being the transition from pit growth to crack growth. Thus, this model eliminates establishing a ΔK_{th} value.

Although these two models describe corrosion fatigue life well, as demonstrated in the presented articles, they are both empirically based. Any effects of hydrogen are assumed from the crack growth rate parameters. Any effects of frequency, waveform or stress levels etc, on pit growth that may occur, are not taken into account. Stage II cracks are assumed to grow directly from the pit, thus implying that either insignificant short crack growth exists, or that pit growth exceeds short crack growth, until a point where an LEFM applicable crack can grow directly.

2.4.4.1 Modified Brown-Hobson Model (Environmental)

Angelova and Akid [129] developed a model based on four stages, or three transition points. The model is based upon the Brown-Hobson model (See **Section 2.3.2.6.4.2**) with subsequent modifications to incorporate environmental effects. The three transitions consist of: *pit to crack transition*; *micro-structurally short shear stage I crack to physically small tensile stage II crack transition*; and *physically small tensile stage II crack to long stage II crack transition*. These transition boundaries, therefore, represent: a stress assisted pitting dependent state; an environment and stress assisted short cracking dependent state, and an environment and stress assisted physically small cracking dependent state. This model still utilises a pit to crack transition point, however, the crack is then assumed to behave as a short crack, taking into account influences of the microstructure.

2.4.4.2 Modified Navarro-de los Rios Model (Environmental)

A final model worthy of mention is that of Rios et al [130]. This model is based on the air fatigue modelling. Again, a critical pit depth is assumed; however, the pit depth was determined empirically for several stress levels, instead of using an LEFM determined crack growth threshold value. Stress concentration factors were determined for the pit, and other parameters required for the Navarro-Rios model (See **Section 2.3.2.6.4.3**) were determined, i.e. environmental fatigue limit and a modified strain hardening parameter. This model takes into account the effects of pitting and also the increase in crack growth rates due to the environment, that are said to occur through an enhancement of the crack tip plasticity and a reduction in the strength of micro-structural barriers.

CHAPTER 3

Surface Engineering Techniques

3.1 Introduction

Fatigue resistance for multigrain materials represents the degree of difficulty for a stage I crack becoming a stage II crack. Fatigue resistance would increase by introducing compressive residual stresses in the surface layer to compensate for tensile loading stresses. This is also complemented by introducing many and variable forms of textural barriers to hinder the development of a stage II crack. The application of suitable surface engineering treatments, alone or combined with other hardening processes, delays the propagation of such cracks. A number of different ways have been identified by which fatigue resistance can substantially be affected: by machining, by rolling, by shot peening, by laser shock peening, and by Ultrasonic Impact Treatment (UIT).

3.2 Shot Peening (SP)

The SP process has for some time been described as an effective mechanical surface treatment in tackling fatigue failure. This method is a cold working process that involves bombarding a metal component with a stream of small and relatively hard shot to induce desirable residual compressive stresses and strains within the surface layers of the component.
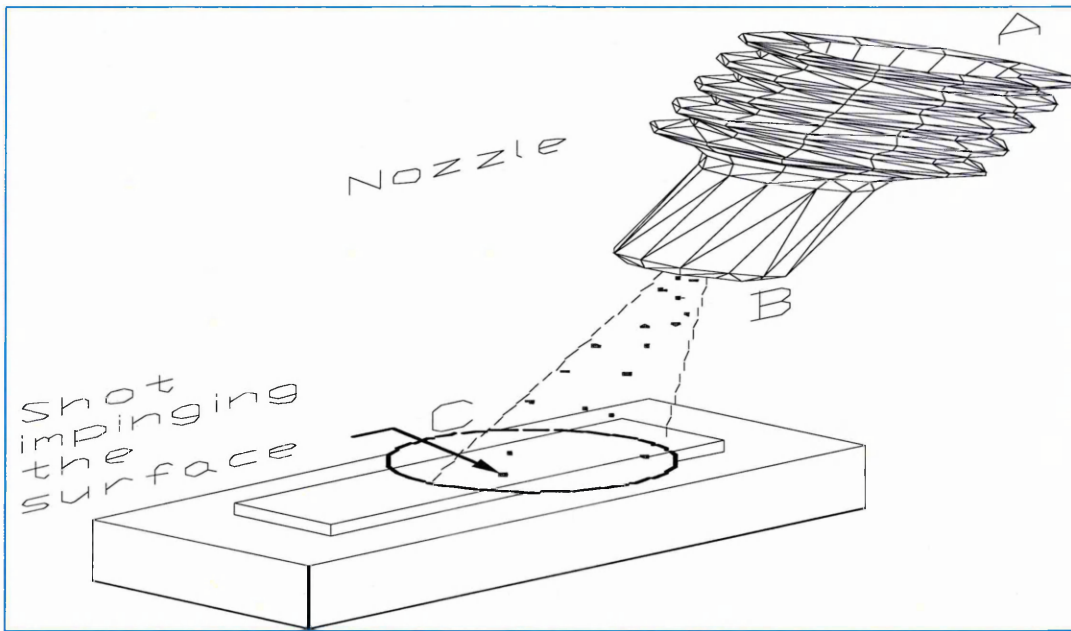
Figure 22: A representation of the SP process.

A general picture of what constitutes the mechanism by which the peening process can alter the microstructure and properties of the peened layer is shown in **Figure 22** [131,132].The particles are propelled by means of compressed air and further accelerated (right side figure) when passing through a nozzle (from point A to B). At point B, the particles, highly loaded with kinetic energy, are projected to the surface (point C). The shot blast pattern is usually of the shape of a narrow cone with a region highly obliterated at the surface.

3.3 Laser Shock Peening

Laser shock peening is a technique similar to shot peening that imparts compressive residual stresses in materials for improved fatigue resistance. During Laser Shock Peening

(LSP), pressures well above the dynamic yield strength of the material are imparted on the target in a fraction of a microsecond. The severity of the loading causes local plastic deformation which ultimately results in the development of the favourable residual stresses [133].
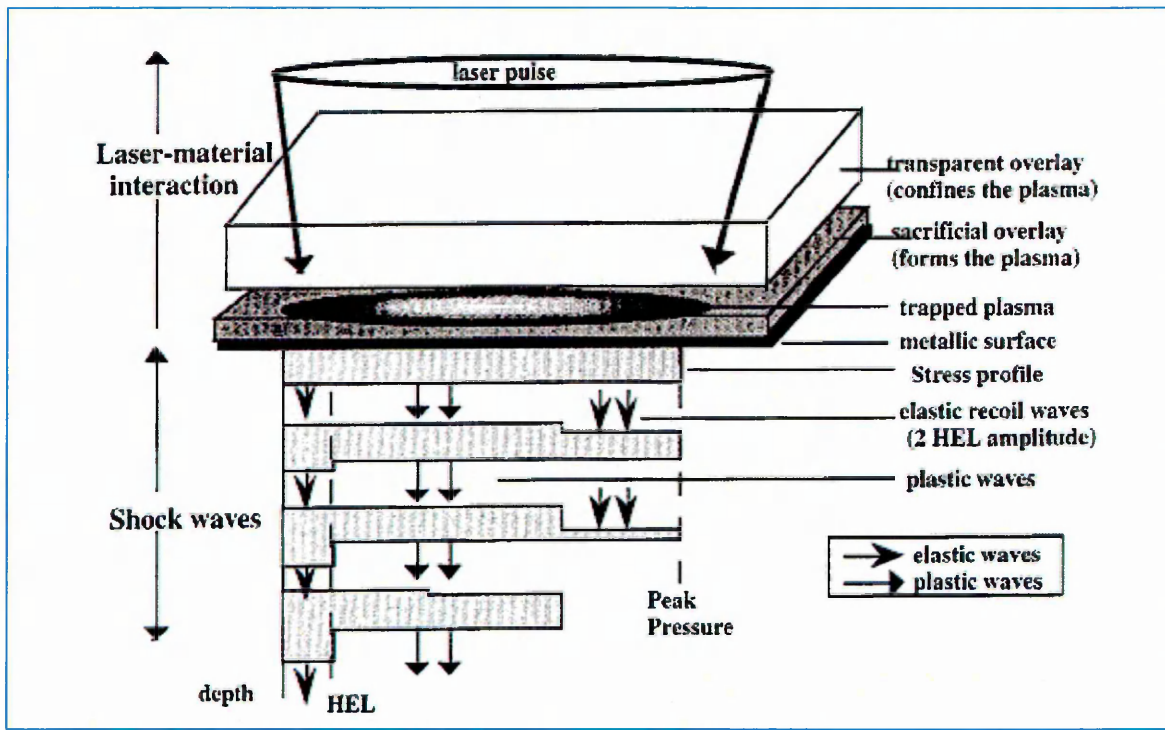
Figure 23: Laser Shock Peening (LSP) in the confined ablation mode [133]

3.4 Ultrasonic Impact Treatment

3.4.1 History

The genesis of the UIT technology begins as early as the 1950's. During this decade many scientists believed that the introduction of ultrasonic energy into metal surfaces would have a positive impact in altering the sub-surface and surface properties of the metal resulting in prolonged life of metal components. A relatively thin surface layer of the treated material was plastically deformed, producing modifications of the surface micro relief and redistribution of residual stresses in this layer. Subsequently in the 1960s, Krylov et al. introduced an intermediate mass in the form of a free ball between the output end of the ultrasonic transducer and the material being treated [134]. In this work, the method of oscillating system excitation replicated the continuous ultrasonic excitation used in the efforts referenced above.

In the early 1970s, Statnikov proposed a method of ultrasonic impact treatment [135], which is finding expanding applications in various industries, including manufacture and maintenance of welded structures and machinery components. This method differs fundamentally in that it employs free needle indenters as impacting elements that move along the axis of the oscillating system and have a normalized wavelength relative to the carrier ultrasonic frequency. The indenters are installed in separate guiding holes and excited by modulation pulses of the carrier resonance frequency of the ultrasonic oscillation system. This engineering solution provides high-intensity ultrasonic impacts accompanied by ultrasonic vibrations of indenters in a gap and together with the surface being treated. These impacts initiate highly effective plastic deformation and transfer through high-intensity ultrasonic vibrations and ultrasonic stress waves into the material being treated. A combination of such factors of the ultrasonic impact creates necessary prerequisites to modify properties and conditions of the surface and subsurface material at a specified depth.

The development of the method [135] in the late 1990s and early 2000s [135] resulted in the *Esonix technology* that supported a firm position of the ultrasonic impact treatment among well-known techniques of improving fatigue resistance including surface plastic deformation (SPD) methods. The technology controls the quality, properties and characteristics of the surface, modifies material properties in the treatment area, improves the fatigue and corrosion resistance, as well as the resistance to abrasion and contact failures, reduces residual stresses and deformations, stabilizes and improves static quality and reliability characteristics in mechanical engineering.

3.4.2 Nano-Crystallisation

It is well known that component failure due to fatigue, corrosion or other forms of operational duty capable of introducing stress concentrators normally initiate on the surface. Hence, optimisation of the surface structure and properties may effectively improve the global behaviour of the material. The physical properties of a metal are dependent on the grain size. The Ultrasonic Impact Treatment process can effectively refine the coarse surface
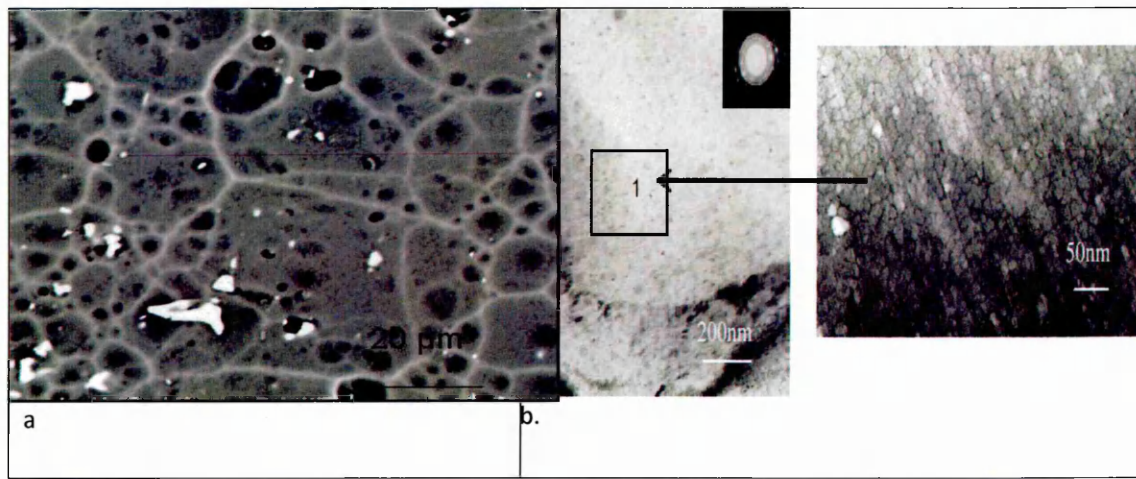
Figure 24: a) Micrograph a shows the crystal structure of bare Al 2024 T351. b) A TEM Micrograph showing crystal structure subjected to UIT. Nanocrystallisation is evident and its measured to be between (10-15) nm [136].

grains into equiaxed nano-crystalline grains of about 10 nm in elongated micro-bands of 15nm to 20nm wide (see **Figure 24**). The affected surface was measured to be around 10-12 microns through cross-sectional depth of the alloy.

3.4.2.1 Effects of Nano-crystallisation

3.4.2.1.1 Mechanical properties

It is well known that grain refinement improves the strength of materials. The plastically deformed zone which is about (1-4) mm from the surface depending on the type of UIT treatment undergone. The Ultimate Tensile Strength (UTS) increases remarkably according
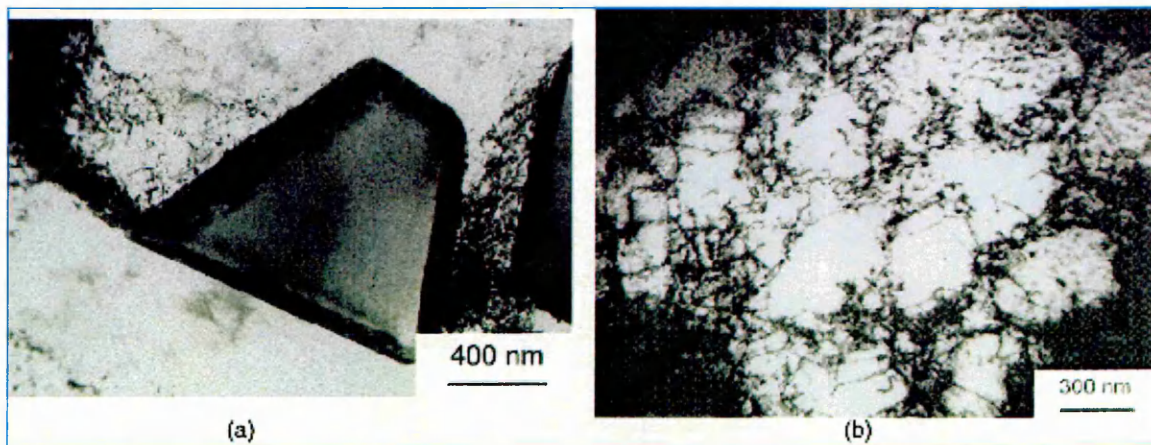
Figure 25: TEM micrographs: (a) Trapezoidal Al2 Cu particle as emission source of dislocations; (b) dislocation cells and tangling in aluminium matrix. (Courtesy: picture is a published work by X. Wu et al [136]).

to the reduction of the grain size. The reason for this increase in UTS has been proposed by *X. Wu et al* [136]. They used ultrasonic shot peening as a Severe Plastic Deformation (SPD)

52

technique. The division into sub-grains was found to be the main mechanism responsible for grain refinement.

The simultaneous evolution of high boundary mis-orientation was ascribed to the sub-grain boundary rotation for accommodating further strains. Exposure of deformation could effectively enhance evolution of low-angle boundary mis-orientations into high-angle ones. The generation of ultrafine sub-grains resulted from the piling-up of dislocations along the {111} primary slip plane. The high stacking fault of Al makes dislocation slip on {111} planes the only deformation mechanism. Severe plastic straining produces a high density of dislocations which are effective at blocking slip at increasing strains and as a result, the mechanism responsible for accommodating large amounts of plastic straining is the subdivision of the original grains in to sub-grains with dislocations forming their boundaries.

3.4.2.1.2 Corrosion resistance

In terms of corrosion resistance, Al-Cu-Mg alloys without copper have good corrosion resistance in most reagents; only in alkaline solutions which attack Cu as well as aluminium their performance is poor. Copper reduces appreciably the corrosion resistance. Porosity decreases corrosion resistance. 2xxx alloys with iron have particularly good resistance to high-temperature water or steam.

UIT causes a division of grains in to sub-grains, thereby producing a microstructure with a higher density of grain boundaries. In addition UIT leads to a decrease in non-metallic inclusion size (physical breakdown) and a re-distribution of copper. Both these effects cause the structure to be less prone to pitting corrosion, resulting in the surface corrosion being more 'uniform'. **Figure 26** shows the effect of UIT1 condition on the corrosion resistance of Al 2024- T351 subjected to 24 hours of exfoliation at 20 ^{0}C. Further SEM images are tabulated in **Appendix A**.

Condition	As-Received	UIT1
24hours at 20°C		
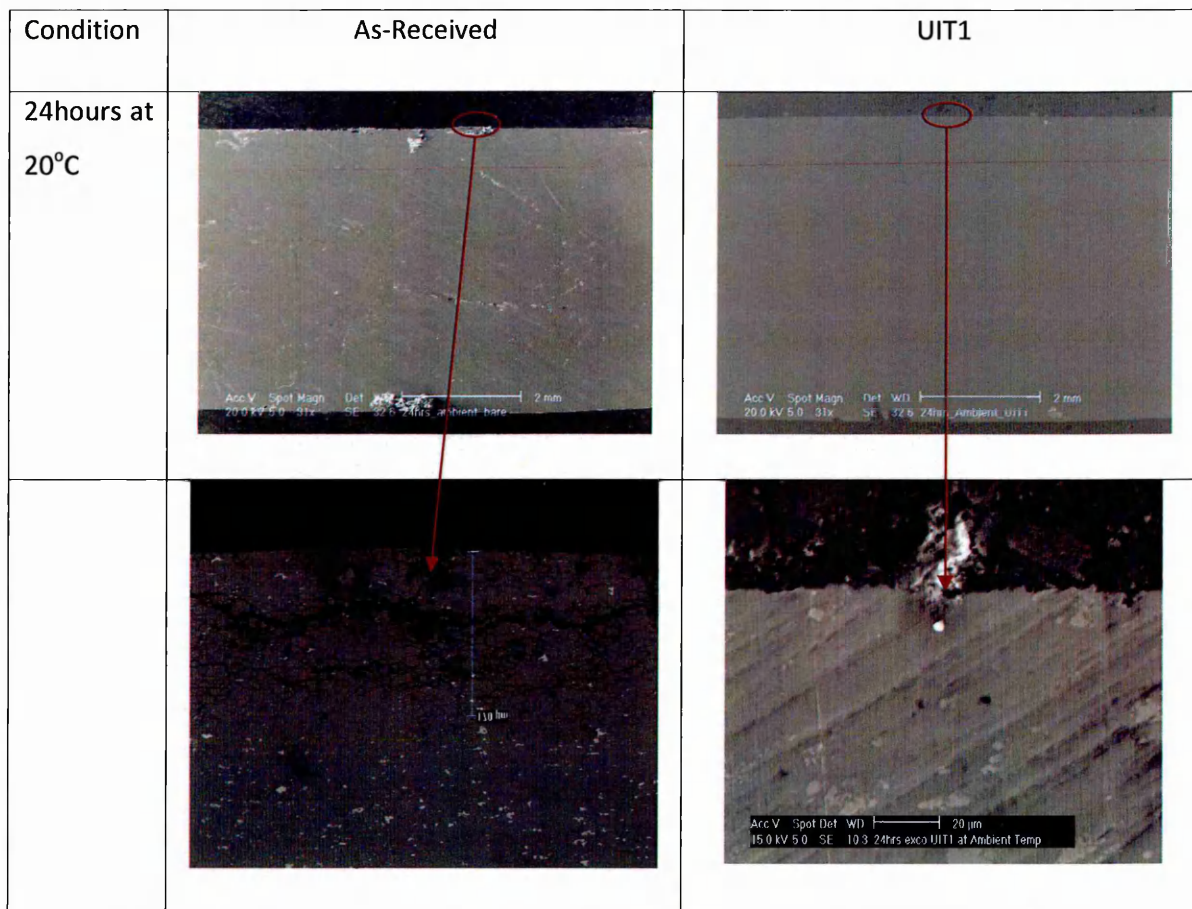
Figure 26: Effect of UIT on corrosion resistance on 24 hours exfoliated at 20 ^{0}C.

3.4.3 Ultrasonic Impact Treatment Mechanism

The Esonix Ultrasonic Impact Treatment (EUIT) is a technique that directly deforms the surface of the materials using ultrasonic impacts. This technique uses an ultrasonic signal to vibrate small diameter silicon-carbide heads at specific magnitudes and frequency. Due to the continuous contact of the peener head with the material surface, the technique can induces condition of ultrasonic strain creep. Hence, the affected surface layer is compacted and recrystalised with the sub-surface and un-corroded material while at the same time, high stable residual stresses are introduced. The device show in **Figure 27** is a single impact EUIT which uses an ultrasonic transducer to converts a ultrasonic signal in to mechanical energy at indenter.
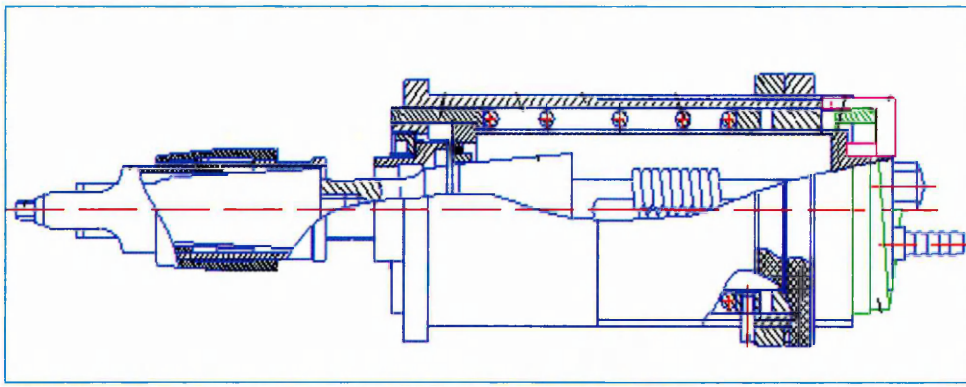
Figure 27: Esonix device for realisation of single impact on specimens.

3.4.4 UIT Conditions

The Ultrasonic Impact Treatment (UIT) conditioning was carried out using the following parameters and was named UIT-1, UIT-2 and UIT-3. However, this research selected UIT-1 considering the results obtained on the first series of immersion tests in exfoliation solution.

UIT-1

Carrier Frequency 36 KHz

Pin $\varnothing$ 5.0 x 17 mm, R25 mm;

Normalized impact – 64 impulses;

Amplitude under load – 18 micron;

Pressure force – 3 Kg

Impact frequency 260 Hz

Feed rate: 400 mm/min,

Cross feed 0.5 mm/work stroke

UIT-2-36

Carrier frequency 36 KHz

Pin ∅ 5x17 mm, R 25 mm;

Normalized impact 64 impulses;

Amplitude under load 15 microns;

Piressure force - 3Kg

Impact frequency 220 Hz

Feed rate 1000 mm/min

UIT-3-36

Carrier frequency 36 KHz

Pin ∅ 5x17 mm, R 25 mm;

Normalized impact 64 impulses;

Amplitude under load 10 microns;

Pressure force - 3 Kg

Impact frequency 220 Hz

Feed rate 1000 mm/min

CHAPTER 4

Experimental Techniques

4.1 Introduction

The main objective of the experimental effort was to determine quantitatively the modifications on the surface and subsurface of the AA2024-T351 caused by Ultrasonic Impact Treatment (UIT) carried out under selected conditions, which may lead to an optimisation of the process in terms of the corrosion and fatigue resistance. To obtain optimum UIT conditions, the significant factors and their interaction for the selected levels were determined. This exercise rendered the best and worst UIT conditions in terms of residual stresses and corrosion resistance. Polarisation curves were also plotted using the Scanning Droplet Cell (SDC) which contradicts the results which were previously attained. The nanocrystallisation layer which is under 12 μm still needs to be investigated. Fatigue testing was undertaken employing such predetermined UIT conditions.

4.2 Glow Discharge Optical Emission Spectroscopy

4.2.1 Introduction

GDOES combines sputtering and atomic emission to provide an extremely rapid and sensitive technique for element depth profiling. During analysis, plasma is generated in the analysis chamber by the applied voltage between the anode and the cathode (the sample surface) in the presence of argon under low pressure. Ionised Ar atoms cause sputtering of the sample area. Sputtered atoms excited in the plasma rapidly de-excite by emitting photons with characteristic wavelengths. Glow Discharge is a rich analytical source for atomic spectroscopy. The Grimm source was the most important historical development for GDOES. This source has external-sample mount geometry which permits almost any sample as long as it has one flat face. This source was extensively developed as a sputter source for both optical emission and absorption spectroscopy. Although GDOES was originally designed to perform bulk analysis, new areas of application continued to emerge such as the surface analysis and depth profiling. As this research mainly needs depth profiling of the samples it is worth discussion.

4.2.2 Principle of Operation

Glow Discharge (GD) operates on the simple principle of two parallel plates, one the cathode and the other the anode are separated by some centimetres in a glass vacuum tube and a carrier gas is introduced and a potential difference applied across the plates (**See Figure 28**). At suitable pressure and potential difference the source is seen to glow strongly, in bright and dark bands between cathode and anode. When the current is sufficiently high the cathode is fully covered by a dark space and some millimetres away from cathode would be a bright band, called a negative glow, this is followed by a dark band and then followed by a positive glow, which extends almost up to anode. When the anode is brought closer towards cathode, the positive glow will disappear and what remains is alternate negative glow in dark bands.

In the cathode dark space the argon is ionised and the argon ions produced there bombard the cathode surface causing sputtering of the cathode. Sputtered material from the cathode passes back through the cathode dark space and enters the negative glow region where it glows brightly by atomic emission. The emission lines are then detected to analyse the material being sputtered from the cathode.
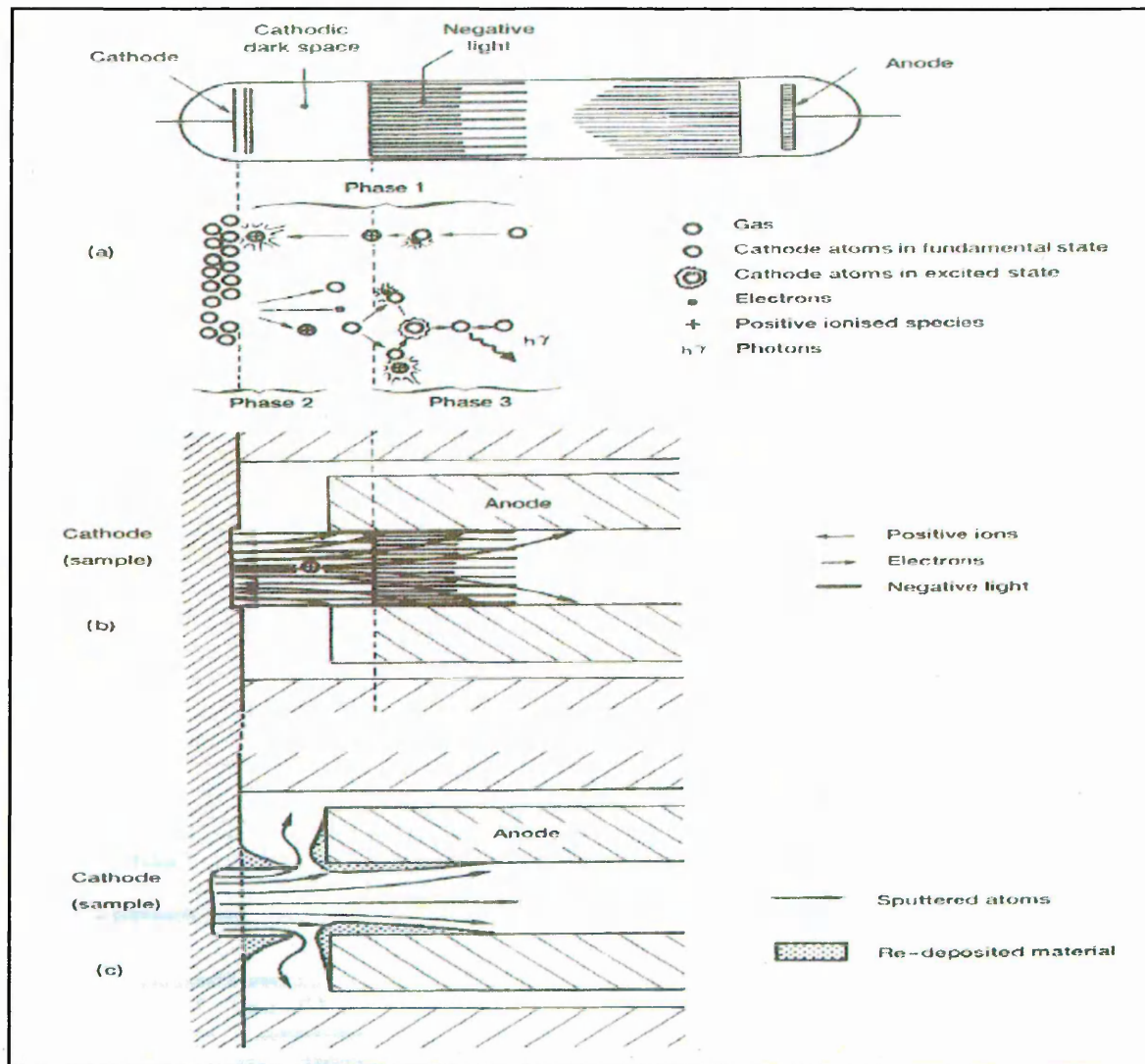
Figure 28: The phenomena present in the neighbourhood of the cathode. (a) Cathodic sputtering, excitation phenomena, ionisation and de-excitation with the emission of light, (b) trajectories of ions and electrons in the source, (c) trajectories of the material removed from the sample (cathode). Picture is a published work from the book GDOES by Payling R [137].

4.2.3 Sputtering

Whenever an energetic particle interacts with a metal, many processes are bound to occur. This particle eventually damages the surface causing considerable damage to the target (**See Figure 29**). Such a process is of interest in GDOES as the material is sputtered from the target, either as atoms or molecules in neutral or ionised states, or electrons may be ejected. In general, neutrals are mostly ejected. All this process takes only a few femtoseconds.
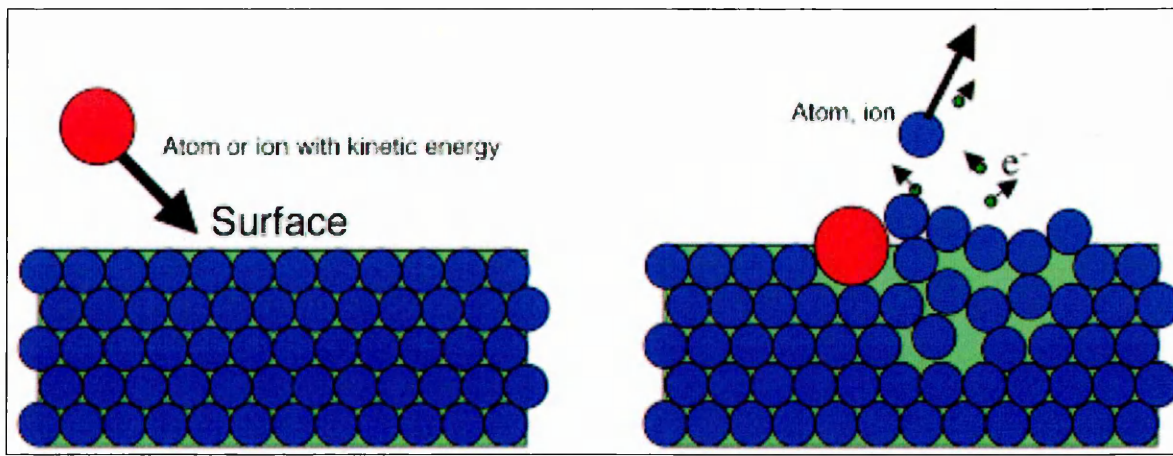
Figure 29: The impact of an atom or ion on a surface produces sputtering from the surface as a result of the momentum transfer from the in-coming particle.

In these so called primary collisions, energy is either transferred to the target nuclei in collisions, so called nuclear energy loss, or to the electrons as either ionisation or excitation, termed electronic energy loss. The energy, E_t which can be transferred to a target nucleus in a single collision is

$$E_t = \frac{4 m_i m_t E_i \cos^2 \theta}{(m_i + m_t)^2} = \eta E_i \cos^2 \theta \qquad \textbf{Equation 27}$$

Where m_i and m_t are the atomic masses of the incoming particle and the target atom respectively, E_i is the energy of the incoming particle and θ is the scattering angle [137].

4.2.4 Sputter Yield

Sputter yield S can be defined as the number of atoms excited per incoming argon ion bombarded. From **Equation 27**, it is evident that S will be zero until E_i reaches minimum threshold energy. Thus at low energies we may not expect sputter yield. Sputter yield depends on number of grounds such as threshold energy, sputtered species alloying components, angle at which target is bombarded etc.

4.2.5 Development of Depth Profiling Applications

GDOES was initially designed for bulk analysis, researchers unveiled Glow Discharge (GD) potential for procuring depth resolved chemical information [137]. The combined sputtering and atomic emission provide a modern, rapid technique for analysing depth profiling surfaces, coatings and interfaces. This technique is widely used in many research fields for a rapid profiling provided the sample is compatible with the vacuum condition.

4.2.6 Specimen preparation

In Grimm's glow discharge source the sample serves not only as the cathode in the discharge, but it has to ensure the vacuum sealing of the chamber against the surrounding environment. Since the cathode plate is a form of a disc carrying a centred O-ring (diameter 10-25 mm), the sample must be flat and large enough to cover the O-ring completely. In addition, when mounting the sample to the cathodic plate, a good electrical contact must be assured.

Depth profiling can be conducted in two ways. The first method is a rather technical version following Bouman's equations [138]. The second method which is used in this research is subjecting the specimen to Grimm's glow discharge source and measuring the depth profile of the GDOES spot created using either a roughness meter or a laser profilometer. Thus, in order to identify the depth of hydrogen ingress into the metal matrix of AA 2024-T351, the depth of the GDOES spot was measured roughness meter as shown in **Figure 30**.
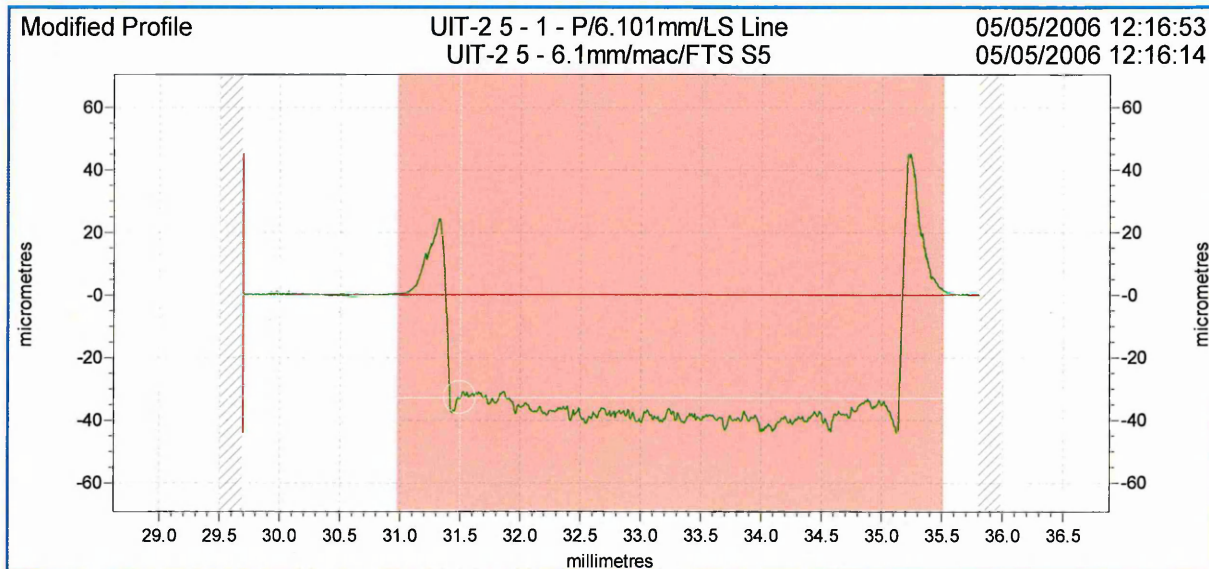
Figure 30: Depth measurement of the GDOES spot using roughness meter.

The surface of the sample with GDOES spot was then ground off up to the depth measured. This will generate a fresh surface and further depth profiling using GDOES and process of measuring depth and grinding off the surface was repeated until the sample exhibited Arbitrary Hydrogen Counts (AHC) which is equal to that of the reference line (As-Received AA 2024-T351).

4.3 Scanning Electron Microscopy

The scanning electron microscope (SEM) is one of the most versatile instruments available for the examination and analysis of the micro-structural characteristics of solid objects. The

61

primary reason for the SEM's usefulness is the high resolution which can be obtained when bulk objects are examined. Advanced research instruments have been described which have achieved resolutions of about 1nm. In general, SEM images are much easier to interpret than Transmission Electron Microscopic (TEM) images, and many SEM images, beyond their scientific value, are actually beautiful.

4.3.1 Scanning Process

In a typical SEM electrons are thermionically emitted from a tungsten or lanthanum hexaboride LaB_6 cathode and move towards an anode. Tungsten is used because it has the highest melting point and lowest vapour pressure of all metals, thereby allowing it to be heated for electron emission (See **Figure 31**).

The Emission current density, J_c, coming from the cathode is expressed by the Richardson Law,

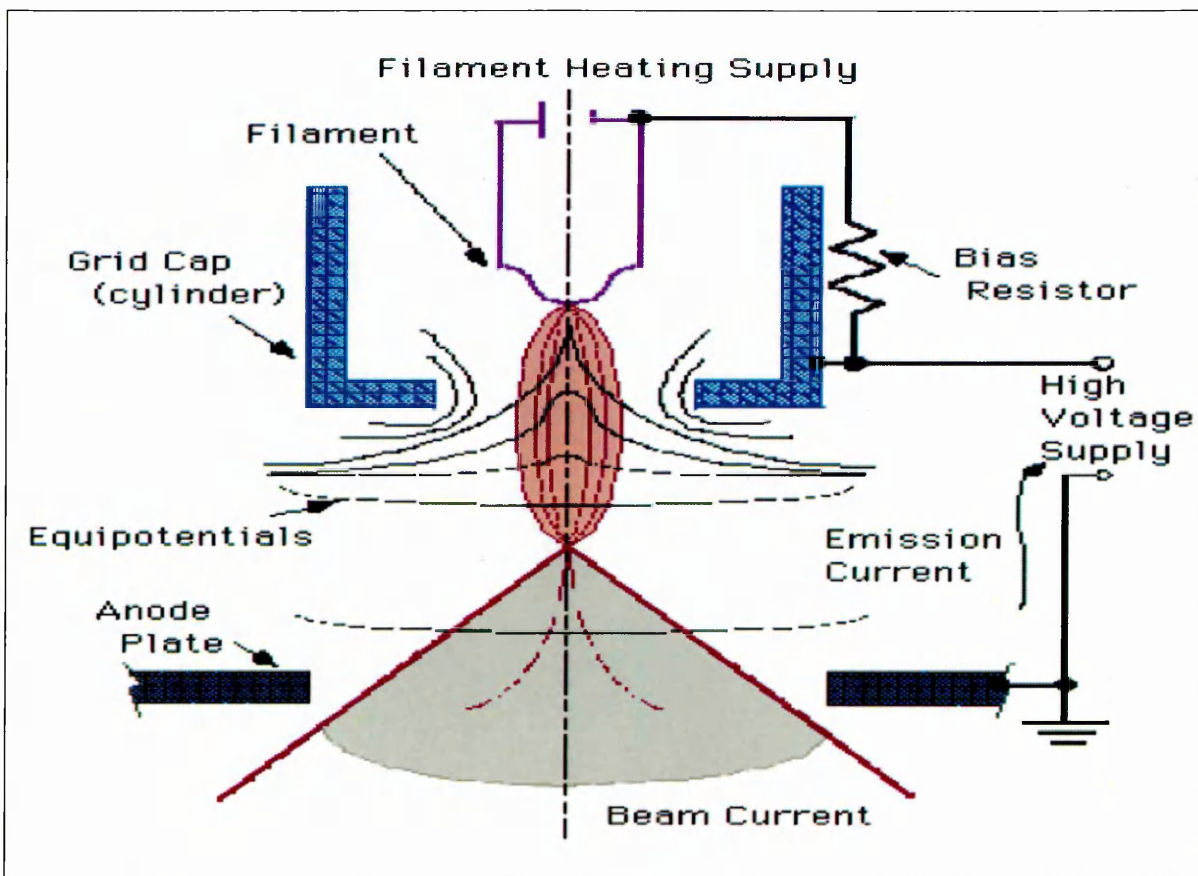$$J_c = AT^2 e^{(-E_w/kT)} A/cm^2 \qquad\qquad \textbf{Equation 28}$$

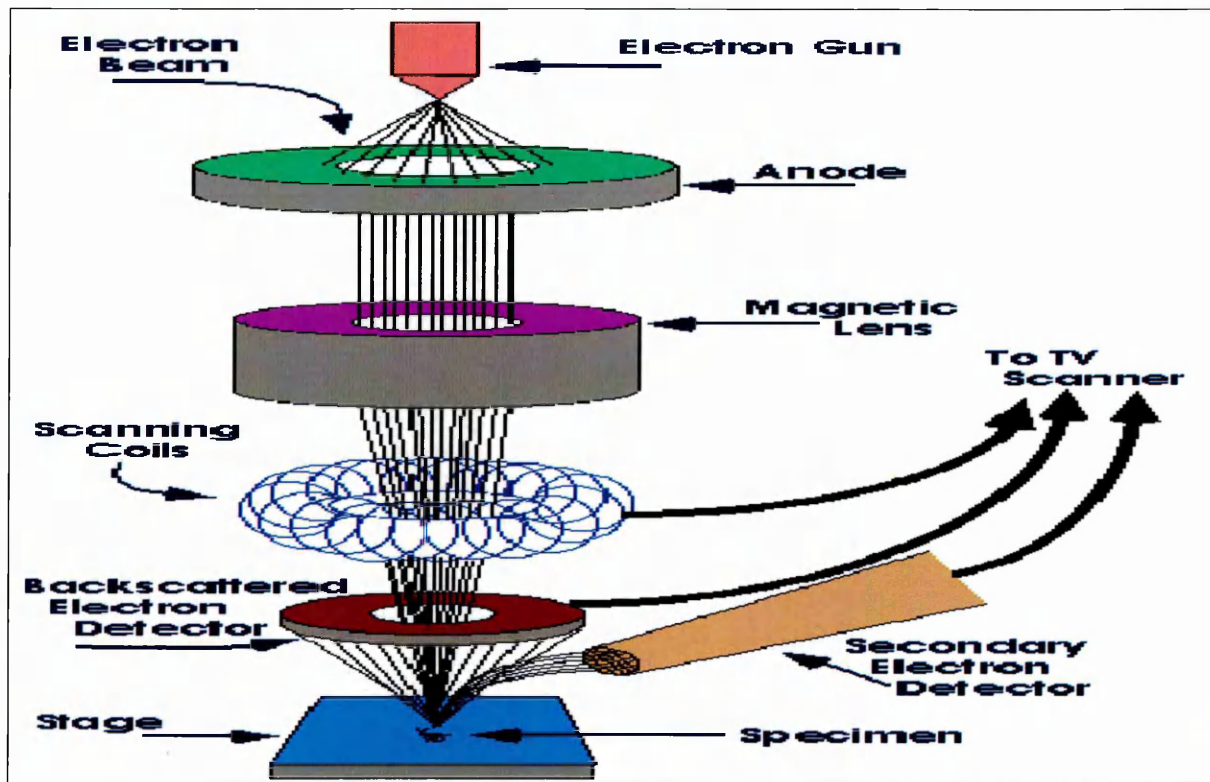**Figure 31:** Configuration of Self-Biased Electron Gun

Figure 32: Schematic Diagram showing the working principle of SEM.

where A is a constant which is a function of the material, T is the emission temperature, and E_w is the work function [139].

The electron beam, which typically has an energy ranging from a few hundred eV to 50 keV, is focused by one or two condenser lenses into a beam with a very fine focal spot sized 1 nm to 5 nm. The beam passes through pairs of scanning coils in the objective lens, which deflect the beam in a raster fashion over a rectangular area of the sample surface.

As the primary electrons strike the surface they are in-elastically scattered by atoms in the sample. Through these scattering events, the primary electron beam effectively spreads and fills a teardrop-shaped volume, known as the interaction volume, extending about less than 100 nm to 5 µm depths into the surface. Interactions in this region lead to the subsequent emission of electrons which are then detected to produce an image.

4.3.2 Detection of Secondary and Backscattered Electrons

The most common imaging mode monitors low energy (<50 eV) secondary electrons. Due to their low energy, these electrons originate within a few nanometres from the surface. The electrons are detected by a scintillator-photomultiplier device and the resulting signal is rendered into a two-dimensional intensity distribution that can be viewed and saved as a

63

Digital image. This process relies on a raster-scanned primary beam. The brightness of the signal depends on the number of secondary electrons reaching the detector.

Backscattered electrons may be used to detect contrast between areas with different chemical composition. These can be observed especially when the average atomic number of the various regions is different. There are fewer backscattered electrons emitted from a sample than secondary electrons. The number of backscattered electrons leaving the sample surface upward might be significantly larger than those that follow trajectories toward the sides. The detector positioned on one side of the sample has low collection efficiency for backscattered electrons due to small acceptance angles. The use of a dedicated backscattered electron detector above the sample in a "doughnut" type arrangement, with the electron beam passing through the hole of the doughnut, greatly increases the solid angle of collection and allows for the detection of more backscattered electrons.

4.3.3 Electron Diffraction X-Ray Spectroscopy

Chemical analysis in the SEM is performed by measuring the energy intensity distribution of the x-ray signal generated by a focused electron beam. The x-ray signal from the sample passes through a thin beryllium window. This x-ray signal then passes through an evacuated chamber containing a cooled, reverse-bias *p-i-n* lithium-drifted silicon crystal. Absorption of the x-rays in the intrinsic region results in the formation of electron-hole pairs, which are collected by the applied bias through a charge pulse, which is then converted to a voltage pulse by a charge sensitive preamplifier. The signal is further amplified and shaped by a main amplifier and passed to a multichannel analyzer (MCA) where the pulses are sorted by voltage. The energy distribution is then displayed on a cathode ray tube.

4.4 Corrosion Testing

Corrosion tests provide the basis for the practical control of corrosion and therefore deserve a more exhaustive discussion than limitations of space will permit. Out of the three mains types of classification of corrosion tests, laboratory tests, although often necessarily conducted under conditions that are not met in service, nevertheless have a number of advantages over the other types of tests.

4.4.1 Electrochemical Corrosion Measurements

In laboratory conditions corrosion can be measured in the following ways:-

- Polarisation curves

- Linear polarisation resistance
- Open circuit potential decay
- Ac impedance measurement
- Electrochemical noise measurement

The mechanism of corrosion is electrochemical; potentiodynamic polarisation is one of the most powerful tools. Using simple probes, potentiodynamic plots can be made in both batch and continuous process. Three things are required to make use of this test method: (1) knowledge of what a potentiodynamic polarisation instrument does, (2) an awareness of conventions for presenting and comparing data, and (3) a basic feel for electrochemical potentials and reactions.

4.4.2 Instrument

A Potentiostat is an instrument for controlling the electrochemical potential of a test electrode relative to some fixed reference potential, and capable of scanning a range of potential differences, an electrode can be defined as an electronic conductor in contact with an ionic conductor. Since adjustments to the potential are made with electrical current a third electrode is necessary in the experiment for the purpose of conducting electricity to or away from the test electrode. The fixed reference potential is usually taken from a special electrode known as reference electrode. Data from experiments of this kind are read out as plots of electrode potential versus the applied current required to produce that potential. Since in corrosion we are interested in rate, we have to add kinetics to the picture. This leads to polarisation curves which introduce kinetics because of the passage of electrical current is a rate function. Since changes in potential of unhindered electrochemical functions are linear with respect to the logarithm of current, a polarisation curve is usually a semi-log plot.
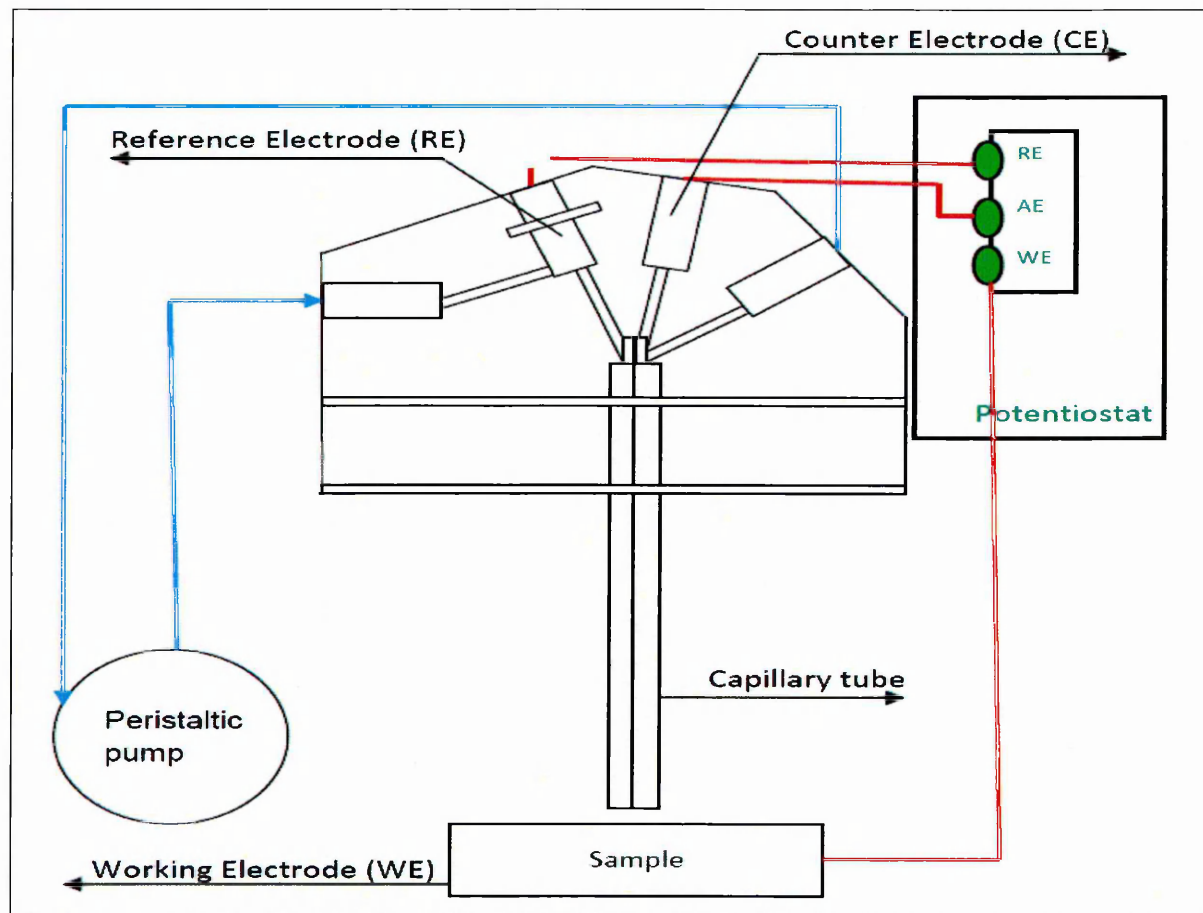
Figure 33: Schematic diagram of Instrumentation setup of electrochemical polarisation tests.

The set up used for conducting potentiodynamic tests was that of a Scanning Droplet Cell (SDC), this is shown in **Figure 33**. The principle of this method is to position a small drop of electrolyte with a capillary on the investigated surface. The wetted area acts as a working electrode and the glass capillary contains the counter and reference electrodes, which are electrolytically connected to the surface through the drop. The single compartmental electrochemical test cell which is communicating via a continuous supply of electrolyte using peristaltic pump is connected to a Potentiostat, which is then setup to the desired voltage. The potential of working electrode is then measured. This technique allows individual areas of the surface to be analysed individually, rather than having an averaged response for the surface.

4.5 Mechanical Testing
4.5.1 Introduction

While it is very common to associate properties with a metal, it is possible to produce a wide range of properties from the same material, by varying the composition slightly, or by

varying its processing. The different ways of processing a metal include how it has been cooled and worked, and any heat treatments it has been subjected to.

These processes and compositional changes affect the microstructure of the material, in particular the grain shape and size and the dislocation density, as well as phase structure and precipitates.

4.5.2 Classification

Mechanical tests are employed to determine relevant material properties of metals and weldments. They may be divided into two groups:

1. Large-scale, structurally representative tests
2. Small-scale materials characterisation tests which determine material properties or give results which are known to correlate with structural behaviour.

It would be relevant to discuss the small-scale materials tests as any large scale testing is not proposed in this project.

However, unlike the former ones not all small-scale tests give results which can be considered a material property. Some obviously do (such as tensile tests) but the predictive capability of others relies frequently on empirical correlations with full-scale behaviour. Such correlations exhibit a degree of inherent uncertainty due to the following factors:

- small-scale specimens do not have the same constraint as the structure due to differences in dimensions and stress state; this can cause, for instance, general yielding of small-scale specimens at stresses when structural behaviour is still elastic
- the loading and strain rates in small-scale tests cannot always simulate structural conditions
- the combination of small-scale specimen compliance and testing machine stiffness is not normally representative of the structure

This means that developed correlations have to be re-established for new materials. Nevertheless, there exist now a large number of material characterisation tests aimed at many different properties, materials and failure modes

The list below gives a brief overview of the various mechanical tests proposed to be used during the course of the project:

1. Tensile Tests (*Strength properties*)
2. Fatigue Testing (*Fatigue Properties*)
   a. Residual fatigue life estimation (S-N Curves)
   b. Fatigue Crack Growth (FCG) analysis

4.5.3 Tensile Testing

The tensile test is the most obvious kind of mechanical test which can be carried out on a material and it is therefore applied more often than most others. Indeed, many of the other forms of mechanical test related to fatigue creep or notch toughness for example, were only developed in each case when it became obvious that simple tensile test results were inadequate to characterise the particular behaviour. Tensile tests are multi-purpose in character, in the sense that the results are typically applied in a variety of contexts.

The quantities derived from a tensile test are best considered by reference to the deformation behaviour of a test piece when subjected to a continuously increasing tension load until it breaks. At yield stress in a mild steel, a sudden elongation occurs without any increase of load which is termed as yielding. Shortly after initial yield, narrow bands of plastically deformed material can be seen clearly in contrast with the generally undisturbed surface. These bands, known as *Luders bands,* extend from one edge of the test piece to the other, inclined at 45° to the axis of tension, along the two directions in which the shear stresses have their maximum value. When yielding is complete the load begins to rise again until it reaches a maximum value. After this, load falls off steadily while a more localized elongation takes place in one part of the test specimen, where it is said to neck. Load continues to fall while necking proceeds, until the reduction in cross-section is appreciable and fracture occurs at a certain failure load.

4.5.3.1 Tensile Test Practice

Prior to conducting tensile testing, all specimens were "pre-exfoliated" at gauge lengths by applying a thick layer of beeswax on the rest of the sample (except gauge length). These samples are then subjected to immersion tests according to conditions tabulated in **Table** 1. A standard specimen of sheet-type was selected with a gage length of 50±0.1 mm. **Figure 34** shows the dimensions of the tension specimen (not to scale).
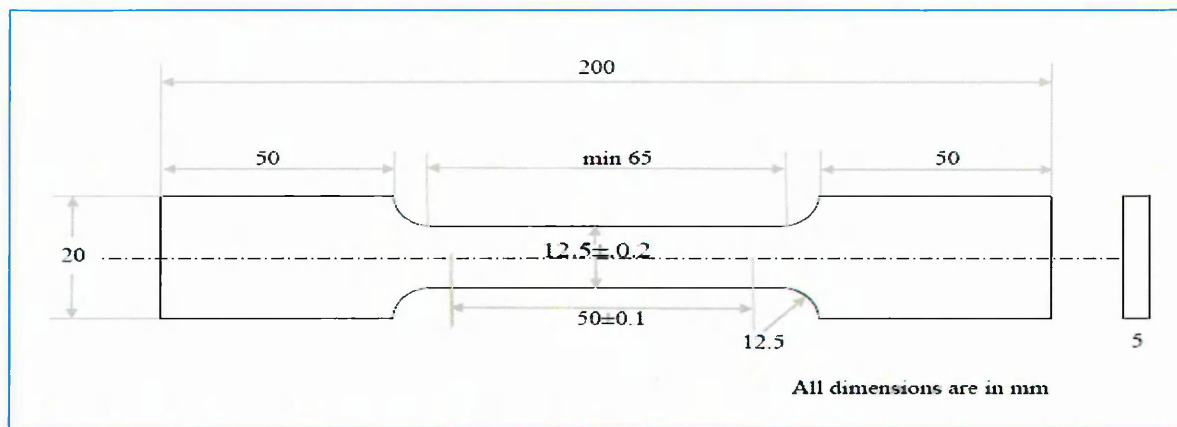
Figure 34: ASTM Standard E8-04, Standard test specimen for tension testing of metallic materials. Specimens were machined perpendicular to the rolling direction (Fig: Not to Scale).

The samples of both As Received (AR) and UIT were exfoliated ranging from 24 hours to a maximum of 96 hours in 24 hour steps and simultaneously, at temperatures ranging from Ambient to a maximum of 80^0C in steps of 20^0C.
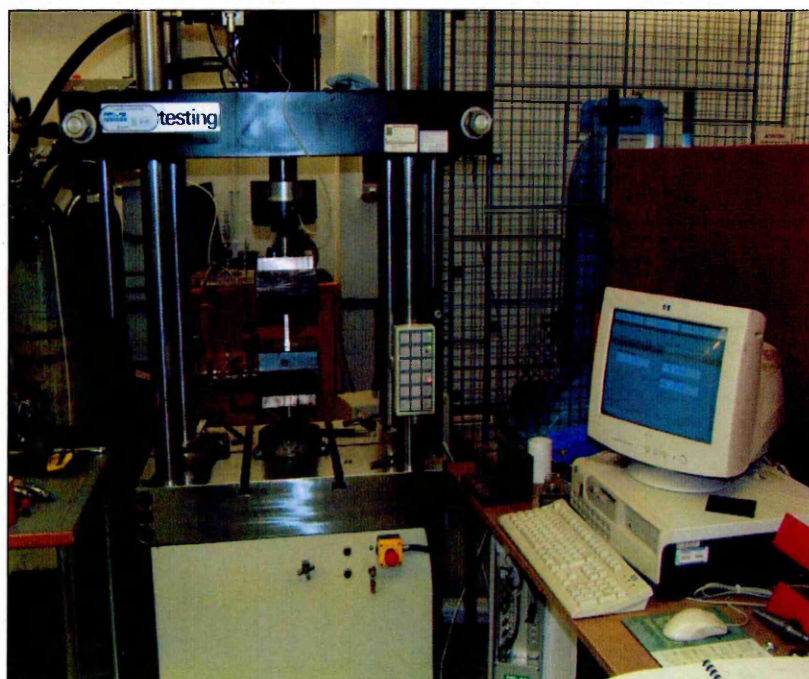

Figure 35: Test set up showing specimen in the ESH servo hydraulic test machine (250KN)

These tests were conducted similar to "coupon testing" and in accordance to ASTM G34 [140] which generated 16 samples for each condition, namely AR and UIT according to **Table 1.** The crosshead displacement reading was taken as strain measurement assuming there is no slip during testing of the sample. Thus, on a Stress Vs Crosshead displacement plot, 0.2% proof stress value was attained.

Table 1: All tests were conducted at various times and temperatures and named accordingly to the table.

Time (hrs)/Temperature (in ^{0}C)	24 hours	48hrs	72hrs	96hrs
20^{0}C	24_20	48_20	72_20	96_20
40^{0}C	24_40	48_40	72_40	96_40
60^{0}C	24_60	48_60	72_60	96_60
80^{0}C	24_80	48_80	72_80	96_80

Tensile testing was conducted to identify the mechanical properties of AR, UIT and UIT-C (UIT-Corroded) samples using a 250kN ESH servo hydraulic test machine as shown in **Figure 35**. These tests were conducted according to ASTM standards E8-04.

4.5.4 Fatigue Testing

Fatigue failures have been known and studied by the practical engineer for at least as long as there have been railways. The definition of fatigue testing can be thought of as simply applying cyclic loading to your test specimen to understand how it will perform under similar conditions in actual use. The load application can either be a repeated application of a fixed load or simulation of in-service loads. The load application may be repeated millions of times and up to several hundred times per second. In many applications, materials are subjected to vibrating or oscillating forces. The behaviour of materials under such load conditions differs from the behaviour under a static load. Because the material is subjected to repeated load cycles (fatigue) in actual use, designers are faced with predicting fatigue life, which is defined as the total number of cycles to failure under specified loading conditions. Fatigue testing gives much better data to predict the in-service life of materials.

4.5.4.1 Fatigue Test Practice

4.5.4.1.1 S-N Curves

Fatigue testing was conducted using a 250 kN ESH servo-hydraulic testing machine as shown in **Figure 36**. The specimens (**see Figure 37**) were subjected to fatigue loading

according to ASTM standards E 466-82 [141] to identify the residual fatigue life for various conditions.
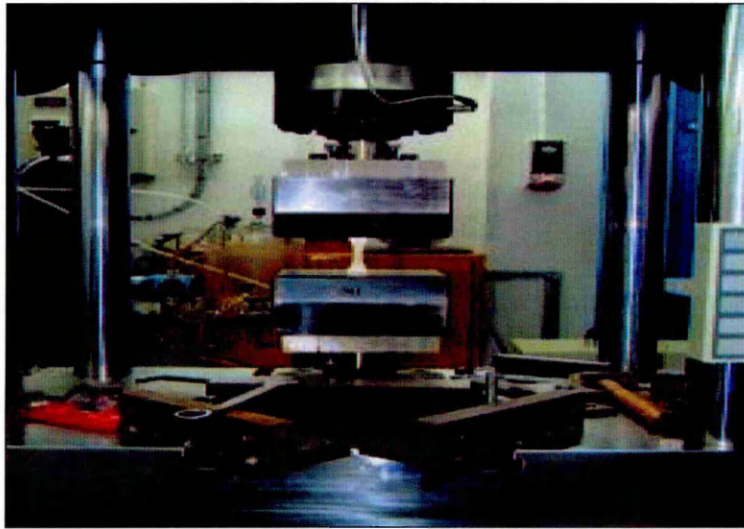

Figure 36: Test setup to produce total life curves.

The fatigue specimens were machined in such a way that the final surface roughness is around 0.2 μm. These samples were then UIT-1 conditioned within the calibrated section on all the four sides of the specimen. These specimens were then covered with beeswax outside the calibrated section and immersion tests were conducted according to **Table 1.**
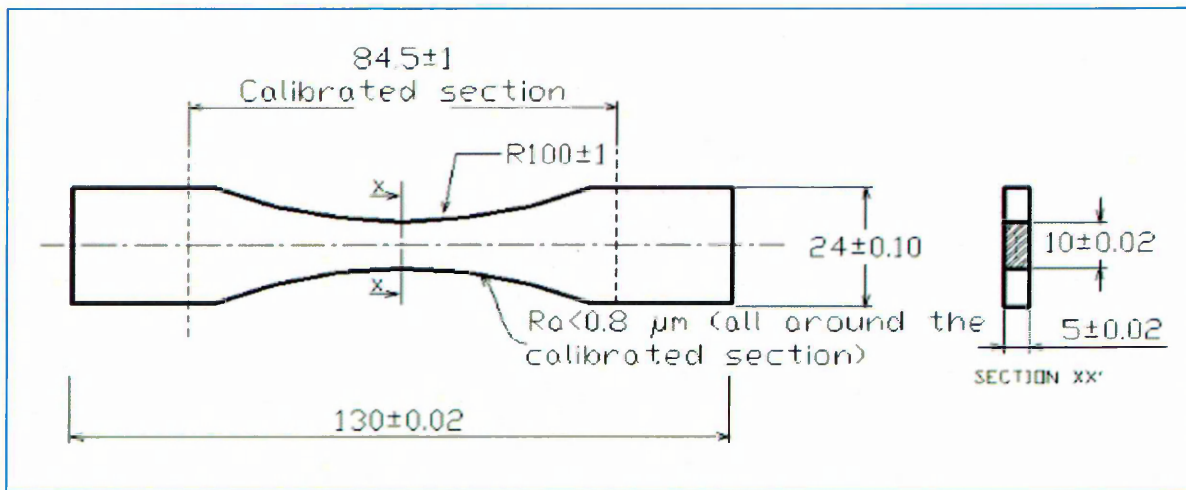

Figure 37: Test specimen design showing the specimen dimensions.

4.5.4.1.2 Fatigue Crack Growth (FCG) Analysis

FCG specimens were prepared according to ASTM standards E 647. These specimens were then pre-notched at the centre of the specimen using Electric Discharge Machining (EDM). Two strips of 10 mm thickness (**not shown in Figure 38**) were treated at various pre-determined conditions both of as-received and UIT conditions. These strips were 10mm

apart from the centre of the notch and marked on either side of the notch. Datum lines were marked on the surface of the specimen to facilitate measurement of crack length, 'a' which is the horizontal distance between the centre of the notch and crack tip. The tests were conducted at various treatment conditions e.g. 24hours exfoliation at 20^0C.
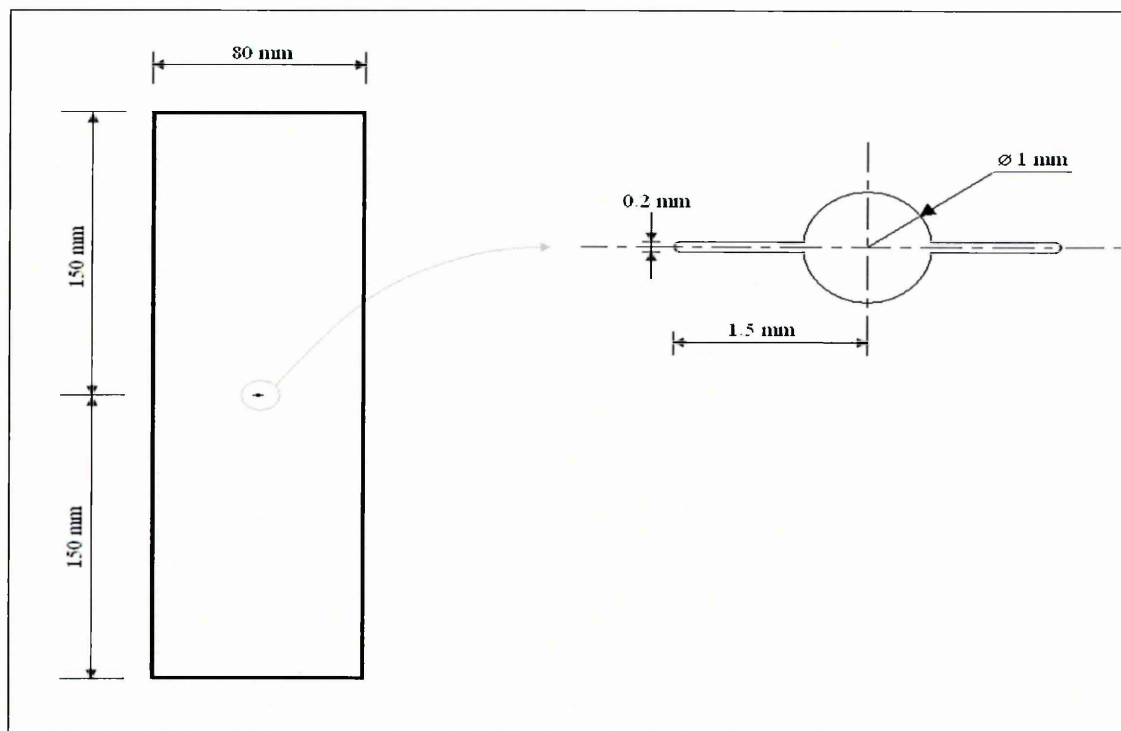

Figure 38: Samples were prepared according to ASTM standards E 647 and pre-notched in the centre of the specimen using Electric Discharge Machining (EDM).

4.5.4.1.2.1 Test Setup

A test setup similar to that used to determine S-N curves was used to determine crack growth rates. Datum lines are drawn across the section of the specimen which is under study as shown in **Figure 39**. AA2024-T351 contain copper as well as aluminium. Some contain magnesium and others as secondary elements (**see Table 2**).

Table 2: Chemical composition of 2024-T351 in wt% based on EDX measurements.

Alloy		Si	Fe	Cu	Mn	Mg	Cr	Zn	Ti	Zr	Al
2024-	min	-	-	3.8	0.30	1.2	-	-	-	-	balance
T351	max	0.50	0.50	4.9	0.90	1.8	0.10	0.25	0.15	-	

According to the temper designation system:

T3. Solution heat-treated, cold worked, and naturally aged to a substantially stable condition. Applies to products that are cold worked

T_51. Applies to cold finished rod or bar when stress-relieved by stretching 1 to 3 % permanent set. Stretching is performed after solution heat treatment or after cooling from an elevated temperature shaping process. No straightening takes place after stretching
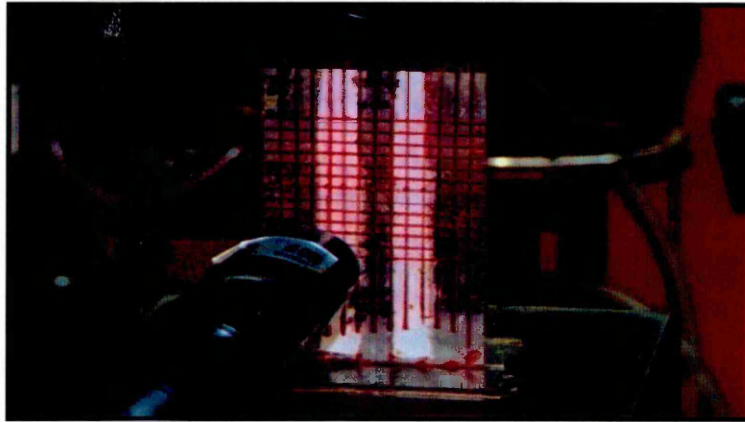

Figure 39: Fatigue crack growth analysis test setup.

Cyclic loading was applied at a stress ratio R = 0.1 at a test frequency of 25Hz. The crack length measurements were taken every 5000 cycles after stopping the cyclic loading either at 60% of the applied tensile load so that the crack tip visibility is resolved. This was necessary due to extremely corroded sections and crack lengths measurements were often difficult to resolve.
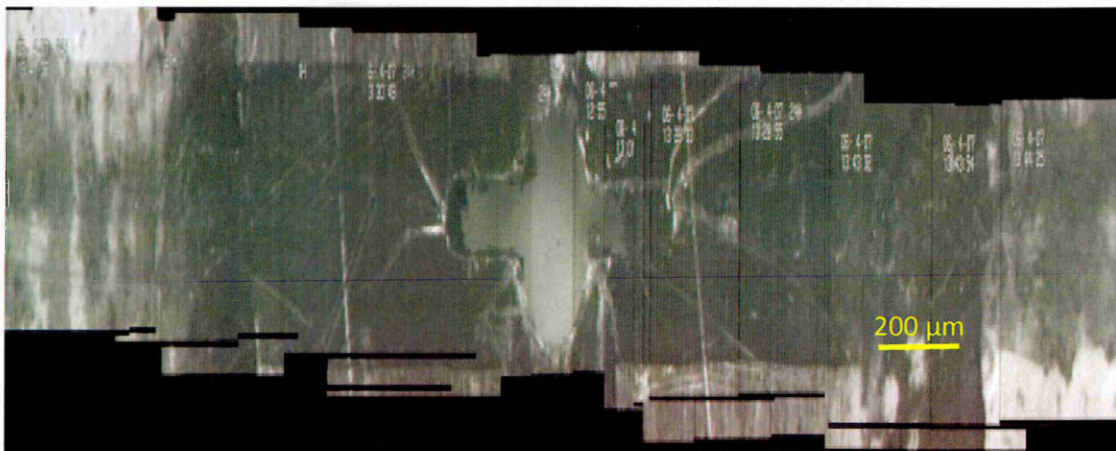

Figure 40: Crack Length at 45000 cycles at 25Hz for UIT1-C exfoliated ambient conditions for 24 hours, R = 0.1

Crack Growth tests were conducted in compliance with ASTM Standard E647 on notched specimens that are pre-exfoliated at various conditions and the crack was followed using a Photo Microscopy (PM) method according to this standard using a high magnification camera. The resulting images were carefully matched using an in-house program as shown in **Figure 40** and crack length 'a' was measured.

The secant method was used to create the da/dN vs ΔK curve, this method fits a line between adjacent data points. The slope of the line is the crack growth rate da/dN. The equations used are,

$$da/dN = (a_{i+1} - a_i)/(N_{i+1} - N_i)$$
Equation 29

$$da/dN = (a_{i+1} - (a_i + a_j))/(N_{i+1} - N_i)$$
Equation 30

$$â = (a_{i+1} + a_i)/2$$
Equation 31

where the **Equation 30** is used when a crack coalescence takes place, and where a_j is the crack length of the small crack considered that joins to the bigger one and a_i is the crack length of the bigger crack.

The stress intensity factor range ΔK is given by the following equation:

$$\Delta K = \left(\frac{\Delta P}{B}\right)\sqrt{\frac{\pi\alpha}{2W}\sec\frac{\pi\alpha}{2}}$$
Equation 32

where $\alpha = 2a/W$, $\Delta P = P_{max} - P_{min}$ for R>0; expression valid for 2a/W<0.95.

CHAPTER 5

Corrosion Analysis

5.1 Introduction

From the perspective of the failure mechanism of aircraft structures, along with fatigue assisted failure of the component, corrosion induced failure is also of serious concern. Corrosion leads to fatigue crack nucleation and facilitates cracks to grow at higher rates and thus is widely considered to be one of the most significant degradation mechanisms in ageing aircrafts. Widespread corrosion pits on the surface and hidden within the fuselage lap and riveted joints are an important cause of Multiple Site Damage (MSD), since the fatigue cracks are observed to nucleate and propagate from these corrosion pits.

Thus, corrosion tests, and application of the results, are considered to be a most important aspect of corrosion engineering. Many corrosion tests are made to select materials for construction for equipment in the process industries. This research gives attention to exfoliation corrosion which occurs on wing and fuselage panels of aircrafts. Modern day aircrafts tend to accumulate more number of flying hours due to their increased usage. Also, the use of number of short haul flights has increased dramatically due to an incredible surge in aviation sector. It is the lowest portion of the earth's atmosphere which contains approximately 75% of the atmosphere's mass and almost all of the water vapour. Laboratory tests were conducted to simulate similar conditions experienced in ascent and descent periods of aircrafts.

5.2 Coupon Testing

Exfoliation corrosion is a more severe form of intergranular corrosion that can occur along aluminium grain boundaries in the fuselage, empennage and wing skins of the aircraft. Exfoliation corrosion can be defined as corrosion that proceeds laterally from the sites of initiation along planes parallel to the surface, generally at the grain boundaries, forming

corrosion products that force metal away from the body of the material giving rise to a laminated appearance (**see Figure 41**).
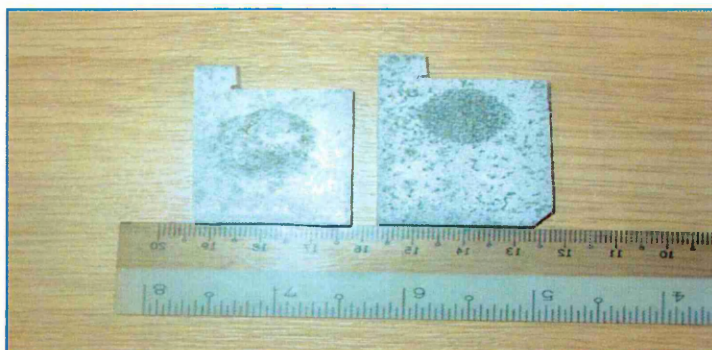

Figure 41: Samples of AR & UI subjected to exfoliation corrosion for 24 hours and at 80^0C.

As discussed in **Chapter 1 (See Section 1.1.1)**, the extent of corrosion damage should be no more than 10% of the nominal thickness of the material. In aircraft wing and fuselage panels, depending on the section of the aircraft the average nominal thickness is 5mm. If the corrosion damage is beyond the 10% limit, the panel should be replaced. Thus, throughout this research, the nominal cross-sectional thickness of the sample is 5mm. Although removal of corroded sites can be removed by grinding, it reduces the cross-sectional area and thus, the strength of the structural member of the aircraft.

In order to simulate these conditions on a laboratory scale, these tests were conducted according to ASTM standards G 34 [142]. G112-92(2003) Standard Guide for Conducting Exfoliation Corrosion Tests in Aluminium Alloys was followed. The exfoliation solution comprises of preparation of one litre molar solution out of 4 M NaCl, 0.5 M KnO_3 and 0.1 M HNO_3. A detailed analysis is indispensable to understand the climatic conditions (**See Section 5.1**) where the varying temperature and water vapour packed atmosphere dominates the throughout flight path of the aircraft. This research focussed on the predefined time and temperatures as tabulated in **Table 1**. Throughout this research **Table 1** is closely followed for both As-Received (AR) and UIT Condition samples. The next section focuses on SEM analysis and Taylor Hobson's Roughness Measurements where a detailed study comparing AR and UIT conditions is performed by considering *depth of exfoliation* as a factor to compare the 32 emerged conditions from **Table 1** both for AR and UIT conditions.

5.2.1 Microstructural Characterisation

5.2.1.1 SEM Analysis

The visual appearance of the cross-sectional surfaces was examined by SEM. A key part of this research concentrated on such cross-sections, UIT being a surface modification technique. **Figure 44** compares the cross-sectional morphology of AR and UIT1 for 24 hours of exfoliation at ambient conditions (20°C). In **Figure 44**, Fig (a) reveals an exfoliated cross-section with depth of exfoliation being present with a maximum of 170 μm. In contrast to this, UIT sample fared exceptionally well subjected to exfoliation testing in similar conditions as there modified surface remained resistant to corrosion damage, as seen in **Figure 42b.**.
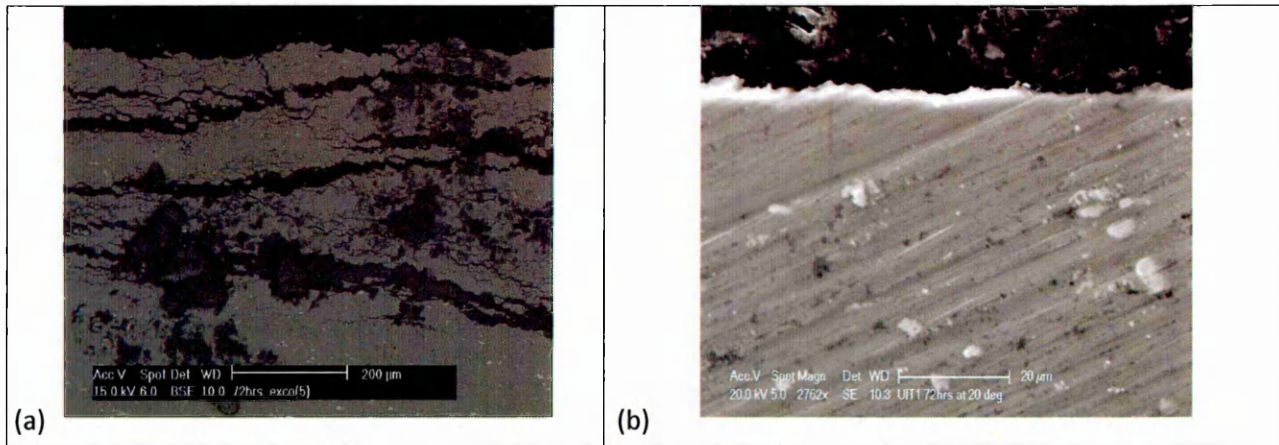
Figure 42: (a) SEM analysis of cross-section of AR sample showing (72_20) with an exfoliation depth of 550 μm. (b) A SEM micrograph showing UIT 1 sample (72_20) with negligible exfoliation corrosion depth.

UIT-1 conditioning was also able to inhibit corrosion even after sample subjected to 72 hours of immersion testing in exfoliation solution as shown in **Figure 42**.
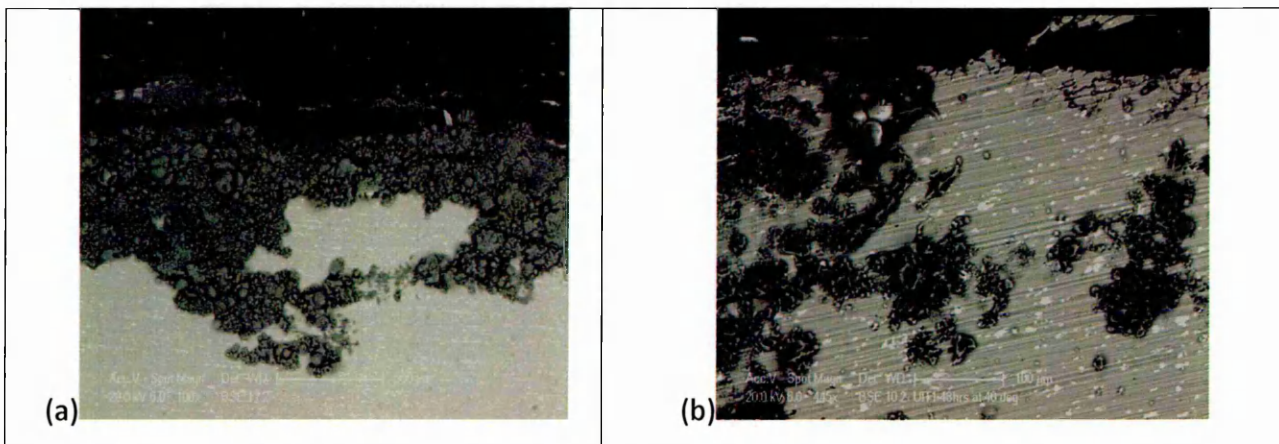
Figure 43: (a) SEM analysis of cross-sectional AR sample showing (48_40) with an exfoliation depth of 700 μm. (b) A SEM micrograph showing UIT 1 sample (48_40) with exfoliation corrosion depth of 500 μm.

However, at higher temperatures UIT exhibited to mitigate the exfoliation corrosion process. For example, at 48 hours of exfoliation at 40 ^{0}C immersion corrosion tests, the depth of exfoliation for UIT-1 sample was 200 μm less than As-Received sample as shown in **Figure 43**.
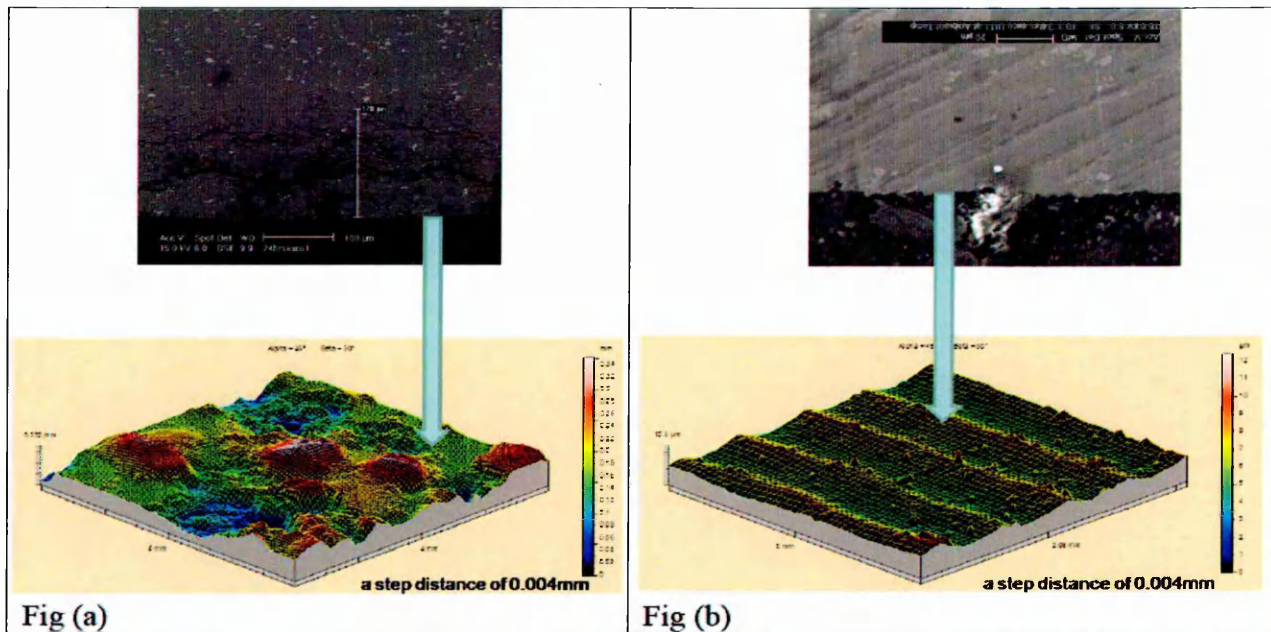

Fig (a)

Fig (b)

Figure 44: SEM micrographs of (a) As-Received Al 2024 T351 treated for 24 hours in exfoliation solution at 20^{0}C. (b) UIT condition samples treated for 24 hours in exfoliation solution at 20^{0}C.

UIT is seen to be acting as an answer for corrosion resistance even at elevated temperatures between 20°C to 40°C in most of the case identified in this research. For example, in **Figure 45**, it is identified that the extent of exfoliation corrosion damage in UIT sample 48_40 is 500 $μm$ when compared to its analogous sample in AR condition is more than 700 $μm$. Similar results were noticed when samples were subjected to higher period of exfoliation time and the results of the SEM analysis are tabulated in **Appendix A**.
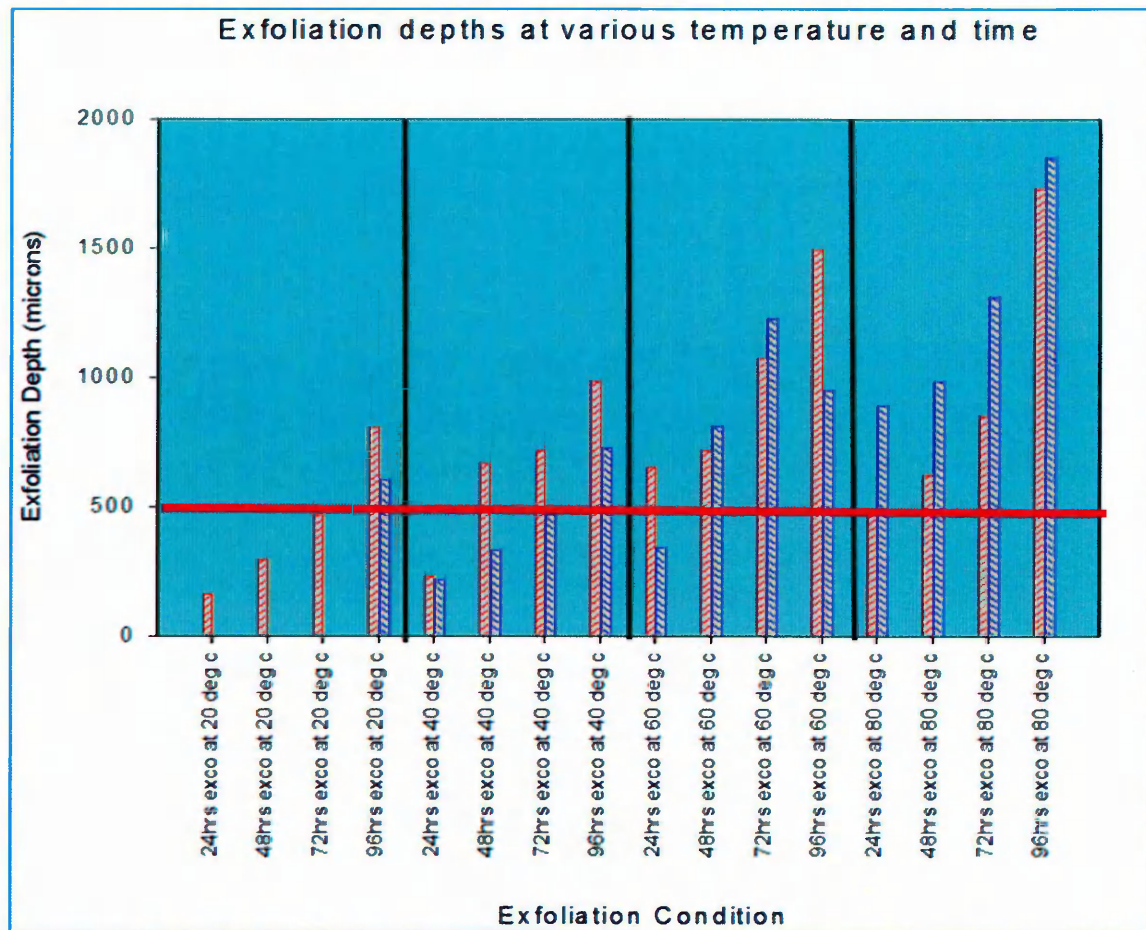
Figure 45: The above figure compares the exfoliation corrosion tests for AR (orange strip blocks) and UIT condition (blue stripe blocks) with respect to temperature and time period of exfoliation. The red line shows the tolerance limit specified where when the panels need to be replaced.

As mentioned in **Section 5.2**, the exfoliation corrosion damage from the cross-sectional surface in to the bulk of the alloy, was analysed using SEM and the depths of exfoliation are tabulated in **Figure 45.** A first glance at **Figure 45,** one can comprehend that unlike any intergranular attack (See **Figure 47**) on Al alloys, exfoliation corrosion is more severe form of intergranular corrosion where the ingress of the corrosion attack is not only severe laterally in the direction of grain boundary as shown in **Figure 46**, but also according to depth as the **Figure 45.** The specimens were at least 50 by 50 mm to remove any edge effects.
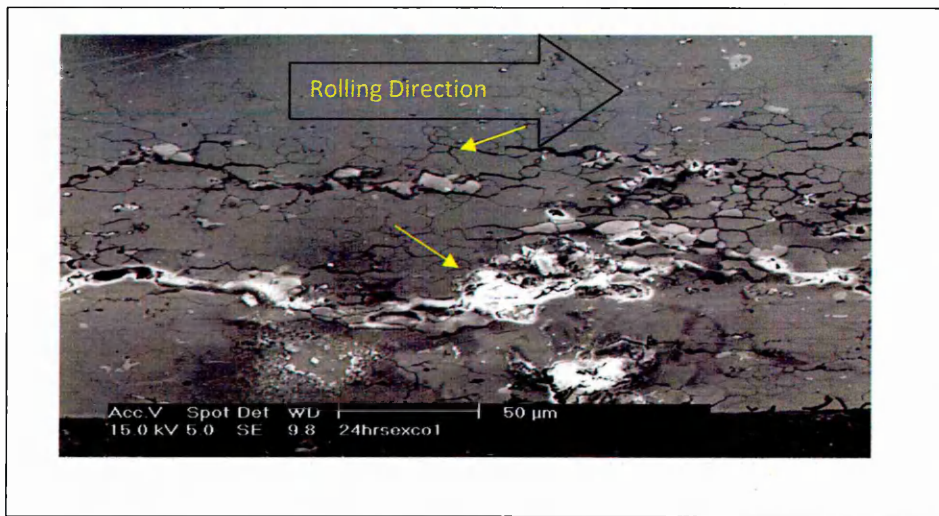
Figure 46: Micrograph f 24hrs exfoliation which shows about 170μm of the cross-section being affected by this form of corrosion.
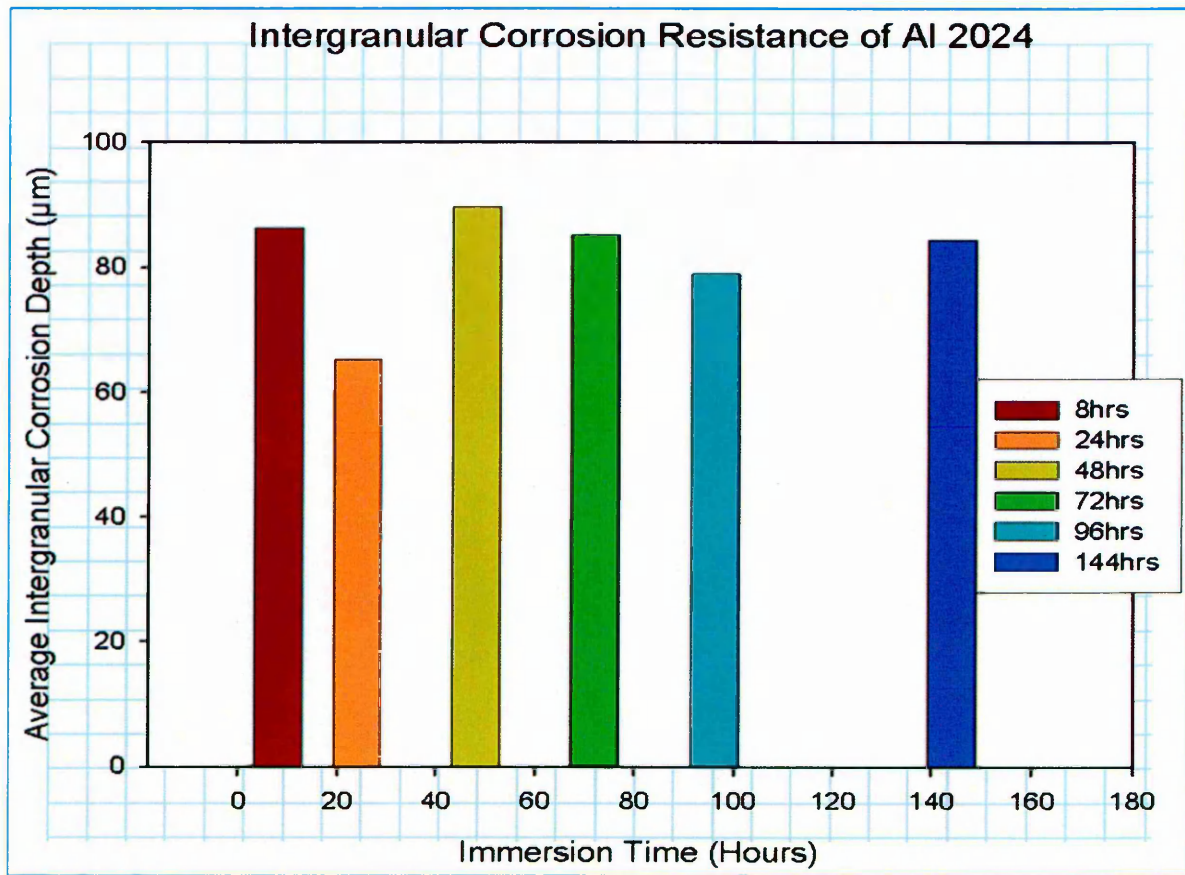
Figure 47: The above graph shows immersion tests performed on AL 2024 T351 coupons according to ASTM standards G110-92. All the tests were conducted at ambient conditions (20^0C).

Figure 45 and **Figure 47** show results from same tests carried out for exfoliation corrosion and intergranular corrosion according to ASTM G110-92 [143] respectively. It can easily be identified that the exfoliation corrosion is time dependent as there is a fivefold increase in exfoliation corrosion depth as we move from samples 24_20 to 96_20. Use of this test method provides a useful prediction of the exfoliation corrosion behaviour in various marine

80

and industrial environments. However, in **Figure 47** at 24_20 there is the depth of intergranular attack is 85 μm and deviates by only a few microns from this value as the immersion time approaches 144 hours. These tests evaluate the adequacy of quenching when performed on material in the as-quenched condition as intergranular corrosion resistance is directly related to quenching conditions applied. Assuming that the depth of penetration is equally important in both mechanisms of corrosion attack, this behaviour can be explained as exfoliation corrosion forms more corrosion products of oxides and hydroxides along with attacking grain boundaries. The formation of oxides and hydroxides is more prevalent in exfoliation testing due to the fact that NaCl in exfoliation solution 4 times higher than test solution prepared for intergranular attack.

5.2.1.2 Copper Distribution Analysis

Alloying elements determine the common basic properties of alloys like mechanical properties, corrosion resistance etc. However, when AA 2024 T351 is subjected to severe environmental conditions, copper being a secondary phase particle, enriches near the surface and sub surface and appears to be responsible in creating galvanic couples between copper rich intermetallic particles (Al_2Cu) and the adjacent copper-depleted matrix which induces localised corrosion [144]. In **Figure 48** & **Figure 49**, copper concentrations which are revealed by backscattered images of AR 24_20 and AR 24_40 are compared against cross-sectional depth of the samples. The results show that there is a higher concentration of copper near the surface of the alloy.
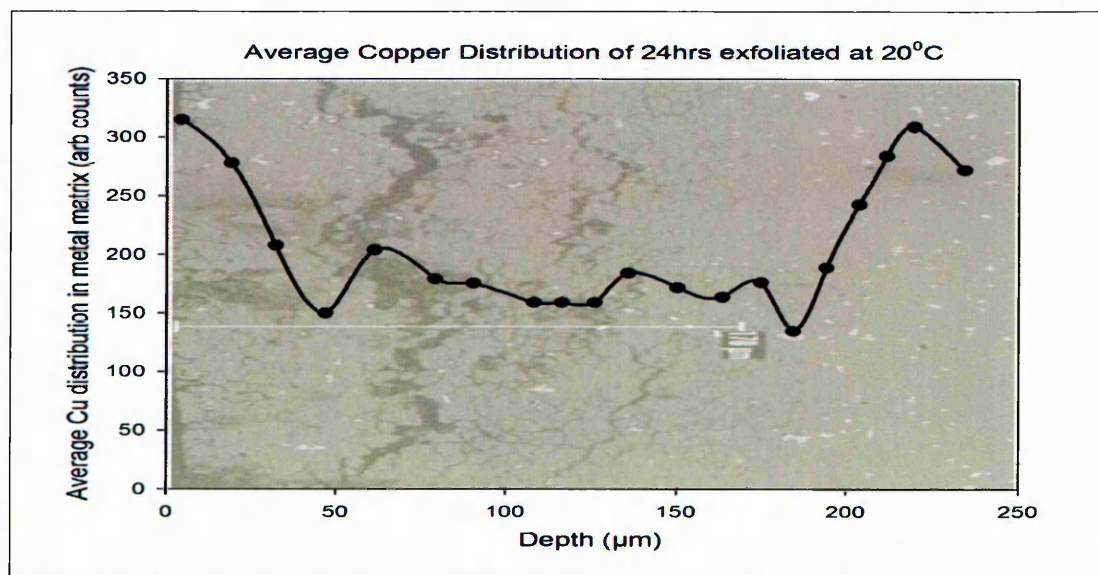

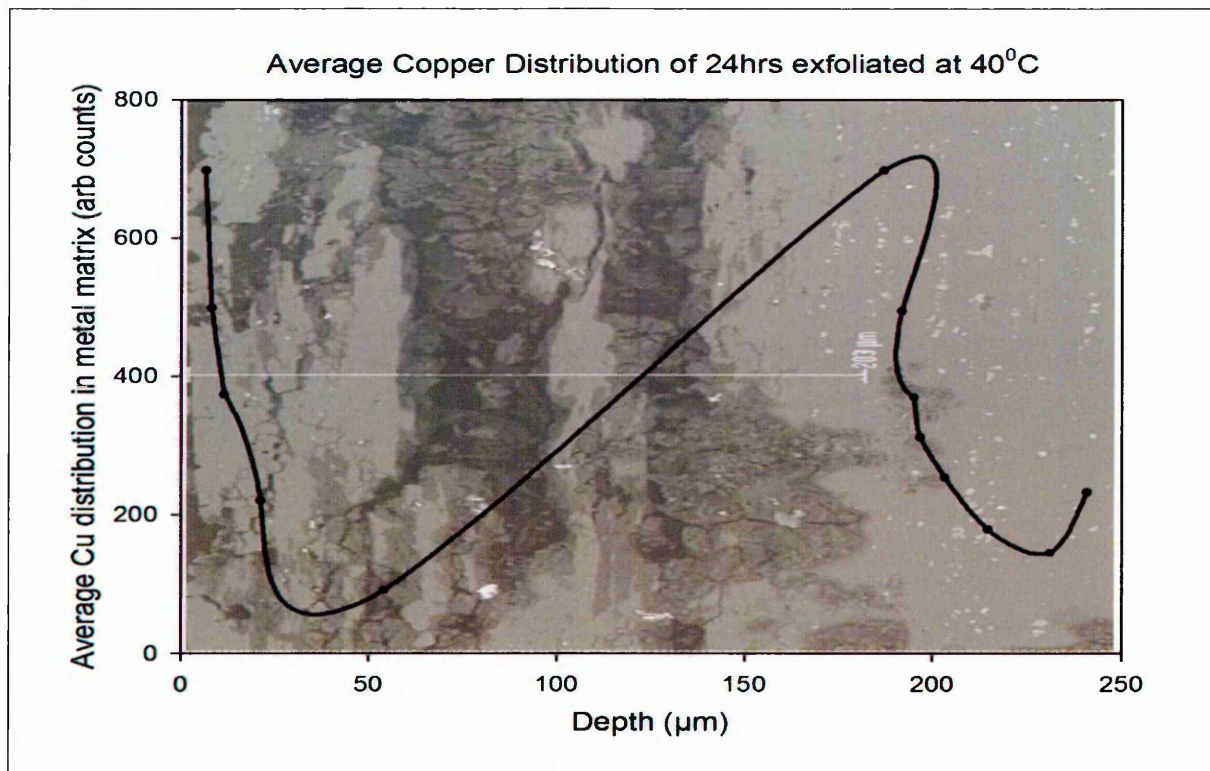**Figure 48:** Average copper distribution of 24 hrs exfoliated at 20°C.

Figure 49: Average copper distribution of 24 hrs exfoliated at 40^0C.

Similar results are seen when samples are subjected to 48hrs of exfoliation at different temperatures. Thus, it is concluded that copper enrichment near the surfaces further reduces the corrosion resistance.
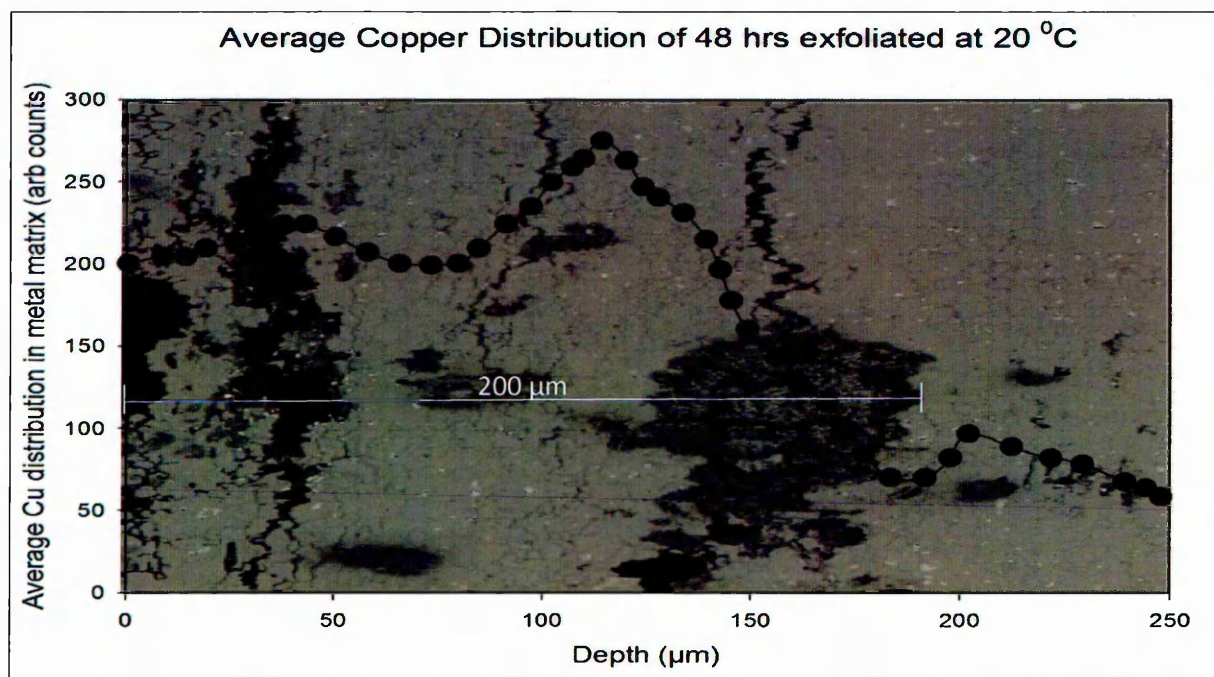

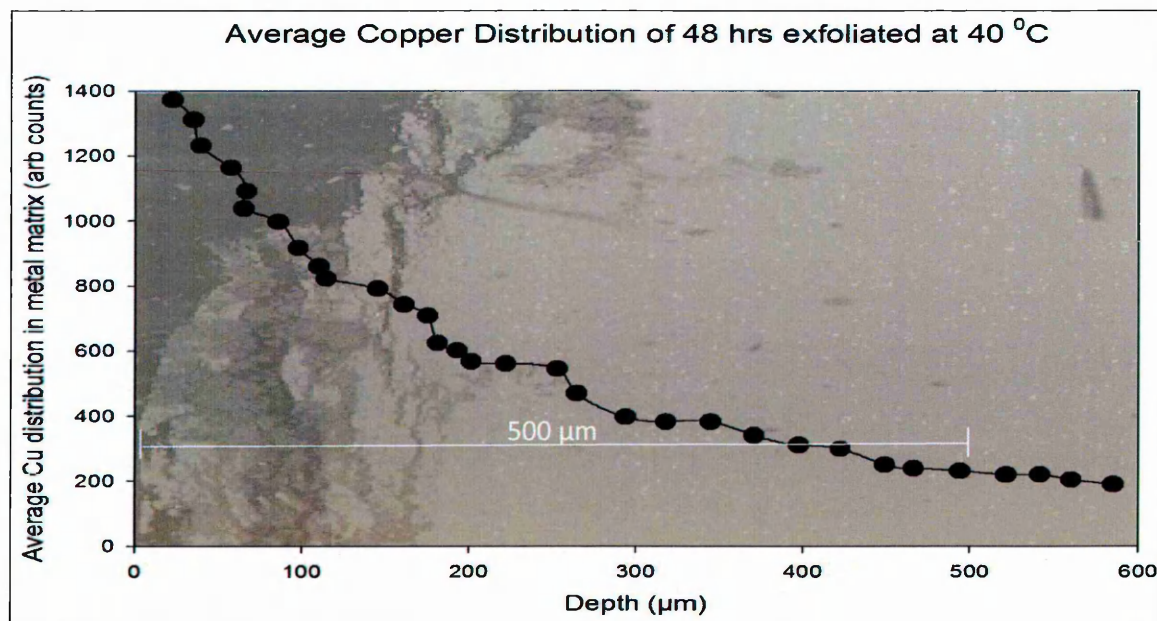**Figure 50:** Copper redistribution for AR samples 48 hours of exfoliation at 20 ^{0}C.

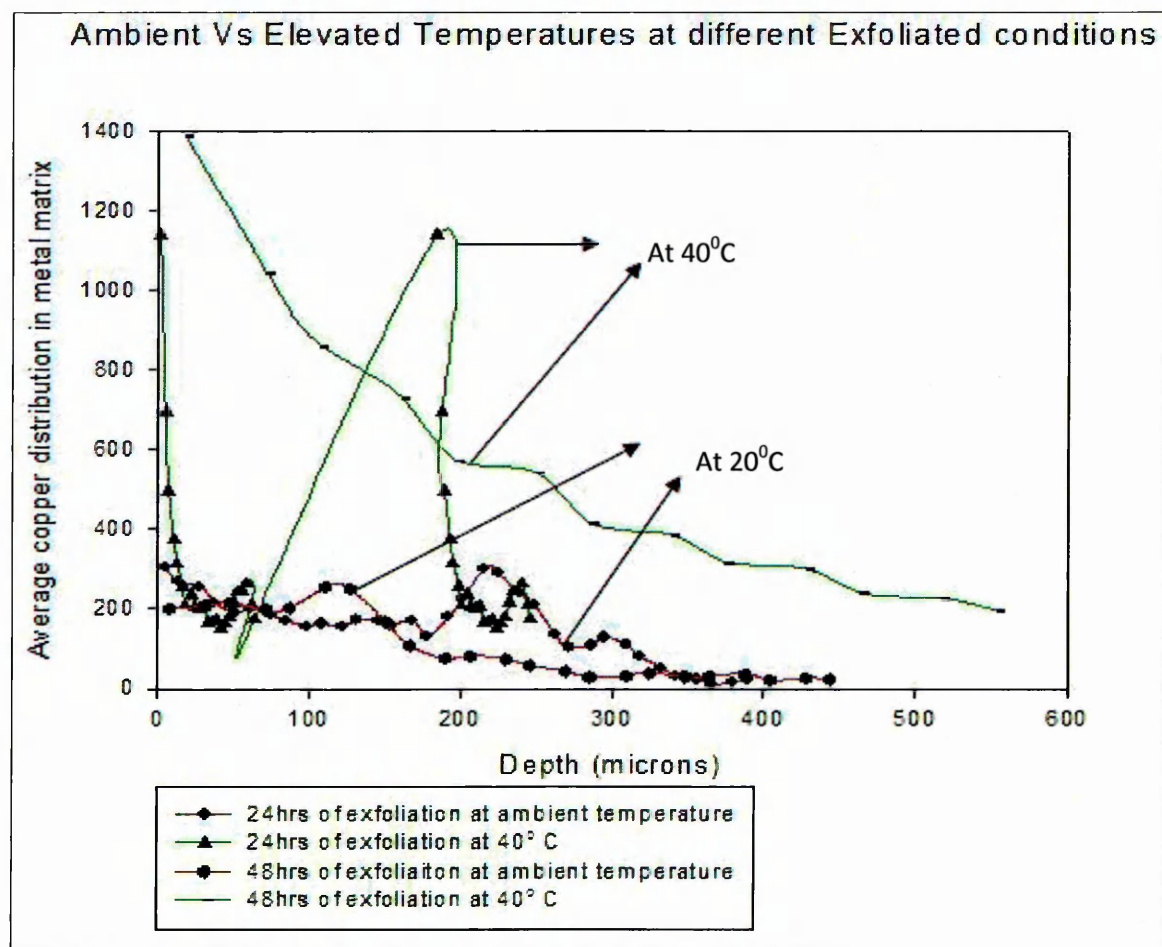**Figure 51:** Copper redistribution for AR samples exfoliated for 48 hours and at 40 °C.

Figure 52: Comparison of copper concentration for AR samples subjected to exfoliation corrosion tests at 20°C and at 40°C.

It is noticed that exfoliation temperature has foremost effect in enriching copper near the surfaces of the alloy. In **Figure 52**, for 20^0C exfoliation tests, it can be said that there is a little effect of exfoliation time as it increases from 24 hours to 48 hours. However, as the temperature is increased to 40^oC, Cu enrichment near the surface is more established.

5.3 Polarisation Curves

Polarisation curves continue to be important in Environmental Assisted Corrosion (EAC) research as they provide rapid, accurate and quantitative evaluation of a materials resistance to corrosion. Potentiodynamic plots have been obtained for different surface conditions. Polarisation curves are plotted using Scanning droplet Cell (SDC) which is discussed in **Section 4.4.2**. 3.5% NaCl solution (0.6 M) was used to characterise corrosion resistance because exfoliation solution tends to clogs the pipes with dried NaCl crystals. All obtained data was fitted using in-house regression software.

5.3.1 Droplet Cell

An electrolyte droplet is dispensed and positioned on the surface of the capillary. Thus the wetted circular area forms the working electrode. Since UIT nanocrystallises the surface of AA 2024-T351, it became quite beneficial to understand the corrosion kinetics on a micro-scale. Moreover, exfoliation corrosion damage often initiates at end grains, Cu enriched areas on the surface as discussed in **Section 5.2.1.2** of the surface and the initiation of the process is much localised. These tests were conducted in open air with a droplet size measured manually by measuring the size of the spot where test was performed. However, due to the nature of the exfoliation solution (which forms salt crystals due to evaporation of water in the process and clogging the tubing); a 3.5% NaCl was used instead.

5.3.1.1 UIT1

The polarisation of AR and UIT1 conditioned AA 2024-T351 in open air with 3.5% NaCl is compared in **Figure 53**. **Figure 54** presents a more detailed plot of the anodic branches of the Tafel slopes. An estimate of corrosion current, made by extrapolating the Tafel slope to E_{corr}, gave values of 30 μA/cm^2 for the AR and 100 μA/cm^2 for the UIT 1 Condition. These results signify a threefold increase in corrosion rate of UIT 1 when compared with AR.

UIT 1 increases the rate of oxidation and reduction reactions. However, the pitting potentials of the AR and UIT 1 remained similar and the break of protective aluminium oxide film occurs at similar potentials. As the potential E is increased the rate of corrosion is increased. AR sample shows a corrosion rate of 7 μA/cm^2 at 100mV above the open circuit potential,

whereas UIT1 is 11 µA/cm² at this value above open circuit potential. Thus, this signifies that UIT1 increases the corrosion rate activity of the surface.
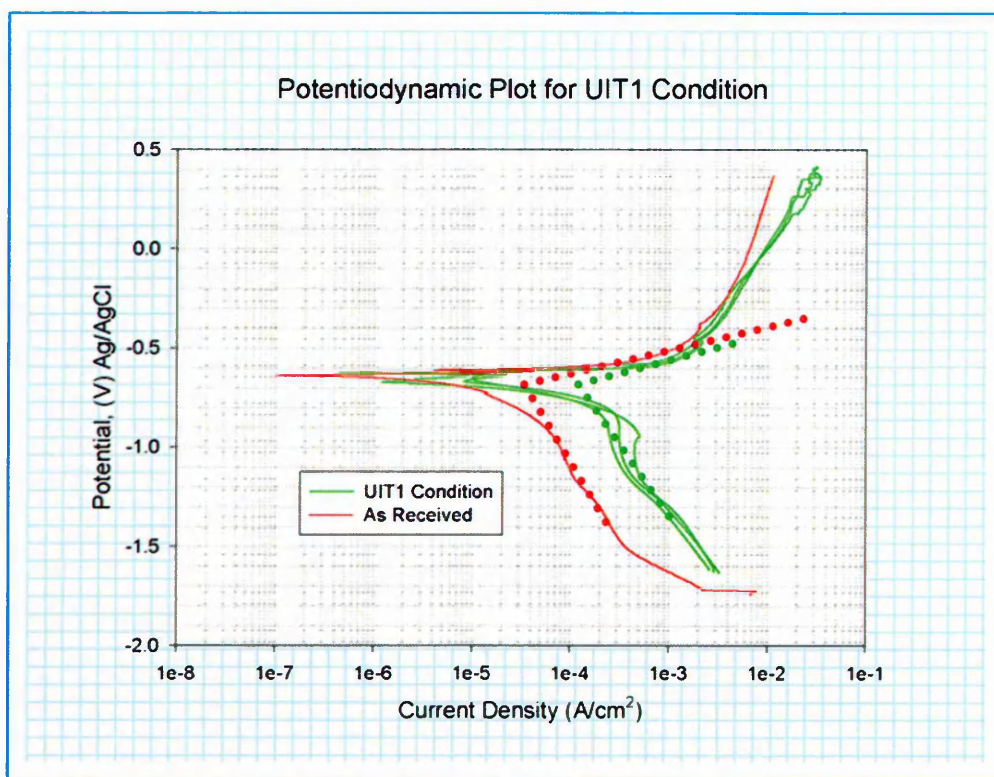

Figure 53: Potentiodynamic polarisation curves of Al 2024-T351 for AR and UIT 1 condition showing a high cathodic activity in 3.5% NaCl solution.
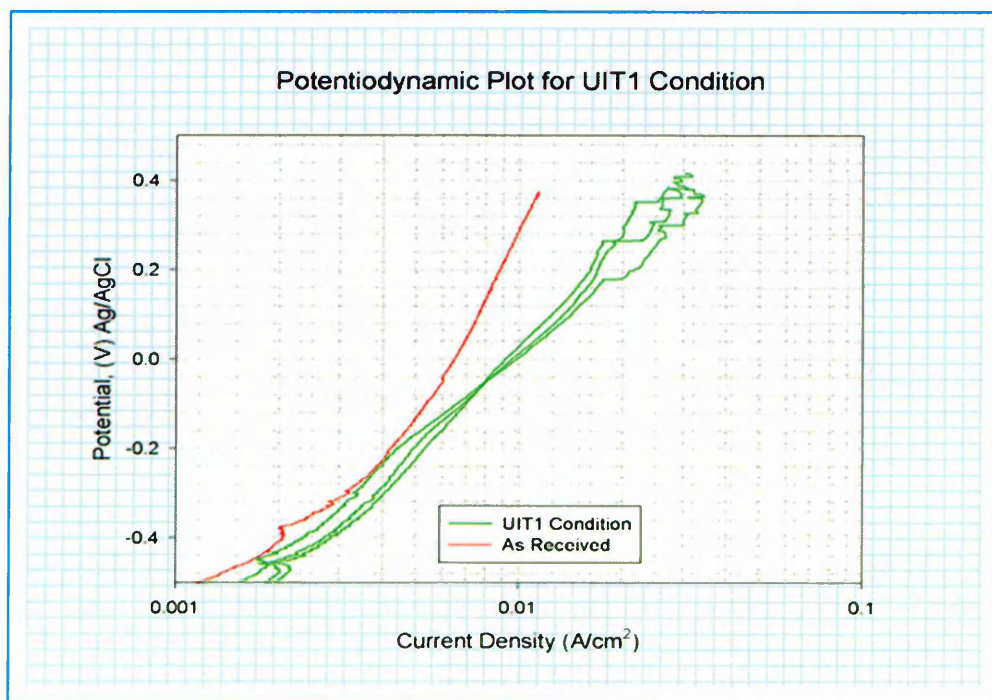

Figure 54: Anodic curve zoom of **Figure 53** shows that the pitting potential of AR and UIT 1 are similar. However, the rate of corrosion increases by 4 µA/cm² at 100mV above open circuit potential.

5.3.1.2 UIT2

An estimate of the corrosion current, made by extrapolating the Tafel slopes to E_{corr}, it was found to be 80 $\mu A/cm^2$ when compared to AR which is 30 $\mu A/cm^2$. However, the three plots of cathodic branch of the curve seem be varying in a bandwidth as seen in **Figure 55** indicating different that free electrons consumption rates are different and thus the pitting potentials are varying in anodic branch. In anodic branch of UIT2 condition (**see Figure 56**), it is noticed that the propensity of the corrosion rate is similar with respect to AR until it reaches pitting potential, E_{pit}.
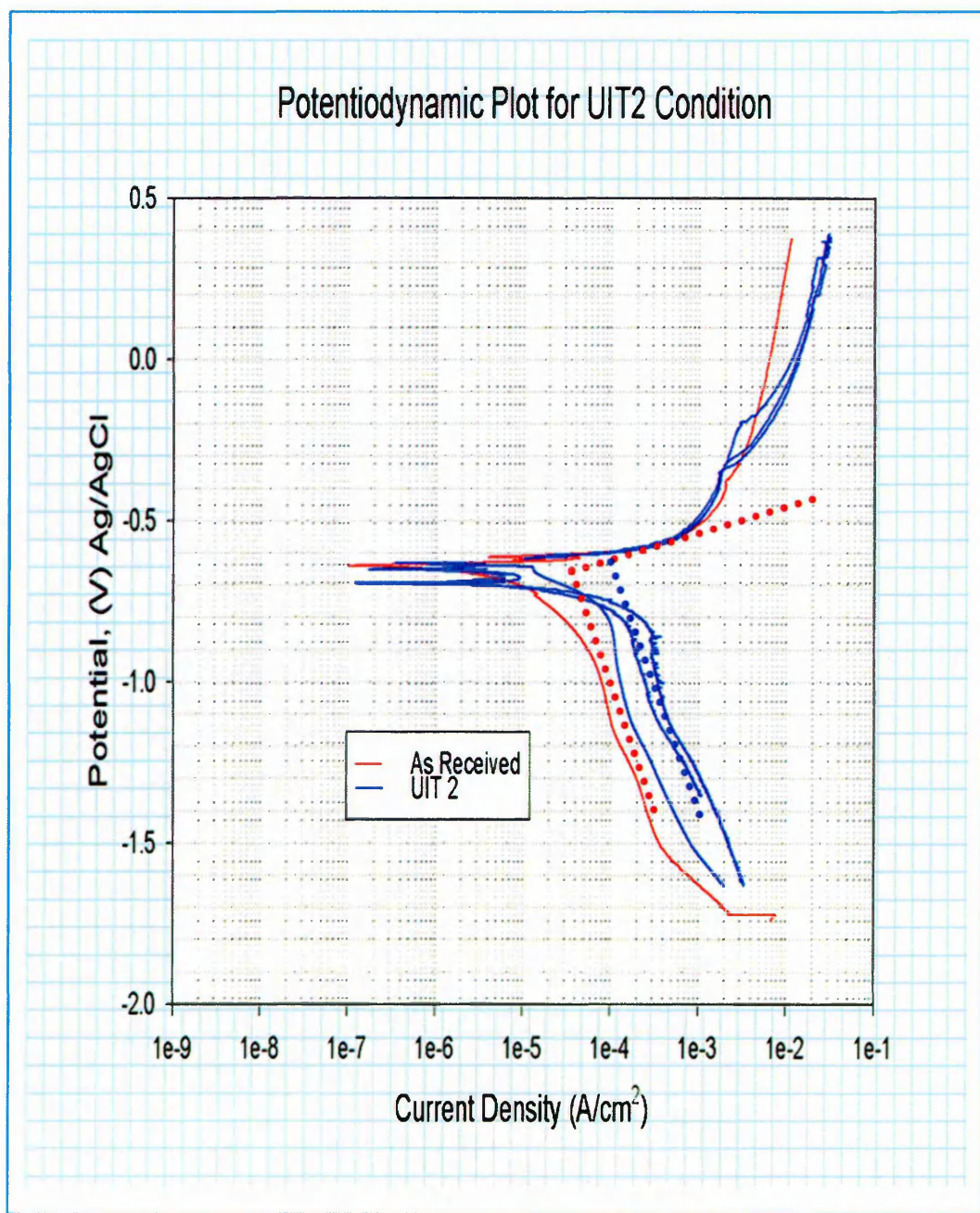
Figure 55: comparison of potentiodynamic plots for UIT 2 and AR conditions.
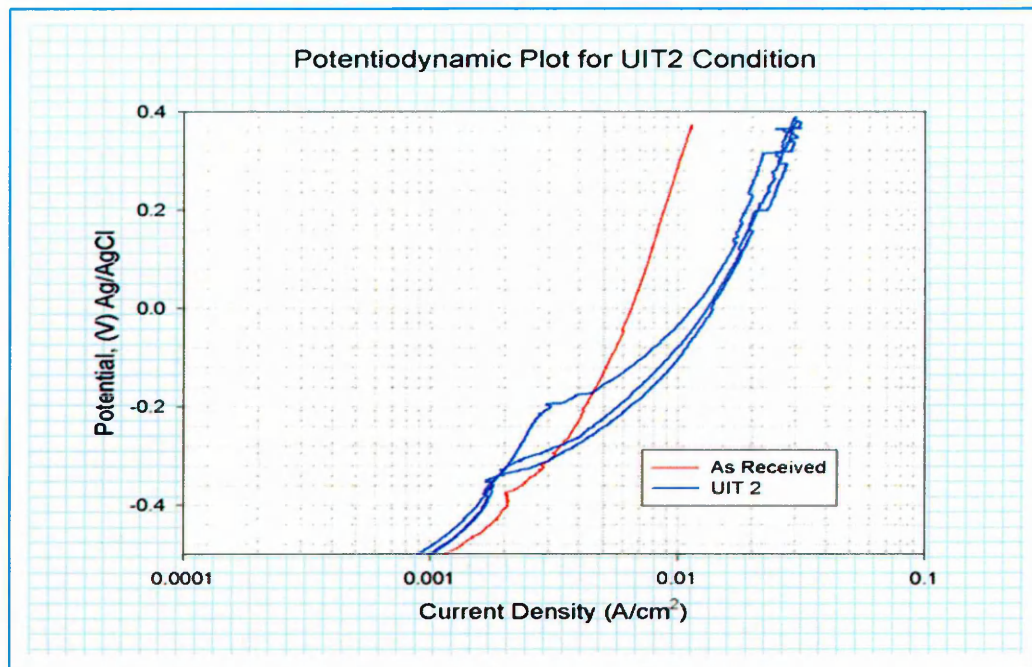
Figure 56: Detailed anodic branch of UIT 2 potentiodynamic curve.

5.3.1.3 UIT3

UIT 3 behaves the same manner as UIT 2 samples. However, it is interesting to note that corrosion current is 60 $\mu A/cm^2$ in comparison to AR samples showing a value of 30 $\mu A/cm^2$.
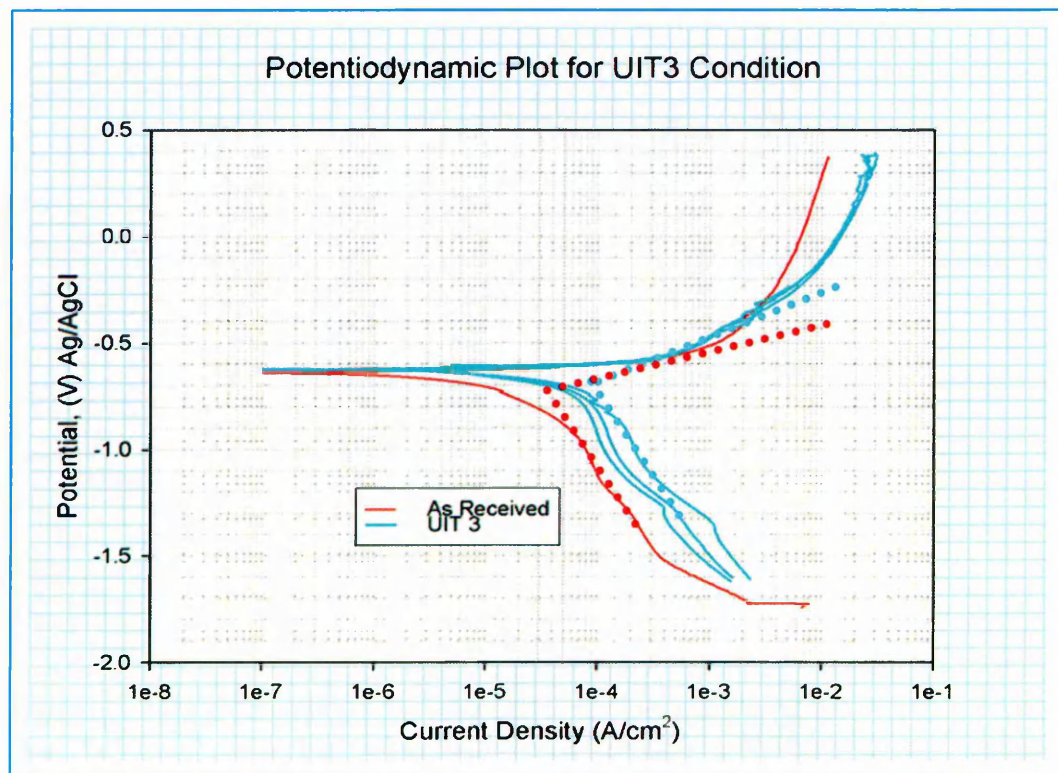

Figure 57: Potentiodynamic curves showing results similar to UIT 2 with lower corrosion rate before the sample reaches its pitting potential.
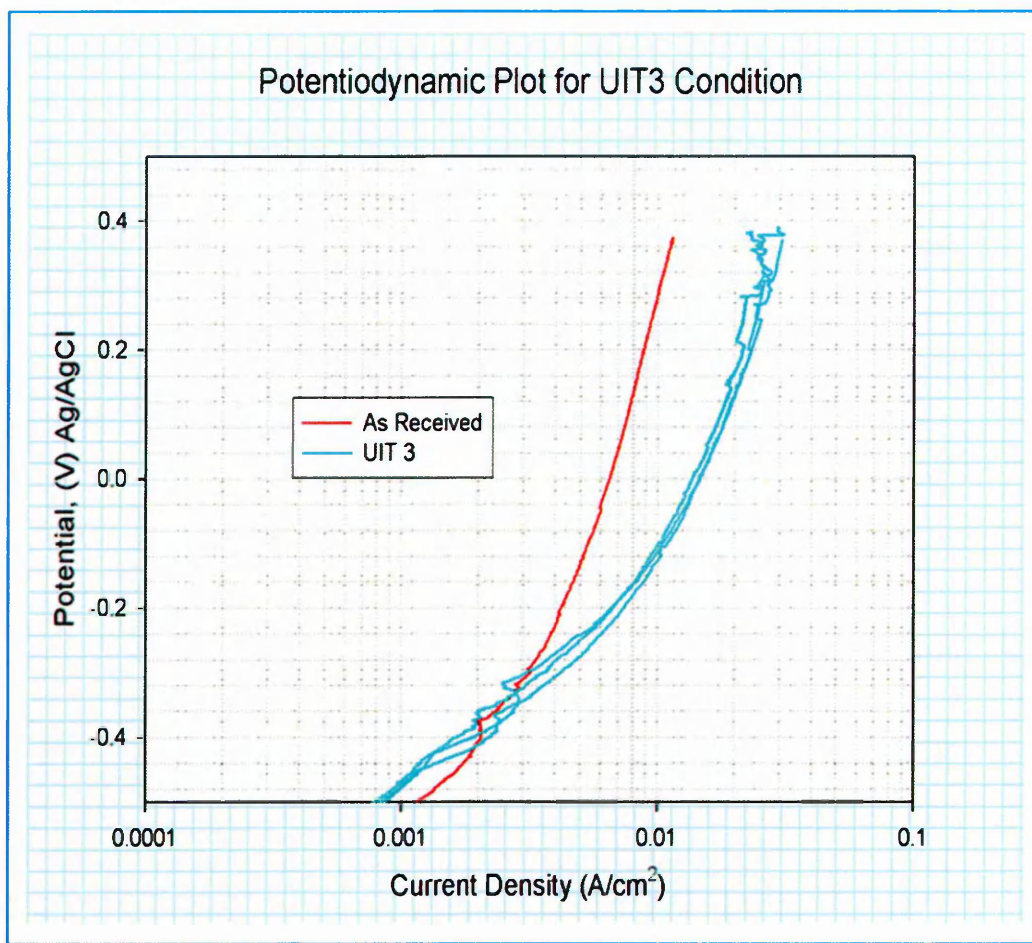
Figure 58: A zoomed anodic section of UIT 3 potentiodynamic curve.

UIT 3 demonstrated a two fold increase in comparison to UIT 1 sample which established a threefold increase in corrosion rate.

5.4 Assessment Potentiodynamic curves with SEM Analysis

Potentiodynamic curves showed results where the corrosion resistance of the UIT conditions are higher than compared to AR samples. However, these results are contradicted by SEM analysis. SEM analysis showed (**See Figure 60**) us that UIT is *"exfoliation corrosion resistant"* where the solution is highly aggressive. However, potentiodynamic curves shown in **Figure 59,** which are conducted using artificial sea water as electrolyte, portray
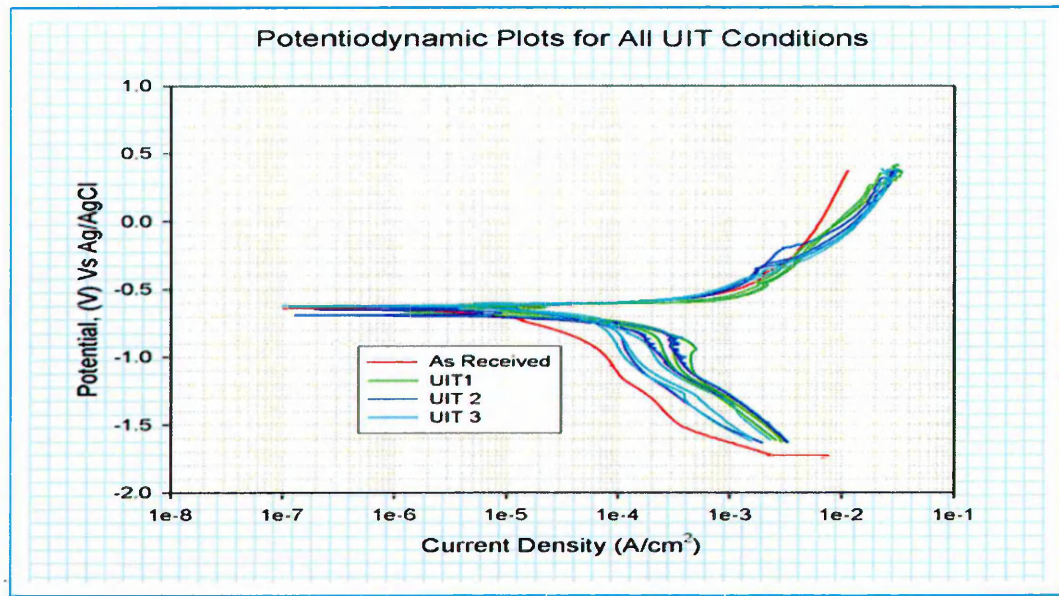
Figure 59: Potentiodynamic plot showing Comparison of all three UIT conditions with the AR condition.

this treatment as more corrosive resistant than the AR samples. Thus, the inclination of this proposed Applied Ultrasonic's research was directed towards using the SEM analysis to proceed with further analysis and hence forth, in this research further testing is carried out to characterise UIT1 condition.
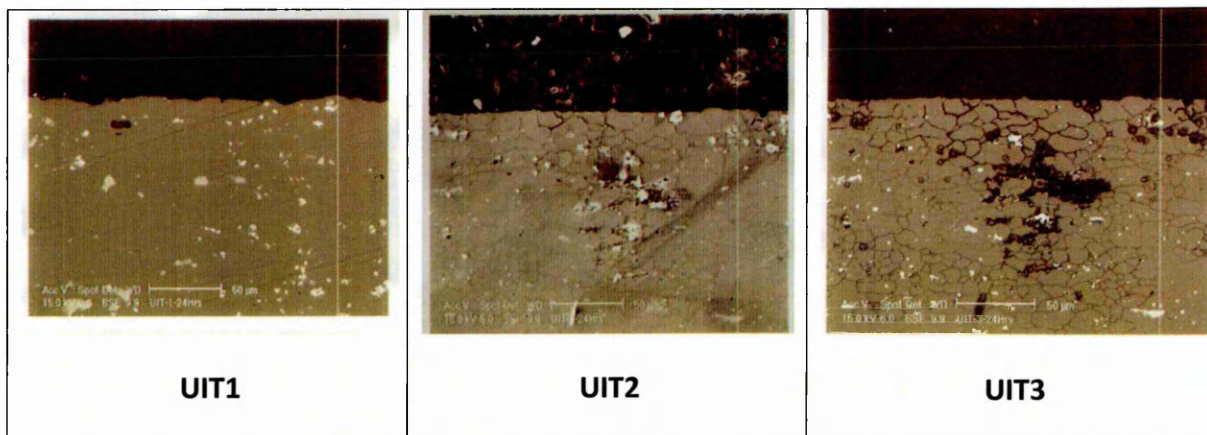

Figure 60: The above micrograph shows the results of exfoliation corrosion testing for all the three samples subjected to 24_20. UIT 1 shows good corrosion resistance.

5.5 Chapter Summary

In this chapter, the effect of exfoliation on subsequent corrosion resistance was assessed following a series of tests in which exfoliation exposure time and temperature were varied systematically. Samples subjected to UIT surface conditioning, followed by exfoliation corrosion have shown increased corrosion resistance. Following exfoliation there is a considerable amount of Cu redistribution with enrichment occurring near the surface. At

ambient temperatures, UIT conditioning of the surface caused the alloy to become electrochemically more active. However SEM cross-sectional analysis showed little difference in corrosion, at temperatures below 40 ^{0}C, between UIT conditioned and compared AR specimens.

CHAPTER 6

Influence of Hydrogen Charging in to the Metal Matrix of Al 2024 due to Exfoliation Corrosion

6.1 Introduction

This study is aimed towards an understanding of the nature of hydrogen embrittlement. Such knowledge is important for understanding the problems involving the embrittlement effects in high strength alloys applied in aerospace. Hydrogen embrittlement occurs at the atomic level, within a metallic material, with little or no visible defects or signs of premature cracking of the part, product or structure. The consequences are much more devastating than corrosion because failures are unexpected, occurring with no warning as the crack initiates at the atomic level, within the metal, often below the surface, unlike corrosion which is a surface phenomenon.

The quantitative analysis of a metal or alloy containing a gas can is often problematic as diffusion of the gas is occurring continually at a rate often undetermined. The present work involves the use of Glow Discharge Optical Emission Spectroscopy (GDOES) (**See Section 4.2**) where the sample is sputtered using Argon ions from low pressure plasma. These sputtered atoms are excited and emit light which are picked up by photomultiplier tube. Qualitative hydrogen diffusion analysis has been performed for AR and UIT samples subjected to exfoliation at ambient temperatures. The results are grouped according to the exfoliation test conditions and were aimed to see the effect of exfoliation time and temperatures.

6.2 Hydrogen Studies

When a metal comes in contact with a source of hydrogen, a thin layer is deposited on the surface which is then followed by activated absorption. Hydrogen Embrittlement (HE) is always an important issue as it can significantly affect the performance of a material. Hydrogen is also the only gas that is appreciably soluble in aluminium and its alloys and reduces the surface energy of many metals and is concentrated on the surfaces of separation [145]. During the cooling and solidification of molten aluminium, this dissolved hydrogen may precipitate in molecular form, resulting in the formation of voids.

6.2.1 As-Received Samples

As Received samples were sputtered for various time periods ranging between 20 sec to 2000 sec. This resulted in to number of sputtered spots of various depths. The last few average hydrogen counts number was taken and plotted for the respective depths of sputter resulting in to hydrogen count Vs depth of sputter as shown in **Figure 61** and a line of regression was plotted.
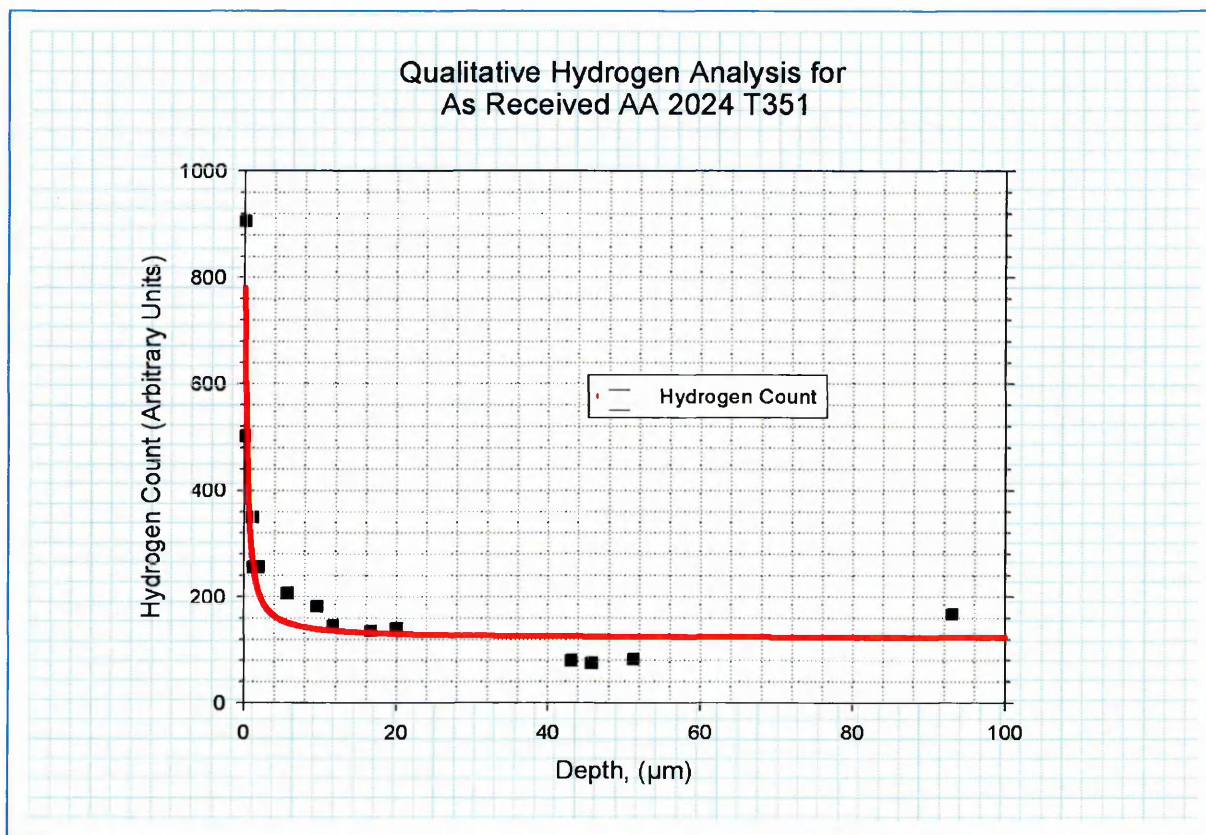
Figure 61: Qualitative hydrogen analysis for AA 2024 T351.

Following the profile of AA 2024 T351 in **Figure 61**, it can be concluded that hydrogen reaches it saturation limit of 150 hydrogen counts within 10μm. This amount of hydrogen is insignificant as it probably could have been detected as in the forms of compound. Thus, **Figure 61** is used as a reference line for AA 2024 T351.

6.2.2 Exfoliated Samples

In accordance with the testing method for Reference curve of AA 2024 T351, AR samples were exfoliated for 24hours at ambient temperature and at 40°C. However, since GDOES requires flat samples for Hydrogen measurements, the exfoliated layer measured using SEM (**See Section 5.1**) was removed by grinding. Thus, it was assumed that hydrogen ingress will be highest in the exfoliated layer.
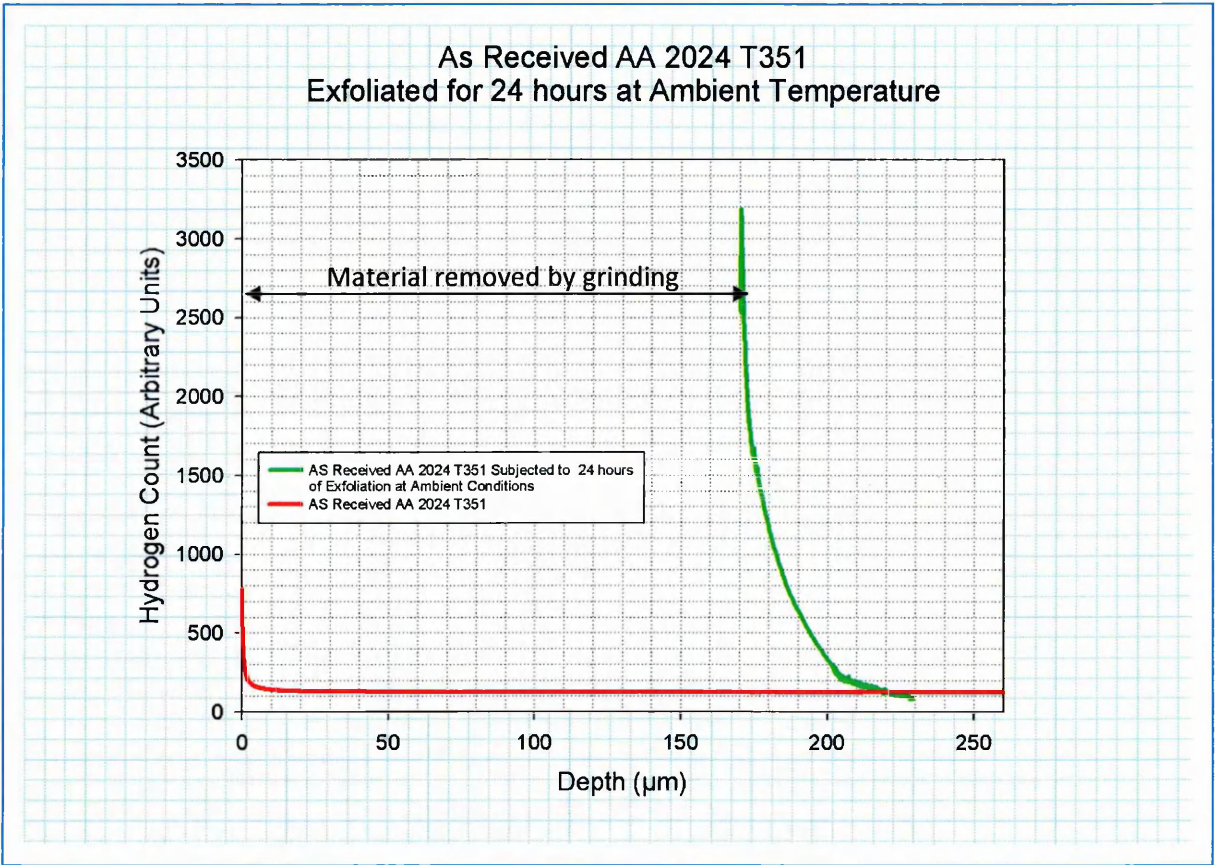
Figure 62: A GDOES result showing the comparison between Reference sample and AR samples exfoliated for 24 hours at ambient conditions (AR_24_20).

From **Figure 62**, the profile of AR_24_20 it can be seen that hydrogen charging takes place as a result of exfoliation corrosion testing. Hydrogen was found in excess of 220μm in cross-sectional depth of AR24_20 sample. **Figure 63** shows the result of AR24_40 sample Vs the reference curve. It is observed that hydrogen ingress, as a result of exfoliation, occurs up to a depth of 512μm.
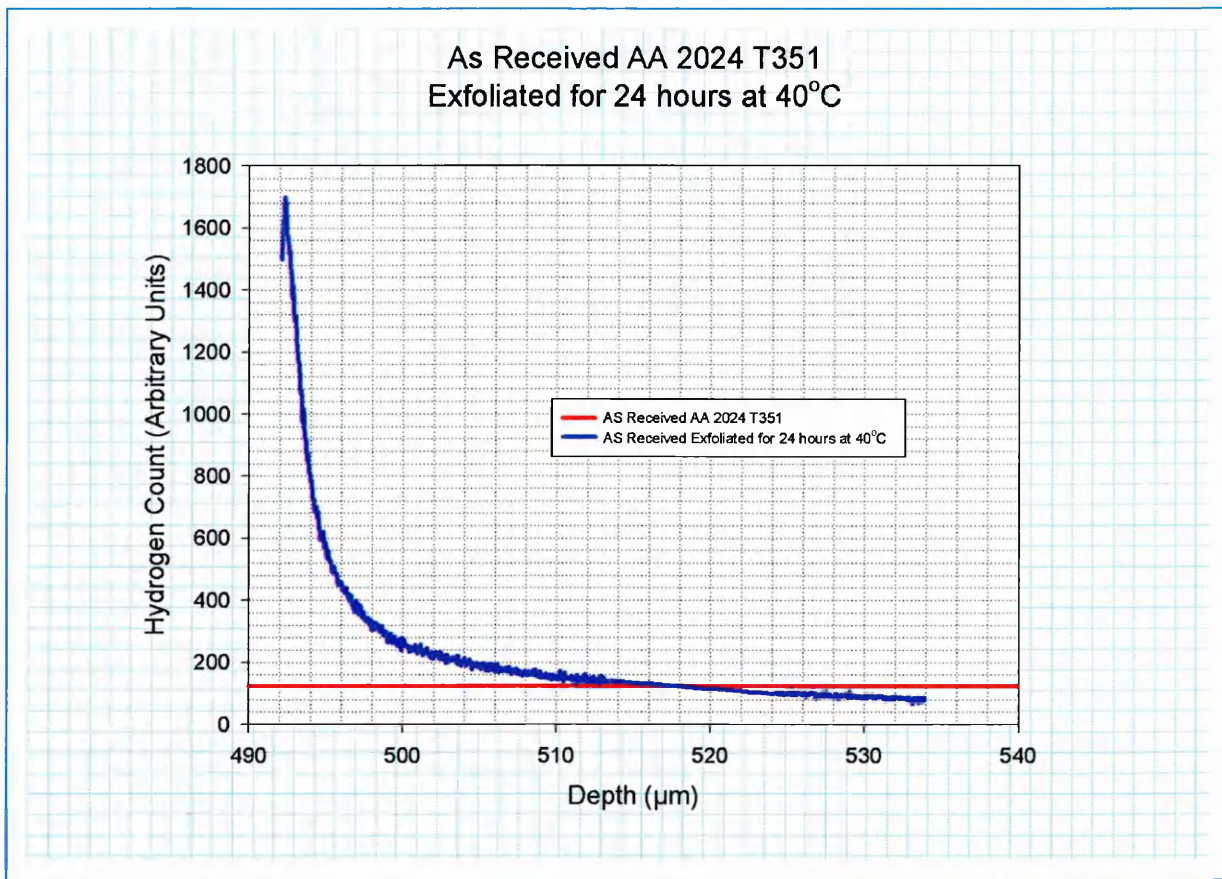
93

Figure 63: A GDOES result for hydrogen showing AR 24hours of exfoliation at 40°C (AR24_40°C) Vs the reference line of AA 2024 T351.

When all the GDOES results are compared, as shown in **Figure 64**, AR 24_20 exhibited maximum hydrogen charging, as about 3000 hydrogen counts were identified on fresh surface (after removal of exfoliated layer by grinding). However, the increase in temperature by 20^0C reduces the hydrogen to 1700 counts, but the exfoliation damage is severe. Thus, it can be further concluded that the increasing exfoliation exposure time alongside with increasing temperature links together the deep pits through simultaneous intergranular corrosion. This newly created intergranular-pit path facilitates further the ingress of exfoliation solution and when the hydrogen evolution occurs as a result of electrochemical reaction taking place, it facilities further hydrogen charging deep in the material. Thus, the current conventional grinding process to tackle corrosion leaves behind the hydrogen diffused embrittled zone which could be catastrophic in any scenario.
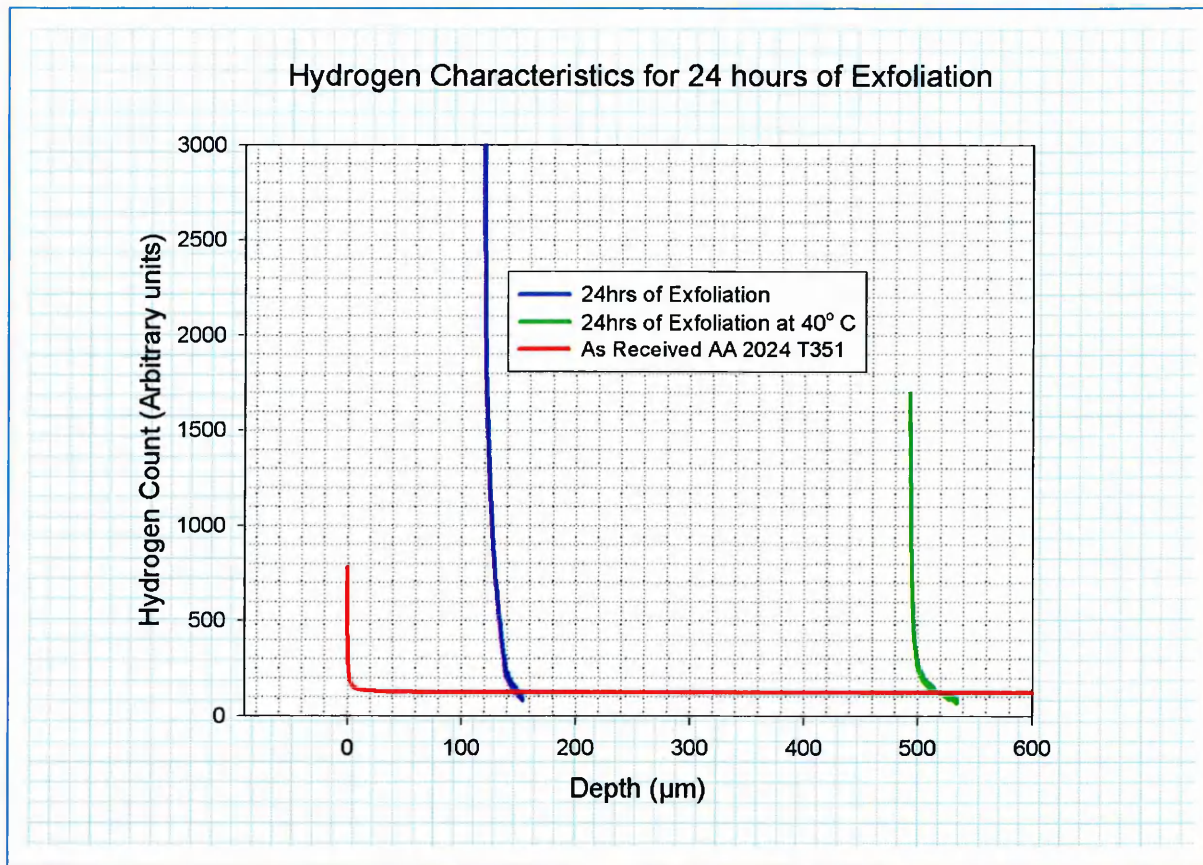
Figure 64: A comparison showing the affect of increasing temperature at same exfoliation conditions.

6.3.3 UIT Treated Samples

From the **Figure 65**, it is observed that the UIT conditioned sample showed 1650 Hydrogen count initially, but this Hydrogen charging is reduced after 10μm and goes below the reference curve. At the same time since Hydrogen being the smallest element in the periodic table, thus having the smallest atomic size, even the nano scale crystallisation effect doesn't impede the Hydrogen charging into the alloy.

When the UIT samples are subjected to exfoliation corrosion testing for 24hours of exfoliation at ambient and at 40°C, it is noticed that UIT samples show a remarkable resistance to hydrogen charging in to the alloy. UIT24_20 follows a similar trend as UIT condition sample and it drops from 1600 to 180 hydrogen counts within a distance of 10μm cross-sectional depth. However, AR24_20 drops from 1800 to 180 hydrogen counts in more than 30μm. This suggests that there is less hydrogen charging in the UIT sample when compared to the AR sample. From these results as shown in **Figure 66**, it can be concluded that the since the
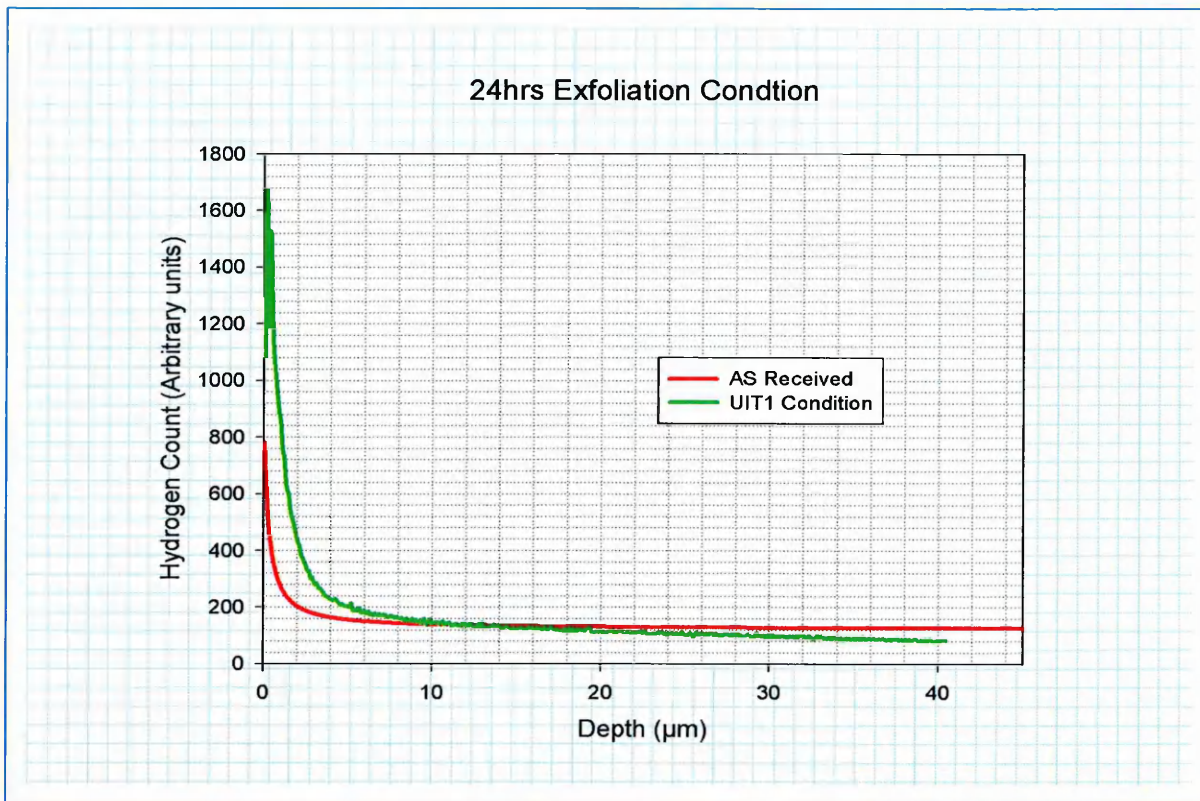
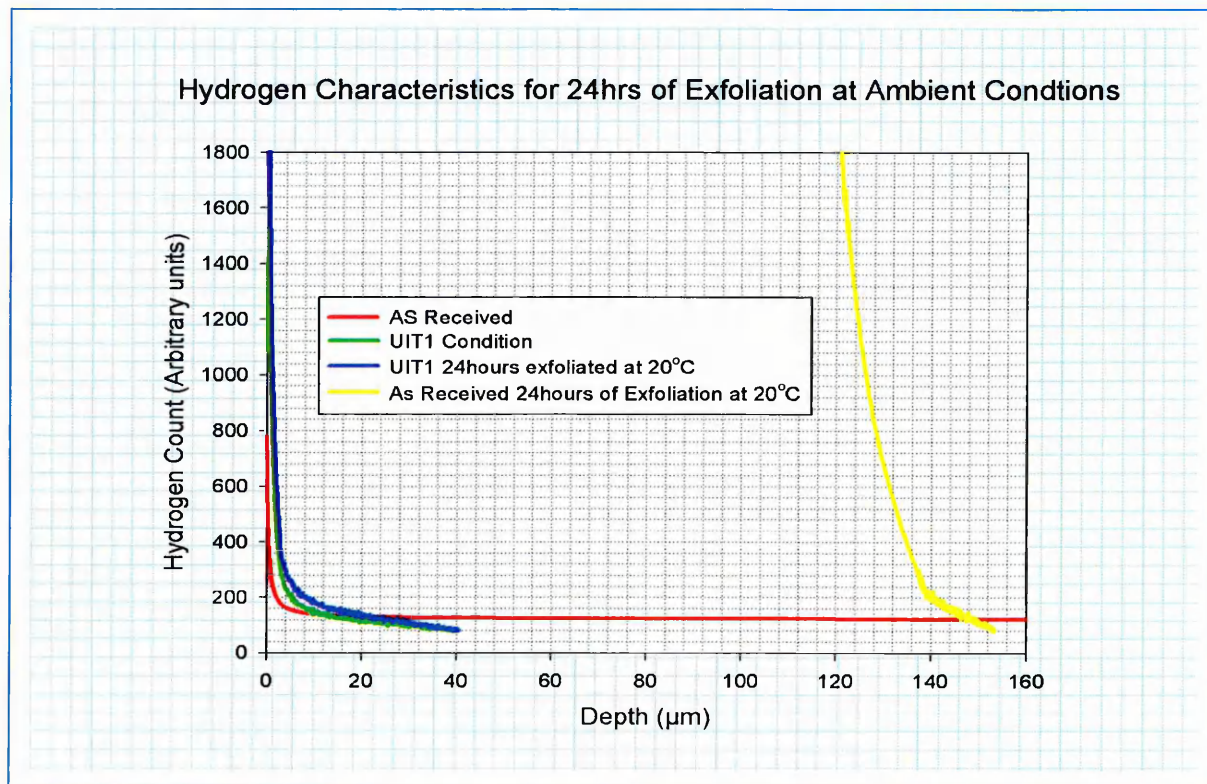**Figure 65:** A comparison between AR & UIT1 condition of AA 2024-T351.

Figure 66: Shows a comparison of UIT and AR samples subjected to Exfoliation testing for 24 hours at ambient conditions.
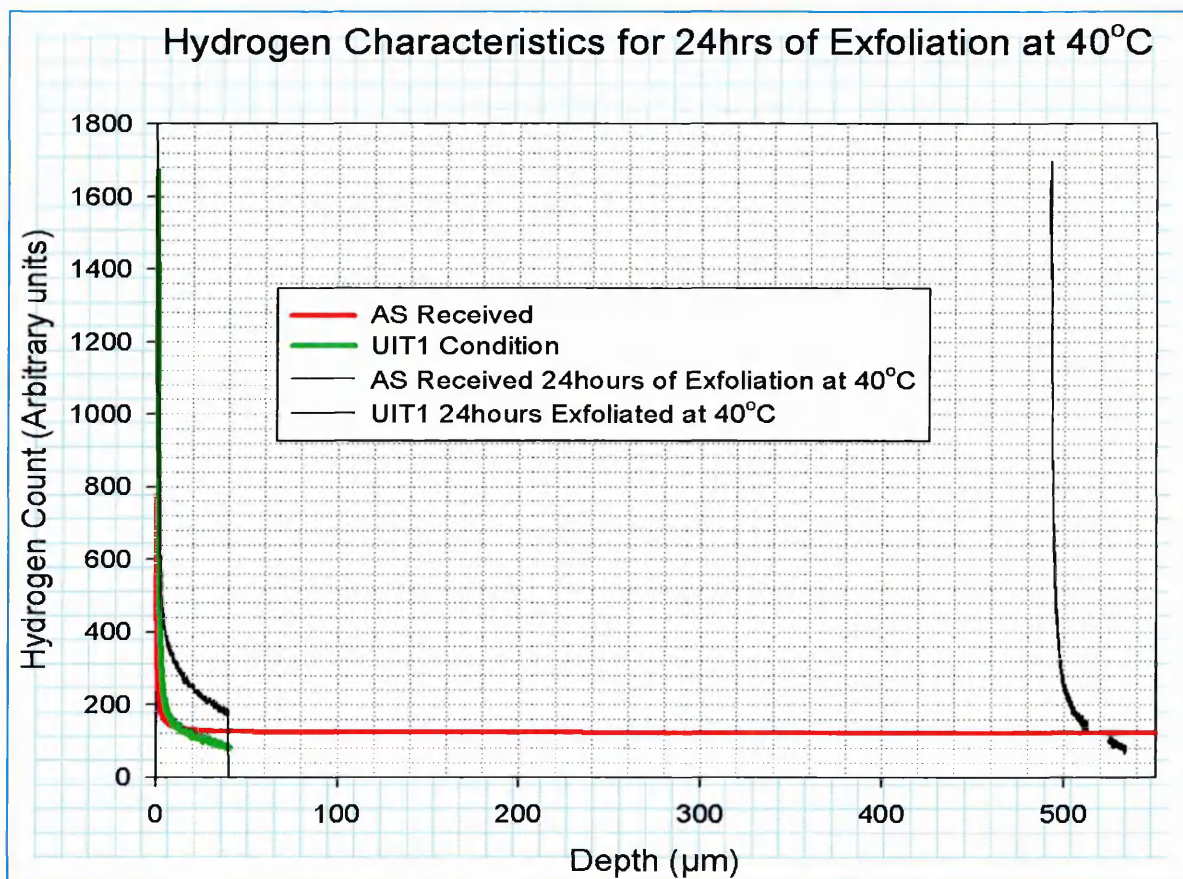
Figure 67: A comparison of AR and UIT conditions at ambient and 40^{0}C subjected to exfoliation corrosion for 24 hours.

UIT condition attenuates the ingress of exfoliation solution in to the alloys cross-section; the hydrogen charging is also minimal. Similar results were obtained at 40 ^{0}C, however, the UIT24_40^{0}C shows a higher hydrogen count in comparison to UIT24_20, suggesting that temperature increases the hydrogen ingress into the alloy.

6.3 Chapter Summary

Hydrogen embrittlement has always been an eminent factor often considered in understanding metal fatigue by material and design engineers as hydrogen illness is very sudden and the component fails without warning. Thus, this chapter summarises that AA 2024-T351 is also prone to HE when subjected to exfoliation corrosion. A reference line for minimal pre-existing hydrogen is identified and the magnitude of hydrogen count is found to be 180. It is also found that, the hydrogen ingress and further charging is prominent at ambient temperatures for AR samples showing damage in greater width of cross-sections. The surface is also charged again showing a greater number of hydrogen counts.

CHAPTER 7

Influence of UIT on Strength Properties of AA 2024-T351 after Corrosion Exposure

7.1 Introduction

Tensile properties are described in terms of the types of force or stress that the metal must withstand and how these forces are resisted. They determine the range of usefulness of the metal and establish the service that can be expected. Corrosion on aircraft components is tackled by removing the corroded area by grinding. Numerous reports have shown that the technique can only reinstate the yield stress and ultimate tensile strength of the component. Elongation to failure and elastic strain density remains unaffected due to hydrogen embrittlement effects [146].

After exposure of the specimens to the corrosive environments conditions tabulated in **Table 1 (See Chapter 4)**, the corroded specimens were subject to tensile testing. The tests series include: (1) to establish the reference for uncorroded tensile specimens, (2) to test the AR specimens corroded to the ASTM standards for accelerated laboratory corrosion tests at different pre-determined time and temperature tabulated in **Table 1 (See Chapter 4)**, (3) to test the UIT specimen thereby establishing the effect of the treatment, and (4) to test the UIT specimens corroded to the ASTM standards and in similitude to **Table 1 (See Chapter 4)**. The tensile tests were performed according to ASTM E8m-94a specification [147].

7.2 Mechanical Characterisation

7.2.1 Reference Materials

The Yield Stress (YS), Ultimate Tensile Stress (UTS) and Elongation at Failure (EOF) AA 2024 T351 are summarised in **Table 3**. Nominal cross-sectional area before exfoliation is used in finding YS and UTS as the post-corrosion specimens were highly corroded for a meaningful cross-sectional area. The reference AA 2024 T351 tensile properties are in good agreement with the results published in material data sheet [148].

Table 3: Yield and tensile strength properties under different exfoliation conditions.

Name	YS-AR (MPa)	YS-UIT (MPa)	UTS-AR (MPa)	UTS-UIT MPa)	EOF- AR (%)	EOF-UIT (%)
Reference AA 2024-T351 (5mm)	341	340	485	492	16.43	15.7
24_20	315	340	446	400	4.4	3.7
24_40	275	302	431	471	5.6	12
24_60	155	285	250	411	5.3	4.4
24_80	152	203	260	365	6.8	3.1
48_20	300	285	438	397	4.1	4.5
48_40	260	300	424	400	5.2	5
48_60	132	216	225	325	5.6	1.75
48_80	110	178	207	268	4.5	1.25
72_20	278	259	410	295	3	2
72_40	222	295	352	388	4.55	4.4
72_60	112	205	195	315	3.3	2.6
72_80	108	150	163	148	2.9	1.5
96_20	271	262	392	365	2.9	4.5
96_40	220	251	350	292	2.1	3.4
96_60	104	141	166	211	1.6	1.15
96_80	102	112	140	164	3.1	1

The results tabulated in **Table 3** suggest that UIT is not necessarily a severe plastic deformation (SPD) technique which can be used to improve the tensile properties of the As-Received AA 2024 T351 alloy. In comparison AR samples, the significance of UIT conditioning is quite evident at temperatures of exfoliation ranging between 20^0C to 40^0C and up to 48 hours of exfoliation time. For example, at 24_20 it is observed that UIT does not have an effect on the yield stress. At 24_40, the effect of UIT is more apparent as a

simple comparison of ultimate tensile stress (UTS) results of respective AR and UIT samples suggests that there is over 8% recovery of UTS. This further suggests that there is further strain hardening in the UIT samples. UIT is providing an increased resistance to the formation of slip bands at the micro scale. This is further discussed in **Section 7.3.2**.

7.2.2 Influence of Exposure Time

From **Table 3**, the data is further plotted with respect to exfoliation corrosion exposure time against the reference AR and UIT samples. It s evident that the corrosion attack tends to decrease Ultimate Tensile Stress (UTS) and Yield Stress (YS). The effect of exfoliation corrosion becomes appreciable with increasing aggressiveness of exposure time as shown in
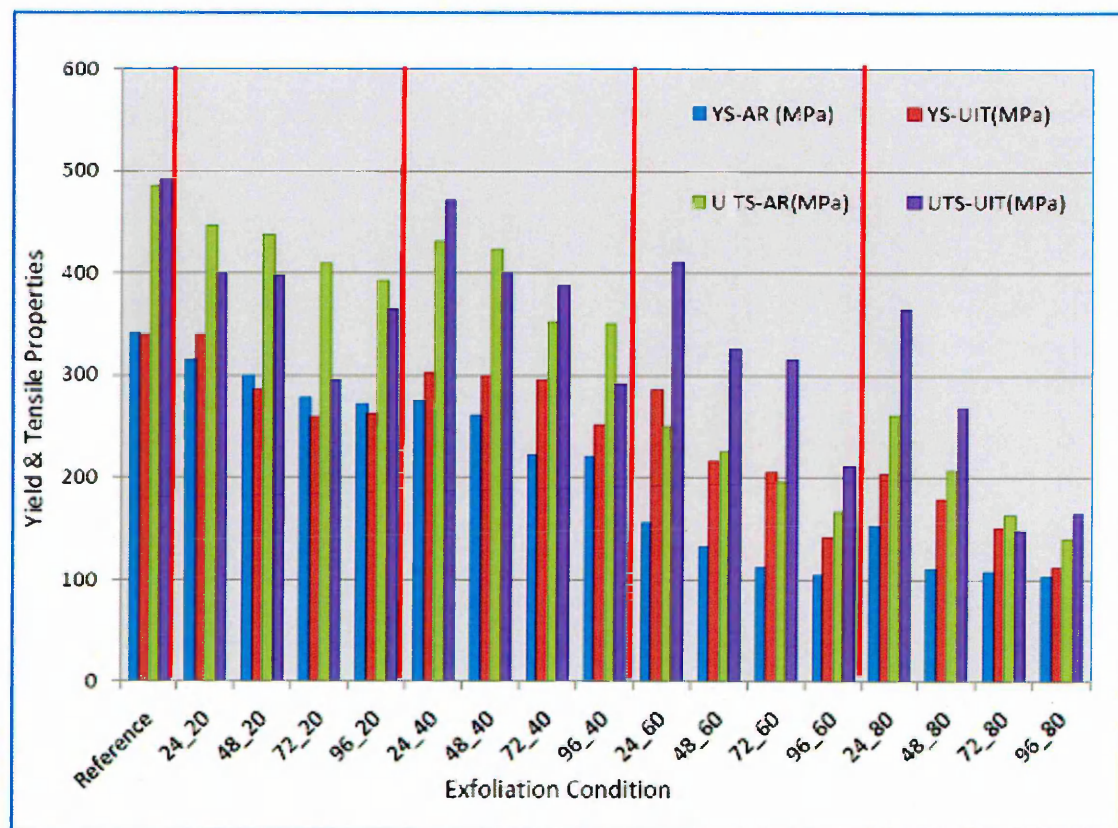
Figure 68: A comparison of AR and UIT samples with respect to time showing gradual tensile properties degradation after exposure in exfoliation corrosion.

Figure 68. A closer look for all the exposure times at ambient and at 40^0C gives the impression of the samples being corrosion resistive. This indicates that UIT samples show resistance to corrosion in the temperature range between ambient and 40^0C. However, the Elongation at Failure (EOF in %) values have always remained dramatic. Tensile ductility reduction was found for all the exfoliation conditions between (4 - 1) % except for 24_40

and 48_40 AR and UIT conditions where the EOF values are found to appreciably standing out as tabulated in **Table 3**.

7.2.3 Influence of Exposure Temperature

As the data is plotted with respect to temperature of exfoliation at constant time (**See Figure 69**), it is observed that there is a steep reduction in tensile properties of AA 2024 T351. However, this is not the occurrence for all the cases of exfoliation exposure times. When AR and UIT results are compared for 24 hours of exfoliation exposure time for various temperatures, it is observed that the rate of loss in yield and tensile properties values for UIT samples is relatively slower than AR samples.
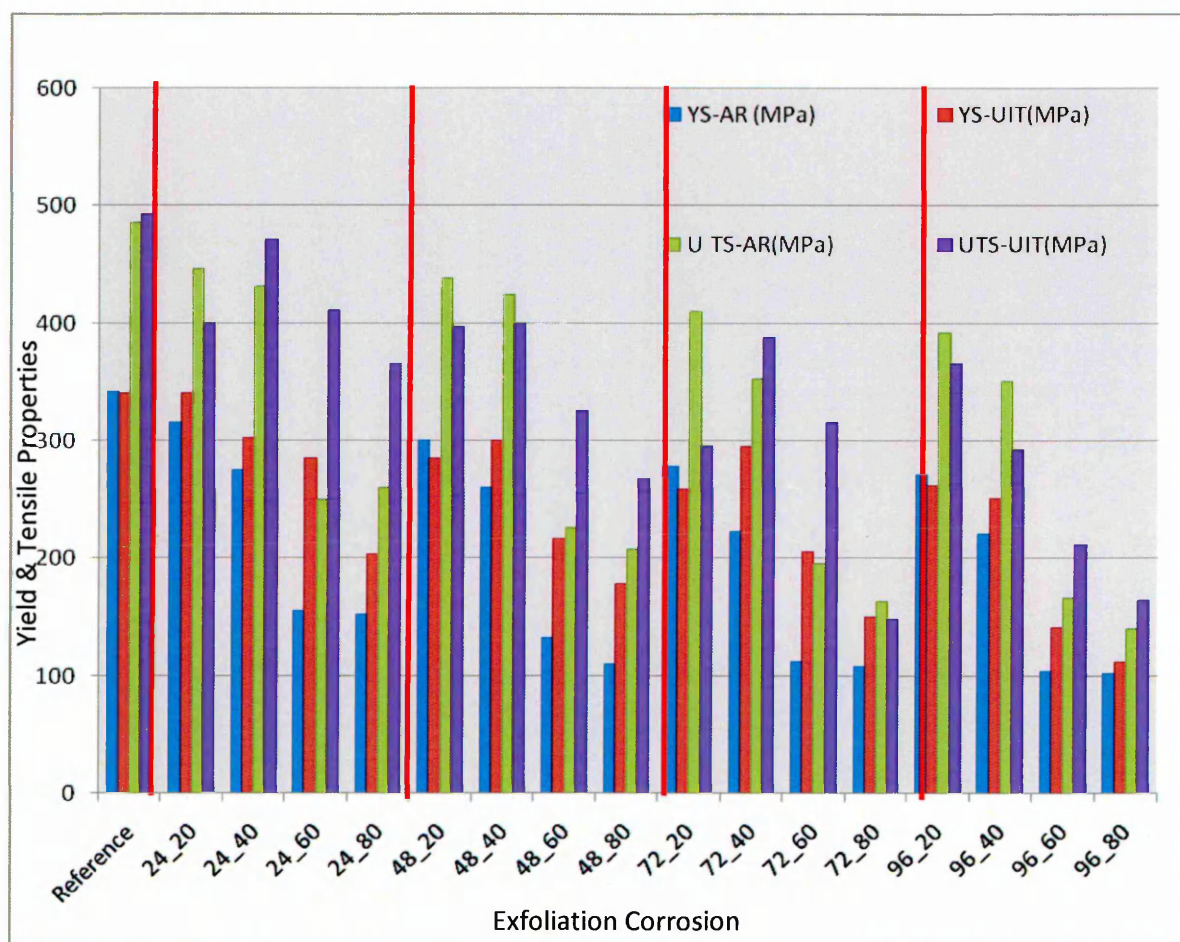
Figure 69: A comparison of AR & UIT samples with respect to temperature at constant time.

Figure 70 shows yield stress values plotted against the exfoliation temperature at constant time period of 24 hours. It is, without difficulty, evident that UIT results in lower loss in mechanical properties than that of the untreated sample (not shown here). The ultimate tensile stress values follow a similar trend except that there is a marked reduction at 40 ^{0}C

(See Figure 71). Similar results are noticed for UIT samples at lower exfoliation exposure temperatures below 40 ^{0}C.
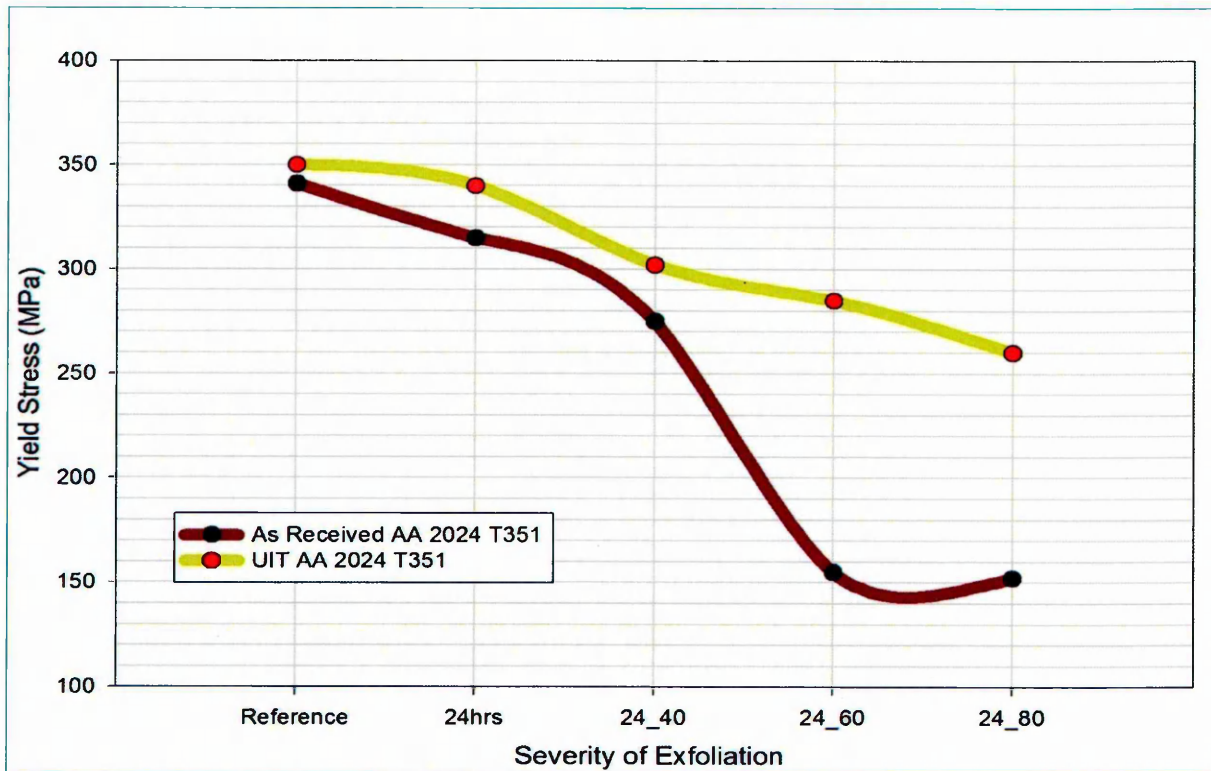
Figure 70: Yield Stress characteristics of AA 2024 T351 subjected to exfoliation corrosion at temperatures ranging from 20^{0}C to 80^{0}C at constant immersion time (24hours).
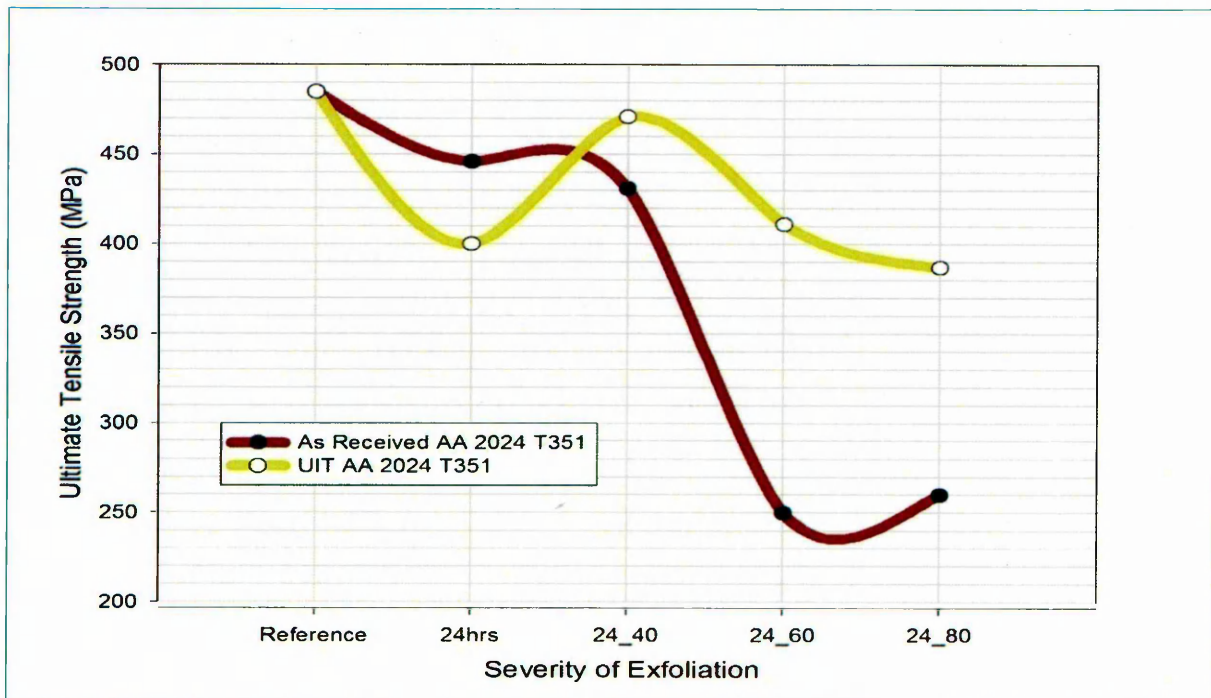
Figure 71: Ultimate tensile strength characteristics of AA 2024 T351 subjected to exfoliation corrosion at temperatures ranging from 20^{0}C to 80^{0}C keep at constant immersion time (24hours).

7.3 Fractographic Analysis & Discussion

7.3.1 Zones of Failure

Initial fractographic analysis of the tensile fractured surfaces using SEM (**See Section 4.3**) revealed three different zones of failure as shown in **Figure 72**. It is clear that the hydrogen embrittled zone is sandwiched between corrosion and ductile fracture zones. Thus this hydrogen induced element embrittles the zones ahead of the crack tip and even after existing grinding techniques are conducted to tackle the corrosion damage, there still exists the HE affected zone which is make alloys more prone to brittle failure.

| Corrosion Assisted Failure | Hydrogen Assisted Failure | Ductile Failure |
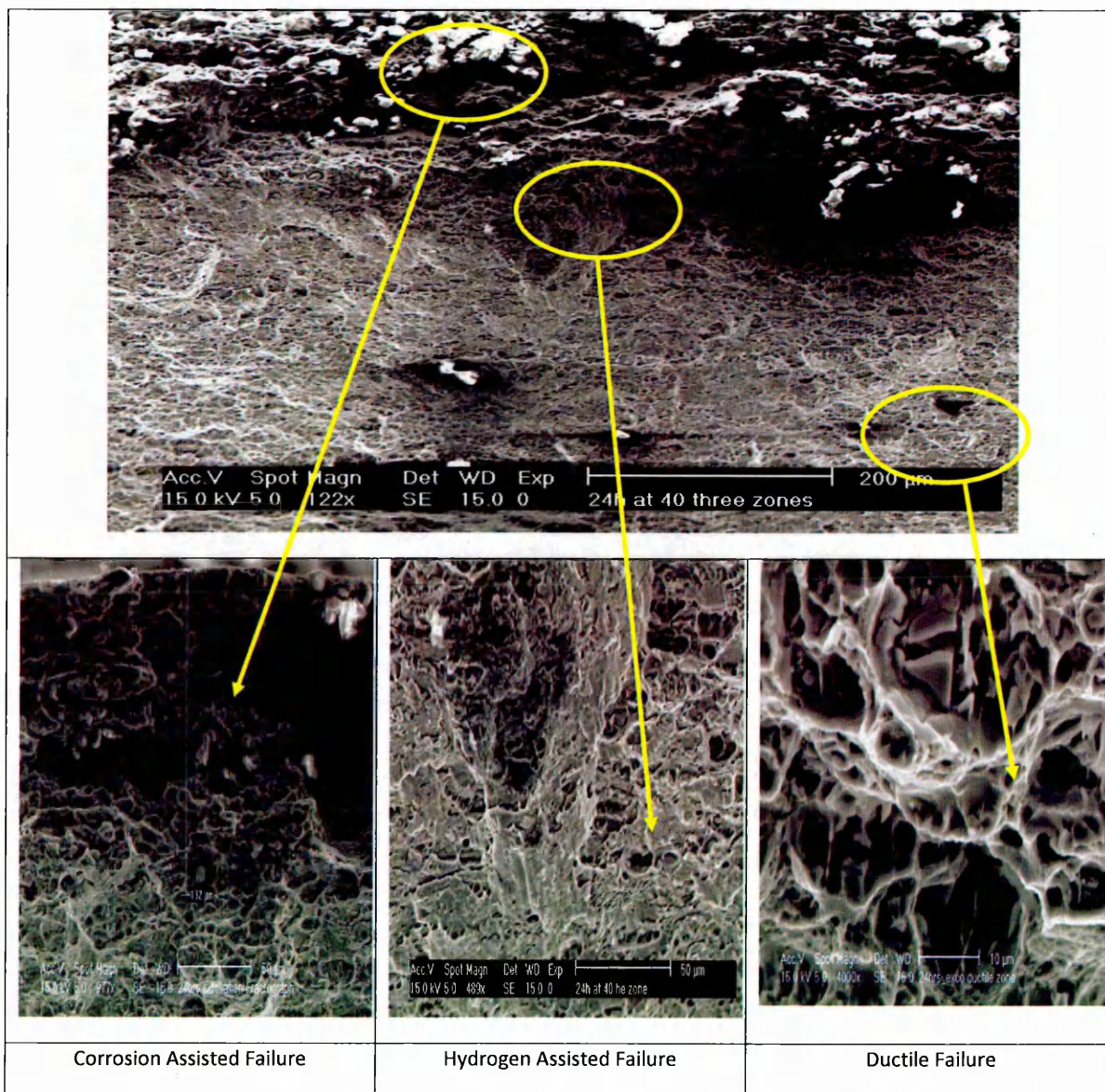
Figure 72: Three modes of failure of AA 2024 T351 subjected to exfoliation corrosion for 24hours at 40 ^{0}C.

Thus this so called "ductile to brittle transition" is found to be varying according to the exfoliation corrosion test time and temperature (**Table 1, Chapter 4**) which the sample has been subjected.
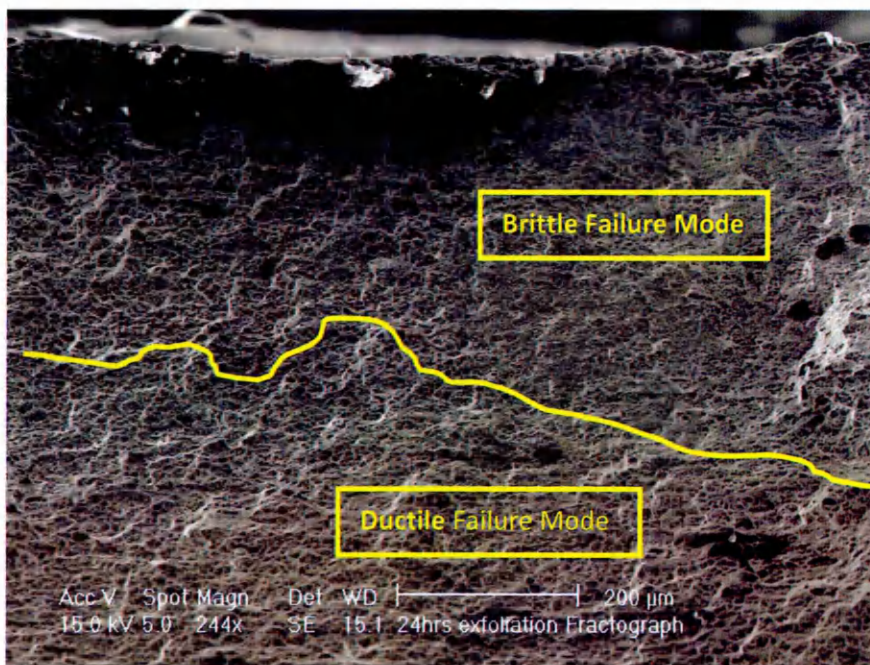
Figure 73: A cross-sectional SEM micrograph of AR 24 hours of exfoliation at ambient conditions showing ductile failure mode transition to brittle mode of failure due to hydrogen induced embrittlement. The average depth of brittle failure is found to be 360 μm.
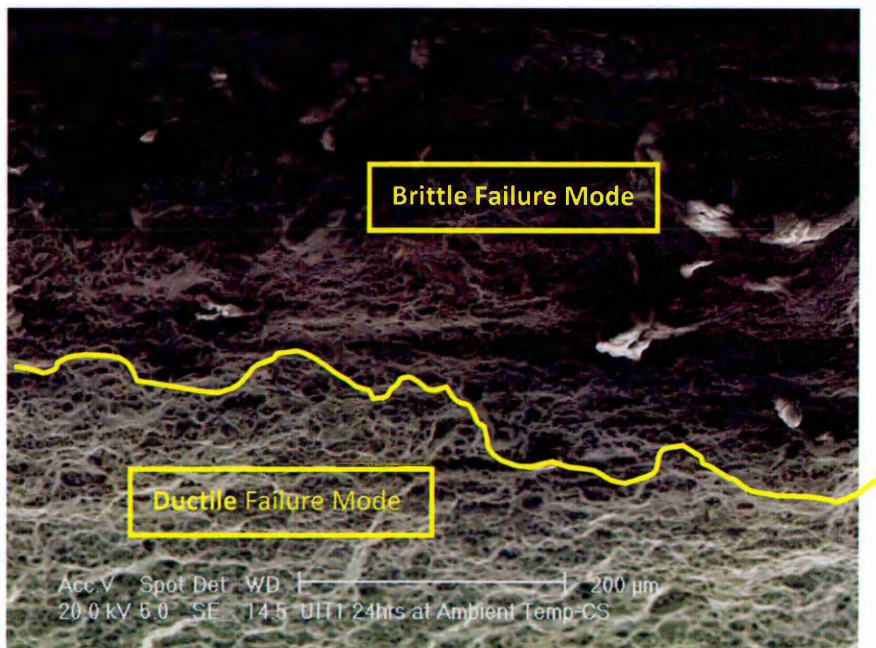
Figure 74: A cross-sectional SEM micrograph of UIT 24 hours of exfoliation at ambient conditions showing ductile failure mode transition to brittle mode of failure. The average depth of brittle failure is found to be 268 μmA.

The micrographs shown in **Figure 73** and **Figure 74** compare the AR and UIT uniaxial tensile fracture cross-sectional surfaces after 24 hours of exfoliation at ambient conditions. Analysis of the micrographs shows that the UIT samples exhibit an average cross-sectional brittle failure depth of 300μm. In contrast to this, the AR sample, under similar conditions

produced more than 360μm of cross-sectional brittle failure depth. This strengthens the exfoliation testing results stating a higher corrosion resistance for UIT condition samples in comparison to AR samples.

7.3.2 Crystallographic Failure

Fracture surfaces of uniaxial tensile loaded specimen surfaces of FCC crystal structure have distinct features. One of them is their mode of crystallographic failure. Also a series of steps resembling a staircase pattern are produced upon monotonic plastic strain.
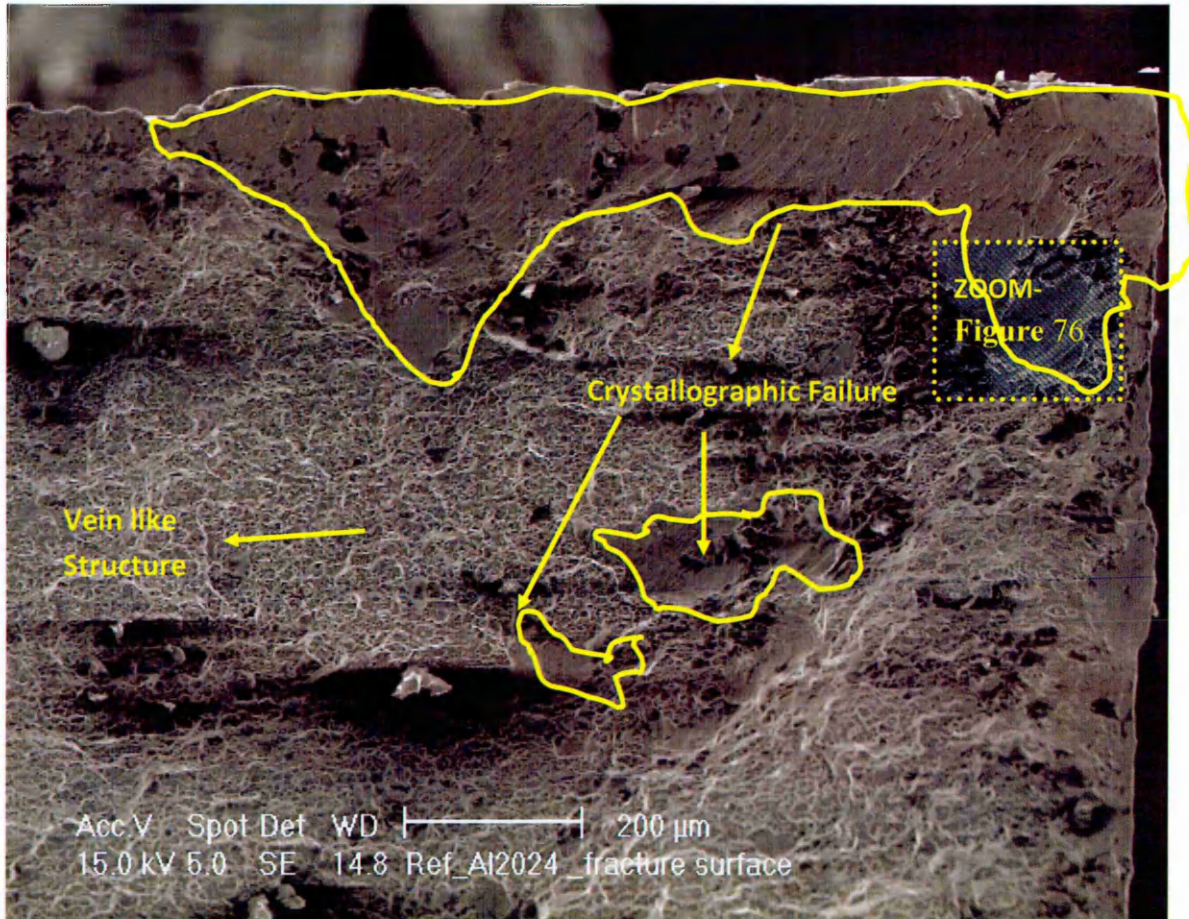
Figure 75: A cross-sectional SEM micrograph of AR AA 2024 T351 showing crystallographic (marked areas).

A series of slip planes forms a flat lamellar structure and span the entire cross section of the single crystal. Thus it is quite evident from **Figure 76** that when the vein like structures, which contains the edge dislocations, disappear, a crystallographic slip plane is initiated and the sample failed in shear mode. **Figure 77** is a zoomed section of **Figure 76** showing the initial stages of the failure where the step pattern is visible and gradually decreasing and shears when a threshold value of far field stress has reached.
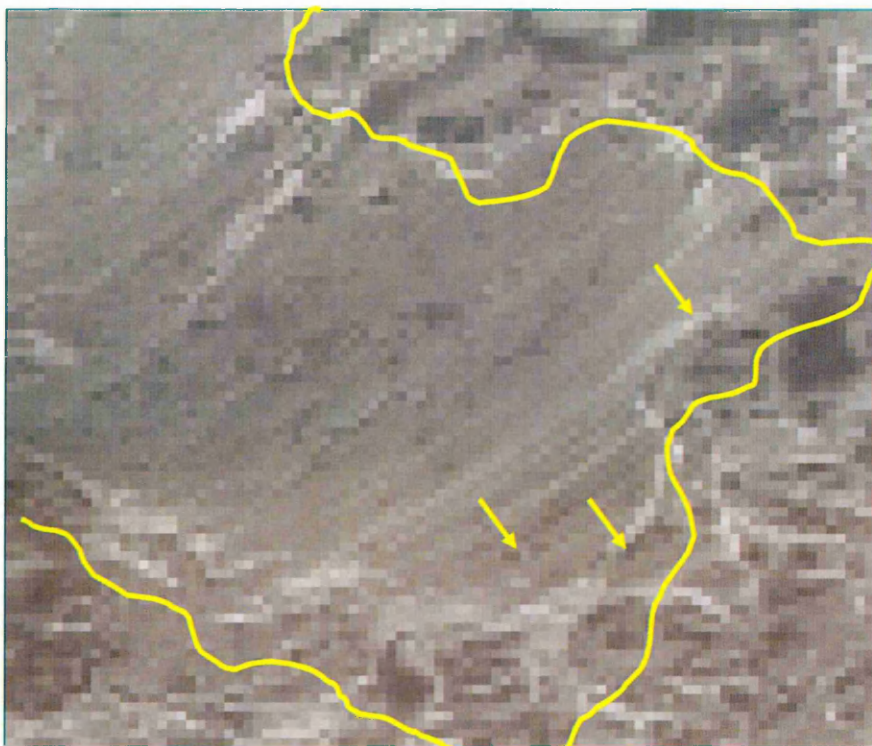
Figure 76: A zoomed image of section marked in **Figure 75** showing a series of step pattern.
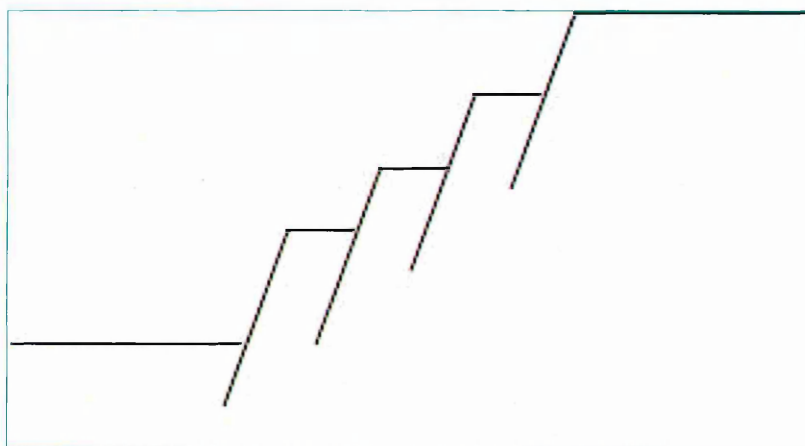
Figure 77: A series of steps resembling a staircase pattern produced by monotonic plastic strain.

No such appreciable crystallographic failures are observed in UIT treated specimens fracture surfaces.

7.4 Chapter Summary

In this chapter, the effect of exfoliation corrosion is well assessed following a series of tests with exfoliation exposure time and temperature as varying parameters. Samples subjected to UIT surface treatment, followed by exfoliation corrosion have shown increased resistance to a reduction in mechanical properties, notably tensile and yield strength. Fractographic

analysis further supported this finding by showing smaller average brittle failure depths for UIT specimens when compared to AR specimens. It is understood that AR samples failed under crystallographic mode of failure where high density slip bands are formed and the initial failure happens to be in step format.

CHAPTER 8

Influence of UIT on Fatigue life AA 2024-T351

8.1 Introduction

The main goal of these experiments was to determine the influence of UIT conditioning on pre-exfoliated AA 2024-T351 where the two main characteristic effects of UIT, are considered to be; nanocrystallisation and induction of compressive residual stresses [149]. Transmission Electron Microscopy (TEM) has revealed Ultra Fine Grain (UFG) refinement (See **Section 3.4.2**) on the surface of samples subjected to UIT. It is widely cited in literature that UFG structures tend to have a high resistance for crack propagation and UIT is understood to actively change the grain orientation.

8.2 Fatigue Life

Numerous failures of engineering structures are caused by fatigue. It is therefore important to be able to predict the lifetime to failure. The fatigue phenomenon is extremely complex, and hence reliable predictions demand detailed knowledge to an extent that is possible to achieve.

This chapter discusses the results of fatigue life curves of pre-exfoliated AR and UIT AA 2024 T351 with respect to reference curves of AR and UIT specimens. The curves are further analysed within the High Cycle Fatigue (HCF) and Low Cycle Fatigue (LCF) regimes. The current fail-safe industrial practice demands for crack propagation studies as a major portion of the structural component are not replaced unless the crack reaches a threshold value (**See Section 2.3.2.3**). Thus, it is necessary that the base material characteristic features are fully understood.

8.2.1 Fatigue Life Curves

Fatigue life data of AA 2024 T351 determined at a cyclic frequency of 25 Hz at a stress ratio R of 0.1 are shown in Figure 78. Arrows indicate unbroken specimens. In ambient air, fatigue data obtained for AA 2024 T351 at constant amplitude loading show endurance limit 240 MPa for $10e^7$. However, when the alloy is subjected to UIT, it is observed that the samples fail at lower stress levels. Post analysis of the fracture surfaces of these samples (See **Figure 79**) revealed that crack initiation of these samples has originated at the edges of the samples.
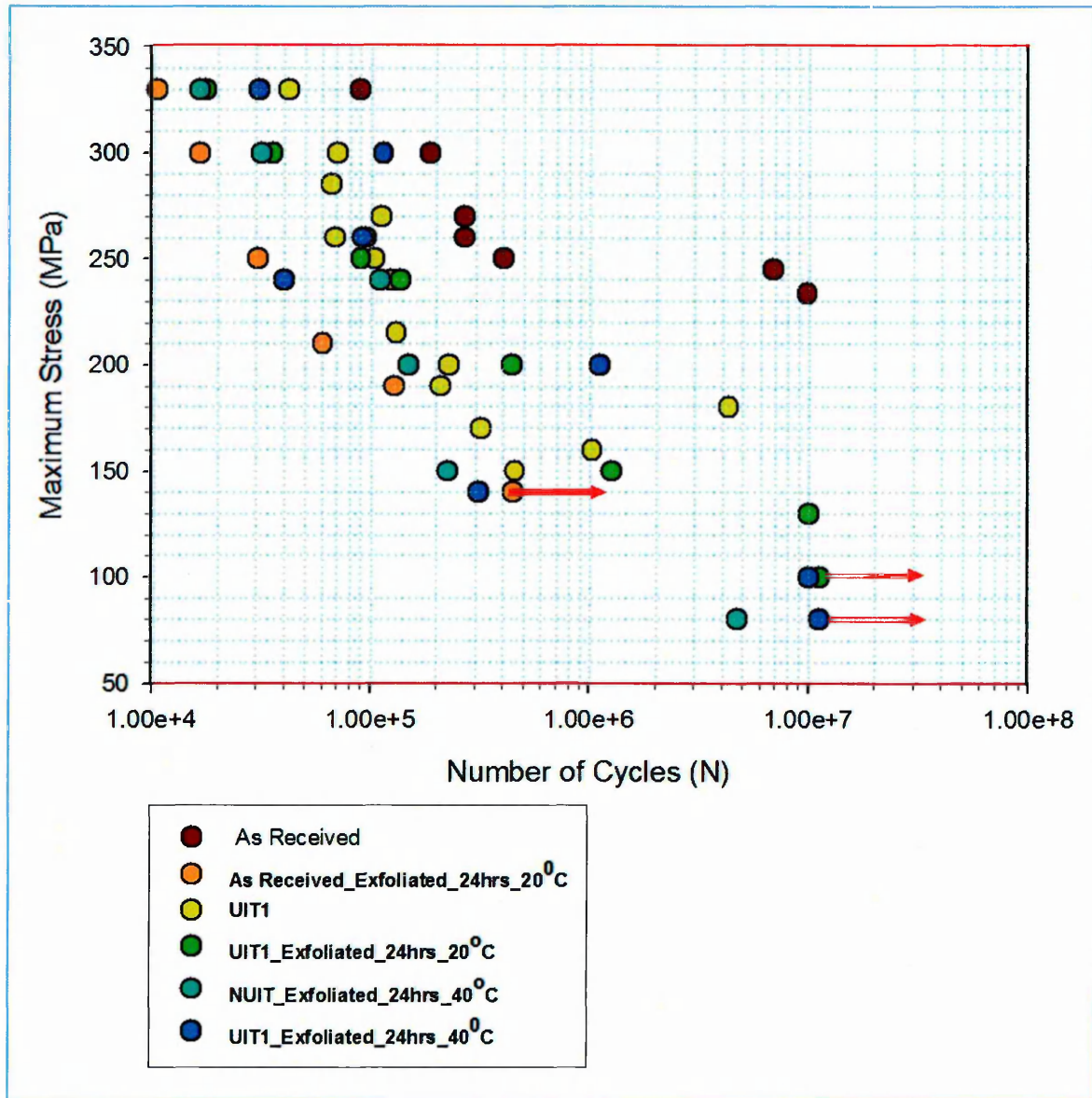
Figure 78: Fatigue life curves of AA 2024 T351 at constant amplitude loading at various exfoliation conditions.

Table 4: Results of the fatigue testing at constant amplitude loading with stress ratio R = 0.1. *Indicates that the sample did not fail AR and UIT-1 test results are referred.

Maximum Stress(MPa)	AR (Cycles)	AR_24_20 (Cycles)	UIT1 (Cycles)	UIT1_24_20 (Cycles)	AR_24_40 (Cycles)	UIT1_24_40 (Cycles)
80		11232576*			4732928	11232576*
100		10000000*		11232576*		10000000*
130				10000000*		
140		446208				311040
150			455248	1261440	225368	
170			317264			
160			1025030			
180			4303104			
190		128200	208872			
200			228920	441904	149448	1114176
210		60198				
215			130640			
234	9814420					
240			124056	135976	110208	40118
245	6883414					
250	403536	30604	103604	89948		
260	268592		68400	95460		91364
270	267888		111760			
285			66472			
300	186512	16520	70616	35640	31555	113864
330	89708	10522	42234	17654	16563	30761
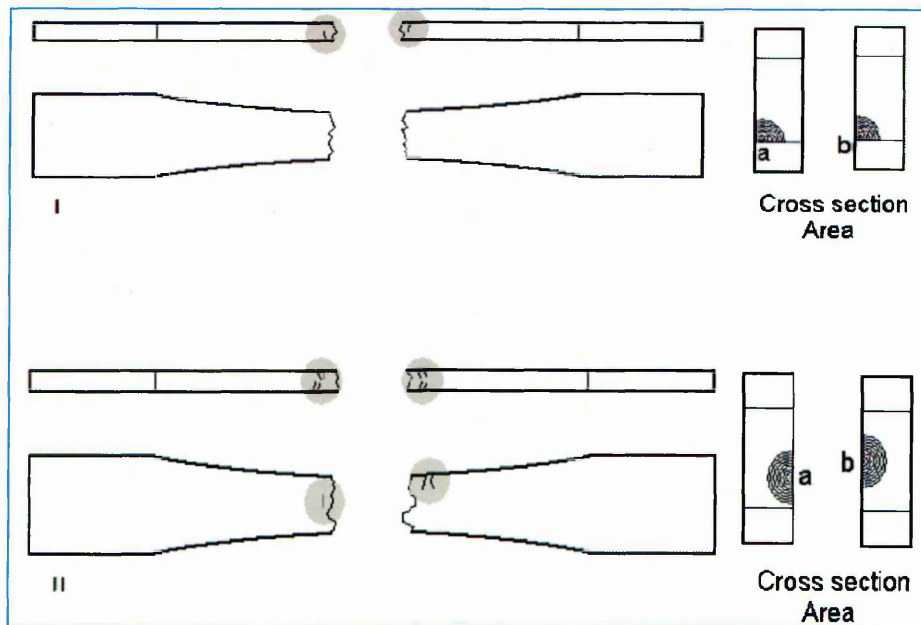
Figure 79: As Received (I) AR samples reveal that there are less significant number of crack initiation points. **UIT Conditioned** (II) More number of crack initiation points are noticed on UIT samples and most of them were originating from the edges of the samples as highlighted in the figure.

8.2.2 Low Cycle Fatigue Curves

Low Cycle Fatigue (LCF) failures typically have a root cause which stems from flaws in the material such as voids and other defects. At maximum stress of 330MPa, **Figure 80** shows the fatigue life of AR sample to be about $9x10^4$ cycles when compared to AR_24_20^{0}C sample failing at $1x10^4$. This suggests that in LCF, the initial exfoliation corrosion condition discussed (AR_24_20^{0}C), therefore reduces fatigue life by a factor of 9. However, this factor becomes smaller when exfoliated samples are compared. For example, at a maximum stress of 200MPa, it is noticed that UIT_24_20^{0}C sample failed at $3.5x10^5$ cycles and AR 24_20^{0}C sample failed at $1.1x10^5$, whereas AR sample reaches its fatigue limit suggesting that UIT condition increases the fatigue life by a factor of over 3.
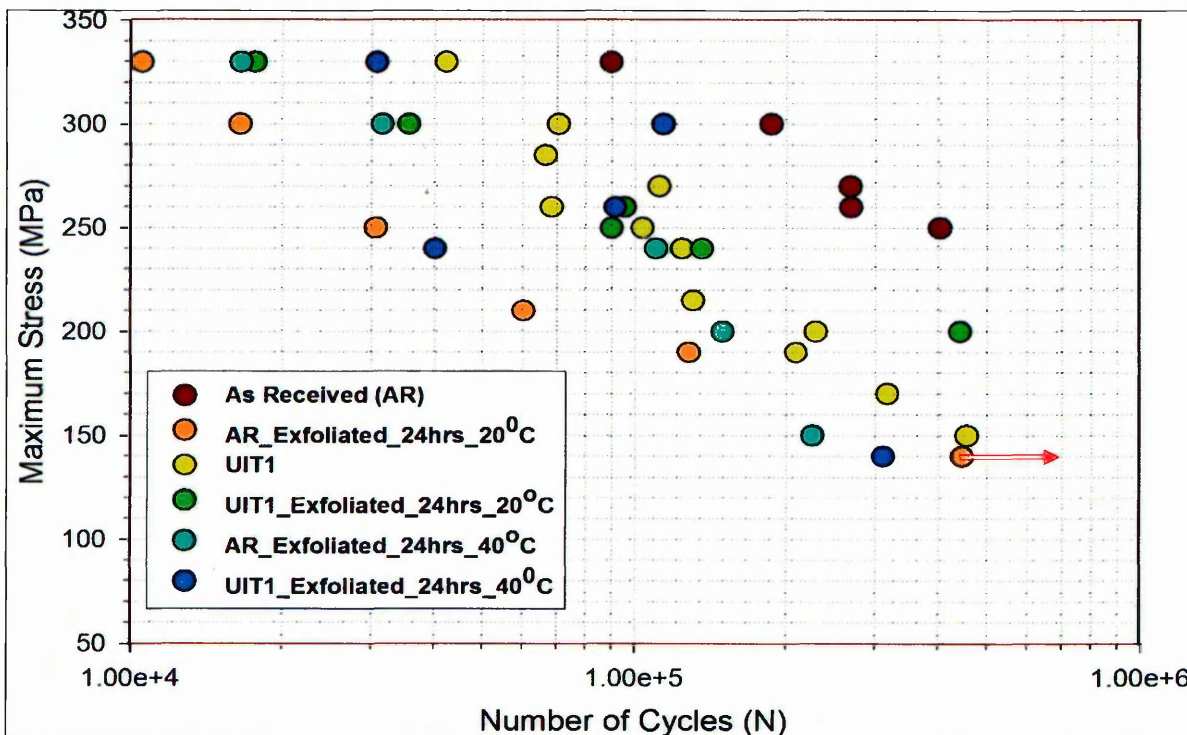
Figure 80: Low Cycle Fatigue regime for different surface treatment conditions.

8.2.3 High Cycle Fatigue Curves

Figure 81 shows the Stress-life plot in various exfoliation conditions. It is clear that the AR AA 2024-T351 alloy shows high fatigue life with a fatigue limit of about 240MPa. It was observed that by subjecting the AR specimen to UIT condition, the fatigue life of the samples is reduced by a factor of 3. The reason for this is considered to be due to the location of crack initiation, which originates from the edge of the sample, see discussion in **Section 8.2.1**.
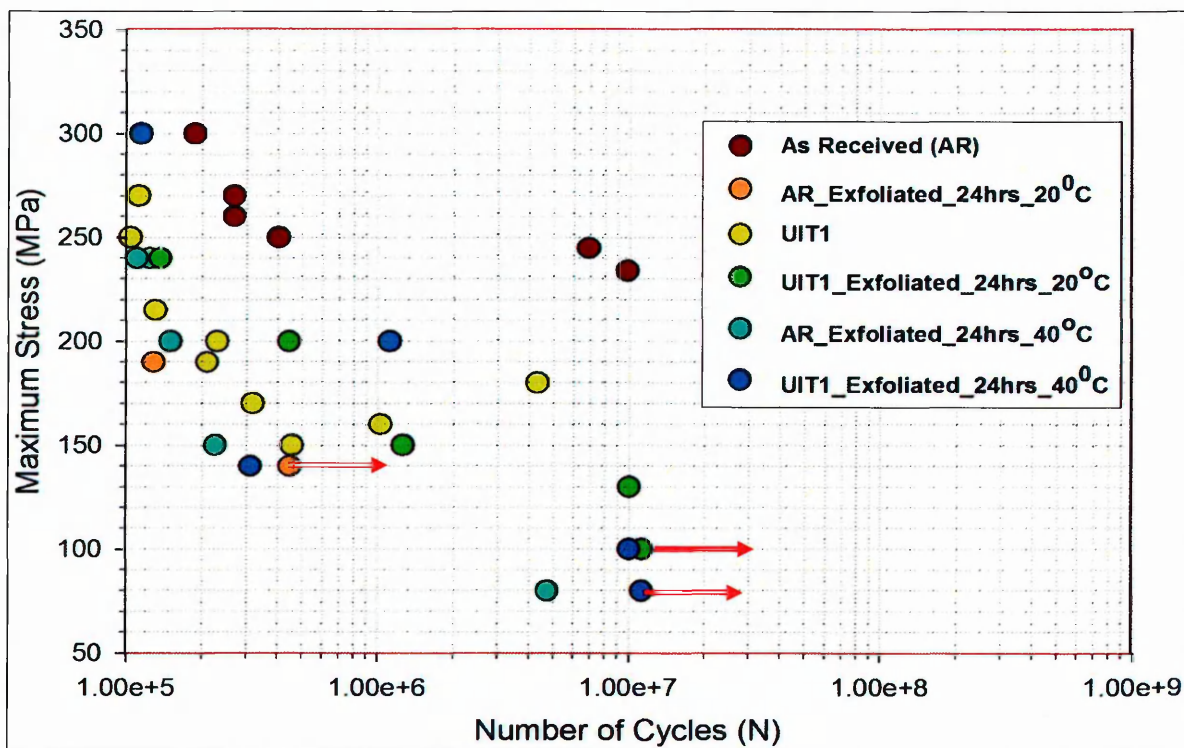
Figure 81: High Cycle Fatigue regime for different surface treatment conditions.

In **Figure 81**, it is noticed that the points of failure are scattered in a significant band. For example, UIT1_24_40^{0}C data points cycles in a bandwidth between 140MPa to 300MPa for 1e^7 fatigue life cycles. This is shifting the HCF regime behaviour more like LCF where the failures typically tend to occur as a result of flaws such as voids in the sample. Exfoliation corrosion, being localised, the pit density plays a vital role failure of the samples. However, it is noticed that the maximum damage occurs at the initial condition (AR_24_20 ^{0}C).

8.3 Exfoliation Condition Number of Cycles Vs Number of Cycles

Figure 82 shows a plot of exfoliation condition as a function of number of cycles to failure. It is noted that AR samples tend to fail at much lower number of cycles when compared to UIT samples suggesting an improvement in fatigue life of treated samples. This phenomenal influence on fatigue life is discussed in the next section.
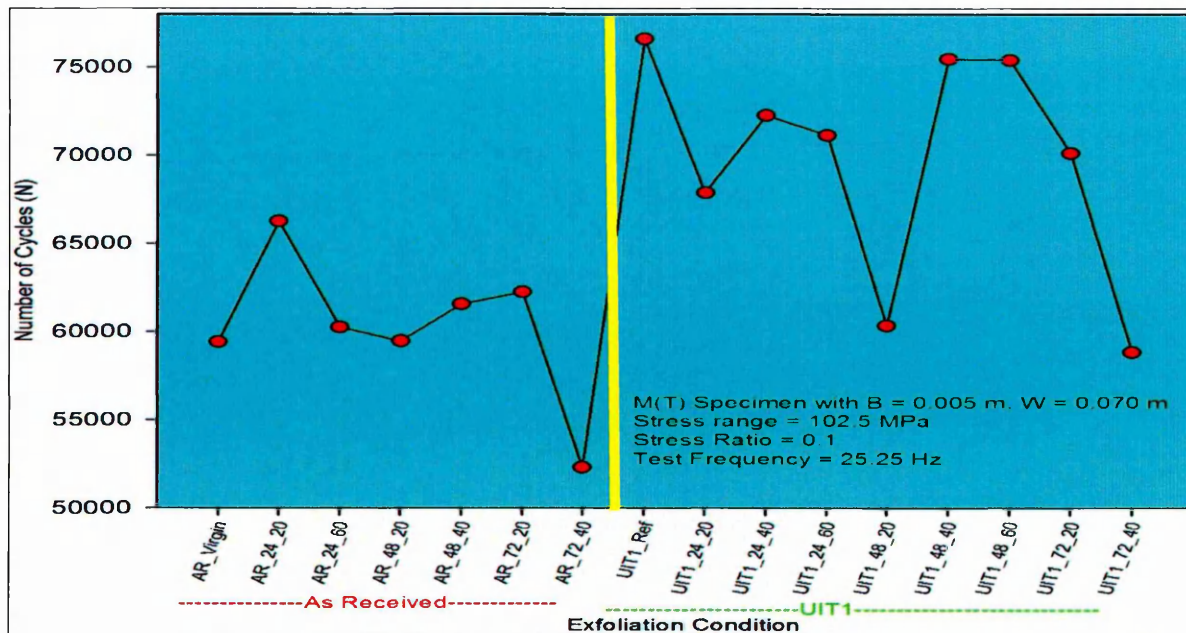
Figure 82: Various exfoliation conditions as a function of number of cycles to failure for AA 2024 T351. The above results are plotted from the data of fatigue crack growth analysis.

8.4 Crack Growth Analysis

8.4.1 Crack Propagation

In fail-safe design approach, the growth kinetics of Fatigue Crack Growth (FCG) is of crucial significance to material resilience. The corrosion fatigue characteristics on pre-exfoliated specimens in aluminium alloy 2024 T351 is established at various exfoliation time periods and temperatures (**Refer Table 1, Chapter 4**). As Stated in **Sec 4.5.5.2**, instantaneous crack lengths were measured from the first detectable crack and thereafter every 5000 cycles using a high resolution travelling microscope according to ASTM standards E647. For understanding of the process certain phenomena, UIT1 crack propagation photo-microscopic images are presented below.
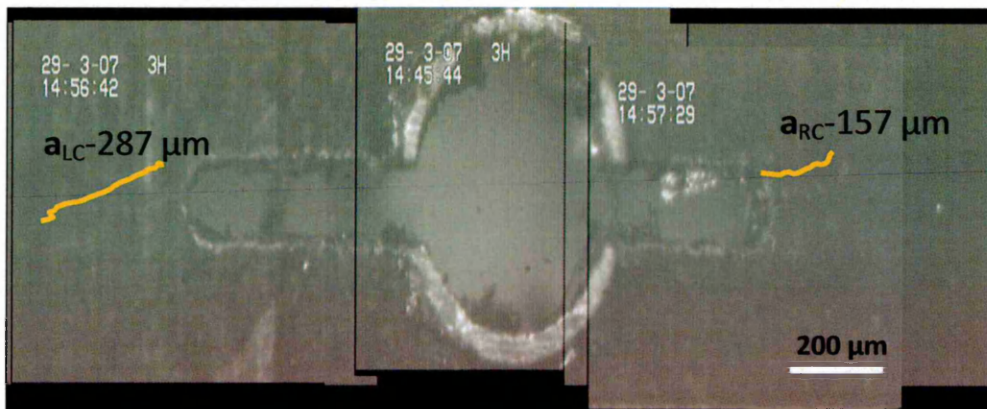
Figure 83: First possible detectable crack for UIT 1 - 25000 cycles.

113

Figure 83 show the first detectable crack recorded using Photo Microscopy (PM) method. It is observed that the crack propagation from the two branches of the notch as shown in **Figure 83** is dissimilar. For example, at 25000 cycles, the crack length on the left side of the notch (a_{lc}) was measured to be 287 µm where following crack path on the right side of the notch, the crack length a_{rc} was found to be 157 µm.
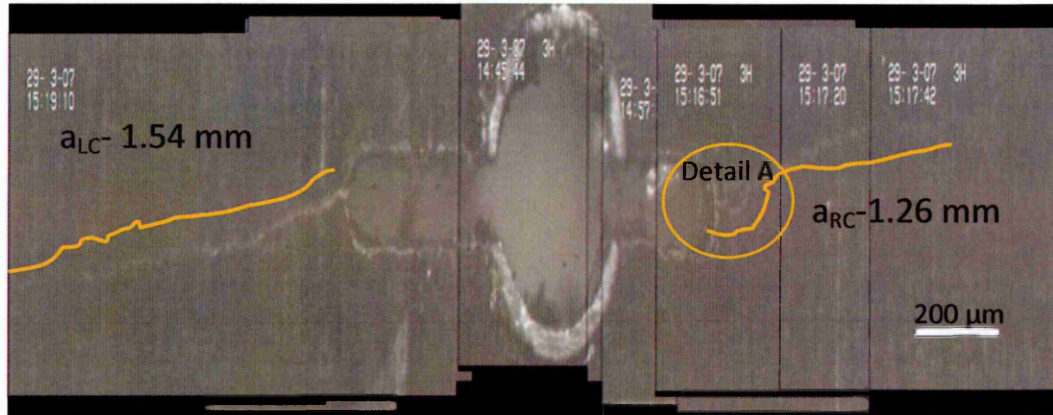
Figure 84: Crack path after 40000 cycles.

At 40000 cycles, this variation in crack length between left and right side of the notch was still evident. Upon closer look on the right side of the crack path as shown in **Figure 85**,
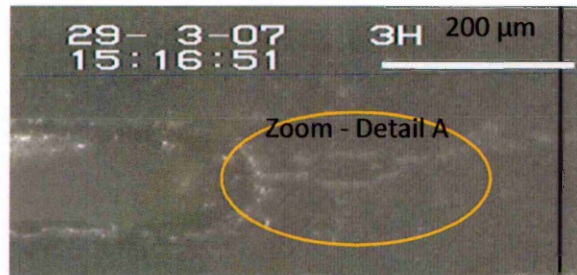
Figure 85: Crack deviation/bifurcation visible in the crack path on the right side of the notch.

Detail A, a deviation in crack path was observed as the crack no longer propagated in the direction normal to the applied far-field stress. However, due to the quality of the image, it is difficult to explain whether it is bifurcation of the crack path along a defect or secondary phase particle. However, this phenomenon explains the difference in crack length between left and right side of the notch.

114
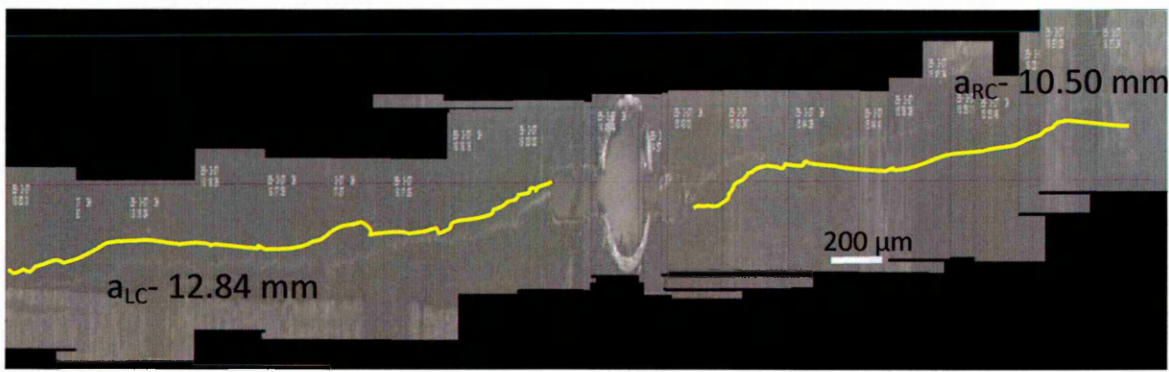
Figure 86: Final photo microscopic image analysis before failure – 75000 cycles.

Figure 86 shows the final photo microscopic analysis images taken for UIT1 crack propagation test before failure occurred at 76572 cycles. The measurements of the crack are 12.84 mm and 10.50 mm, left and right respectively.

8.4.2 Fatigue Crack Growth (FCG) Analysis

To compare the growth rate data for the various conditions (**Refer Table 1, Chapter 4**), plots of crack length versus number of cycles and their respective crack propagation rate,

$$\frac{da}{dN}$$

, dependence on stress intensity amplitude, ΔK, are discussed in this Section. It should be noted that the observed scatter in crack growth rates of pre-exfoliated specimens is characteristic of these tests [150,151]. The FCG analysis focuses on the effect of a varying stress intensity factor while keeping the stress ratio constant during constant amplitude loading. The lines marked on the graphs shown in **Section 8.4.2.1** indicate the treated strips of 10 mm in thickness and were 10 mm apart from the centre of the notch and marked on either side of the notch as explained in **Section 4.5.4.1.2**.

8.4.2.1 FCG dependence on exfoliation corrosion of AR AA 2024 T351

In **Figure 87**, it is quite evident that the fatigue crack propagation follows a similar trend until it reaches the exfoliated strip according to various conditions mentioned in the graph. In **Figure 87**, AR, AR_24_20, AR_48_20 and AR_72_20 specimens are compared. It is quite evident that at about 52000 cycles, the crack length, a, of all the specimens reaches the exfoliated strip. As this strip is exfoliated according the various conditions, it is evident that the all the exfoliated specimens showed failure within the exfoliated strip where as the As-Received AA 2024 T351 failed beyond this strip. This clearly exhibits the effect of exfoliation corrosion. In comparison to AR specimen, a faster crack growth is also noticed in exfoliated specimen as shown in **Detail A, Figure 87**.
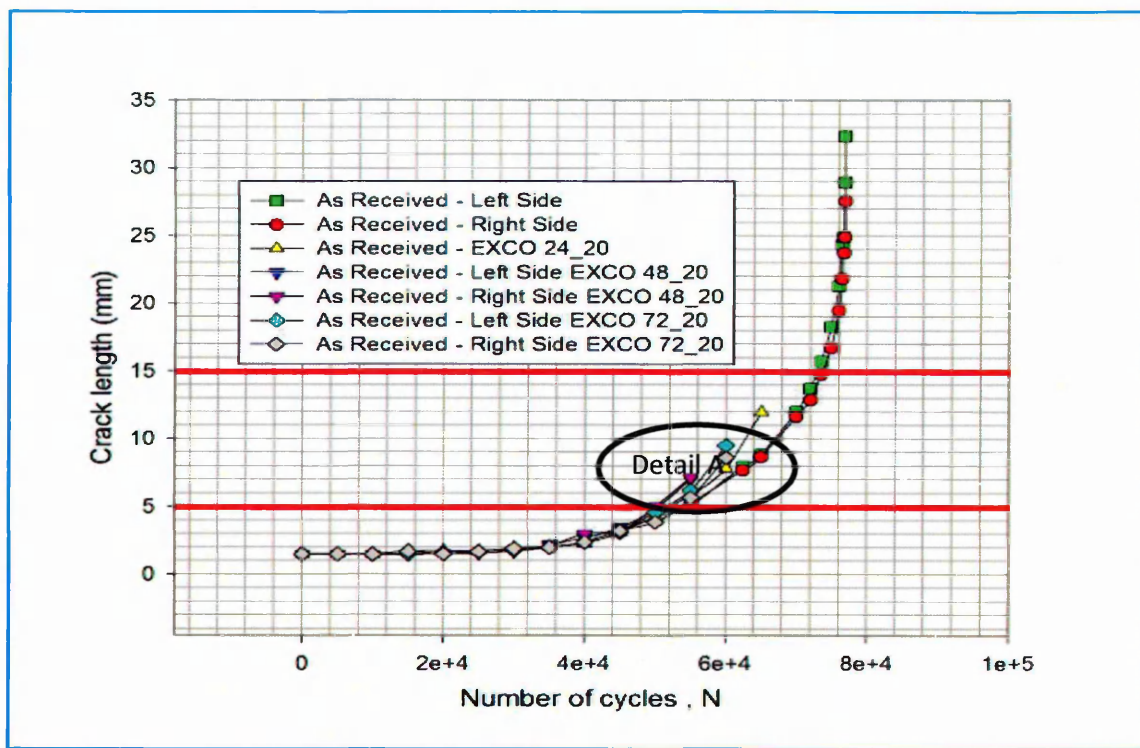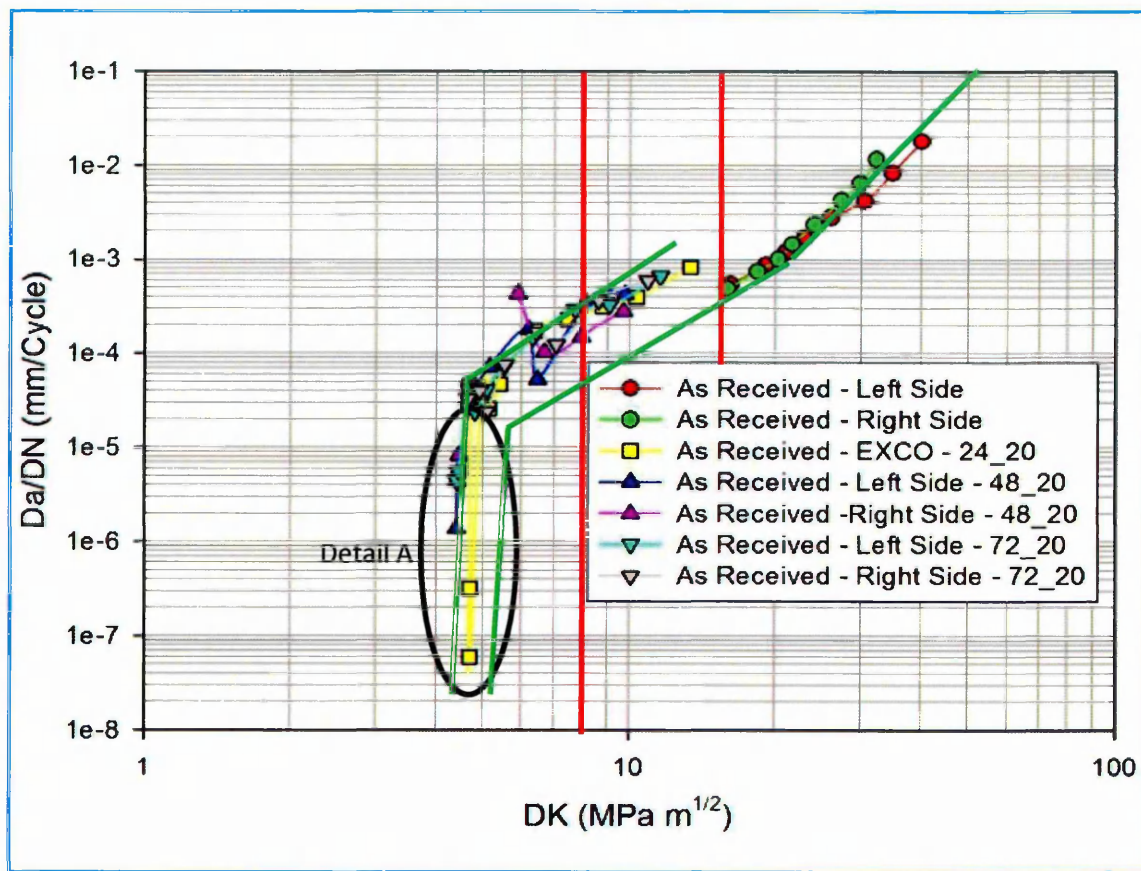
Figure 87: Crack length (a) versus number of cycles (N) graph for AR AA 2024 T351 at exfoliation time of 24 hours to 72 hours in steps of every 24 hours at ambient conditions (20 ^{0}C).

Figure 88 shows a graph of crack propagation rate, $\dfrac{da}{dN}$, dependence on stress intensity amplitude, ΔK, for AR, AR_24_20, AR_48_20 and AR_72_20 specimens. On first look it is clearly visible that all exfoliated samples failed at much lower stress intensity levels than As-Received specimen. It is also noted that exfoliated samples exhibited failure in stage II (**See** 2.3.2.5.2) of stable crack propagation which lies within the exfoliated strip. In stage I regime, slower crack growth is expected where microstructural effects are large. However, as the specimens are also subjected to exfoliation corrosion, hydrogen embrittlement effects are also large. Thus, a faster crack propagation rate is observed in stage I regime as shown in **Detail A, Figure 88**. However, due to the nature of the effect of exfoliation time is not clearly understood.

116

Figure 88: FCG graph of AA 2024 T351 at exfoliation time of 24 hours to 72 hours in steps of every 24 hours at ambient conditions (20 ^{0}C).

8.4.2.2 FCG dependence on exfoliation corrosion of UIT AA 2024 T351

In **Figure 89** & **Figure 90**, the effect of UIT condition is evident as the UIT conditioned sample exhibited retardation in crack length value, a, when AR and UIT specimens are subjected to same number for cycles. However, UIT1_24_60 specimen showed no retardation but followed a similar trend to AR specimen failing within the UIT conditioned strip. This suggests that the heating of the sample at 60 ^{0}C for 24 hours has affected the beneficial compressive residual stresses induced during the time of UIT process.
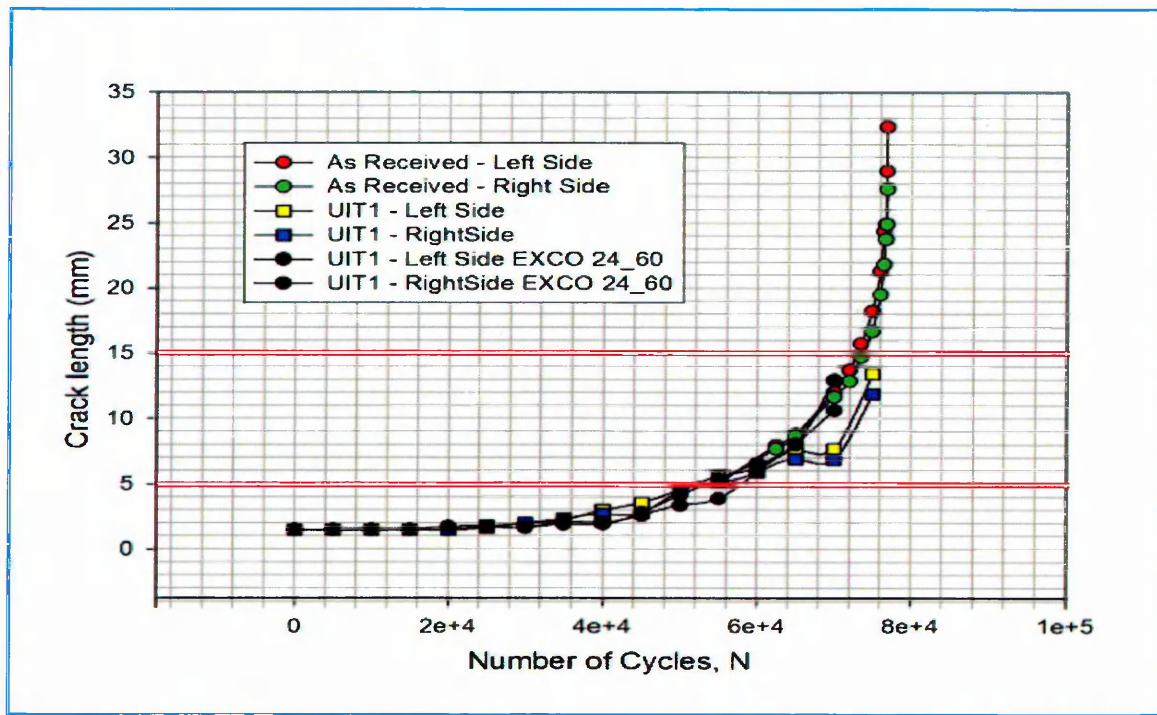
Figure 89: Crack length (a) versus number of cycles (N) graph for UIT conditioned AA 2024 T351 at exfoliation time of 24 hours and at temperatures of 20 ^{0}C and 60 ^{0}C.
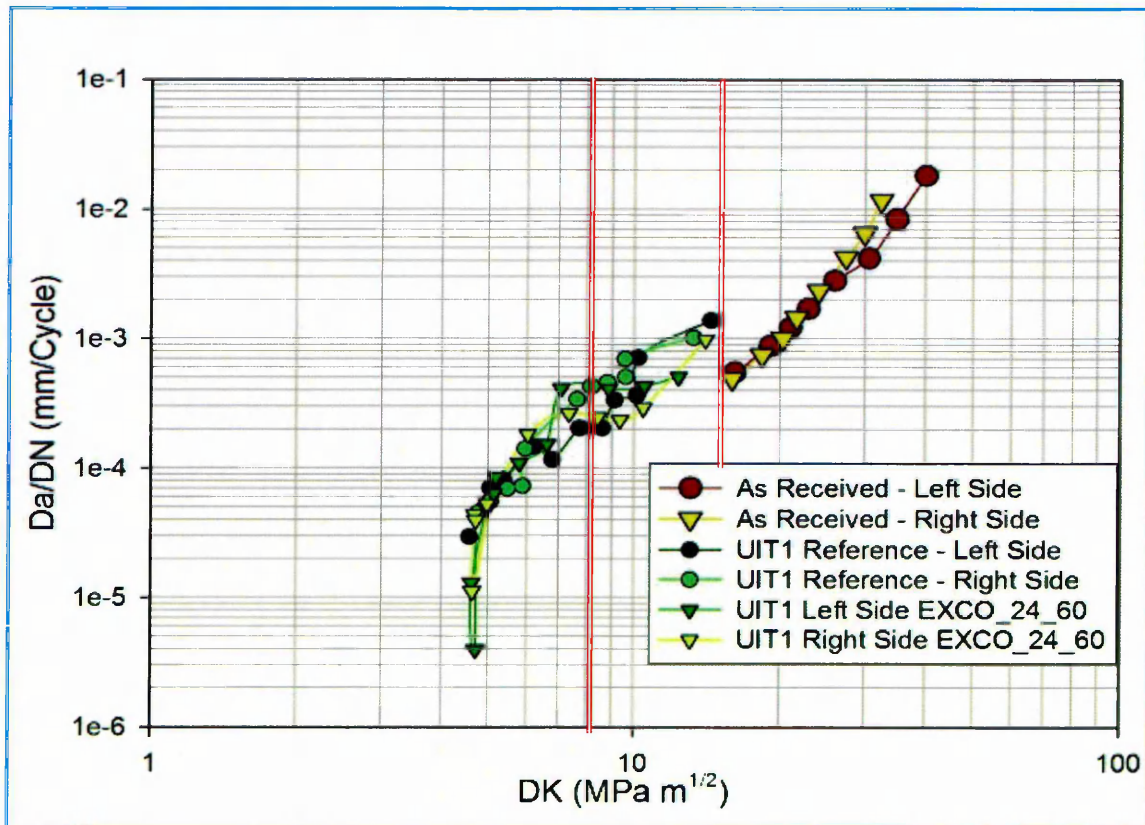
Figure 90: FCG graph of UIT conditioned AA 2024 T351 at exfoliation time of 24 hours and at temperatures of 20 ^{0}C and 60 ^{0}C.

Appendix B consists of crack length, a, versus number of cycles, N, data for the various conditions (**Refer Table 1, Chapter 4**). Appendix C consists of their respective crack propagation rates, $\frac{da}{dN}$, dependence on stress intensity amplitude, ΔK.

8.5 Chapter Summary

The fatigue life of UIT AA 2024 T351 is strongly affected by the pitting and localised corrosion as it is noted that there is a massive bandwidth for most of the samples when they fail. This further suggests that the AA 2024 T351 is strongly affected by pit density. Secondly, it is further identified that UIT condition at the edges of the sample is configuring AA 2024 T351 more susceptible to crack initiation regions. A slight improvement In Low Cycle Fatigue (LCF) life is observed for pre-exfoliated and UIT conditioned sample but not for UIT conditioned samples only. Little effect is observed for either treatment in the High Cycle Fatigue (HCF) region.

Fatigue crack propagation of exfoliated specimens exhibited faster crack propagation than As-Received specimens. UIT specimen did show retardation in crack propagation, but the samples failed within the treated strip due to various environmental effects. Increasing temperatures affects the compressive residual stresses. It is also noted that crack deviation can happen even upon the crack tip reaches a secondary phase particle.

CHAPTER 9

Summary of Results

9.1 Summary of the Results

In the previous chapters, a detailed description of the results obtained during these studies, was given. This chapter will discuss the main results. It will furthermore provide a snapshot of the conclusions.

In this study, a novel Severe Plastic Deformation (SPD) technique namely Ultrasonic Impact Treatment (UIT), was investigated in detail with respect to an aggressive corrosive environment. Here, a short overview of the results obtained will be given.

9.1 Exfoliation Corrosion

9.1.1 Current Practice

One of the existing industrial process to tackle corrosion and corrosion initiated fatigue cracks is grinding. Corroded layer is ground off from the component. This process is pursued until the component cross-sectional area does not reduce by more than 10 % of the nominal thickness of the component as shown in **Figure 91**. This affects the fatigue life of the component and thus reducing, for example the number of flying hours of an aircraft. In this research the nominal thickness of the AA 2024 T351 specimen was 5 mm. Following industrial standards, a tolerance of 10 % of the nominal thickness allows only 500 µm upon which the specimen is regarded redundant. Referring to **Figure 45**, At 20 ^{0}C, UIT conditioned specimens exhibited a remarkable resistance to exfoliation corrosion for exfoliation time up to 72 hours. However, the As Received specimens showed a significant corrosion attack.
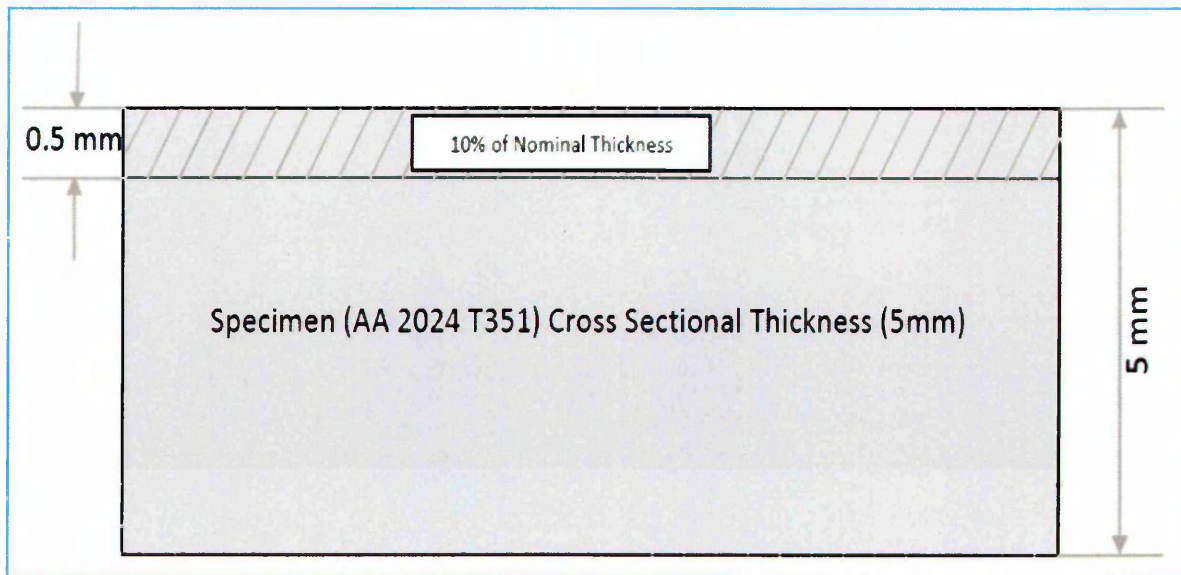
Figure 91: Schematic diagram showing current industrial practice of grinding.
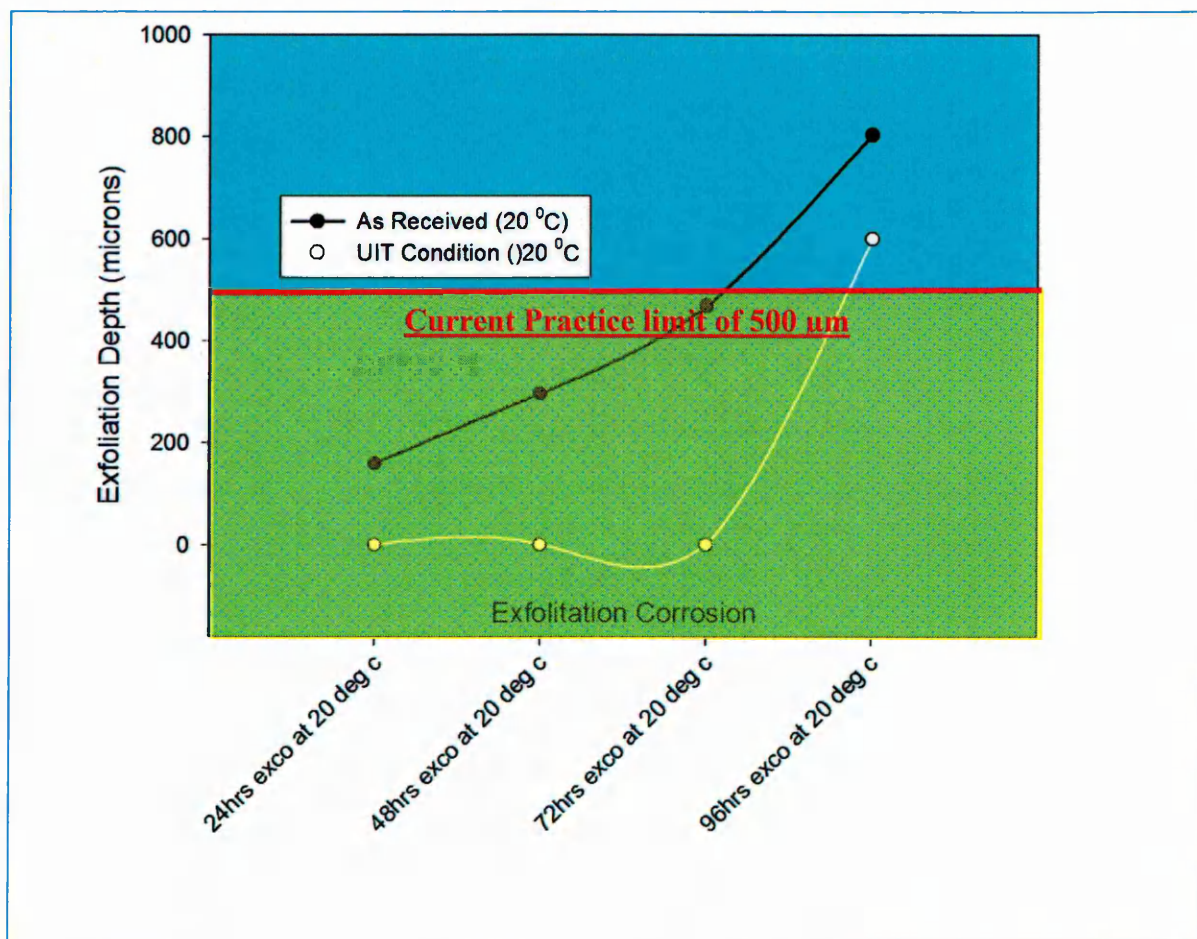
Figure 92: Results of exfoliation corrosion tests at 20 ^{0} C exhibiting corrosion resistance of UIT conditioned specimens.

121
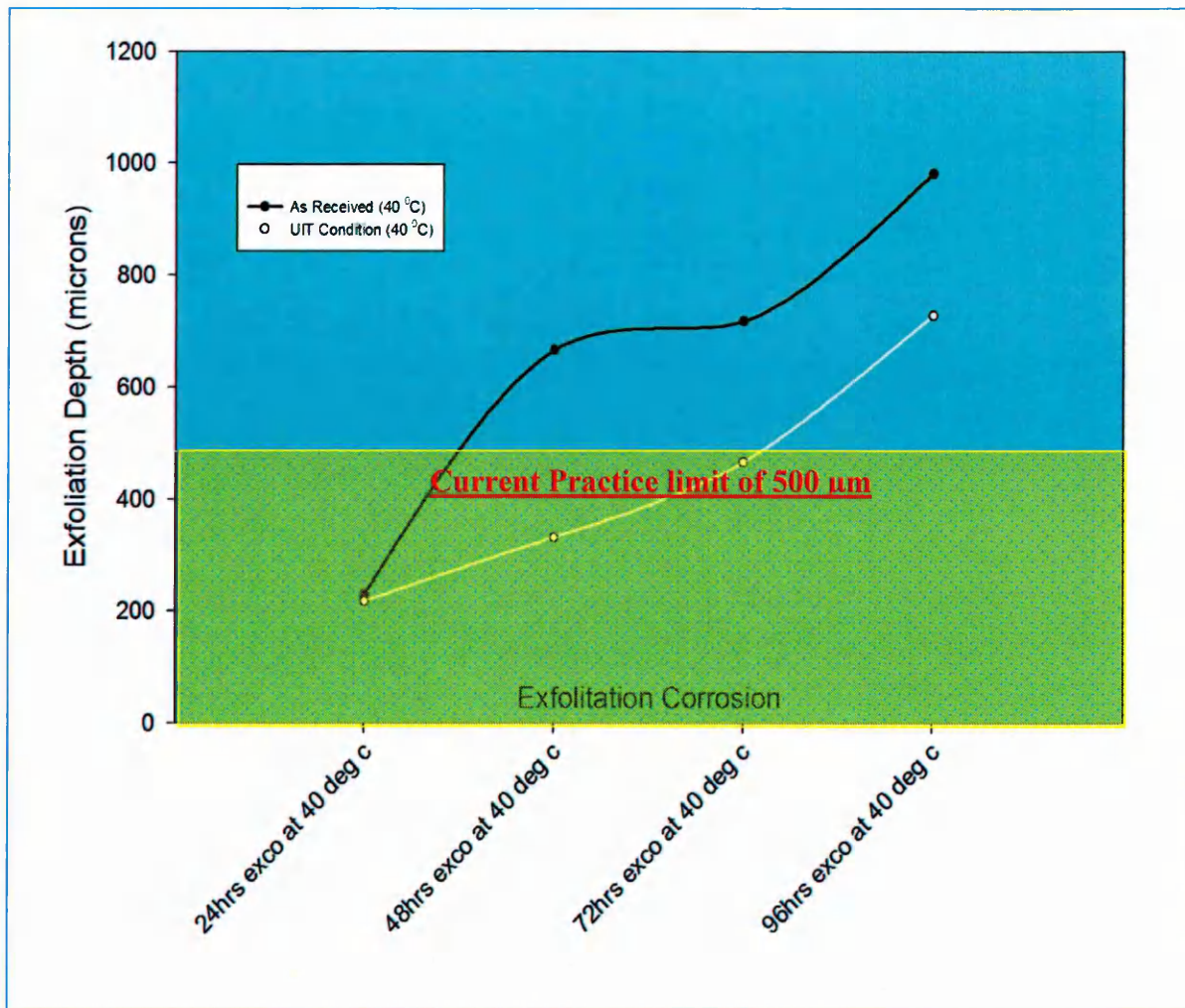
Figure 93: Results of exfoliation corrosion tests at 40 ^{0} C exhibiting corrosion resistance of UIT conditioned specimens.

Figure 92 and **Figure 93** exhibits the effect of UIT against corrosion attack. UIT retards the loss of thickness in comparison to As Received AA 2024 T351.

9.1.2 Effects of Testing Parameters

9.1.2.1 Effect of Time

Referring to **Figure 92**, it is noticed that UIT exhibited excellent corrosion resistance. For UIT conditioned specimens, the process pitting (which is visible under microscopic examination from the surface) does not initiate until the specimen accrues more than 72 hours of exfoliation corrosion testing. However, for AR specimens, pitting is initiated within first 4 hours of the exfoliation immersion tests as shown in **Figure 94**. This phenomenon can be ascribed to nano-crystallisation effect which the UIT conditioning produces as discussed in **Section 3.4.2** however it is still not completely understood as the pitting

potential of UIT conditions specimens were slightly higher than the AR specimens as discussed in **Section 5.3.1**.
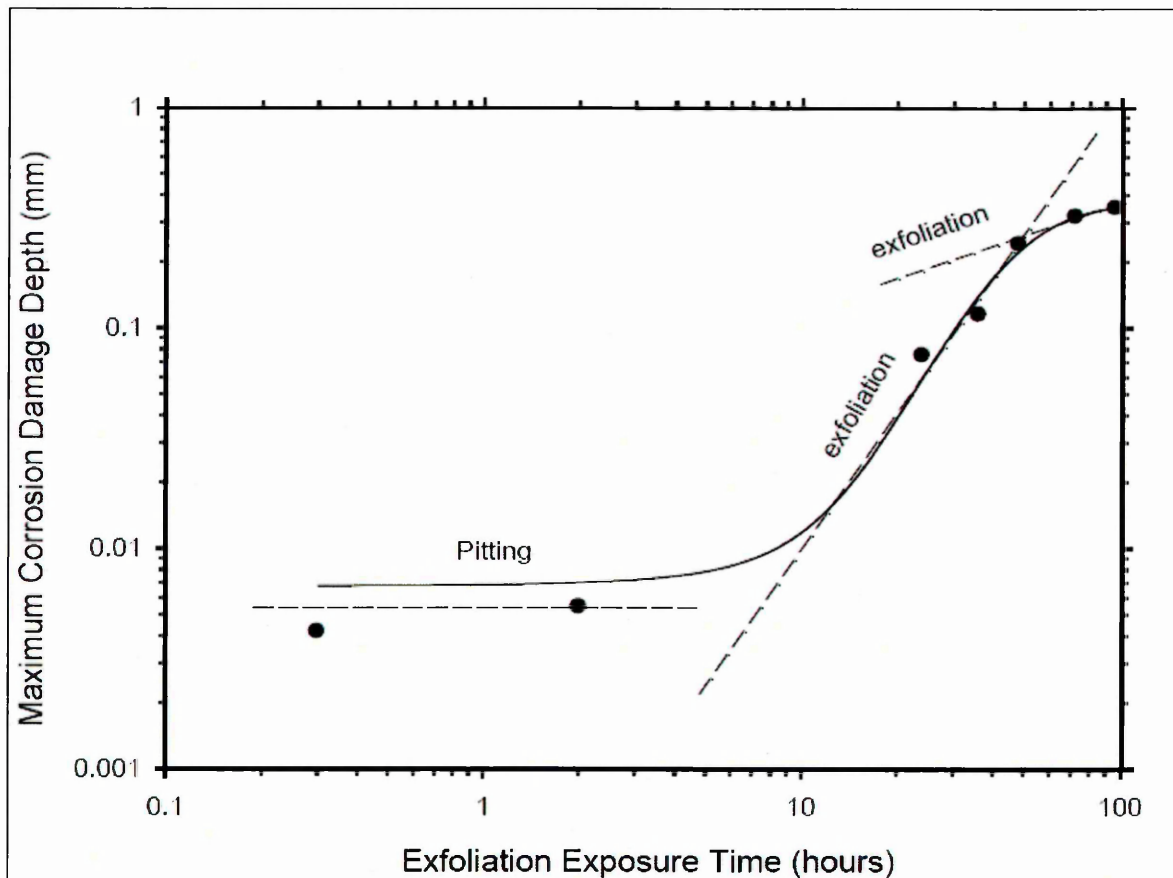
Figure 94: Schematic graph showing transition from pitting to exfoliation corrosion with respect to time.

9.1.3 Copper Enrichment

Exfoliation corrosion enriches the secondary phase particles and enriches at the near surface of the alloy surface. One of the beneficial effects of UIT conditioning is creation of homogeneous surface and at the near surface region of the alloy [152]. UIT conditioned specimens reduce this copper enrichment effect and preserve the homogeneity of the specimen surface.

9.2 Fatigue

Crack growth initiates at the most susceptible grain on the surface of a component at a location where the most favourable conditions exist (stress raisers) such as a simple scratch, secondary phase particle, pit, grain orientation, inclusions or section changes. In a F.C.C structure, for stage I, the crack propagation initiates at an angle where maximum shear stresses exist which is approximately 45^0 to the loading axis. As the crack propagates to

123

stage II, the growth is more or less normal to the far-field stress. At stage III, a very high unstable growth is noticed.

9.2.1 Effects of Nanocrystallisation

As discussed in **Section 3.4.2**, UIT process modifies the surface of AA 2024 T351 by producing a nanocrystalline structure, nano- crystal grain in (6-8) nm and parallel micro bands as wide of (15-20) nm in certain orientation. This process of grain refinement takes places by grain sub division due to continuous impact of the peener head. Thus, this process of sub division of grains creates a network of sub grains which are highly oriented randomly. This random nature of nano-scale grain reduces the crack propagation as the crack path has to face more grain boundaries, as shown in **Figure 95**.
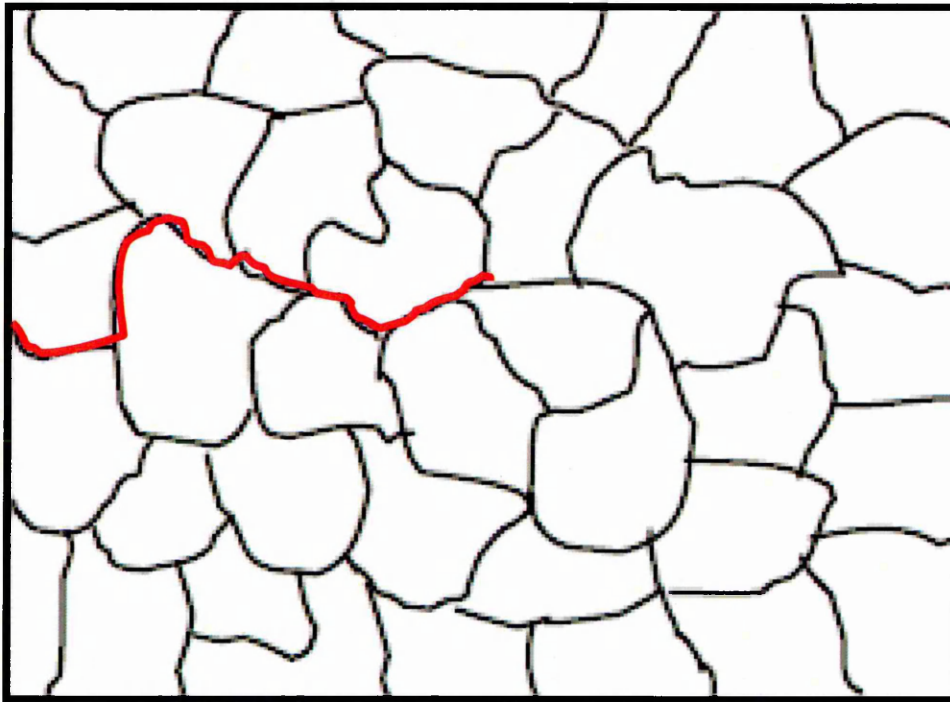
Figure 95: A Probable crack path showing the effect of disoriented sub grains due to UIT process.

9.2.2 Effects of Residual Stresses

Residual stresses developed from UIT process [152] should be sufficient to mitigate some of the fatigue life lost due to the pitting and general corrosion. Fatigue crack growth analysis exhibited retardation in crack propagation rates as soon as the crack front reached the modified strip. Once again, observations from these FCG data would imply that UIT should extend fatigue life of the pre-exfoliated specimens. **Figure 96** depicts the general representation of the technical effects caused by UIT in samples at least 25 mm thick.
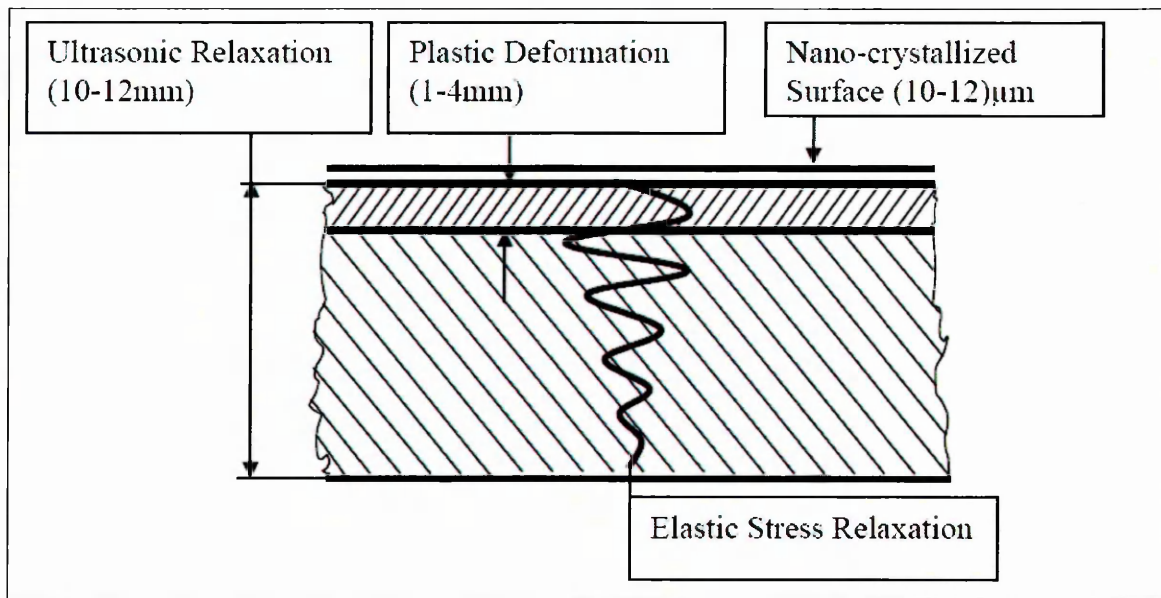
Figure 96: Physical zones of UIT effect on material properties and condition of Al2024 T351.

Figure 78 indicates that UIT can substantially decrease the fatigue resistance on As-Received specimens. However, UIT can have a significant effect on increasing the fatigue resistance of exfoliated material. FCG data further gave a substantial confirmation that the enhancement is due to the development of almost similar compressive residual stresses throughout the crack path. The technology requires further investigation towards optimisation.

9.2.3 Effect of Hydrogen Embrittlement

Hydrogen effects on the degradation of the alloy are noted. For all the exfoliated specimens, regardless of treatment, FCG was very unstable as soon as the crack front reached the exfoliated strip. Almost all the samples failed within the strip except the As Received specimen. Thus, this indicates that the plain stress fracture toughness values (K_{IC}) would have been much lower than the As Received.

CHAPTER 10

Conclusions

From the experimental work conducted on the fatigue of AA 2024 T351 in both As Received and UIT condition, the following conclusions can be drawn:

- UIT surface treatment, followed by exfoliation corrosion have shown increased resistance to a reduction in mechanical properties, notably tensile and yield strength. Fractographic analysis further supported this finding by showing smaller average brittle failure depths for UIT specimens when compared to AR specimens. SEM analysis of AR samples (without exfoliation) showed a crystallographic contribution to the mode of failure where high density PSBs are formed and the initial failure exhibits a step format.

- It is observed that during exfoliation, hydrogen ingress and adsorption is more prominent at ambient temperatures for AR samples.

- A slight improvement In Low Cycle Fatigue (LCF) life is observed for pre-exfoliated and UIT conditioned sample but not for UIT conditioned samples only. Little effect is observed for either treatment in the High Cycle Fatigue (HCF) region.

- Fatigue crack initiation occurred from the edges for all samples.

- Fatigue crack propagation of exfoliated specimens exhibited faster crack propagation than As-Received specimens. UIT caused retardation in crack propagation rate in

AR samples but not in corroded samples. Failure of pre-exfoliated, UIT treated samples failed within the treated strip. It is also noted that crack deviation can occur when the crack tip reaches a secondary phase particle.

- Nanocrystallisation generates uniformity of the surface which refines the secondary phase particles and helps mitigate crack initiation sites.

CHAPTER 11

Future work

The field of study and SPD techniques are both interesting and complex. To comprehend the complexities of this environmental assisted failure research on AA 2024 T351, and the influences of UIT process on the alloy in the context of fatigue, the following suggestions are made:

Residual Stresses:
It is recommended that residual stress analysis of pre-exfoliated specimens should be performed. Future work should include in this department should include the following:-
   a) Identification of manufacturing scatter
   b) Effect of manufacturing
   c) Real-time determination of residual stress profile with loading cycles.

Real-time Corrosion Fatigue Analysis:
It is highly desirable that all the testing to be conducted in real-time analysis at higher temperatures as well. A better alternative method should be investigated in this case to measure the crack length in FCP analysis.

Optimisation of UIT Process:
Alternative UIT parameters should be investigated to determine whether UIT can improve corrosion fatigue performance in the same way in which it is known to improve air fatigue performance.

Scaling Effect:
The effect of specimen thickness should be investigated as the stringer panels of aircraft fuselage don't necessarily maintain similar cross-sectional thickness.

Hydrogen Embrittlement:
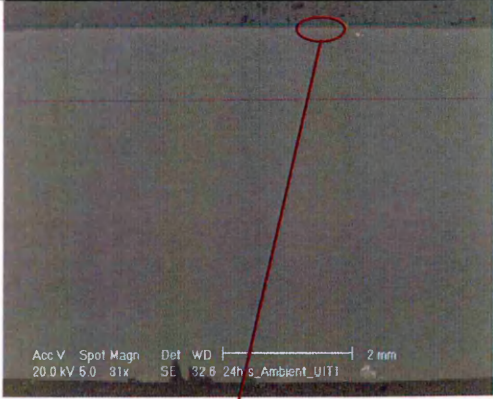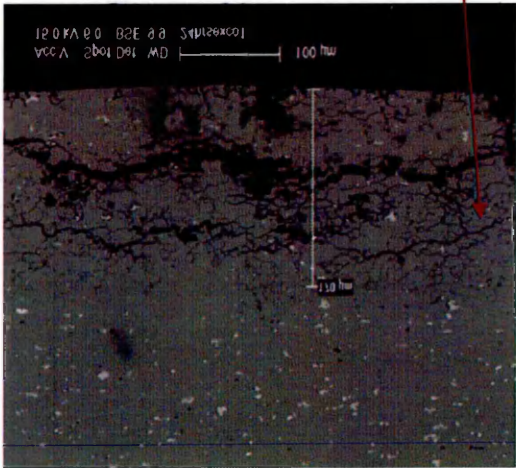
Plain stress fracture toughness (K_{IC}) values should be determined for both the conditions, namely UIT and As-Received specimens. This will give an estimation of the effect of hydrogen in the alloy.
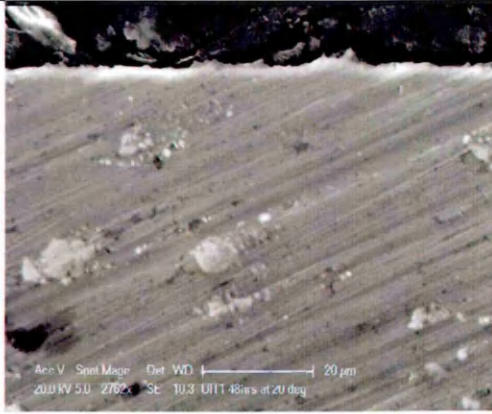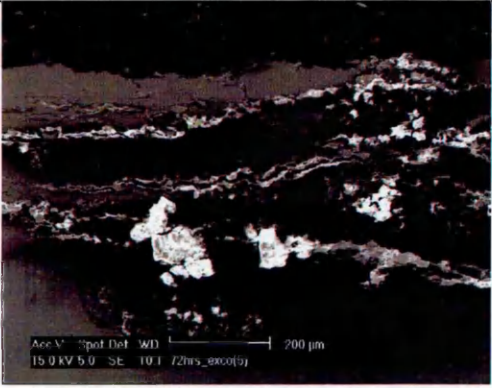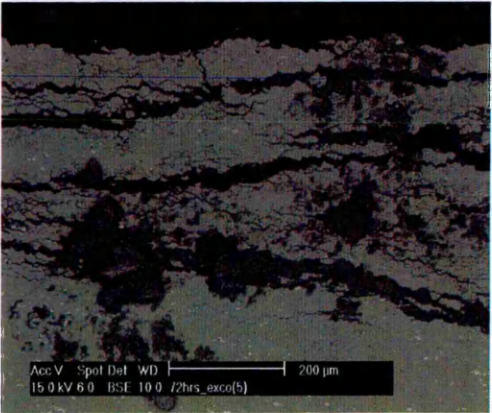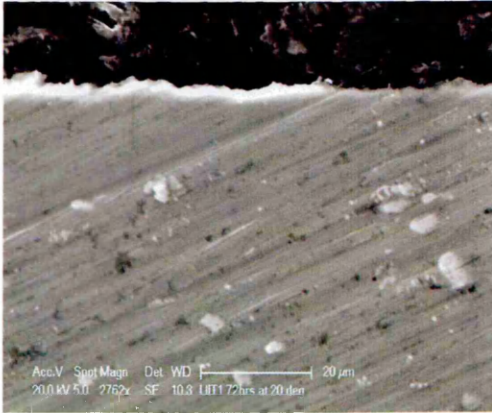
Appendix A

Coupon Testing

Introduction

G112-92(2003) & G34 standard guide for conducting exfoliation corrosion Tests in aluminium 2xxx Alloys was followed. The exfoliation solution comprises of 4M NaCl, 0.5M KnO_3 and 0.1M HNo_3 in 1 ltr of ionised water. The tests were performed at 4 different timescales (24hrs, 48hrs 72hrs and 96hrs) and at different temperatures (Ambient, 40° C, 60° C and 80° C).

Condition	As-Received	UIT1
24 hours at 20°C		
48 Hours at 20°		

72 Hours at 20°C

iii
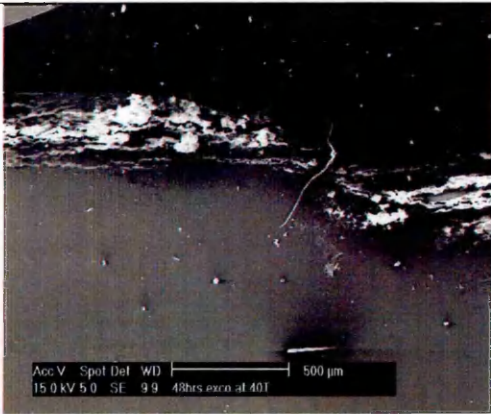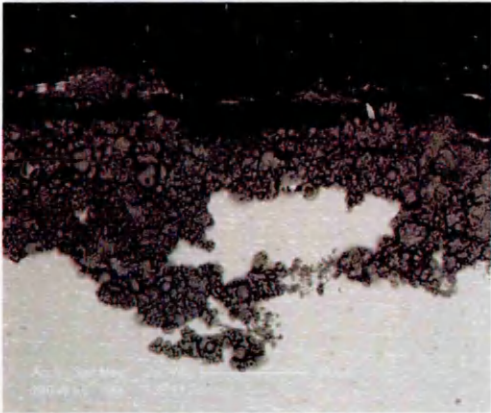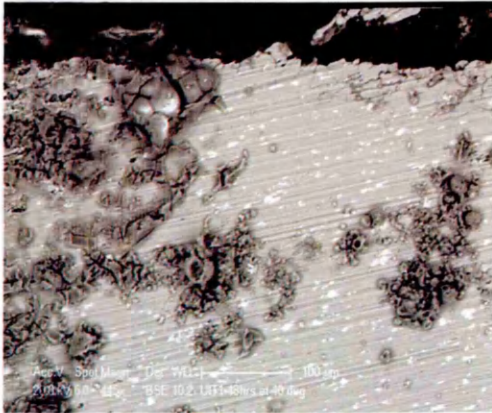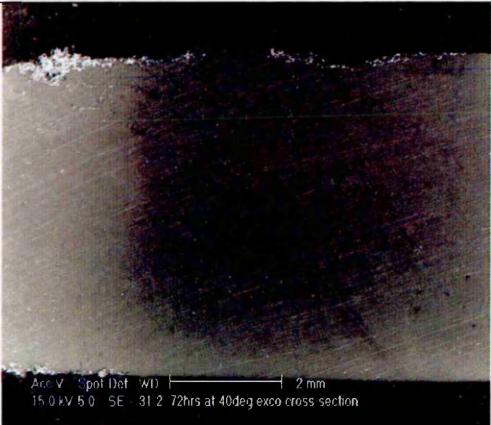
96 hours at 20°C		
24 hours at 40° C		

iv
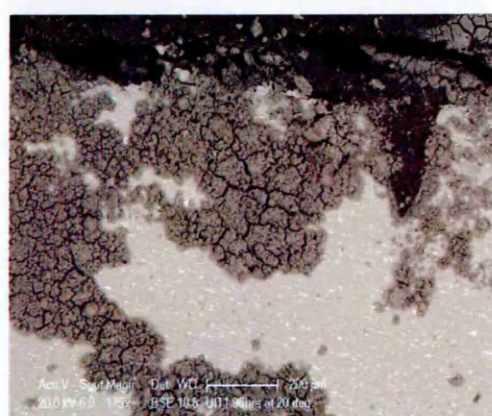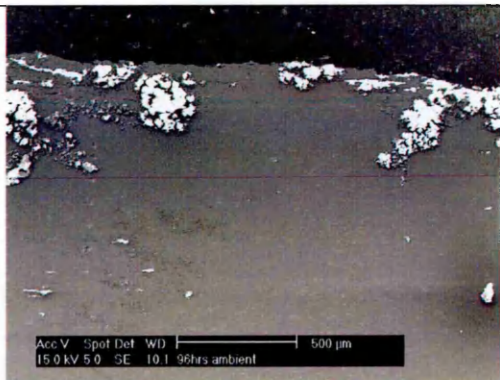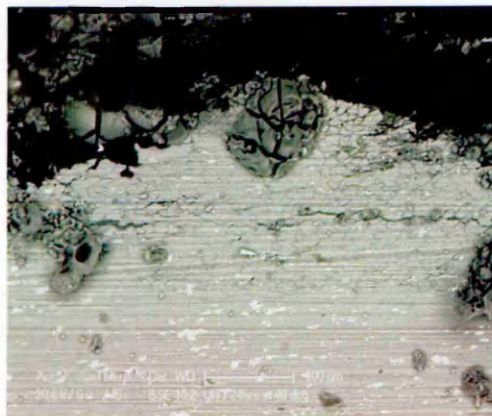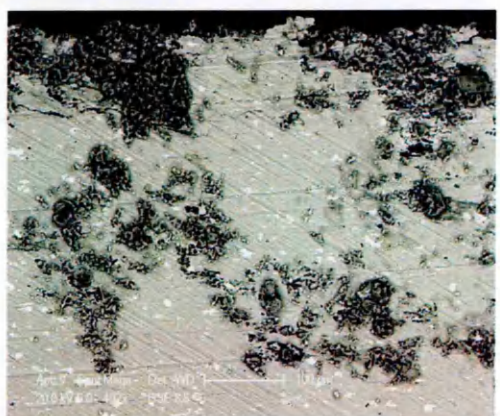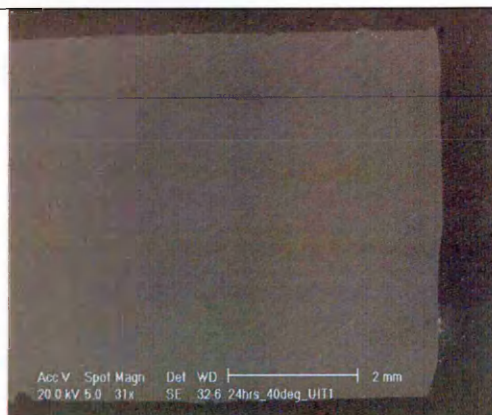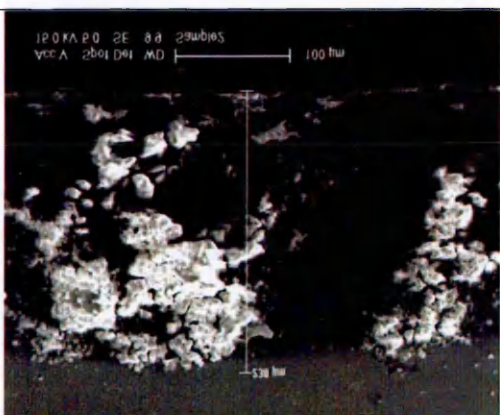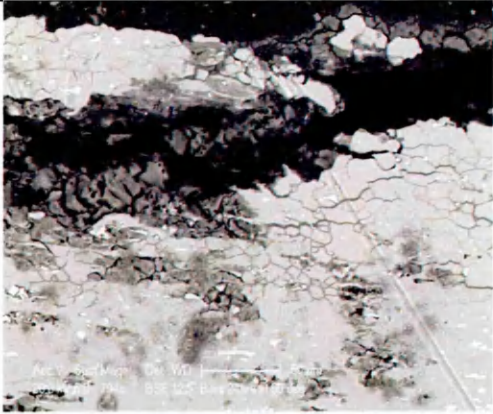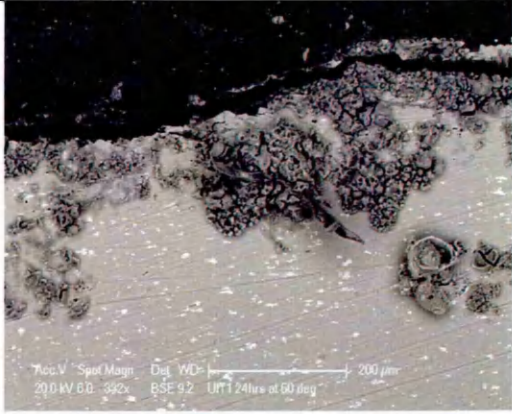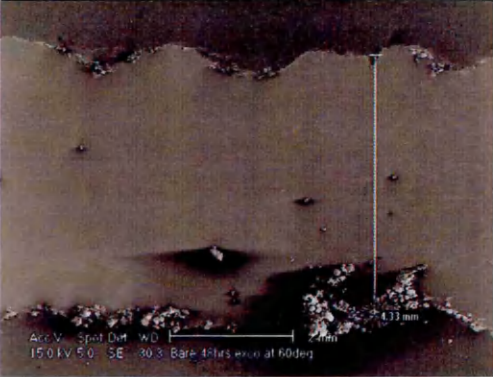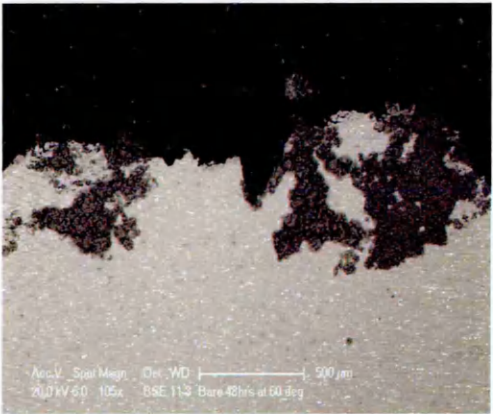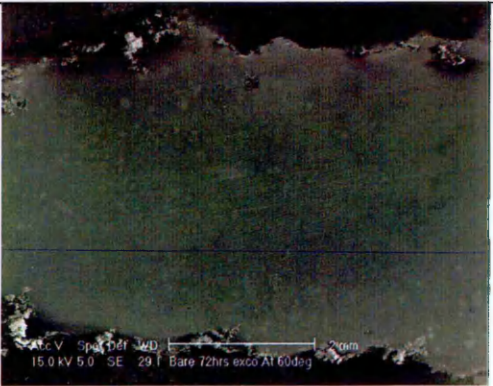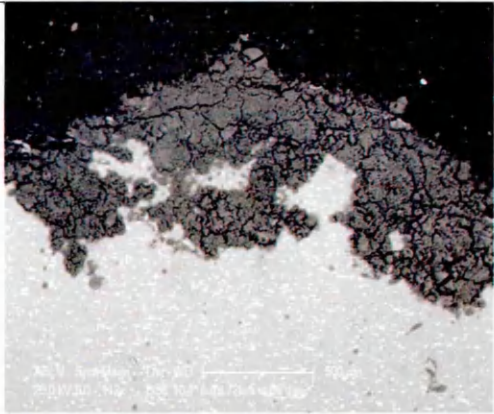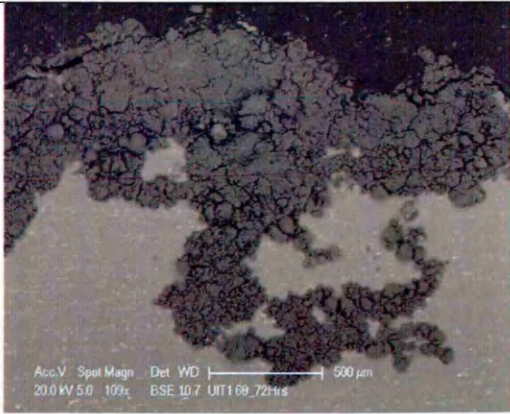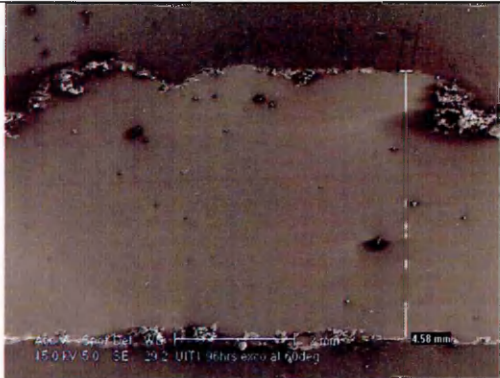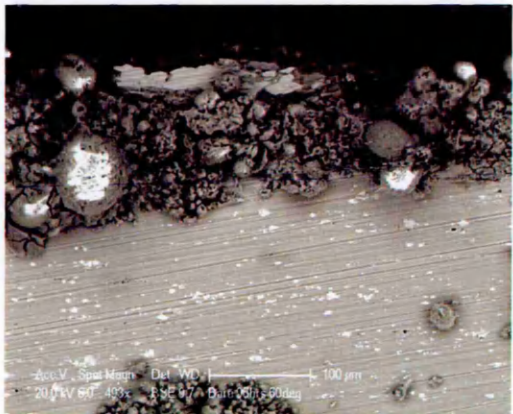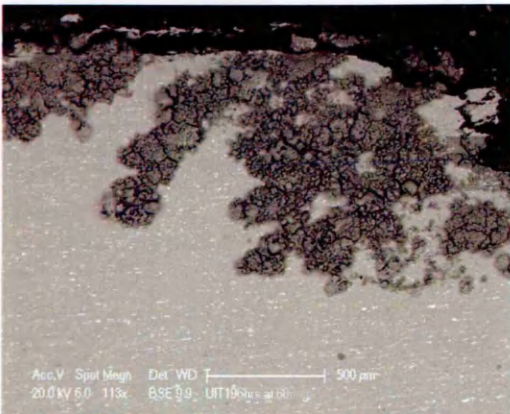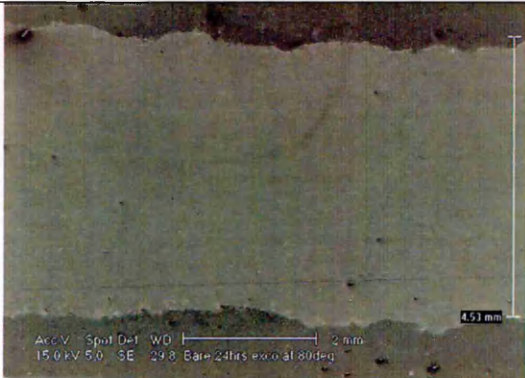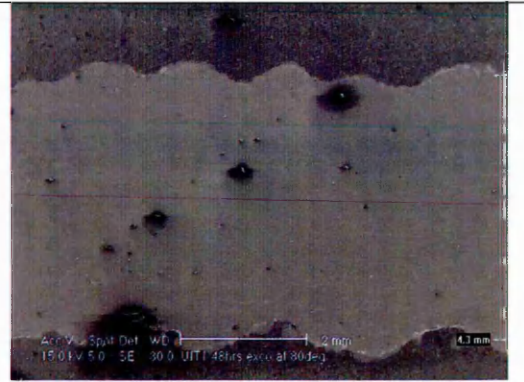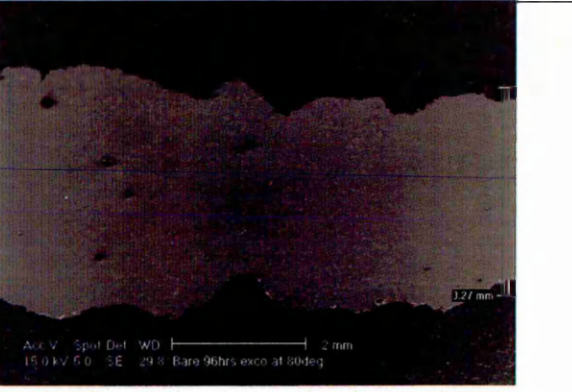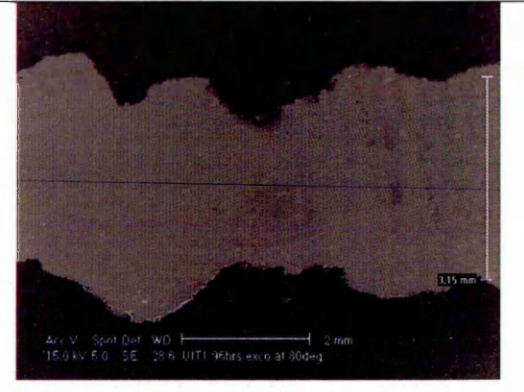
48 hours at 40° C		
72 hours at 40° C		

96 hours at 40° C		
24 hours at 60°C		

48 hours at 60°C	
72 hours at 60° C	

96 hours at 60°C	

24hours at 80°C	

48 hours at 80°C		
72 hours at 80° C		
96 hours at 80°C		

Appendix B

Crack Length versus Number of Cycles

1 Introduction

This appendix collates all the crack length versus number of cycle's graph for all the FCG test conducted on M (T) specimen.

Temperature Dependent Analysis

2.1 As Received

2.1.1 24 hours exfoliation at different temperatures - As Received
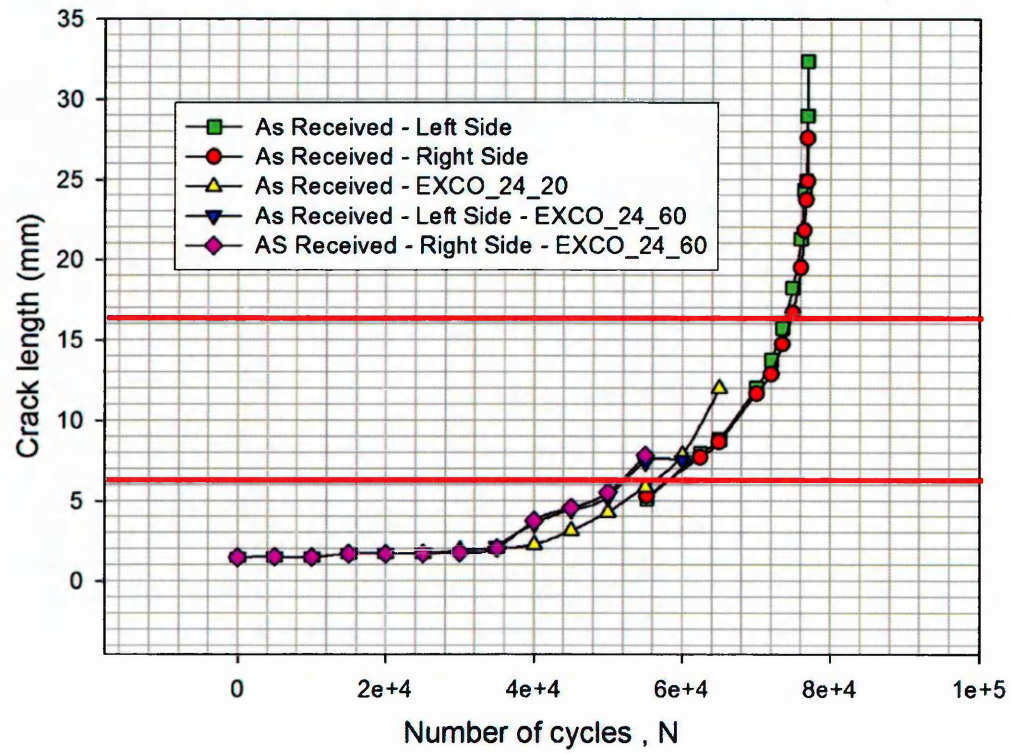
2.1.2 48 hours exfoliation at different temperatures - As Received

2.1.3 72 hours exfoliation at different temperatures - As Received

2.2 UIT1 Condition

2.2.1 24 hours exfoliation at different temperatures – UIT1

2.2.2 48 hours exfoliation at different temperatures – UIT1

3 Time Dependent Analysis

3.1 As-Received

3.1.1 20 ^{0}C exfoliation at different time - As Received

3.1.2 40 ^{0}C exfoliation at different time - As Received

3.1.3 60 ^{0}C exfoliation at different time - As Received

3.2 UIT Condition

3.2.1 20 ^{0}C exfoliation at different time – UIT1

3.2.2 40 ^{0}C exfoliation at different time – UIT1

Figure legend:
- As Received - Left Side
- As Received - Right Side
- UIT1 - Left Side
- UIT1 - RightSide
- UIT1 - Left Side - EXCO 48_40^0 C
- UIT1 - Right Side - EXCO 48_40^0 C
- UIT1 - Left Side - EXCO 72_40^0 C
- UIT1 - Right Side - EXCO 72_40^0 C

Y-axis: Crack length (mm)
X-axis: Number of Cycles, N

3.2.3 60 ^{0}C exfoliation at different time – UIT1

Appendix C

$$\frac{da}{dN} \text{ Vs } \Delta K$$

1 Introduction

This appendix collates all the FCP rates versus stress intensity factor for all the FCG test conducted on M (T) specimen.

2 Temperature Dependent Analysis

2.1 As Received

2.1.1 24 hours exfoliation at different temperatures - As Received

2.1.2 48 hours exfoliation at different temperatures - As Received

Figure axes: Da/DN (mm/Cycle) versus DK (MPa m$^{1/2}$)

Legend:
- As Received - Left Side
- As Received - Right Side
- As Received - Left Side EXCO 48_20
- As Received - Right Side EXCO 48_20
- As Received - Left Side EXCO 48_40
- As Received - Right Side EXCO 48_40
- As Received - Left Side EXCO 48_60
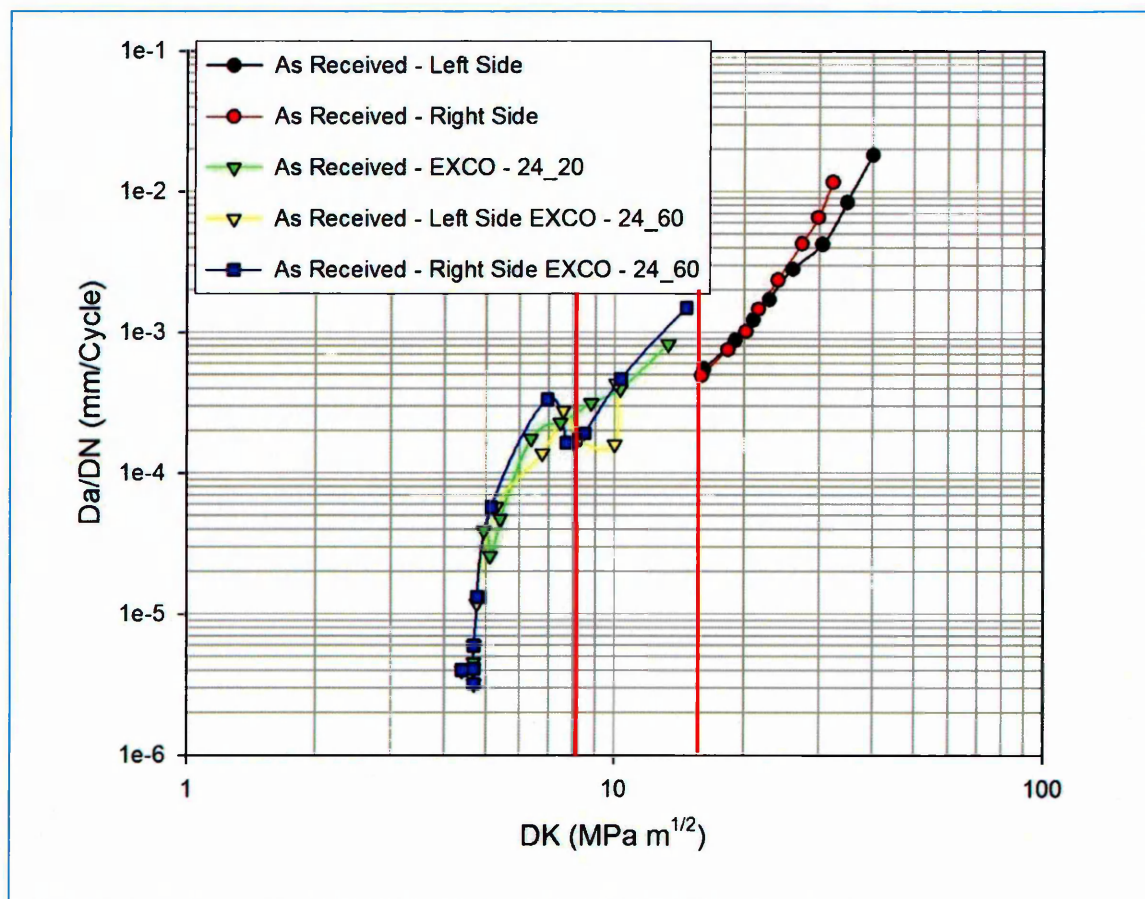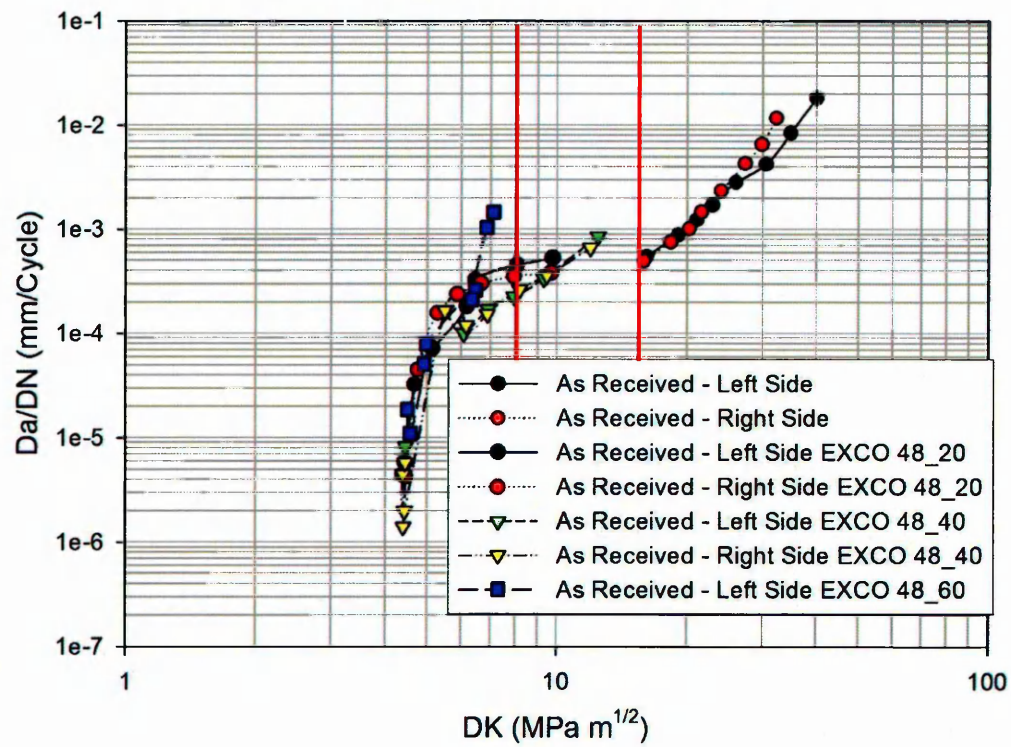
1.3 72 hours exfoliation at different temperatures - As Received
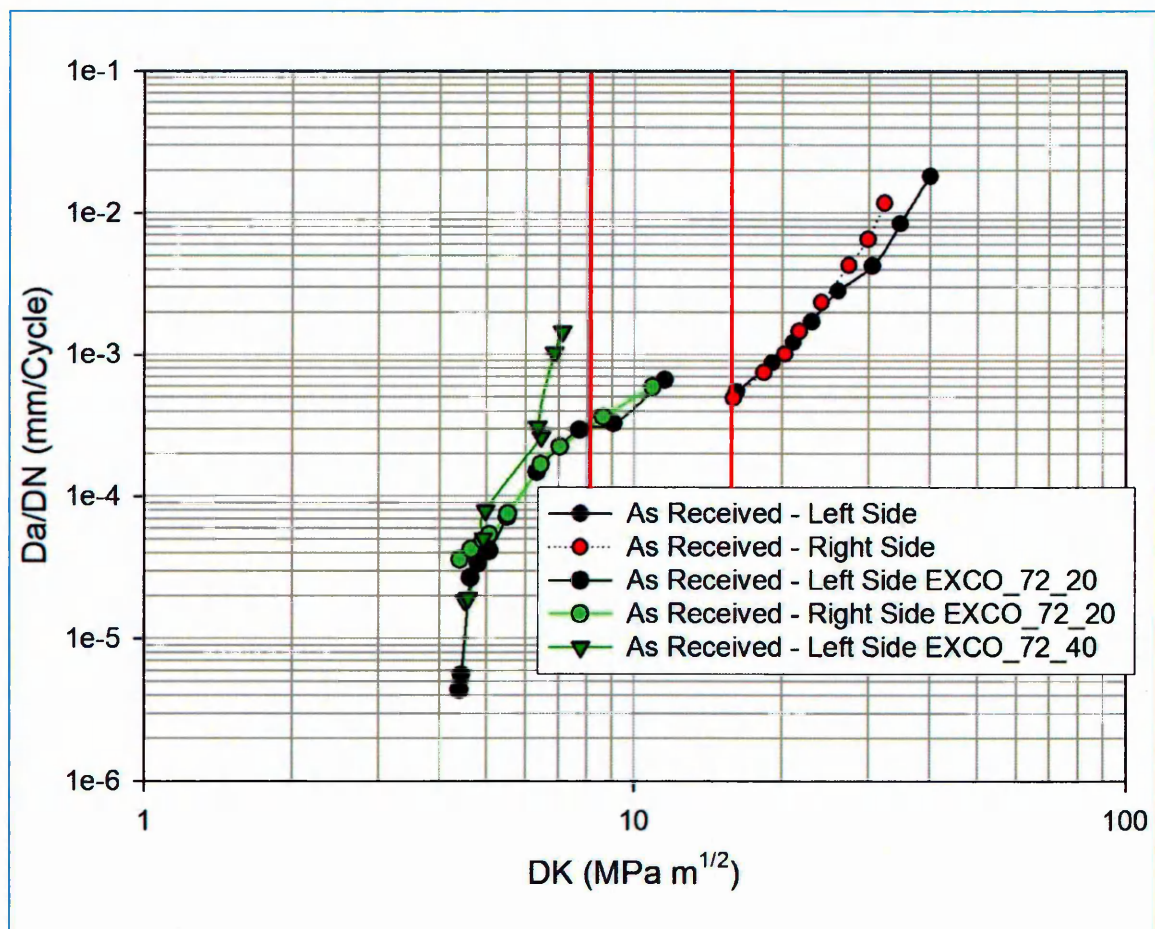
2.2 UIT1 Condition

2.2.1 24 hours exfoliation at different temperatures – UIT1
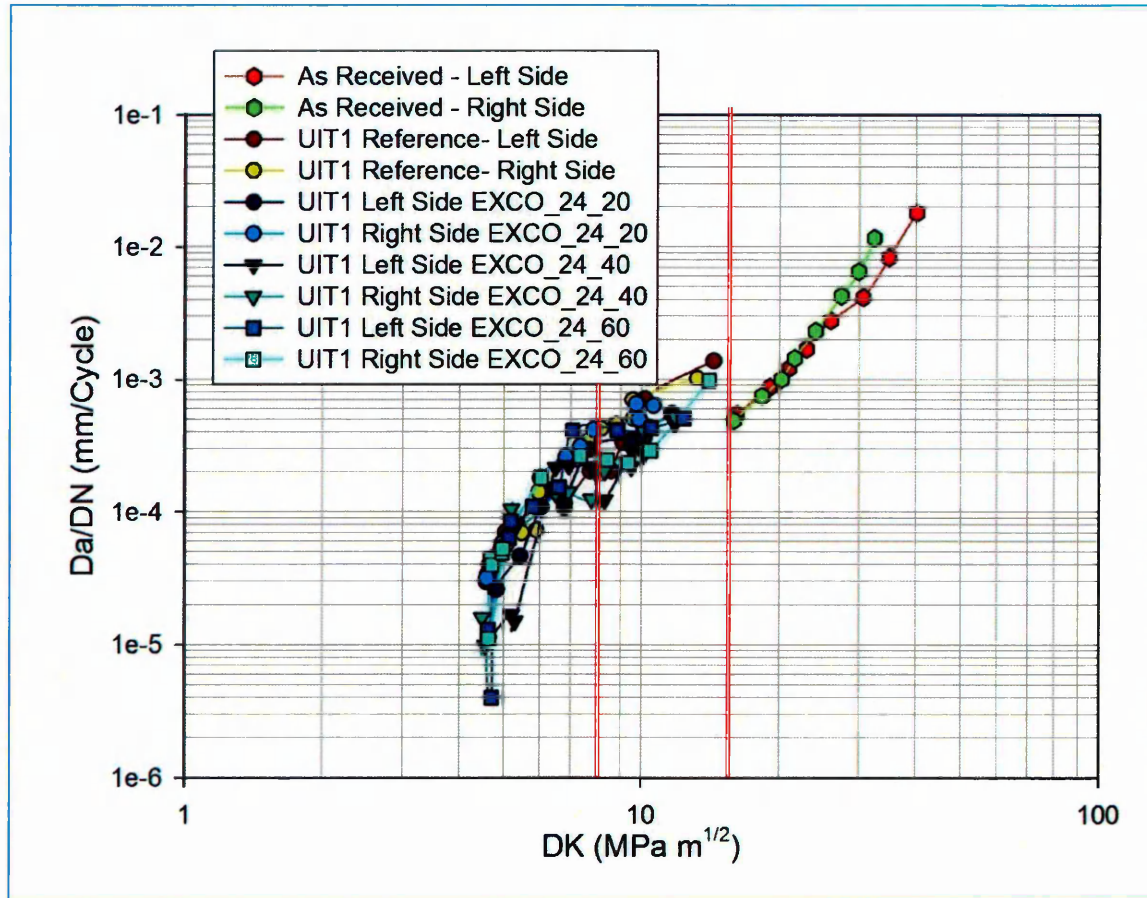
2.2.2 48 hours exfoliation at different temperatures – UIT1
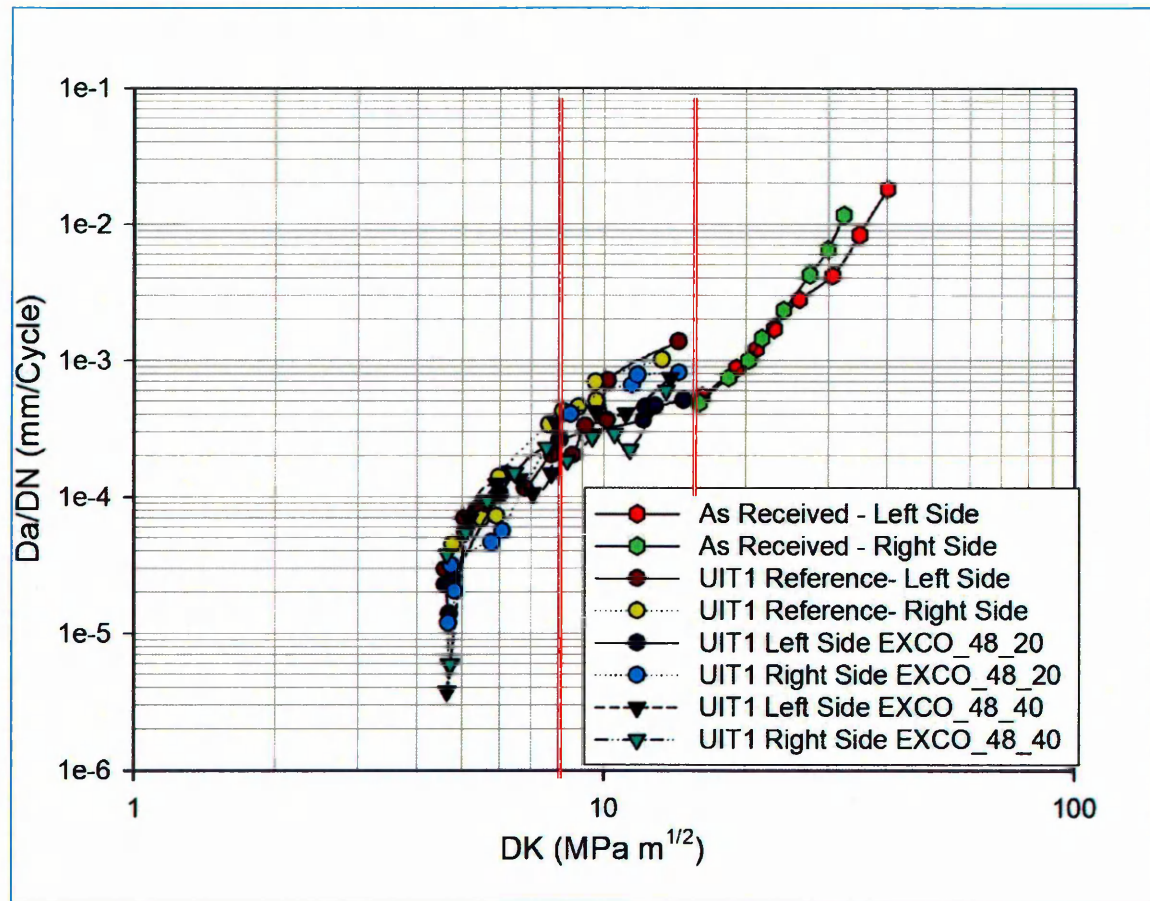
2.2.3 72 hours exfoliation at different temperatures – UIT1
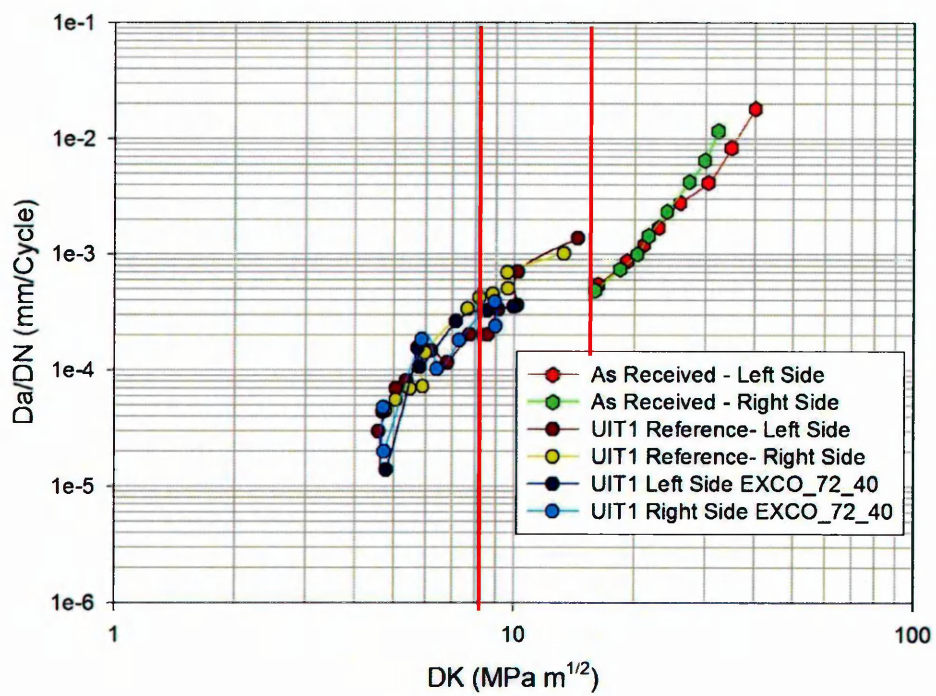
3 Time Dependent Analysis

3.1 As-Received

3.1.1 20 ^{0}C exfoliation at different time - As Received
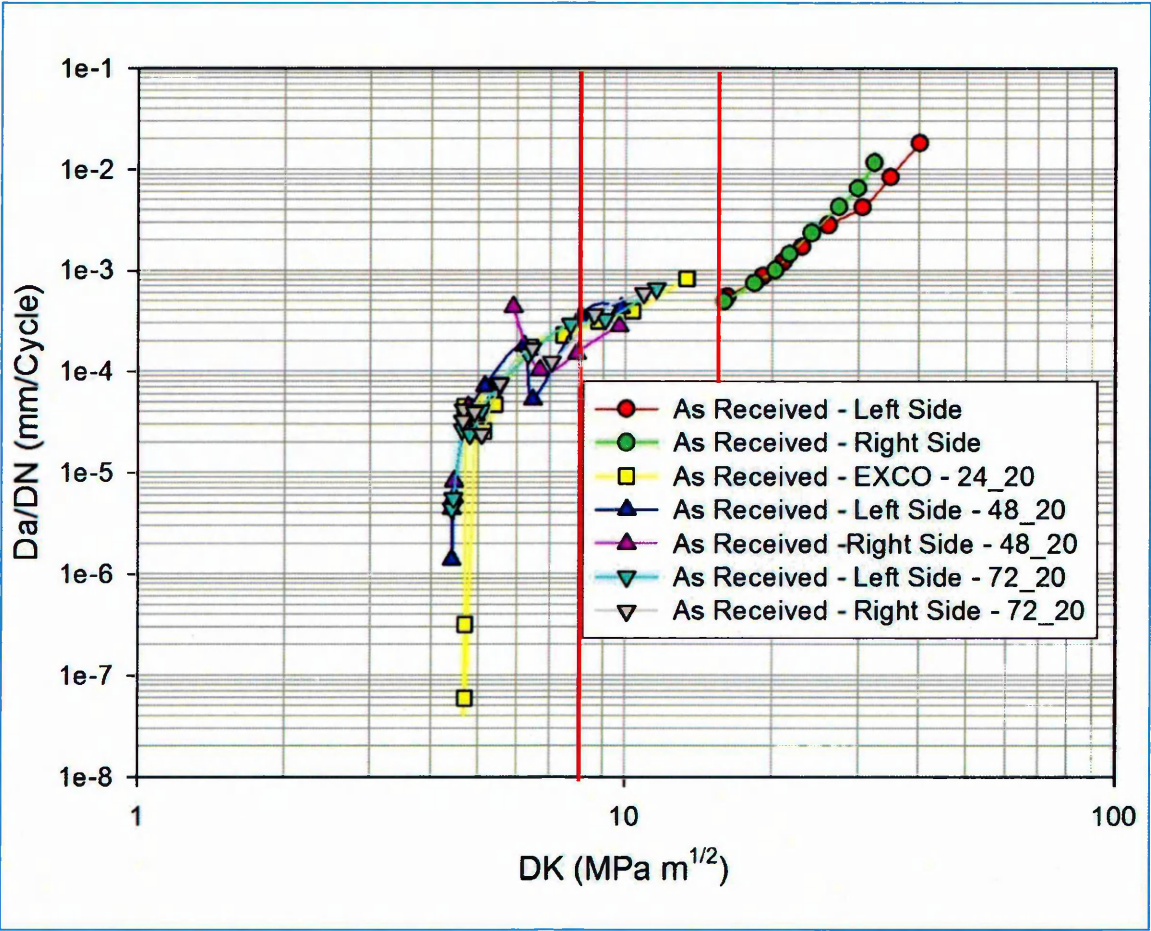
3.1.2 40 ^{0}C exfoliation at different time - As Received
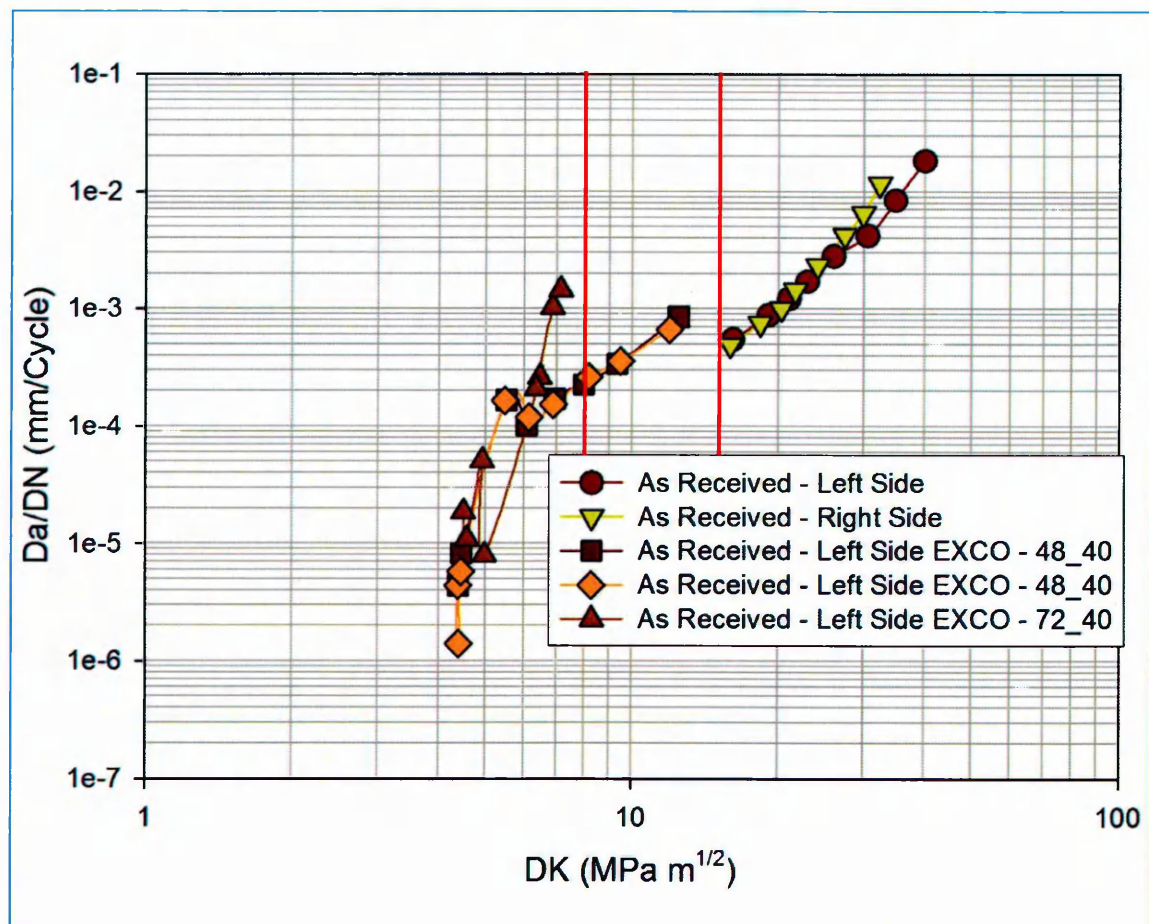
3.1.3 60 ^{0}C exfoliation at different time - As Received
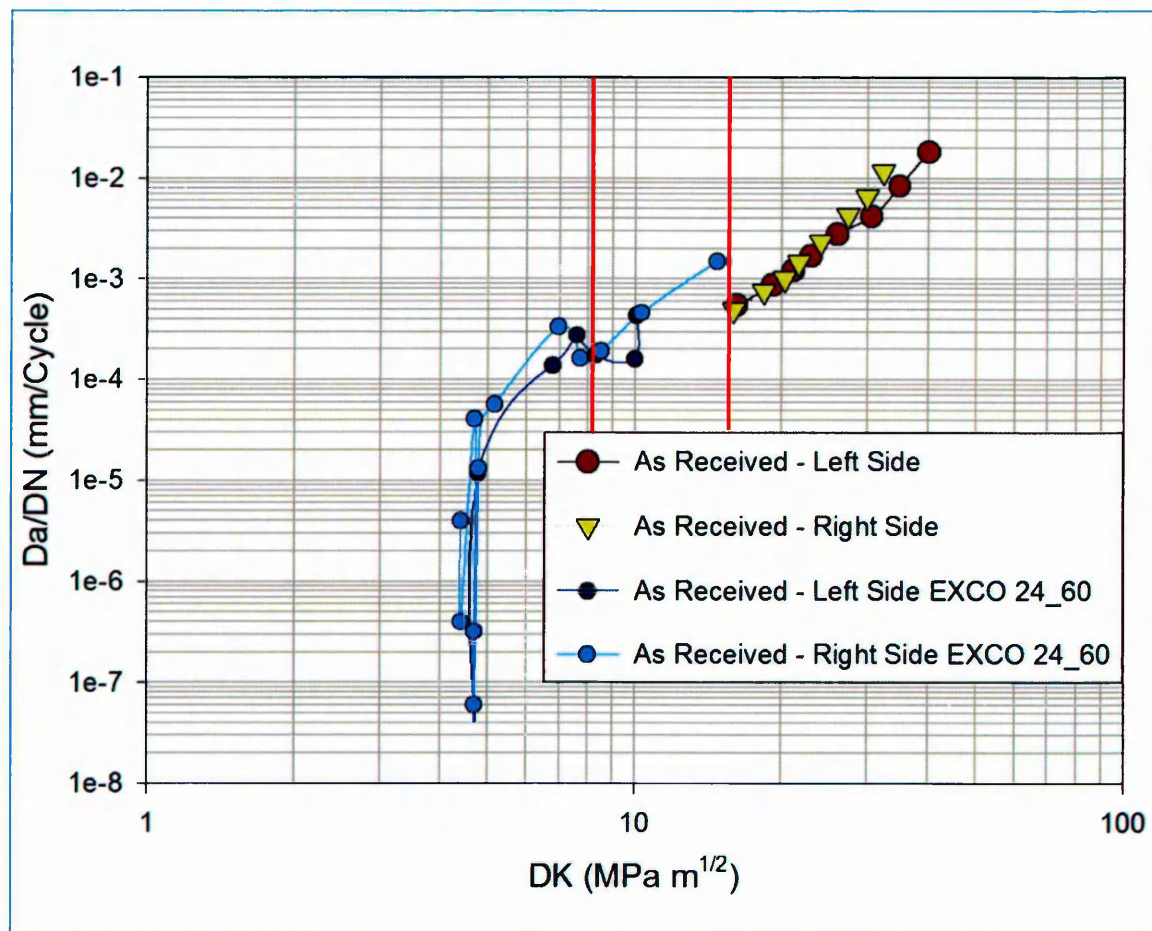
3.2 UIT Condition

3.2.1 20 ^{0}C exfoliation at different time – UIT1
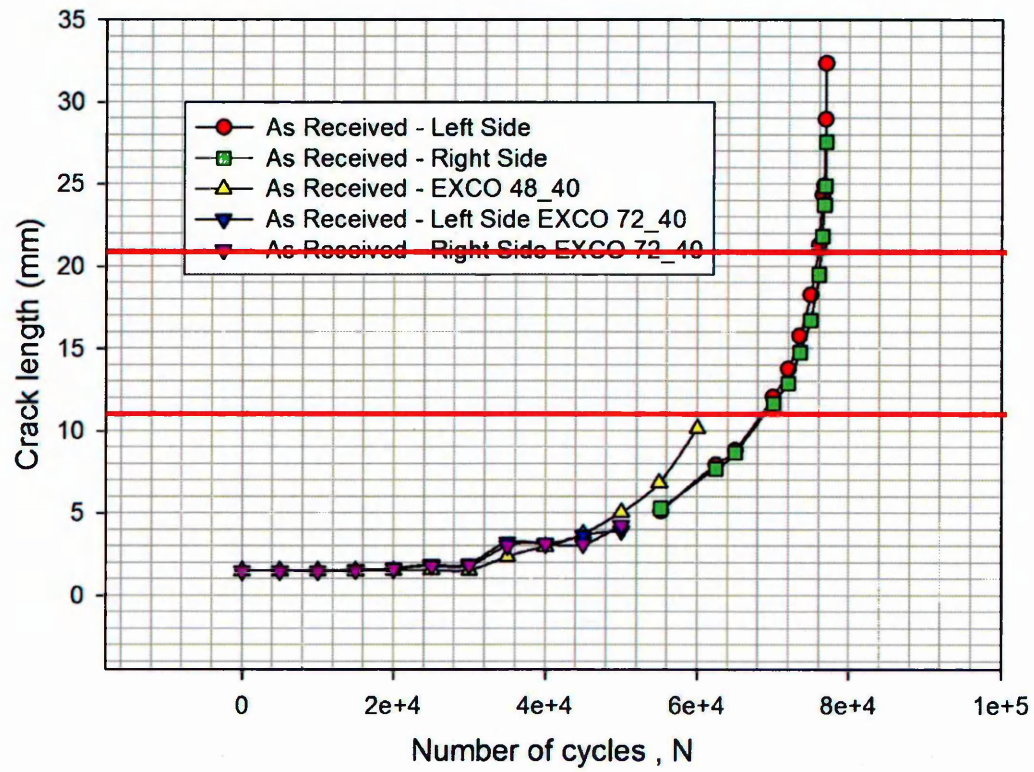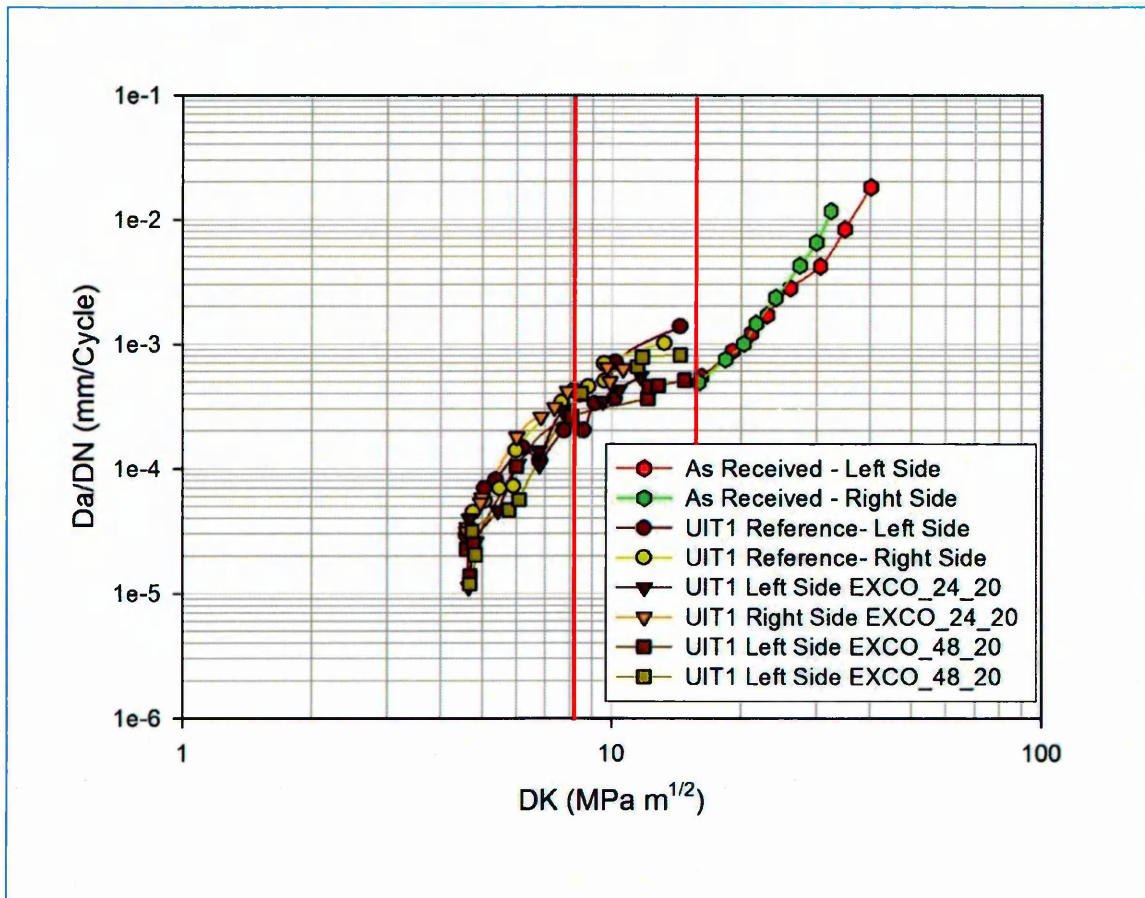
3.2.2 40 ^{0}C exfoliation at different time – UIT1
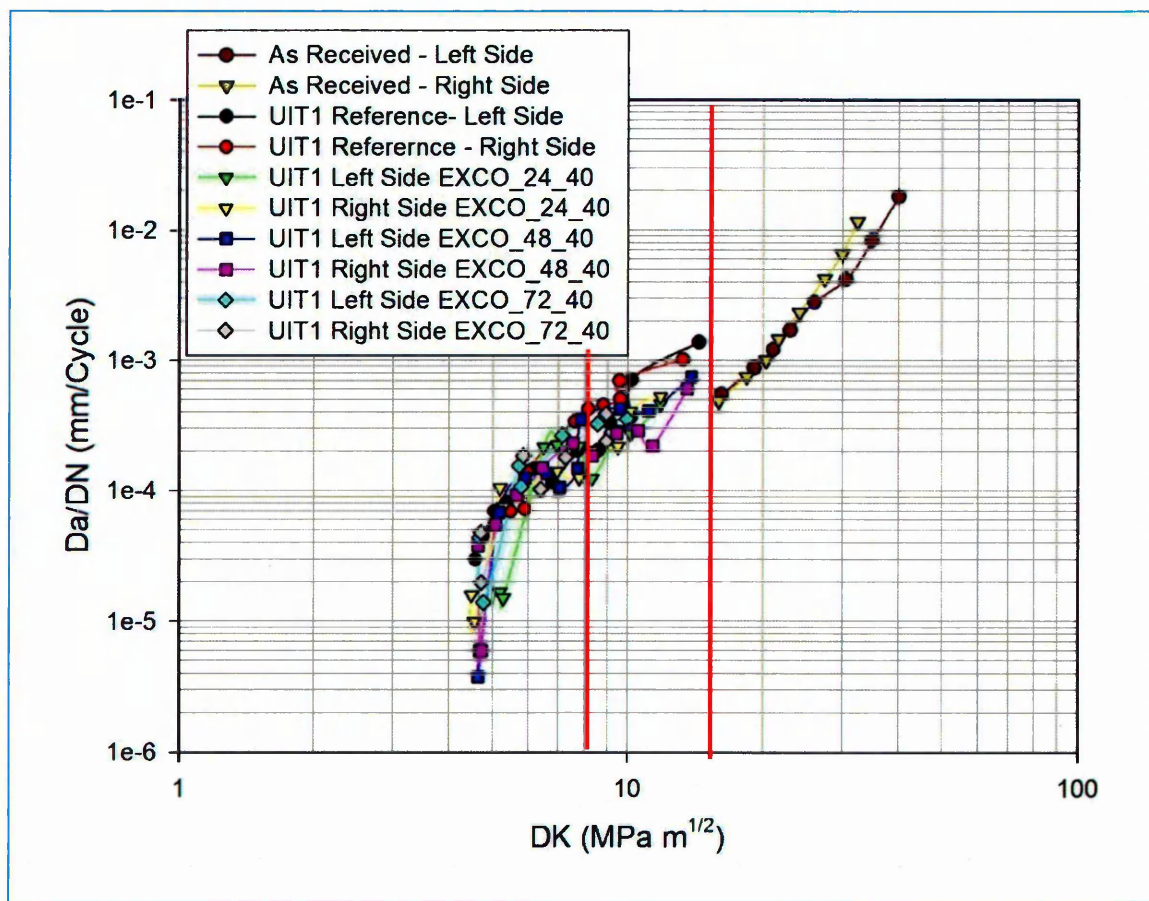
3.2.3 60 ^{0}C exfoliation at different time – UIT1
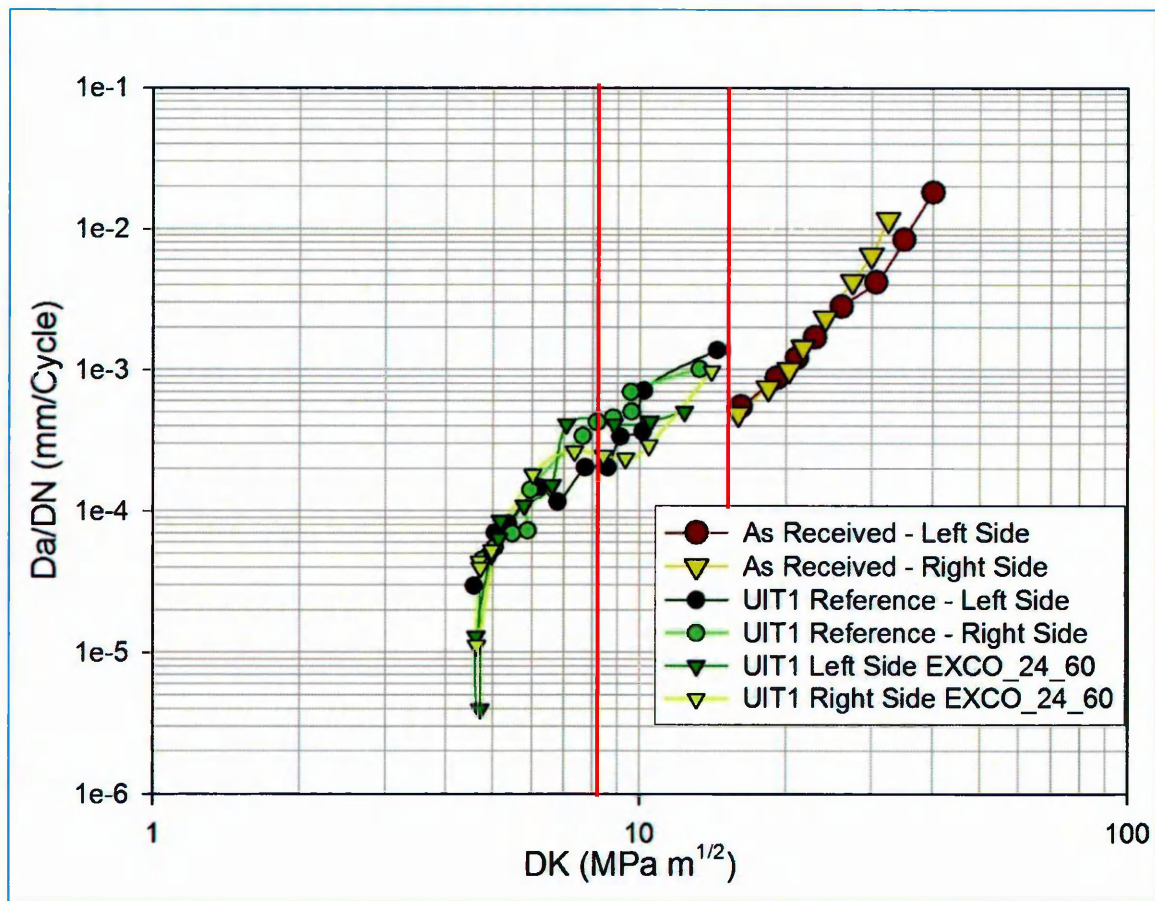
References

1   D. Miller "Corrosion control on Aging Aircraft: What is being done?", Materials Performance, October 1990, pp.10-11.

2   Aircraft Accident Report, Aloha Airlines, Flight 243, Boeing 737-200, N73711, Near Maui, Hawaii, April 28 1988, NTSB Report No. NTSB/AAR-89/03, National Transportation Safety Board, Washington, D.C., USA, 1989.

3   Massoud Bazargan, Kenneth Knopp, Charles Nipper, The effect of ageing on General Aviation Accidents, Embry-Riddle Aeronautical University (ERAU), College of Business, FL 32114, USA.

4   Corrosion-induced hydrogen embrittlement of 2024 and 6013 aluminium alloys Petroyiannis, P.V. (Dept. of Mech. Eng./Aeronautics, Lab. of Technol./Strength of Mat., University of Patras); Kermanidis, Al.Th.; Papanikos, P.; Pantelakis, Sp.G. Source: Theoretical and Applied Fracture Mechanics, v 41, n 1-3, April, 2004, p 173-183 ISSN: 0167-844.

5   Institute of Materials, Minerals & Mining (IoM3), Corrosion Committee of surface engineering division.

        Available: http://www.iom3.org/content/corrosion-committee

6   Fontana, M.G; Corrosion Engineering 3rd Edition, McGraw-Hill, Singapore, (1987) ISBN: 0072939737

7   Dolley, E.J; Lee, B.; Wei, R.P, The effect of pitting corrosion on fatigue life, fatigue and fracture of engineering materials and structures, 23, 55-560, (2000).

8   Chen, G.S; Wan, K.C; Gao, M; Wei, R.P, Flournoy, T.H, Transition from pitting to fatigue crack growth - Modelling of corrosion fatigue crack nucleation in a 2024-T351 aluminium alloy, Materials Science and Engineering A, 219, 126-132, (1996).

9   Z. Szklarska-Smialowska (1986) Pitting Corrosion of Metals, National Association of Corrosion Engineers, Houston, Texas.

10   D. A. Jones (1982) Localized Corrosion, In: Corrosion Processes, Ed. R. N. Parkins, Applied Science Publishers, Barking, Essex, 161-207.

11   Shreir, L.L, Corrosion 1, 2nd Ed., Newnes-Butterworth, London, England, (1976)

12   ASTM G110 - 92(2003)e1 Standard Practice for Evaluating Intergranular Corrosion Resistance of Heat Treatable Aluminum Alloys by Immersion in Sodium Chloride + Hydrogen Peroxide Solution Active Standard ASTM G110 Developed by Subcommittee: G01.05 Volume: 03.02

13   H.K Birnbaum, I.M Robertson, P. Sofronis D. Teter, (1996), Mechanisms of hydrogen induced fracture – a review. In: Magnin T, editor. Second Int. Conf Corrosion-Deformation Interactions CDI '96, The institute of Materials, Nice, France, P. 172-95.

14   D. Delafosse, T. magnin, (2000) Hydrogen Induced plasticity in stress corrosion cracking of engineering systems, Engineering Fracture Mechanics 68, 693-729.

15   Suresh S., Fatigue of Materials, 2nd ed, Cambridge : Cambridge University Press, 1998, ISBN 0521570468.

16   N.E. Dowling, Mechanical Behaviour of Materials: Engineering Methods of Deformation, Fracture, and Fatigue, 2nd ed., ISBN 0-13-905720-X, Prentice-Hall, Upper Saddle River, New Jersey, 830 pages, 1999. ISBN 0135790468.

17   J. A. Ewing and J. C. Humphrey (1903) The Fracture of Metals under Rapid Alterations of Stress, Philosophical Transactions of the Royal Society, London, A200, 241-250.

18   Irwin G.R (1956), Onset of fast fatigue crack propagation in high strength steel and aluminium alloys, In Proceedings of the second sagamore conference Vol II, pp 289-305.

19   Inglis, C.E, (1913), Stress in a plate to the presence of cracks and sharp corners, Transactions of the Institute of Naval Arachitects 55, 219-41.

20   P. C. Paris and F. Erdogan (1963) A Critical Analysis of Crack Propagation Laws, Journal of Basic Engineering, 85, 528-534.

21   J. C., Jr. Newman, Wolf (EDT) Elber, Mechanisms of fatigue crack closure, ASTM International, Jun 1, 1988, page 6, ISBN 0803109962.

22   S. P. Timoshenko (1953) History of Strength of Materials, McGraw-Hill Publishing Company Ltd. ISBN 0486611876.

23   H. Neuber (1958) Theory of Notch Stresses, Springer Publishers, Berlin. ISBN 079236841X

24   R. E. Peterson (1974) Stress Concentration Factors, John Wiley and Sons, New York. ISBN 0470048247.

25   A. S. Tetelman and A. J. McEvily Jr. (1967) Fracture of Structural Materials, John Wiley & Sons, Inc.

26   N. Thompson, N. J. Wadsworth and N. Louat (1956) The Origin of Fatigue Fracture in Copper, Philosophical Magazine, 1, 113-126. ISBN 0871700182.

27   Jaap Schijve (2001) Fatigue of Metals, Published by Springer. ISBN 0792370147.

28   B. T. Ma and C. Laird (1989) Overview of Fatigue Behaviour in Copper Single Crystals – II. Population, Size, Distribution and Growth Kinetics of Stage I Cracks for Tests at Constant Strain Amplitude, Acta Metallurgica, 37, 337-348.

29   Gerber, H., (1874),"Bestimmung der zulässigen Spannungen in Eisen-konstructionen". Zeitschrift des Bayerischen Architeckten und Ingenieur- Vereins 6, pp. 101-110.

30   Goodman, J., (1899), "Mechanics Applied to Engineering". London: Longmans Green 1919. Original from the University of California.

31   Z.Wang and X.Zhang (2003) Predicting fatigue crack growth life for cold-worked holes based on existing closed-form residual stresses models, In: International Journal of Fatigue, 25, 9-11, 1285-1291.

32   C. R Soderberg (1939). Factor of safety and working stress. Transactions of the American society of mechanical engineers. 52, 13-28.

33   H. Gerber (1874), Identification of the allowed load of iron constituents, Journal of the Bavarian architects and engineers club, 6 101-10.

34   N.J Petch (1958) Phil.Mag.3, 1089.

35   R.W.K Honeycombe (1968) Edward Arnold Publishers Ltd. London, ISBN: 07131 2181 5.

36   L. Campbell (1967), The influence of Metallurgical structure on the mechanisms of fatigue crack propagation, Fatigue crack propagation, ASTM STP 415, pp. 131

37   C. A. Rodopoulos and J. R. Yates (2002) Fatigue Damage Tolerance Analysis Using the Fatigue Damage Map, In: Recent Advances in Experimental Mechanics, Ed. E. E. Gdoutos, Kluwer Academic Publishers, 197-202.

38   P. J. E. Forsyth (1962) A Two Stage Process of Fatigue Crack Growth, In: Crack Propagation, Proceedings of Cranfield Symposium, London: Her Majesty's Stationery Office, 76-94.

39   K. Tanaka and Y. Nakai (1983) Propagation and Non-propagation of Short Fatigue Cracks at a Sharp Notch, Fatigue of Engineering Materials and Structures, 6, 315-327.

40   C. A. Zappfe and C. O. Worden (1951) Fractographic Registrations of Fatigue, Transactions of the American Society for Metals, 43, 958-969.

41   P. J. E. Forsyth and D. A. Ryder (1960) Fatigue Fracture, Aircraft Engineering, 32, 96-99.

42   C. E. Richards and T. C. Lindley (1972) The Influence of Stress Intensity and Microstructure on Fatigue Crack Propagation in Ferritic Materials, Engineering Fracture Mechanics, 4, 951-978.

43   G. R. Irwin (1957) Analysis of Stresses and Strains Near the End of a Crack Traversing a   Plate, Journal of Applied Mechanics, 24, 361-364.

44   K. J. Miller (1982) The Short Crack Problem, Fatigue of Engineering Materials and Structures, 5, 223-232.

45   R. W. Hertzberg (1996) Deformation and Fracture Mechanics of Engineering Materials, 4th Edition, John Wiley and Sons, New York.

46   E647 (1999) Standard Test Method for Measurement of Fatigue Crack Growth Rates, Annual Book of ASTM Standards.

47   S. Pearson (1975) Initiation of Fatigue Cracks in Commercial Aluminium Alloys and the Subsequent Propagation of Very Short Cracks, Engineering Fracture Mechanics, 7, 235-247.

48   J. F. Knott (1973) Fundamentals of Fracture Mechanics, Butterworths, London. ISBN 0470495650.

49   J. R. Rice (1968) A Path Independent Integral and the Approximate Analysis of Strain Concentrations by Notches and Cracks, Journal of Applied Mechanics, 35, 379-386.

50   J. W. Hutchinson (1968) Singular Behaviour at the end of a Tensile Crack in a Hardening Material, Journal of the Mechanics and Physics of Solids, 16, 13-31.

51   J. R. Rice and G. F. Rosengren (1968) Plane Strain Deformation near a Crack Tip in a Power Law Hardening Material, Journal of the Mechanics and Physics of Solids, 16, 1-12.

52   Suresh S, (1998). Fatigue of Materials, Cambridge press, Second edition, Pg 93-94. ISBN 0521570468.

53   J. W. Hutchinson and P. C. Paris (1979) The Theory of Stability Analysis of J-Controlled Crack Growth, In: Elastic – Plastic Fracture, ASTM STP 668, 37-64.

54   N. E. Dowling and J. A. Begley (1976) Fatigue Crack Growth During Gross Plasticity and the J – Integral, In: Mechanics of Crack Growth, ASTM STP 590, 82-103.

55   A. A. Wells (1961) Unstable Crack Propagation in Metals: Damage and Fast Fracture, Proceedings of the Crack Propagation Symposium Cranfield, The College of Aeronautics, Cranfield, England, 1, 210-230.

56   F. M. Burdekin and D. E. W. Stone (1966) The Crack Opening Displacement Approach to Fracture Mechanics in Yielding, Journal of Strain Analysis, 1, 145-153.

57   W. Elber (1970) Fatigue crack closure under cyclic tension, Engineering fracture mechanics, 2. 37-45.

58   R. Akid, K.J Miller (1991), Short fatigue crack growth behaviour of a low carbon steel under corrosion fatigue conditions, Fatigue & fracture of engineering materials and structures.

59   S. Pearson (1975) Initiation of Fatigue Cracks in Commercial Aluminium Alloys and the Subsequent Propagation of Very Short Cracks, Engineering Fracture Mechanics, 7, 235-247.

60   Lankford, J., (1982), "The growth of small fatigue cracks in 7075-T6 aluminum". Fatigue and Fracture of Engineering Materials and Structures. Vol. 5, No. 3: pp. 233-248.

61   Miller, K. J., (1987), "The Behaviour of short fatigue cracks and their initiation. Part I - A review of two recent books". Fatigue and Fracture of Engineering Materials and Structures. Vol. 10, No. 1: pp. 75-91.

62   Miller, K. J., (1987), "The Behaviour of short fatigue cracks and their initiation. Part II - A general summary". Fatigue and Fracture of Engineering Materials and Structures. Vol. 10, No. 1: pp. 75-91.

63   Tokaji, K. and Ogawa, T., (1992), "The growth behaviour of microstructurally small fatigue cracks in metals". Short Fatigue Cracks, ESIS 13 (Edited by K.J. Miller and E.R. de los Rios). Mechanical Engineering Publications, London. pp. 85- 99.

64   H.Kitagawa and S. Takahashi (1976), Applicability of fracture mechanics to very small cracks or the cracks in the early stage, In: Proceedings of the second international conference on mechanical behaviour of materials, ASM, 627-631.

65   M. W. Brown Interfaces between short, long, and non-propagating cracks, the behaviour of short fatigue cracks, EGF Pub. 1 (Edited by K.J Miller and E.R. de los Rios) 1986, Mechanical Engineering Publications, London, pp. 423-439.

66   ASTM F1801-97 (2004), Standard Practice for corrosion fatigue testing of metallic implant materials, F04.15, Vol. 13.01.

67   W. Schütz (1995) Corrosion Fatigue – The Forgotten Factor in Assessing Durability, In: Estimation, Enhancement and Control of Aircraft Fatigue Performance, Eds. J. M. Grandage and G. S. Jost, ICAF 95, EMAS Publications, 1-51.

68   L. B. Vogelesang (1976) Some Factors Influencing the Transition from Tensile Mode to Shear Mode under Cyclic Loading, Report LR-222, Aerospace Department, Delft University of Technology, The Netherlands.

69   M. P. Blinn, M. Miller and D. W. Hoeppner (1995) The Effects of Frequency and Anisotropy on the Corrosion Fatigue Crack Propagation Behaviour of AA 2224-T351511, In: Estimation, Enhancement and Control of Aircraft Fatigue Performance, Eds. J. M. Grandage and G. S. Jost, ICAF 95, EMAS Publications, 1041-1052.

70 P. M. Scott (1983) Chemistry Effects in Corrosion Fatigue, In: Corrosion Fatigue: Mechanics, Metallurgy, Electrochemistry and Engineering, Eds. T. W. Crooker and B. N. Leis, ASTM STP 801, 319-350.

71 C. Q. Bowles and J. Schijve (1983) Experimental Observations of Environmental Contributions to Fatigue Crack Growth, In: Corrosion Fatigue: Mechanics, Metallurgy, Electrochemistry and Engineering, Eds. T. W. Crooker and B. N. Leis, ASTM STP 801, 96-114.

72 C. Q. Bowles (1978) A Study of Crack Tip Geometry Resulting from Fatigue Crack Propagation in Air and Vacuum, Report LR-261, Aerospace Department, Delft University of Technology, the Netherlands.

73 W. Schütz (1995) Corrosion Fatigue – The Forgotten Factor in Assessing Durability, In: Estimation, Enhancement and Control of Aircraft Fatigue Performance, Eds. J. M. Grandage and G. S. Jost, ICAF 95, EMAS Publications, 1-51.

74 J. M. Barsom (1972) Effect of Cyclic Stress Form on Corrosion Fatigue Crack Propagation below KIscc in a High Yield Strength Steel, In: Corrosion Fatigue: Chemistry, Mechanics and Microstructure, NACE 2, Eds. O. F. Devereux, A. J. McEvily and R. W. Staehle, National Association of Corrosion Engineers, Houston, Texas, 424-436.

75 J. Schijve (2001) Fatigue of Structures and Materials, Kluwer Academic Publishers, The Netherlands.

76 R. J. H. Wanhill, J. J. De Luccia and M. T. Russo, 1989, The Fatigue in Aircraft Corrosion Testing (FACT) Programme, Agard Report R-713.

77 W. Schütz (1979) Fatigue Life under Realistic Load Sequences and Corrosion, In: Structural Fatigue as a Design Factor, Ed. A. Maenhout, ICAF 79, EMAS Publications, Document no. 1169.

78   Y. Nakai, A. Alavi and R. P. Wei (1988) Effects of Frequency and Temperature on Short Fatigue Crack Growth in Aqueous Environments, Metallurgical Transactions A, 19, 543-548.

79   R. P. Wei and G. Shim (1983) Fracture Mechanics and Corrosion Fatigue, In: Corrosion Fatigue: Mechanics, Metallurgy, Electrochemistry and Engineering, Eds. T. W. Crooker and B. N. Leis, ASTM STP 801, 5-25.

80   D. J. Duquette and H. H. Uhlig (1968) Effect of Dissolved Oxygen and NaCl on Corrosion Fatigue of 0.18% Carbon Steel, Transactions of ASM, 61, 449-456.

81   K. C. Wan, G. S. Chen, M. Gao and R. P. Wei (2000) Interactions between Mechanical and Environmental Variables for Short Fatigue Cracks in a 2024-T351 Aluminium Alloy in 0.5M NaCl Solutions, Metallurgical and Materials Transactions A, 31, 1025-1034.

82   F. J. Bradshaw and C. Wheeler (1969) The Influence of Gaseous Environment and Fatigue Frequency on the Growth of Fatigue Cracks in some Aluminium Alloys, International Journal of Fracture Mechanics, 5, 255-268.

83   H. P. Chu and J. G. Macco (1978) Corrosion Fatigue of 5456-H117 Aluminium Alloy in Seawater, In: Corrosion-Fatigue Technology, Eds. H. L. Craig Jr, T. W. Crooker and D. W. Hoeppner, ASTM STP 642, 223-239.

84   L. V. Corsetti and D. J. Duquette (1974) The Effect of Mean Stress and Environment on Corrosion Fatigue Behaviour of 7075-T6 Aluminium, Metallurgical Transactions, 5, 1087-1093.

85   T. C. Lindley, P. McIntyre and P. J. Trant (1982) Fatigue-Crack Initiation at Corrosion Pits, Metals Technology, 9, 135-142.

86   G. S. Chen, C. M. Liao, K. C. Wan, M. Gao and R. P. Wei (1997) Pitting Corrosion and Fatigue Crack Nucleation, In: Effects of the Environment on the Initiation of Crack Growth, Eds. W. A. Van Der Sluys, R. S. Piascik and R. Zawierucha, ASTM STP 1298, 18-31.

87   S. Ishihara, T. Goshima, A. J. McEvily, S. Sunada and S. Nomata (2001) Corrosion-Pit-Growth Behaviour During the Corrosion Fatigue Process in Aluminium, In: International Conference on Fracture 10, Hawaii, Eds. K. Ravi-Chandar, B. L. Karihaloo, T. Kishi, R. O. Ritchie, A. T. Yokobori Jr, Elsevier Science Ltd, Oxford, UK, Paper no. 0805.

88   S. Kawai and S. Kasai (1985) Considerations of Allowable Stress of Corrosion Fatigue (Focused on the Influence of Pitting), Fatigue and Fracture of Engineering Materials and Structures, 8, 115-127.

89   M. R. Bayoumi, A. A. Ismail and A. K. Abdel-Latif (1996) Finite Element Analysis of Stresses due to Pitting of Steel Specimens under Different Cyclic Bending Stresses, Engineering Fracture Mechanics, 53, 141-151.

90   S. A. Curtis, E. R. de los Rios, C. A. Rodopoulos and J. R. Yates (2002) Investigating Pitting Characteristics of Aluminium Alloy 2024-T35151 using Surface Roughness Measurements, In: New Challenges in Mesomechanics, Eds. R. Pyrz, J. Schjødt-Thomsen, J. C. Rauhe, T. Thomsen and L. R. Jensen, 635-639.

91   S. Zhou and A. Turnbull (1999) Influence of Pitting on the Fatigue Life of a Turbine Blade Steel, Fatigue and Fracture of Engineering Materials and Structures, 22, 1083-1093.

92   Y. Murakami and M. Endo (1983) Quantitative Evaluation of Fatigue Strength of Metals Containing Various Small Defects or Cracks, Engineering Fracture Mechanics, 17, 1.

93   Y. Murakami and M. Endo (1986) Effects of Hardness and Crack Geometries on ΔK_{th} of Small Cracks Emanating from Small Defects, In: The Behaviour of Short Fatigue Cracks, Eds. K. J. Miller and E. R. de los Rios, Mechanical Engineering Publications, London, 275-293.

94   Y. Murakami and M. Endo (1983) Quantitative Evaluation of Fatigue Strength of Metals Containing Various Small Defects or Cracks, Engineering Fracture Mechanics, 17, 1.

95   R. Akid (1997) The Role of Stress-Assisted Localized Corrosion in the Development of Short Fatigue Cracks, In: Effects of the Environment on the Initiation of Crack Growth, Eds. W. A. Van Der Sluys, R. S. Piascik and R. Zawierucha, ASTM STP 1298, 3-17.

96   E. R. de los Rios, Z. Y. Sun and K. J. Miller (1994) A Theoretical and Experimental Study of Environmental Hydrogen-Assisted Short Fatigue Crack Growth in an Al-Li Alloy, Fatigue and Fracture of Engineering Materials and Structures, 17, 1459-1474.

97   J. Congleton and I. H. Craig (1982) Corrosion Fatigue, In: Corrosion Processes, Ed. R. N. Parkins, Applied Science Publishers, Barking, Essex, 209-269.

98   K. Endo, K. Komai and T. Shikida (1983) Crack Growth by Stress-Assisted Dissolution and Threshold Characteristics in Corrosion Fatigue of a Steel, In: Corrosion Fatigue: Mechanics, Metallurgy, Electrochemistry and Engineering, Eds. T. W. Crooker and B. N. Leis, ASTM STP 801, 81-95.

99   J. Congleton, I. H. Craig, R. A. Olieh and R. N. Parkins (1983) Some Electrochemical and Microstructural Aspects of Corrosion Fatigue, In: Corrosion Fatigue: Mechanics, Metallurgy, Electrochemistry and Engineering, Eds. T. W. Crooker and B. N. Leis, ASTM STP 801, 367-389.

100   Z. F. Wang, J. Q. Wang, J. Li and W. Ke (1995) Relation between CF Crack Propagation Rate and Dissolution Rate at a Crack Tip for Iron in 3.5% NaCl Solution, Scripta Metallurgica et Materialia, 32, 487-492.

101   Sp. G. Pantelakis, P. G. Daglaras and Ch. Alk. Apostolopoulos (2000) Tensile and Energy Density Properties of 2024, 6013, 8090 and 2091 Aircraft Aluminium Alloy after Corrosion Exposure, Theoretical and Applied Fracture Mechanics, 33, 117-134.

102   A. Toshimitsu Yokobori Jr., Yasrou Chinda, Takenao Nemoto, Koji Satoh, Tetsuya Yamada, (2001) The characteristics of hydrogen diffusion and concentration around a crack tip concerned with hydrogen embrittlement, Corrosion Science 44, 407-424.

103   Sp. G. Pantelakis, P. G. Daglaras and Ch. Alk. Apostolopoulos (2000) Tensile and Energy Density Properties of 2024, 6013, 8090 and 2091 Aircraft Aluminium Alloy after Corrosion Exposure, Theoretical and Applied Fracture Mechanics, 33, 117-134.

104   Al. Th. Kermanidis, P. Papanikos and Sp. G. Pantelakis (2001) Mesodamage of 2024-T351 Aluminium Alloy Specimen due to Corrosion-Induced Localized hydrogen Embrittlement, In: International Conference on Fracture 10, Hawaii, Eds. K. Ravi-Chandar, B. L. Karihaloo, T. Kishi, R. O. Ritchie, A. T. Yokobori Jr, Elsevier Science Ltd, Oxford, UK, Paper no. 1047.

105   I.C. Howard (1979) Models of the Reduction of Fracture Toughness due to Hydrogen in Strong Steels, ICM 3, 463-474.

106   P. Papanikos and Al. Th. Kermanidis (2002) Effect of Corrosion-Induced Hydrogen Embrittlement on the Fracture Toughness of 2024-T351 Aluminium Alloy, In: New Challenges in Mesomechanics, Eds. R. Pyrz, J. Schjødt-Thomsen, J. C. Rauhe, T. Thomsen and L. R. Jensen, 627-633.

107   C. Zappfe and C. E. Sims (1941) Hydrogen Embrittlement, Internal Stress and Defects in Steel, Transactions of the American Institute of Mining, Metallurgical and Petroleum Engineers, 145, 225-271.

108   J. G. Morlet, H. H. Johnson and A. R. Troiano (1958) A New Concept of Hydrogen Embrittlement in Steel, Journal of Iron and Steel Institute, 189, 37-44.

109   R. A. Oriani and P. H. Josephic (1974) Equilibrium Aspects of Hydrogen-Induced Cracking in Steels, Acta Metallurgica, 22, 1065-107.

110   N. J. Petch (1956) Lowering of Fracture Stress due to Surface Adsorption, Philosophical Magazine, 1, 331-337.

111   A. Toshimitsu Yokobori Jr., Yasrou Chinda Takenao Nemoto, Koji Satoh, Tetsuya Yamada The characteristics of hydrogen diffusion and concentration around a

crack tip concerned with hydrogen embrittlement, Corrosion science 44 (2002) 407-424.

112   J.R. Scully, G.A. Young Jr., S.W. Smith, (2000) Hydrogen solubility, Diffusion and trapping in high purity aluminium and selected Al-Base alloys, Centre for Electrochemical Science & Engineering, Charlottesville, VA 22903-2442, USA.

113   ASTM G34 - 01(2007) Standard Test Method for Exfoliation Corrosion Susceptibility in 2XXX and 7XXX Series Aluminum Alloys (EXCO Test).

114   S. C. Mittal (1997) Hydrogen Embrittlement during Fatigue in Austenitic Steel, In: Engineering Against Fatigue, Eds. J. H. Beynon, M. W. Brown, T. C. Lindley, R. A. Smith and B. Tomkins, A. A. Balkema, Rotterdam, 625-632.

115   E. R. de los Rios, Z. Y. Sun and K. J. Miller (1993) The Effect of Hydrogen on Short Fatigue Crack Growth in an Al-Li Alloy, Fatigue and Fracture of Engineering Materials and Structures, 16, 1299-1308.

116   A. R. Troiano (1960) The Role of Hydrogen and other Interstitials in the Mechanical Behaviour of Metals, Transactions of ASM, 52, 54-80.

117   T. Tabata and H. K. Birnbaum (1983) Direct Observations of the Effect of Hydrogen on the Behaviour of Dislocation in Iron, Scripta Metallurgical, 17, 947-950.

118   T. Matsumoto, J. Eastman and H. K. Birnbaum (1981) Direct Observations of Enhanced Dislocation Mobility due to Hydrogen, Scripta Metallurgica, 15, 1033-1037.

119   G. M. Bond, I. M. Robertson and H. K. Birnbaum (1987) The Influence of Hydrogen on Deformation and Fracture Processes in High-Strength Aluminium Alloys, Acta Metallurgica, 35, 2289-2296.

120   R. P. Wei and J. D. Landes (1969) Correlation between Sustained-Load and fatigue Crack growth in High Strength Steels, Materials Research and Standards, 9, 25-28.

121   R. P. Wei (1979) On Understanding Environment-Enhanced Fatigue Crack Growth – A Fundamental Approach, In: Fatigue Mechanisms, Ed. J. Fong, ASTM STP 675, 816-840.

122   R. P. Wei and M. Gao (1983) Reconsideration of the Superposition Model for Environmentally Assisted Fatigue Crack Growth, Scripta Metallurgica, 17, 959-962.

123   R. P. Wei, G. Shim and K. Tanaka (1984) Corrosion Fatigue and Modelling, In: Embrittlement by the Localized Crack Environment, Ed. R. P. Gangloff, The Metallurgical Society of AIME, 243-263.

124   R. P. Wei and D. G. Harlow (1993) A Mechanistically Based Probability Approach for Predicting Corrosion and Corrosion Fatigue Life, In: Durability and Structural Integrity of Airframes, Ed. A. F. Blom, ICAF 93, EMAS Publications, 347-366.

125   D. G. Harlow and R. P. Wei (1998) A Probability Model for the Growth of Corrosion Pits in Aluminium Alloys Induced by Constituent Particles, Engineering Fracture Mechanics, 59, 305-325.

126   I. M. Austen and P. McIntyre (1978) Corrosion Fatigue of High-Strength Steel in Low-Pressure Hydrogen Gas, Metal Science, 13, 420-428.

127   D. W. Hoeppner (1979) Model for Prediction of Fatigue Lives based upon a Pitting Corrosion Fatigue Process, In: Fatigue Mechanisms, Ed. J. Fong, ASTM STP 675, 841-870.

128   Y. Kondo (1989) Prediction of Fatigue Crack Initiation Life based on Pit Growth, Corrosion, 45, 7-11.

129   D. Angelova and R. Akid (1998) A Note on Modelling Short Fatigue Crack Behaviour, Fatigue and Fracture of Engineering Materials and Structures, 21, 771-779.

130   E. R. de los Rios, X. D. Wu and K. J. Miller (1996) A Micro-Mechanics Model of Corrosion-Fatigue Crack Growth in Steels, Fatigue and Fracture of Engineering Materials and Structures, 19, 1383-1400.

n

131 Corporation, American Wheelabrator & Equipment, (1947), Shot Peening. 3rd ed. USA. Mishawaka, Indiana: p. p. 82.

132 Inc., Metal Improvement Company, (1989), Shot peening applications. 7th ed. ed. USA. Paramus.

133 P. Peyre, R Fabbro/ Materials Science and Engineering A210 (1996) 102-113).

134 Krylov, N.A., A.M. Polischuk, The Use of Ultrasonic Equipment for Metal Structure Stabilization (in Russian), In: Basic Physics of Industrial Ultrasonic Applications, Part 1, LDNTP, p. 70, 1970.

135 Statnikov, E.Sh., L.V. Zhuravlev, A.F. Alekseev et al., Ultrasonic Head for Strain Hardening and Relaxation Treatment (in Russian), USSR Inventor's Certificate No. 472782, Published in Byull. Izobret., No. 21 (1975).

136 X. Wu, N.Tao, Y. Hong, B Xu, J. Lu, K. Lu, Microstructure and evolution of mechanically-induced ultrafine grain in surface layer of AL-alloy subjected to USSP, Acta Materialia, 2002, 50, 8, 2075-2084.

137 Richard Payling, Delwyn Jones, Arne bengston, Glow discharge optical emission spectroscopy, ISBN 0-471-96683 5.

138 Thomas Nelis, Max Aeberhard, Richard Payling, Johann Michler, Patrick Chapon, (2004) Relative calibration mode for compositional depth profiling in GD-OES, JAAS, Vol 19, Pg 1354-1360.

139 Practical scanning electron microscopy: electron and ion microprobe analysis/ edited by Joseph I Goldstein and Harvey Yakowitz, Plenum Press, 1976.

140 ASTM G34 - 01(2007) Standard Test Method for Exfoliation Corrosion Susceptibility in 2XXX and 7XXX Series Aluminum Alloys (EXCO Test)

141 ASTM E466-82 , Standard Practice for Conducting Constant Amplitude Axial Fatigue Tests of Metallic Materials.

143 ASTM G110 - 92(2003)e1 Standard Practice for Evaluating Intergranular Corrosion Resistance of Heat Treatable Aluminum Alloys by Immersion in Sodium Chloride + Hydrogen Peroxide Solution.

144 J. R Scully, R. R Frankenthal, K.J Hanson, D.F Siconolfi, J.D Sinclair, (1990), Journal of Electrochemical Society, 137, 1373.

145 B. A Kolachev, (1968) Hydrogen Embrittlement of Nonferrous Metals, Israel Program for Scientific Translations ltd. Pg. 24.

146 Kamoutsi, H, Haidemenopoulos, G.N, Bontozoglou V, Pantelakis S., Corrosion induced hydrogen embrittlement in aluminium alloy 2024, Corrosion Science 48(2006) 1209.

147 ASTM E8M-94a, Standards tests methods for tension testing of metallic materials (metric), Annual Book of ASTM Standards, Section 3, Metal Test Methods and Analytical Procedures, West Conshohocken, ASTM, Philadelphia, USA, pp. 88-96.

148 Michael Bauccio, ASM Metals Reference Book, Third Edition, Ed. ASM International, Materials Park, OH, 1993.

149 Statnikov, E.Sh., L.V. Zhuravlev, A.F. Alekseev et al., Ultrasonic Head for Strain Hardening and Relaxation Treatment, USSR Inventor's Certificate No. 472782, Published in Byull. Izobret., No. 21 (1975).

150 Small Fatigue cracks, R.O. Ritchie and J. Lankford, eds., TMS-AIME, Warrendale, PA (1986)

151 The behaviour of short fatigue cracks, K.J. Miller and E.R. de los Rios, eds., Mechanical Engineering Publications Limited, London, U.K (1986).

152   C.A. Rodopoulos, A.Th. Kermanidis, E. Statnikov, V. Vityazev and O. Korolkov ; The Effect of Surface Engineering Treatments on the Fatigue Behavior of 2024-T351 Aluminum Alloy, Journal of Materials Engineering and Performance, Vol 16, No. 1, 2007.